# 論文 / 著書情報
# Article / Book Information

| | |
|---|---|
| 題目(和文) | チャンドラ衛星を用いたパルサー風星雲の研究 |
| Title(English) | Study of Pulsar wind nebulae with Chandra |
| 著者(和文) | 谷津陽一 |
| Author(English) | Yoichi Yatsu |
| 出典(和文) | 学位:博士（理学）,<br>学位授与機関:東京工業大学,<br>報告番号:甲第7085号,<br>授与年月日:2008年3月26日,<br>学位の種別:課程博士,<br>審査員:河合 誠之 |
| Citation(English) | Degree:Doctor of Science,<br>Conferring organization: Tokyo Institute of Technology,<br>Report number:甲第7085号,<br>Conferred date:2008/3/26,<br>Degree Type:Course doctor,<br>Examiner: |
| 学位種別(和文) | 博士論文 |
| Type(English) | Doctoral Thesis |

# Study of Pulsar Wind Nebulae with Chandra

Department of Physics, Graduate School of Science,
Tokyo Institute of Technology

Yoichi Yatsu

February 2008

## Abstract

A study of pulsar wind nebula around a young energetic pulsar PSR B1509−58 utilizing the *Chandra* X-ray observatory is reported. An isolated pulsar in supernova remnant is believed to lose most of its rotating energy by the particle acceleration process in the pulsar's magnetosphere. The accelerated particles generate a diffuse synchrotron nebula, so-called "Pulsar Wind Nebula (PWN)". Recent X-ray imaging observations revealed that the PWNe possess common morphological features, namely "Jets" and "Tori (rings)", however, the theoretical understandings of the PWNe are still poor. In this study we aim to investigate the mechanism generating tori and jets in PWNe by means of imaging and spectroscopy utilizing *Chandra*. As a target object we selected a PWN accompanied by PSR B1509−58 which has the largest apparent diameter of $\sim$ 20 arcmin. We performed a spatially-resolved spectroscopy in arcs-second scale with particular attention to jets and tori.

Unprecedented fine X-ray image with 190 ks exposure revealed a ring-like structure with a radius of $\sim$ 10 arcsec, which is analogous to the inner ring seen in the Crab nebula and then may correspond to a wind termination shock. It is the second case of the discovery of the pulsar wind termination shock, since the first case in the Crab nebula. The shock radius can constrain the wind magnetization, $\sigma \geq 0.01$. The obtained $\sigma$ is one order of magnitude larger than that of the Crab nebula ($\sigma \sim 0.003$), however, the higher magnetization well explains the observed weak deceleration of the post-shock flow and the rapid spectral evolution in the torus rather than the smaller one.

At the pulsar vicinity, the south jet appears to extend beyond the wind termination shock, in contrast with the jet of the Crab nebula which appears to sprout out directly from the pulsar. The morphology of the jet with a broad base is coincident with the theoretical model in which a magnetic hoop stress diverts and squeezes the equatorial flow towards the poloidal direction generating a jet. The self collimation process by magnetic hoop stress requires a wind magnetization of $\sigma \geq 0.01$, which is already satisfied favorably as mentioned above.

Temporal imaging analysis comparing four *Chandra* observations from 2004 to 2005 provided a jet velocity of $v_{\rm jet} \sim 0.7c$. Adopting the velocity, the energy injection rate into the south jet amounts to 7.8 % of the total spin down luminosity of $\dot{E} = 1.8 \times 10^{37}$ ergs $s^{-1}$. While the evolution of the spectral photon index along the jet is unacceptably fast comparing with the flow velocity, namely the photon index starts getting steeper within 1 arcmin from the pulsar. If the jet is originated in the torus, the particles injected into the jet can be cooled in the torus before arriving at the root of the jet.

# Contents


**1 Introduction** **9**

**2 Review of Pulsar Wind Nebulae** **11**

2.1 Rotating Powered Pulsars . . . . . 11

2.2 Pulsar Winds . . . . . 13

2.2.1 Goldreich & Julian Density . . . . . 13

2.2.2 At the Light Cylinder... . . . . 13

2.2.3 Wind Termination Shock . . . . . 14

2.3 Formation of Tori . . . . . 15

2.3.1 Kennel and Coroniti (1984) Model . . . . . 16

2.3.2 Interpretation of $\sigma$-parameter . . . . . 20

2.3.3 Observational constraints . . . . . 21

2.4 Formation of Jets . . . . . 22

2.4.1 Collimation by Magnetic Hoop stress and its problem . . . . . 23

2.4.2 Magnetic pinch after the shock . . . . . 23

2.5 Interesting target: PSR B1509−58 . . . . . 26

2.5.1 Selection criteria . . . . . 26

2.5.2 Pulsar and PWN . . . . . 26

2.5.3 TeV $\gamma$-ray emission from the PWN . . . . . 27

2.5.4 Surrounding SNR G320.4−0.12 . . . . . 28

2.5.5 Associating HII-region RCW 89 . . . . . 29

**3 Instrumentation** **31**

3.1 The *Chandra* X-ray Observatory . . . . . 31

3.1.1 Mission Overview . . . . . 31

3.1.2 Launch and Orbit . . . . . 31

3.1.3 Unique Capabilities . . . . . 33

3.2 The High Resolution Mirror Assembly . . . . . 33

3.2.1 Description and Physical Configuration . . . 33
3.2.2 HRMA Effective Area . . . 33
3.2.3 Point-Spread Function . . . 35
3.3 Advanced CCD Imaging Spectrometer (ACIS) . . . 37
3.3.1 Overview . . . 37
3.3.2 Basic Principles . . . 39
3.3.3 Basic Properties . . . 40
3.3.4 Operating Modes . . . 42
3.3.5 Telemetry Formats . . . 42
3.3.6 Inherent phenomenons of CCDs . . . 44

**4 PSR B1509-58 in G320.4−01.2** **47**
4.1 Observations . . . 47
4.2 Data Reductions . . . 47
4.3 X-ray Imaging . . . 48
4.3.1 Entire structure . . . 48
4.3.2 Compact structures around the pulsar vicinity . . . 51
4.4 Spectroscopy . . . 53
4.4.1 The pulsar . . . 54
4.4.2 The PWN . . . 54
4.4.3 The azimuthal dependence . . . 56
4.4.4 The Torus . . . 58
4.4.5 Along the south jet . . . 61
4.5 Temporal changes . . . 66

**5 HII region RCW 89** **72**
5.1 Review . . . 72
5.2 Data Analysis . . . 74
5.2.1 *Chandra* observations . . . 74
5.2.2 *XMM-Newton* observation . . . 78
5.3 Imaging Analysis . . . 81

**6 Discussion** **86**
6.1 Spatial variation of the column density . . . 86
6.1.1 Measurement of the column density . . . 86
6.1.2 What's absorbing the X-rays? . . . 87
6.1.3 Constraints on the proton number density . . . 87

6.2 Nature of the double Tori . . . 90
6.2.1 Spectral evolution on the equatorial plane . . . 90
6.2.2 Bulk velocity of the torus . . . 92
6.2.3 What's the Outer-Torus? . . . 96
6.3 Inner Ring . . . 97
6.3.1 Appearance . . . 97
6.3.2 Pressure balance at the ring feature . . . 99
6.3.3 Estimation of the $\sigma$ parameter . . . 99
6.4 Nature of the pulsar Jet . . . 100
6.4.1 Velocity of the Jet . . . 100
6.4.2 Spectral evolution along the jet . . . 103
6.4.3 Energy budget . . . 105
6.5 Comparing with theoretical models . . . 105
6.6 Proper motion of RCW 89 . . . 110
6.7 Redshift variation in RCW 89 . . . 111
6.7.1 Radial velocity from the redshift . . . 111
6.7.2 Model dependence of the redshift . . . 111
6.8 Geometry of RCW 89 . . . 112
6.8.1 Reconstruction of 3D geometry . . . 112
6.8.2 Constraint on the inclination angle . . . 112

**7 Conclusion** **116**
7.1 PWN of PSR B1509−58 . . . 116
7.2 RCW 89 . . . 118

**A Synchrotron Emission** **120**
A.1 Synchrotron Energy loss . . . 120
A.2 Power spectrum of synchrotron . . . 121
A.3 Cooling time scale . . . 121
A.4 Synchrotron spectrum of a power-law electron energy distribution . . . 122
A.5 Equipartition Condition . . . 122

**B Analysis** **125**
B.1 Point source reduction and exposure correction . . . 125
B.2 Unsharp Masking technique . . . 125
B.3 Temporal analysis . . . 125
B.3.1 South jet . . . 125

B.3.2 North jet . . . . . 125
B.4 X-ray Spectra of RCW 89 . . . . . 125
B.4.1 Chandra Data (ObsID: 5562) . . . . . 125
B.4.2 XMM-Newton Data (ObsID: 027050201) . . . . . 125

# List of Figures


2.1 Schematic drawing of the pulsar wind . . . . . 14
2.2 Density profile of a spherically symmetric PWN . . . . . 15
2.3 Magnetization dependence of the post-shock conditions . . . . . 18
2.4 Simulated post-shock speed and magnetic filed . . . . . 20
2.5 Comparison between the Crab's surface brightness and simulated results . 21
2.6 H-R plot of the Crab nebula . . . . . 22
2.7 Simulated shape of a wind term nation shock . . . . . 25
2.8 3 color image of PSR B1509-58 by Chandra . . . . . 27
2.9 H.E.S.S. image of PSR B1509−58 . . . . . 28
2.10 ATCA image of G320.4−01.2 . . . . . 29
2.11 HII image of RCW 89 . . . . . 30

3.1 Outline drawing of the Chandra . . . . . 32
3.2 Schematic view of the Chandra orbit . . . . . 32
3.3 The HRMA and X-ray optics . . . . . 34
3.4 Effective area of the HRMA . . . . . 35
3.5 Point Spread Function of the HRMA . . . . . 36
3.6 Coma-aberration of the HRMA . . . . . 37
3.7 Schematic drawing of the ACIS . . . . . 38
3.8 Quantum efficiency of the ACIS . . . . . 41
3.9 Energy resolution of the ACIS . . . . . 41
3.10 Sub-array options of the ACIS . . . . . 44
3.11 Pile-up and trailed image of the ACIS . . . . . 46

4.1 *Chandra* Image of G320.0−01.2 . . . . . 49
4.2 Hardness Ratio Map . . . . . 50
4.3 Schematic drawing of the geometry of PSR B1509−58 . . . . . 52
4.4 Inner ring of PSR B1509−58 . . . . . 53
4.5 Unsharp masked image . . . . . 54

4.6 Spectra of PSR1509-58 and its PWN . . . . . 55
4.7 Regions to be analyzed . . . . . 55
4.8 Radial profile of X-ray spectra of PSR B1509−58 . . . . . 57
4.9 Azimuthal profile of the X-ray spectra of PSR B1509−58 . . . . . 59
4.10 Spectroscopy just around the torus . . . . . 61
4.11 Photon index evolution around the torus . . . . . 62
4.12 Surface brightness evolution around the torus radius . . . . . 63
4.13 Spectroscopy along the south jet . . . . . 64
4.14 Width of the south jet . . . . . 64
4.15 Projected vertical profile of the south jet . . . . . 65
4.16 Spectral variations along the Jet . . . . . 67
4.17 The unsharp masked images of the nebula core at four epochs . . . . . 68
4.18 Temporal variation of surface brightness profiles . . . . . 69
4.19 Cross correlation function as a function . . . . . 70
4.20 Travel distance as a function of time interval . . . . . 71

5.1 Multiwavelength observations of RCW 89 . . . . . 73
5.2 X-ray images of RCW 89 taken by *Chandra* . . . . . 74
5.3 X-ray spectrum of the brightest portion of RCW 89 . . . . . 76
5.4 X-ray image taken by *EPIC MOS1* aboard *XMM-Newton* . . . . . 79
5.5 Variation of redshift in RCW 89 . . . . . 79
5.6 FoV of the two *Chandra* observations . . . . . 83
5.7 PSF variation of the two *Chandra* observations . . . . . 83
5.8 Proper motions of the individual knots in RCW 89 . . . . . 84

6.1 Selected regions for absorption measurements . . . . . 88
6.2 HI emission from G320.4−01.2 . . . . . 89
6.3 Magnetic field strength of the NE-Torus . . . . . 93
6.4 Magnetic field strength of the SW-Torus . . . . . 94
6.5 Schematic drawing of the Torus and the Shock front . . . . . 98
6.6 Flow velocity as a function of inclination angle . . . . . 101
6.7 Schematic drawing of a typical evolution of a power law spectrum . . . . . 104
6.8 Magnetic field in the south Jet . . . . . 106
6.9 Comparison of the root of the jets . . . . . 107
6.10 MHD simulations by Del Zanna et al. (2004) . . . . . 108
6.11 Schematic view of the stream lines and corresponding spectral indexes . . . 109
6.12 Schematic drawing of RCW 89 . . . . . 113

6.13 3D structure of RCW 89 . . . . . 113
6.14 Allowable range of the inclination angle . . . . . 115

A.1 Utilized data tables . . . . . 124

B.1 Image processing (1) . . . . . 126
B.2 Image processing (2) . . . . . 127
B.3 Image processing (3) . . . . . 128
B.4 CCF of peak-A . . . . . 129
B.5 CCF of peak-B . . . . . 130
B.6 CCF of peak-C . . . . . 131
B.7 CCF of peak-D . . . . . 132
B.8 Spectra of RCW 89 by *Chandra* with NEI model . . . . . 133
B.9 Spectra of RCW 89 by *Chandra* with MEKAL model . . . . . 134
B.10 Spectra of RCW 89 by *XMM* with NEI model . . . . . 135
B.11 Spectra of RCW 89 by *XMM* with MEKAL model . . . . . 136
B.12 Spectra of RCW 89 by *XMM* with MEKAL model-2 . . . . . 137

# List of Tables


3.1 The HRMA Characteristics . . . . . 34
3.2 ACIS Characteristics . . . . . 43

4.1 Observation Summary of PSR B1509−58 . . . . . 48

5.1 Spectral fit to region "A" in Figure 5.2. . . . . 76
5.2 Spectral fit to the individual knots of RCW 89 . . . . . 77
5.3 Spectral fit to the individual knots of RCW 89 with *XMM* . . . . . 80
5.4 Results of position measurements of RCW 89 . . . . . 85

6.1 Results of the absorption measurements . . . . . 88
6.2 Summary of the flow velocity . . . . . 103

# Chapter 1

# Introduction

Recent high-resolution imaging observations revealed fine structures in celestial objects. The most intriguing discovery is existence of collimated outflow or "jet", which are observed commonly in various rotating objects. So far, radio pulsars, superluminl galactic objects, AGNs, protostars, and GRBs are observed to be associated with jets. However the mechanism which accelerates and collimates the jets has not been understood, and is an important issue in high energy astrophysics. Nevertheless these objects must have rather different natures and different scales from sub-pc to Mpc, there may exist a mechanism which operates very well for all these objects, such as magnetic acceleration or collimation of jets.

Pulsars are generally believed to be a rotating neutron stars formed in supernovae of massive stars. Most of the spin-down energy seem to be carried away in a form of ultra-relativistic particle flow, so-called a pulsar wind. A pulsar wind ejected into a supernova remnant (SNR) generates a wind termination shock near around the pulsar, at which the kinetic energy of the wind is converted into the internal energy. And then the compressed post-shock flow radiates synchrotron radiation and forms a pulsar wind nebula (PWN). Recently NASA's X-ray space telescope *Chandra* observed young energetic pulsars and has revealed the ubiquitous presence of "jet" and "torus", as seen in the Crab pulsar (Hester et al., 2002; Weisskopf et al., 2000a), the Vela pulsar (Pavlov et al., 2003; Helfand et al., 2001), and PSR B1509−58 (Gaensler et al., 2002).

In Comparison with the accretion powered objects such as AGNs or superluminal galactic objects, isolated young pulsars appear to be simple; the pulsar jets are probably formed by the relativistic outflows consisting of electron positron pair plasma and are purely driven by the pulsar's rotating energy via the pulsar's magnetosphere. Moreover, the energy injection rate can be determined precisely by the pulse profile. Therefore remaining open questions are (1) how to accelerate the jet and (2) how to collimate the

jet. In this sense, isolated pulsars can be excellent probe investigating relativistic jets.

Most of theoretical models of PWNe have been proposed aiming to figure out the Crab nebula. For the torus structure lying on the equatorial plane had been well explained by 1-D MHD model by Kennel and Coroniti (1984a). While the jets are still unclear because they are unisotropic three-dimensional structures, because the two dimensional (or higher dimension) relativistic MHD model cannot be solved straightforwardly. Furthermore this problem may not have an analytical solution. Fortunately, recent progress in numerical methods for relativistic gas dynamics and MHD has made it possible to approach this problem numerically. In fact recent several numerical simulations succeeded in producing poloidal out flow (Komissarov and Lyubarsky, 2003; Del Zanna et al., 2004). The basic scenario forming jets follows the prediction by Lyubarsky (2002), in which the pulsar jets are originated in the mildly relativistic post-shock equatorial flow, namely the tori. This self collimation process is due to magnetic hoop stress, therefore the wind magnetization would control the formation of pulsar jets.

In this study, we aim to investigate the nature of relativistic jets via the PWN of PSR B1509−58, which is one of the largest PWN ever known. Utilizing *Chandra*, we investigated arc-second scale fine structures just around the pulsar. In order to determine the magnetization of the pulsar wind, a spatially-resolved spectroscopy was performed, which can constrain the flow dynamics and the spectral properties along the streamlines. Moreover we also performed temporal analysis using a series of four monitoring observations spanning 10 months to follow the temporal variation of the fine structures. Finally, recent results of numerical MHD studies were examined based on those data analyses.

The thesis structure is as follows. In Chapter 2 the current understandings of the pulsar wind nebulae and recent observational approaches are briefly reviewed. Then the *Chandra* X-ray observatory which is mainly used in this study is described in Chapter 3. Chapter 4 describes the data analysis of for PSR B1509−58. We also investigate an associating HII region RCW 89 in Chapter 5. In Chapter 6 we discuss the observational results of the pulsar wind nebula comparing with recent numerical studies. Finally the results are summarized in Chapter 7.

# Chapter 2

# Review of Pulsar Wind Nebulae

In this chapter we present the current understanding of the pulsar wind nebulae. First we describe the pulsar wind nebulae schematically. Then a more theoretical approach proposed by Kennel & Coroniti is introduced. Next we briefly introduce recent numerical approaches to the jet structure. Finally past observational studies are described.

## 2.1 Rotating Powered Pulsars

In most cases the only energy source of isolated neutron star is its rotational energy.[1] In some cases, such a neutron star radiates pulsed emission in the energy range from radio to Gamma-ray with a constant period. The observed pulse periods are believed to represent their spin periods. Therefore we can precisely constrain the energy dissipation of the pulsar by the accurate timing analysis of the pulse signals. Moreover, the ages and the surface magnetic fields of the pulsars are also available with certain assumptions. Here we briefly describe the basic parameters featuring pulsars' characters.

### Spin-down Luminosity

Suppose an isolated pulsar has a spin period, $P$, and a period derivative with respect to time, $\dot{P}$. The rate at which rotating kinetic energy is dissipated is referred to as "spin down luminosity", and is given by an equation of the basic physics:

$$\dot{E} = 4\pi^2 I_{45} \frac{\dot{P}}{P^3} , \tag{2.1}$$

where $I_{45}$ is the pulsar's moment of inertia, usually assumed to be $1 \times 10^{45}$ g cm$^{-1}$. For example, the crab pulsar has a spin down luminosity of $\dot{E} = 4.8 \times 10^{38}$ ergs s$^{-1}$. The

[1] In a few cases other energy sources such as its internal magnetic field, a accretion of ambient matter are proposed.

dissipated energy is believed to be utilized for not only the electromagnetic radiation but also the particle acceleration via the rotating magnetosphere of the pulsar.

### Characteristic Age

The evolution of the pulse period can be described by an simple empirical equation:

$$\dot{\Omega} = -k\Omega^n, \tag{2.2}$$

where $\Omega$ is the angular frequency corresponding to the pulse period ($\Omega = 2\pi/P$), $k$ is a constant, and $n$ is the "braking index". Integrating this equation yields the age of the system :

$$\tau = \frac{P}{(n-1)\dot{P}}\left[1 - \frac{P_{\rm init}}{P}^{n-1}\right], \tag{2.3}$$

where $P_{\rm init}$ is the spin period at the birth time, and is usually unknown. Unfortunately it is also difficult to measure the braking index $n$, which requires the second derivative of the pulse period. Therefore we assume a typical case in which the initial spin period is infinitesimally short and the braking index is set to be $n = 3.0$ which corresponds to spin down via magnetic dipole radiation. For this condition, an characteristic age, $\tau_c$, is derived

$$\tau_c = \frac{\dot{P}}{2P}. \tag{2.4}$$

Note that the characteristic age are larger than the true age of the pulsar, caused by the assumed initial spin period. The observed braking index also are smaller than the assumed value of $n = 3.0$. In fact the measured braking indices of four pulsars (Crab, Vela, PSR B1509−58, and Kes75) are in the range of 2∼3, which make the pulsars somewhat younger. In spite of the above rough assumptions, the characteristic age provides an applicable estimation in many cases. It is because the spin down rate is proportional to $(1/P)^{n-1}$, thus the underestimate of the initial period can be neglected.

### Surface Magnetic Field

If the magnetic braking mechanism is responsible for the slow-down of the pulsar, the magnetic field strength at the surface of the pulsar, $B_*$, can be estimated. The emissivity of the electromagnetic radiation from a magnetic dipole moment $\mathbf{p}_{\rm m}$ is

$$-\frac{dE}{dt} = \frac{\mu_0|\ddot{\mathbf{p}}_{\rm m}|^2}{6\pi c^3} = \frac{\mu_0\Omega^4\mathbf{p}_{\rm m0}^2}{6\pi c^3}, \tag{2.5}$$

where $\mathbf{p}_{\rm m} = \mathbf{p}_{\rm m0}\sin\Omega t$. Assuming that the neutron star with a radius of $R_*$ has a dipole magnetic field of $B_* = \mu_0\mathbf{p}_{\rm m0}/4\pi R_*^3$ yields

$$-\frac{d\Omega}{dt} = \frac{8\pi\Omega^3 R_*^6 B_*^2}{3\mu_0 c^3 I_{45}}. \tag{2.6}$$

For a typical radius of the neutron stars, $R_* = 10$ km, we find $B_* = 3.2 \times 10^{19}(P\dot{P})^{1/2}$ G, where $P$ is in seconds.

## 2.2 Pulsar Winds

As mentioned above, the pulsar's rotational energy is believed to be transferred into not only the electromagnetic radiation but also into the particle acceleration. The particle flows from pulsars are called "Pulsar Winds", which generate synchrotron nebulae. Here we briefly describe the basic picture of the formation of pulsar winds.

### 2.2.1 Goldreich & Julian Density

Schematically, a rotation powered pulsar can be considered as a strong magnet consisting of a perfect conducting sphere. Due to the pulsar's rotation, the unipolar induction makes a strong electric polarization between the polar and the equator on the pulsar:

$$\Delta\Phi = \frac{B_*\Omega^2 R_*^3}{2c} \sim 6 \times 10^{12} \left(\frac{B_*}{10^{12}\ \mathrm{G}}\right) \left(\frac{R_*}{10\ \mathrm{km}}\right)^3 \left(\frac{P}{1\ \mathrm{s}}\right)^{-2} \quad \mathrm{V} \tag{2.7}$$

The induced electric field is so strong sufficient to pull out the charged particles from the pulsar against the strong gravity. The induced charged particles fill the pulsar's magnetosphere and will cancel the electric fields. The production rate of the charged particle is $\dot{N}_{\mathrm{GJ}} = (B_*\Omega^2 R_*^3)/Zqc$, where $Zq$ is the ion charge. This model was proposed by Goldreich and Julian (1969) and the obtained number density is called Goldreich-Julian density.

### 2.2.2 At the Light Cylinder...

The induced charged particles would co-rotate with the pulsar's magnetosphere as the charged particles are frozen in the magnetic field. And then they are accelerated by the centrifugal force. At the radius of light cylinder,$R_{\mathrm{LC}}$, defined by $R_{\mathrm{LC}}\Omega = c$, the charged particles catch up with the light speed, and the magnetic field no longer closes and opens to outward. Via the open field lines, the particles are finally ejected from the pulsar's magnetosphere together with the magnetic field. This is the particle flow called "Pulsar Wind". In the crab nebula, the ejected wind reaches a *Lorentz* factor $\gamma \sim 10^6$. A schematic drawing of the pulsar wind is shown in Figure 2.1.

Based on the above idea, subsequent models were constructed with some modifications, and they predicted that the wind leaving the pulsar magnetosphere is dominated

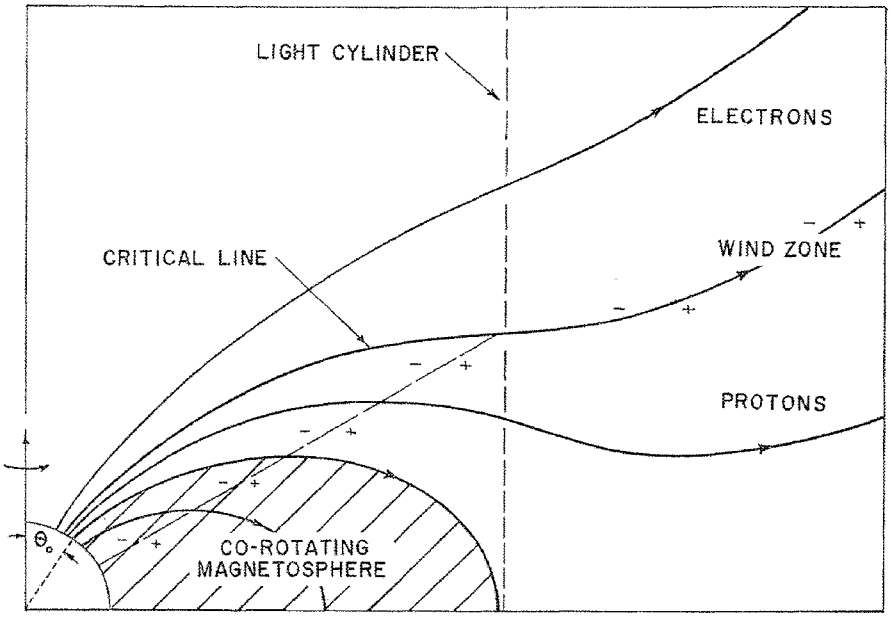


Figure 2.1: Schematic diagram showing the co-rotating magnetosphere and the wind zone from Goldreich and Julian (1969). In the calculation they set the dipole axis to be aligned with the rotating axis.

by the Poynting flux,$F_{E\times B}$, with a much smaller contribution from the particle energy flux,$F_{\rm particle}$. Here we introduce a magnetization parameter, $\sigma$, defined as:

$$\sigma = \frac{F_{E\times B}}{F_{\rm particle}} = \frac{B^2}{4\pi\rho\gamma c^2}, \tag{2.8}$$

where $B$, $\rho$, $\gamma$ are the magnetic field, the mass density, and the *Lorentz* factor, of the wind, respectively. The predicted value of $\sigma_0$ is typically larger than $\sim 10^4$.

### 2.2.3 Wind Termination Shock

A young pulsar is usually surrounded by a supernova remnant (SNR). The expansion of a SNR is non-relativistic and is decelerated by ISM. Since the pulsar wind is flowing almost at the light speed ($\gamma \sim 10^6$ for the crab), it catch up with the ejecta and terminated by a reverse shock. When the wind passes through the termination shock, the kinetic energy of the wind is converted into the internal energy. In metaphorical sense, the pulsar wind is "thermalized" at the termination shock. Note that the "thermalized" post-shock flow has an energy spectrum of $dN/dE \propto E^{-p}$, namely a power-law function formed by the collision-less dissipation process, in which the shocked flow hardly achieves the thermal equilibration. Therefore we cannot define its typical temperature.[2] The "thermalized"

[2]Therefore these power-law spectra are often called "non-thermal".

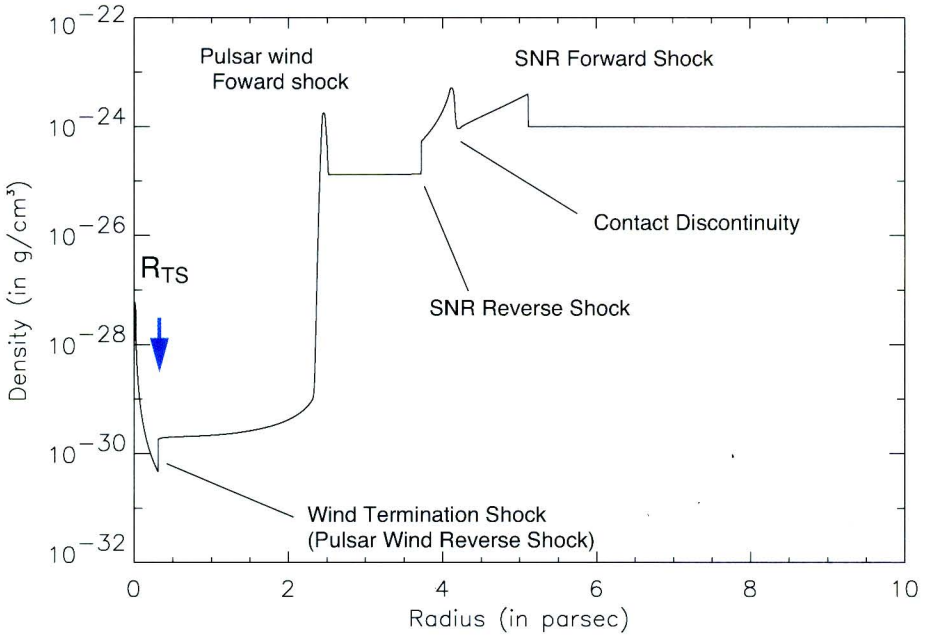


Figure 2.2: Density profile of a spherically symmetric PWN expanding within a pre-Sedov SNR (van der Swaluw et al., 2001)

plasma in the post-shock region radiates synchrotron emission, forming a so-called pulsar wind nebula.

Figure 2.2 shows a simulated density profile of a spherically symmetric PWN which is interacting with the surrounding SNR (van der Swaluw et al., 2001). A reverse shock at a distance from the pulsar $r_{\rm TS}$ is formed near the center of the nebula, where the cold relativistic wind from the pulsar is terminated. Within the shock, $r < r_{\rm TS}$, the wind is not randomized yet and hence in the co-moving frame of the bulk flow the particles have very little time to radiate before encountering the shock. At the termination shock, the ram pressure of the wind is expected to be balanced with the internal pressure $p_{\rm PWN}$ of the PWN. Thus we obtained a relation:

$$\frac{\dot{E}}{4\pi R_{\rm TS}^2 \phi c} = p_{\rm PWN}, \tag{2.9}$$

where $\phi$ is the equivalent filling factor for an isotropic wind.

## 2.3 Formation of Tori

Recent X-ray observatories revealed that a part of PWNe have common structures of "Torus + Jets", as typified by the crab nebula. Here we briefly describe the theoretical understandings of these structures.

### 2.3.1 Kennel and Coroniti (1984) Model

For the torus in the Crab nebula, a generally accepted model which based on the magneto-hydrodynamic (MHD) was proposed by Kennel and Coroniti (1984a,b) (KC-model), in which the nebula was assumed to be in a spherically symmetric steady state.

The pulsar wind is parametrized by a magnetization parameter $\sigma$ as mentioned above. For a spin-down luminosity of $\dot{E}$, they defined that

$$\dot{E} = 4\pi n_1 \gamma_1 u_1 r_{\rm TS}^2 mc^3(1+\sigma), \tag{2.10}$$

$$\sigma = \frac{B_1^2}{4\pi n_1 u_1 \gamma_1 mc^2}, \tag{2.11}$$

where $n$ is the proper density (while the observer's frame density is $N = \gamma n$), $u$ is the radial four speed of the flow ($u = \gamma\beta$), $\gamma^2 = 1 + u^2$, $r_{\rm TS}$ is the radial distance of the shock from the pulsar, $m$ is the electron mass, $c$ is the speed of light, and $B$ is the observer frame magnetic field. The subscriptions of "1" and "2" represent the upstream and the downstream, respectively. Here they assumed that the magnetic field is almost exactly toroidal far from the pulsar.

#### The Rankine-Hugoniot Relation

In order to estimate the post-shock condition the Rankine-Hugoniot relation was utilized. The junction conditions between the upstream and downstream of the shock are described as follows:

$$n_1 u_1 = n_2 u_2 \qquad \text{(Particle flux)} \tag{2.12}$$

$$\frac{u_1 B_1}{\gamma_1} = \frac{u_2 B_2}{\gamma_2} = E \qquad \text{(Electric field)} \tag{2.13}$$

$$\gamma_1 \mu_1 + \frac{EB_1}{4\pi n_1 u_1} = \gamma_2 \mu_2 + \frac{EB_2}{4\pi n_2 u_2} \qquad \text{(Energy)} \tag{2.14}$$

$$\mu_1 u_1 + \frac{p_1}{n_1 u_1} + \frac{B_1^2}{8\pi n_1 u_1} = \mu_2 u_2 + \frac{p_2}{n_2 u_2} + \frac{B_2^2}{8\pi n_2 u_2} \qquad \text{(Momentum)}, \tag{2.15}$$

$$\tag{2.16}$$

where $p$ is the pressure, and $\mu$ is the specific heat ratio for a gas with a specific heat ratio of $\Gamma$ defined by

$$\mu = mc^2 + \frac{\Gamma}{\Gamma - 1}\frac{p}{n}. \tag{2.17}$$

Above four relations represent the conservation laws of the particle flux, the perpendicular component of the electric field, the energy, and the momentum, respectively.

Usually it is difficult to solve these equations. Therefore certain approximations are adopted for simplification. The strong shock condition allows approximations of

$$\begin{aligned} p_2 &\gg n_2 mc^2, \\ p_1 &\sim 0, \\ u_1 &\gg u_2, \\ u_1/\gamma &\simeq 1. \end{aligned}$$

Adopting above approximations yields the physical parameters describing the post-shock flow, as a function of magnetization parameter, $\sigma$, just behind the shock. Figure 2.3 shows the result from Rankine-Hugoniot solutions for strong relativistic MHD shock by Kennel and Coroniti (1984a). It would be convenient to have simplified approximation forms at the two extreme limits as follows:

**Large $\sigma$ Limit**

$$u_2^2 = \sigma + \frac{1}{8} + \frac{1}{64\sigma} + ..., \tag{2.18}$$

$$\gamma_2^2 = \sigma + \frac{9}{8} + \frac{1}{64\sigma} + ..., \tag{2.19}$$

$$\frac{B_2}{B_1} = \frac{n_2}{n_2} = 1 + \frac{1}{2\sigma} + ..., \tag{2.20}$$

$$\frac{p_2}{n_1 mc^2 u_1^2} = \frac{1}{8\sigma}\left(1 - \frac{1}{16\sigma} + ..\right). \tag{2.21}$$

**Small $\sigma$ Limit**

$$u_2^2 = \frac{1+9\sigma}{8}, \tag{2.22}$$

$$\gamma_2^2 = \frac{9+9\sigma}{8}, \tag{2.23}$$

$$\frac{B_2}{B_1} = 3(1-4\sigma), \tag{2.24}$$

$$\frac{p_2}{n_1 mc^2 u_1^2} = \frac{2}{3}(1-7\sigma). \tag{2.25}$$

$$\tag{2.26}$$

(The magnetic field, the number density, and the pressure are presented in unit of upstream values.)

In the large $\sigma$ limit, the shock becomes weak, and the flow speed in the downstream approaches to the light speed. Thus the shock compression is inefficient. While in the small $\sigma$ limit, the shock is strong, approaching the hydrodynamic limit. At the limit,

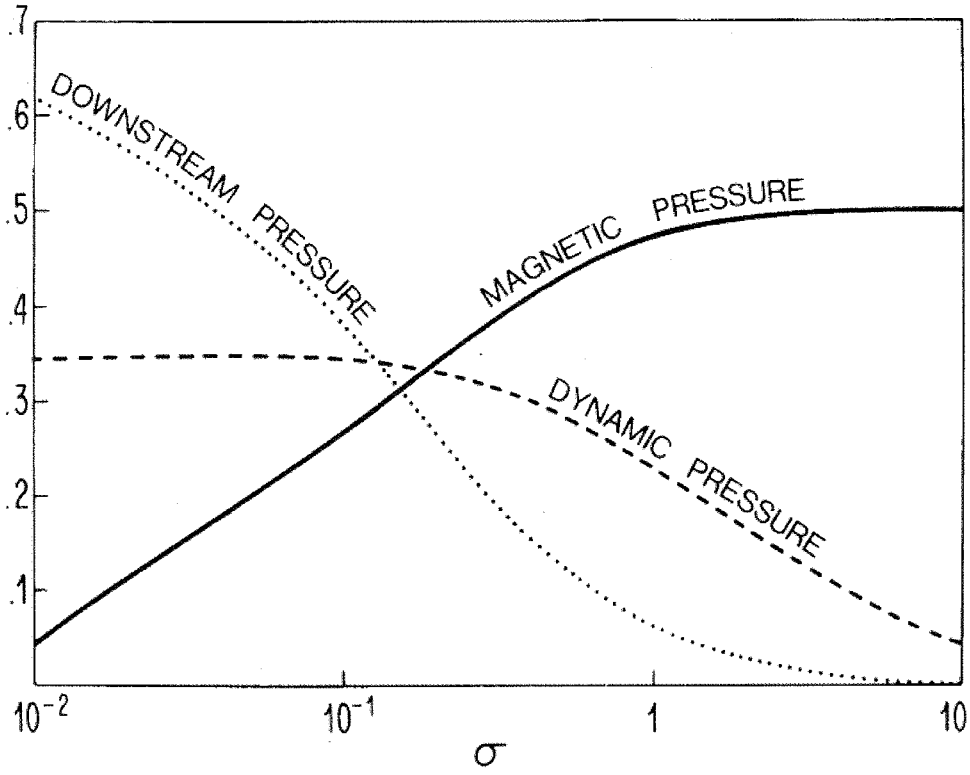


Figure 2.3: Magnetization dependence of the post-shock condition based on the Rankine-Hugoniot relations. The solid line, dashed line and dotted line describe the magnetic, dynamic, and particle, pressures, respectively. All parameters are normalized to the total upstream energy density (Kennel and Coroniti, 1984a).

we obtained a downstream flow velocity of $c/3$, and the compression ratio of $B_2/B_1 = N_2/N_1 = 3$. Past studies on the Crab nebula revealed that the $\sigma$ parameter of the unshocked pulsar wind seems to be small; $\sigma \sim 0.003$ (Kennel and Coroniti, 1984a), $\sigma \sim 0.03$ (Mori, 2002). Hereafter, we will assume the small limit condition only.

### Evolutions in the downstream

The Rankine-Hugoniot relation predicts the condition just after the shock. We then trace the downstream flow. The shock-heated plasma will follow the steady state equations in the toroidal approximation:

$$\frac{d}{dt}(cnur^2) = 0, \tag{2.27}$$

$$\frac{d}{dr}\left(\frac{ruB}{\gamma}\right) = 0, \tag{2.28}$$

$$\frac{d}{dr}(nu_2 r^2 e) + p\frac{d}{dr}(r^2 u) = 0, \tag{2.29}$$

$$\frac{d}{dr}\left[nur^2\left(\gamma\mu+\frac{B^2}{4\pi n\gamma}\right)\right]=0. \tag{2.30}$$

These four equations describe the conservation of number flux (Eq. 2.27), the conservation of magnetic flux in the magneto-hydrodynamic approximation (Eq. 2.28), the propagation of internal energy (Eq. 2.29), where $e$ is the relativistic energy per particle ($\mu = e + p$), and the conservation of total energy (Eq. 2.30), respectively.

In case of the strong shock induced by a pulsar wind with a small magnetization ratio $\sigma < 1$, the post-shock flow speed becomes non-relativistic ($< c/3$) everywhere, and thus we can set the bulk Lorentz factors of $\gamma$ and $\gamma_2$ equal to unity. Then the above equations reduce to the four speed $u(z)$ and the magnetic field $B(z)$ as a function of the normalized distance $z = r/r_{\rm TS}$,

$$u(z) = u_2 \times \frac{1}{z^2}\left(\frac{\triangle}{1+\triangle}\frac{G}{3}\right)^3, \tag{2.31}$$

$$B(z) = B_2\frac{u_2}{z\,u(z)} = B_2 \times z\left(\frac{\triangle}{1+\triangle}\frac{G}{3}\right)^{-3}, \tag{2.32}$$

where

$$G = 1+[1+y^2+\sqrt{(1+y^2)^2-1}]^{1/3} + [1+y^2-\sqrt{(1+y^2)^2-1}]^{1/3}, \tag{2.33}$$

$$y = z\left[\frac{27(1+\triangle)^2}{2\triangle^3}\right]^{1/2}, \tag{2.34}$$

$$\triangle = \frac{u_2^2/\sigma - 1/2}{u_2^2+1/4} \approx 1/U_{\rm A2}^2. \tag{2.35}$$

The constant $\triangle$ depends only on $\sigma$ and is related to the Alfvén four speed downstream of the shock, $U_{\rm A2}^2 = B_2^2/(4\pi n_2\gamma_2^2\mu_2)$. Then the constant $G$ depends on $z$ and $\sigma$. When $z$ is small ($y \ll 1$), $G^3$ approaches a constant value ~27, and when $z$ is large $G^3$ increases as $z^2$. Figure 2.4 shows simulated post-shock speed and magnetic field by Kennel and Coroniti (1984a). The four velocity decreases as $u(z) \propto 1/z^2$ ($z \ll U_{\rm A2}$) and then approaches a constant value. While the magnetic filed $B(z)$ has a peak when $\sigma$ is small. The strength of the magnetic field can be explained by the magnetic flux conservation law of $rvB$ = const. When the particle flow is decelerated, the toroidal magnetic field is accumulated. And then the pair plasma radiates X-rays strongly because the synchrotron emissivity is proportional to the magnetic energy density, $I_{\rm sync} \propto B^2$ (see A.1). The X-ray torus seen in the Crab therefore coincides with the peak radius of $B(z)$.

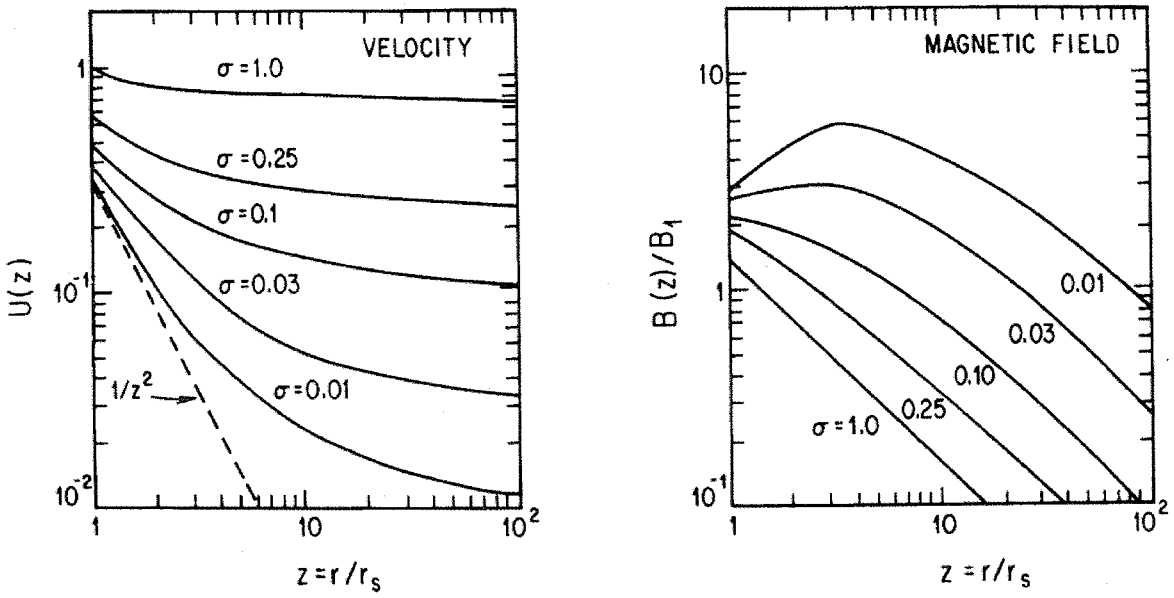


Figure 2.4: Simulated post-shock speed (left) and magnetic field (right) for magnetization conditions of $\sigma = 0.01$, 0.03, 0.1, 0.25, and 1.0. The values at $z = 1$ emerge from solutions of the Rankine-Hugoniot relations (Kennel and Coroniti, 1984a)

### 2.3.2 Interpretation of $\sigma$-parameter

As shown in Figure 2.4, the equatorial flow in a PWN would be decelerated more strongly as the magnetization $\sigma$ decreases. Therefore a pulsar wind with small $\sigma$ would generate a large X-ray torus. Conversely we can evaluate the $\sigma$ based on the geometry of PWN.

In the termination shock, only the kinetic energy in the pulsar wind is transformed into the thermal energy. Thus the magnetization parameter can be redefined as (Shibata et al., 1998)

$$\sigma \equiv \frac{B_1^2/4\pi}{U_{\rm k1}} \approx \frac{B_1^2/4\pi}{U_{\rm Th2}} \approx \frac{B_1^2/4\pi}{B_{\rm Eq2}^2/4\pi}, \tag{2.36}$$

where $U_{\rm k1}$ is the kinetic energy density of the unshocked pulsar wind, $U_{\rm Th2}$ is the thermal energy density after the shock, and $B_{\rm Eq2}$ is the equipartition magnetic field after the shock (see A.5). Combining Eq. 2.36 with the equation of continuity, $r_{\rm TS}^2 c/3 \approx r_{\rm Torus}^2 v_{\rm Torus}$, and frozen-in condition, $r_{\rm TS} c B_1 \approx r_{\rm Torus} v_{\rm Torus} B_{\rm Eq2}$, we find a relation between the $\sigma$-parameter and the size of nebula:

$$\frac{r_{\rm Torus}}{r_{\rm TS}} \approx \frac{1}{3\sqrt{\sigma}}. \tag{2.37}$$

We also obtained a relation between the $\sigma$ and expansion velocity,

$$\frac{v_{\rm Torus}}{c} \approx 3\sigma. \tag{2.38}$$

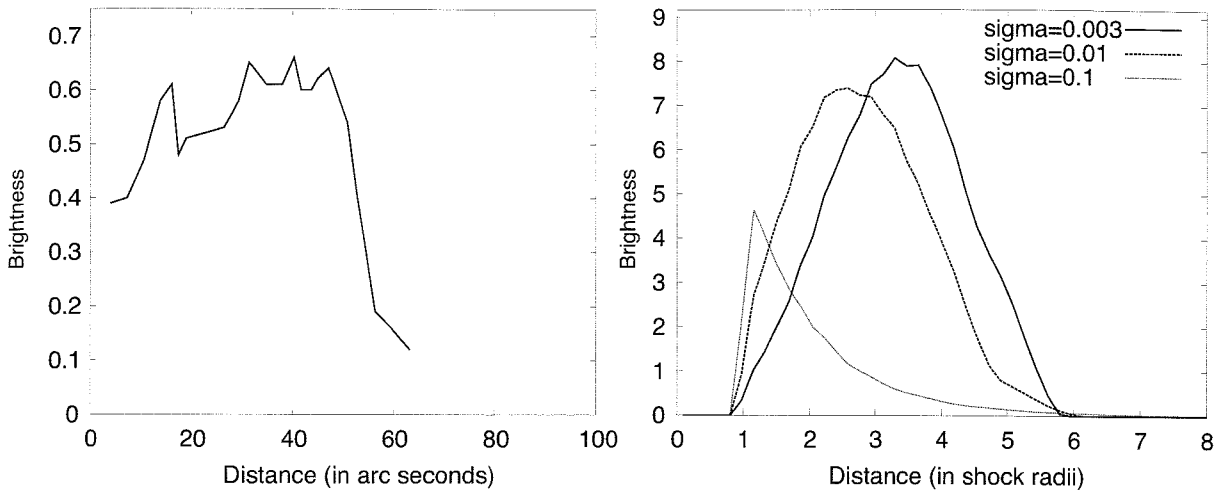


Figure 2.5: **Left**—Simulated surface brightnesses along the radial direction for $\sigma = 0.003$, 0.01, and 0.1 (Shibata et al., 2003). **Right**—The observed surface brightness (Mori, 2002). The horizontal axes were normalized by the shock radius ($r_{\rm TS} \sim 13 - 14$ arcsec).

Note that a constant number density is assumed in the above evaluations ($nr^2v = \text{const} \rightarrow rv^2 \approx \text{const}$).

### 2.3.3 Observational constraints

The theoretical model above described (hereafter KC-model) gave a beautiful explanation for the observed morphology in the Crab nebula. Because the shock radius had not been measured, Kennel and Coroniti (1984a) evaluated the magnetization parameter based on the expansion velocity of the SNR and obtained $\sigma = 0.003$, which is the generally believed value now.

Recent Chandra observations revealed the termination shock in the Crab nebula (Weisskopf et al., 2000a). Subsequently Mori (2002) obtained a new constraint of $\sigma = 0.03$ by comparing the X-ray surface brightness with the KC-model. Figure 2.5 shows the simulated surface brightness for various $\sigma$ parameters based on the KC-model (Shibata et al., 2003) and the observed surface brightness of the Crab nebula by *Chandra* (Mori, 2002). Shibata et al. (2003) also claimed that the present model does not reproduce the first peak in the observation, which corresponds to the termination shock[3]. Either case required rather small $\sigma$ than the predicted initial wind magnetization of $\sigma_0 \sim 10^4$, the so-called $\sigma$-paradox.

[3]The brightness distribution of the inner ring is similar to that for the $\sigma = 0.1$ model (Shibata et al., 2003).

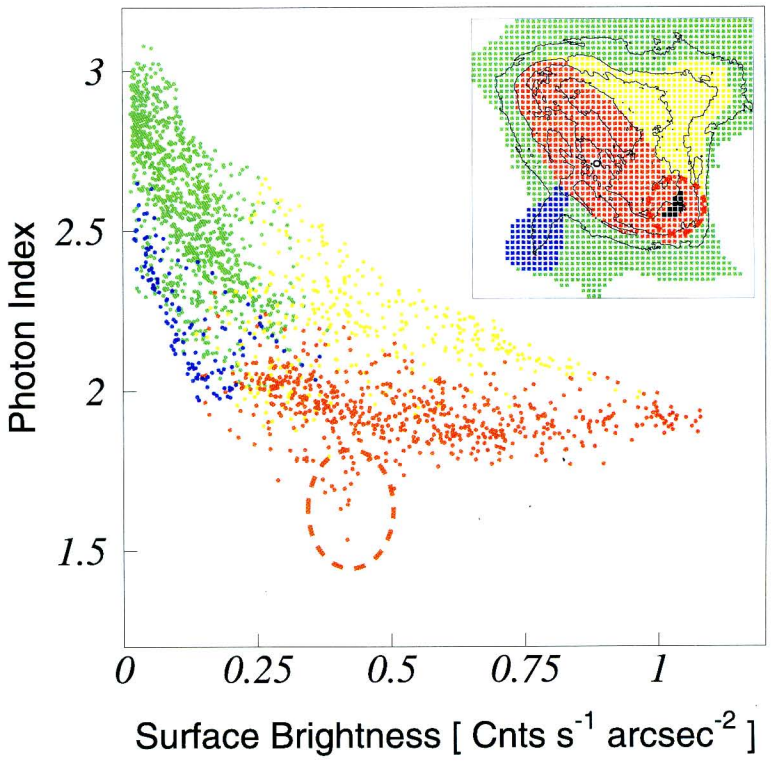


Figure 2.6: Plot of photon index against surface brightness. The data points of the torus, the jet, the umbrella-shaped northwest region, and the faint peripheral region are color-coded as red, blue, yellow, and green, respectively (Mori et al., 2004). We can see that the torus has a constant photon index $\Gamma \sim 2$ and the ambient region shows more steep spectra.

On the other hand, the outer boundary of the torus in the Crab seems to be provided by the synchrotron burn-off. Figure 2.6 shows a plot of photon index against surface brightness. In the torus region the spectral index is constant at $\Gamma \sim 1.9$, while the ambient regions show more steep spectra than the torus, implying that the charged particles burned off at the outer boundary of the torus(Mori et al., 2004).

## 2.4 Formation of Jets

The most mysterious feature in the Crab nebula is probably the presence of jets oriented along an axis perpendicular to the plane of the torus and emerging from the pulsar. Similar features have been observed also in a number of other objects. While the presence of the X-ray tori may be at least qualitatively explained within the framework of standard 1-D relativistic MHD models as described above, the physical mechanism forming pulsar jets has not been understood at all. However, in case of a PWN, its jets are obviously driven

by the pulsar's rotating energy probably via its magnetosphere. Therefore the remaining open questions are:

1. How to accelerate the plasma up to $\sim 0.7c$ ?

2. How to collimate the accelerated plasma narrowly?

### 2.4.1 Collimation by Magnetic Hoop stress and its problem

For the collimating mechanism it is frequently suggested that magnetic hoop stresses in the pulsar wind may collimate the flow. However the jets of the Crab nebula cannot be explained so straightforwardly within the pulsar wind model, as well as jets of other pulsars. The most of jets in PWNe appear to originate from the pulsar (Weisskopf et al., 2000a; Pavlov et al., 2003), which seems to indicate that they may be formed within the pulsar wind via collimation by magnetic hoop stress. However, the closer look reveals a number of problems with the explanation.

The most critical problem is the inefficiency of the magnetic hoop stress in an ultra-relativistic flow. Bogovalov (2001) claimed that electric force nearly compensates hoop stress in ultra-relativistic flows, therefore the resultant fraction of the collimated poloidal flux should be rather small. Namely, the curvature radius of the poloidal field line which coincide with the flow line may be estimated as (Lyubarsky, 2002)

$$R_{\rm c} \sim r\gamma^2 \left(1 + \frac{1}{\sigma'}\right), \tag{2.39}$$

where $r$ is the cylindrical radius, $\gamma$ the local flow Lorentz factor, $\sigma'$ the local magnetization parameter. One can see that in an ultra-relativistic wind ($\gamma \gg 1$) the flow lines are nearly straight, which enables the collimation exactly. Nevertheless the collimation is applied only near the axis. Moreover, the direct observations of proper motions in the jets of the Crab and Vela nebulae indicate rather moderate velocity of only 0.3−0.7c (Pavlov et al., 2003; Hester et al., 2002).

### 2.4.2 Magnetic pinch after the shock

In order to overcome these problems, Lyubarsky (2002) proposed an alternative idea in which the jets are formed downstream of the termination shock, where velocities are no longer ultra-relativistic and the magnetic collimation is much more effective. However the interaction between a ultra-relativistic MHD wind from the pulsar and a dense, relativistic surrounding is a very complicated problem in case of anisotropic wind. Of course it has not been solved analytically so far (Komissarov and Lyubarsky, 2003). Therefore

we qualitatively describe recent numerical MHD simulations by Bucciantini (2006); Del Zanna et al. (2004); Komissarov and Lyubarsky (2003) here.

### An Oblate Wind Termination Shock

Suppose an "aligned rotator" whose magnetic dipole is aligned along the rotating axis. Recent numerical simulations both in the force-free and MHD regime revealed that the energy flux in the wind has a strong latitudinal dependence of the form

$$L(\theta) = L_0(1 + \alpha \sin^2\theta), \tag{2.40}$$

where $\alpha$ is a constant controlling the pole-equator anisotropy ($\alpha \gg 1$). While the toroidal magnetic field in the wind follows $B(\theta) \propto \sin\theta$. Thus the magnetization of the wind should be a function of the polar angle $\sigma(\theta)$. Figure 2.7 (Left) shows a simulated shape of the termination shock in case of a small magnetized wind, $\sigma = 0.003$. Due to the higher equatorial energy flux, the simulated termination shock exhibits an oblate shape. As the magnetization increase, the termination shock becomes more oblate, caused by the strong magnetic stresses on the axis.

Due to the termination shock shape, the flow is slowed down to speed $\sim c/3$ close to the equator, but at higher latitudes, where the shock is oblique, the post shock flow is still super-fast magnetosonic. Moreover, plasma at higher latitude is deflected toward the equatorial plane. Consequently almost all of the downstream plasma seems to be confined in the equatorial region (Figure 2.7).

### Distortion of the equatorial flow by a Hoop stress

As the post-shock flow expands and decelerates in the equatorial plane, the magnetization increases, until equipartition is reached. Now the post-shock flow is only mildly relativistic, so hoop stresses can produce collimation. Since the magnetization of the post-shock flow has a latitudinal dependence, $\sigma(90°) > \sigma(\theta)$, the flow close to the equator reaches equipartition before that at higher latitudes. Given the extra degree of freedom with respect to the simple radial model by Kennel and Coroniti (1984a), the plasma can now move also in $\theta$ direction. Once equipartition is reached on the equatorial plane the magnetic pressure prevents further compression of the magnetic field, and the flow is then diverted back toward the axis. This is the basic scenario of collimation and the formation of a jet along the axis. Right panel in Figure 2.7 shows a numerical result for the velocity profile inside a nebula describing streamlines of diverted back flow.

Note that the key parameter which controls collimations is the wind magnetization, $\sigma$. If magnetization is too small, then equipartition is not reached inside the nebula,

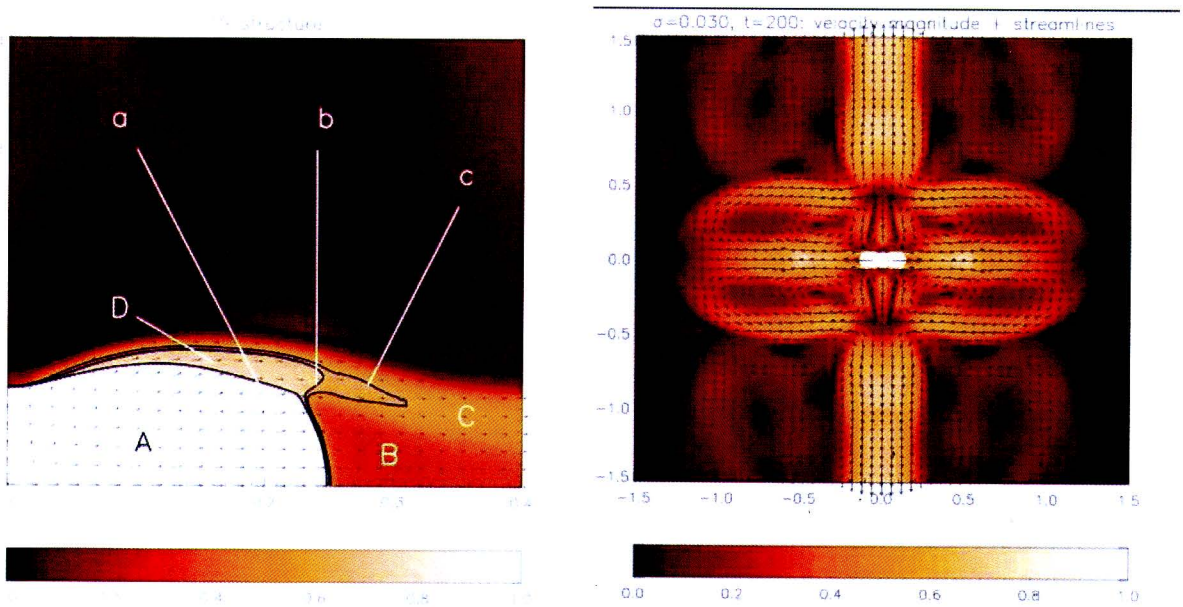


Figure 2.7: **Left**— Structure of the flow at the termination shock for a wind of $\sigma = 0.03$ (Del Zanna et al., 2004). Assumed energy flux anisotropy is about $L(0°)/L(90°) \sim 0.1$. **Right**— Result of a numerical simulation showing the details of the formation of the polar jet (Del Zanna et al., 2004). In the both panel, gray scale and allows indicate velocity magnitude and streamlines, respectively.

thus hoop stresses never become effective, consequently no jet is formed. While at higher magnetization, equipartition is reached in the close vicinity of the termination shock, and most of the plasma is diverted and collimated into a jet. So far, the lower limit of $\sigma$ which allows existences of pulsar jets are still ambiguous. However Del Zanna et al. (2004) confirmed that formations of jet from a pulsar wind with a magnetization larger than $\sigma \geq 0.01$.

## 2.5 Interesting target: PSR B1509−58

### 2.5.1 Selection criteria

Our motivation in this study is to investigate the underlying mechanism which forms the common structures of "jet" and "torus" as seen in PWNe generally. However the above theoretical approaches had been aimed to describe only the crab nebula. Examining the theoretical scenarios on the other pulsars is essential to understand the ubiquitous mechanism in PWNe.

The criteria for target selection are described below. The acceptable PWNe should possess (1) known pulsar which energize the nebula, (2) axisymmetric structures, such a as "tori" and "jets", surrounding SNR and (4) sufficient surface brightness and angular size for spatially resolved spectroscopy.

As PWNe are purely driven by the pulsars' spin-down energy, the pulse profiles provide many useful physical constraints. In order to consider the energy budget between PWNe and pulsars, the acceptable PWNe should include well studied pulsars. On the other hand, to investigate fine structure of "jet" and "torus", the PWNe should have axisymmetric structures as seen in the Crab nebula. These structures, however, seem to be easily distorted by the ram-pressure against the interstellar medium (ISM). Therefore the PWNe running through ISM which exhibit "comet-like" long tails are excluded. The existence of surrounding supernova remnant is also essential. This condition is required to study the pressure balance between pulsar wind and confining SNR.

According to the criteria mentioned above, a young energetic pulsar PSR B1509−58 embedded by PWN with largest angular size ever known is selected. In the following sections, we briefly describe the properties of the SNR-Pulsar system.

### 2.5.2 Pulsar and PWN

PSR B1509−58 exhibits 150 ms radio, X-ray, and Gamma-ray pulsation (Seward and Harnden, 1982; Manchester et al., 1982; Ulmer et al., 1993). From the spin parameter, a characteristic age $\tau_c = 1700$ yr, a spin-down luminosity $\dot{E} = 1.8 \times 10^{37}$ ergs s$^{-1}$ and a surface magnetic field $B_{\rm p} = 1.5 \times 10^{13}$ G have been obtained, making it one of the youngest the most energetic, and highest field pulsars known. Timing observations also yielded a breaking index of $n = 2.837 \pm 0.001$ (Seward and Harnden, 1982; Kaspi et al., 1994).

Figure 2.8 shows a 3-color image of the pulsar taken by *Chandra* (Four observational data-sets, $\sim$ 200 ks exposure total, are combined.). PSR B1509−58 is accompanied by

a bright PWN which is one of the most largest PWNe ever known. Thanks to the large angular size, a torus and jets structures are unambiguously identified. (Gaensler et al., 2002).

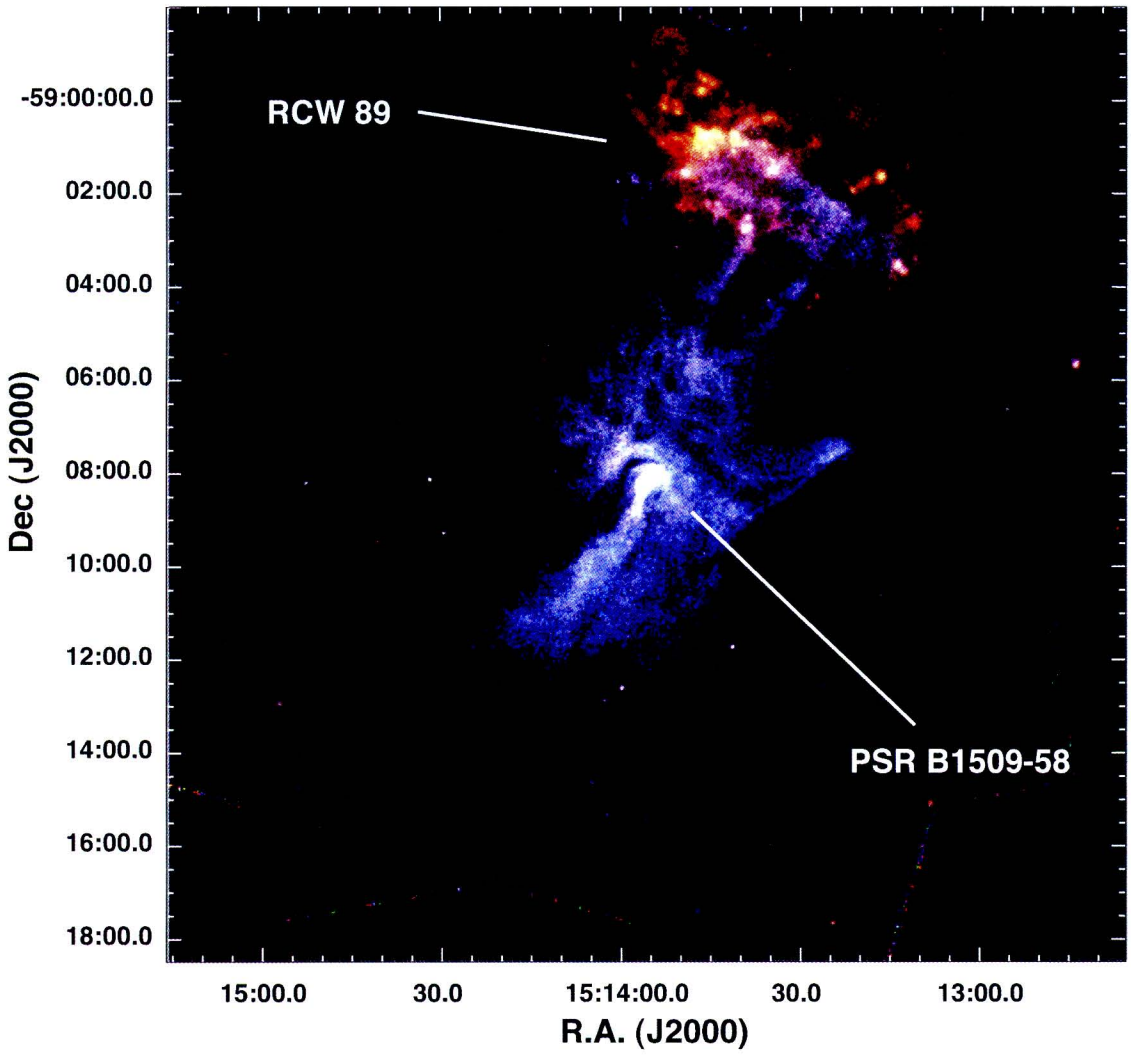


Figure 2.8: *Chandra* image of PSR B1509−58. Colors corresponds to the energy bands 0.4−1.5 keV (Red), 1.5−2.0 keV (Green), and 2.0−8.0 keV (Blue). From the pulsar, bilateral jets are ejected into south and north direction. At the end point of the northern jet, thermal plasma nebula RCW 89 exists.

### 2.5.3 TeV $\gamma$-ray emission from the PWN

Recently the High Energy Stereoscopic System (*H.E.S.S.*) provided the precise image of PWN in the very high energy (VHE) gamma-ray band (Figure 2.9). Surprisingly, the emission region is clearly extended along the jet axis, indicating the presence of electrons

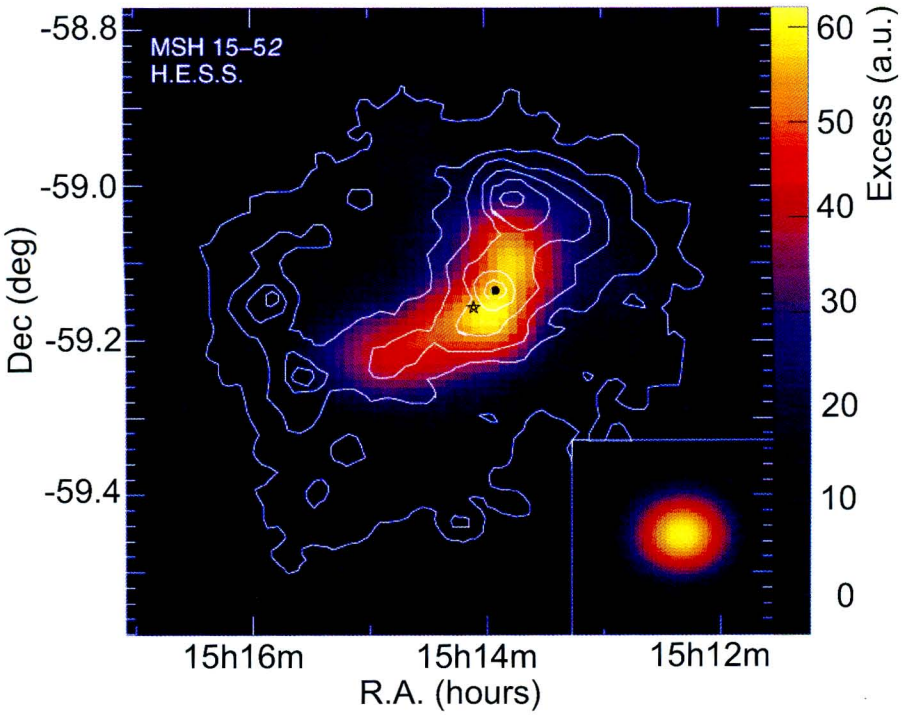


Figure 2.9: TeV $\gamma$-ray image by H.E.S.S. The map was smoothed with a Gaussian of $\sigma = 0.04$. The white contour lines denote the X-ray (0.6-2.1 keV) count rate measured by *ROSAT* (Trussoni et al., 1996). The black point and black star lie at the pulsar position and at the excess centroid, respectively. The right-bottom inset shows the simulated PSF smoothed identically (Aharonian et al., 2005).

which are accelerated up to energies of tens of TeV in the jet structure. Aharonian et al. (2005) proposed that the observed TeV $\gamma$-rays are produced by the inverse Compton process in which the CMB photons and IR photons from the dust in the SNR are scattered by synchrotron electrons.

### 2.5.4 Surrounding SNR G320.4−0.12

The pulsar and its PWN appears to be embedded in a 30 arcmin radio shell (Figure 2.10), SNR G320.4−01.2 (MSH 15−52). An observation of HI absorption yielded the distance of $D = 5.2 \pm 1.4$ kpc from the earth (Gaensler et al., 1999). For this distance, an age of 6-20 kyr for the SNR has been derived for standard parameters of the ISM and supernova explosions (Seward et al., 1983). According to the positional coincidence between the pulsar and the radio shells, it is inferred that these have the same progenitor. However the discrepancy in the age of the pulsar-SNR system has been discussed and is still unclear.

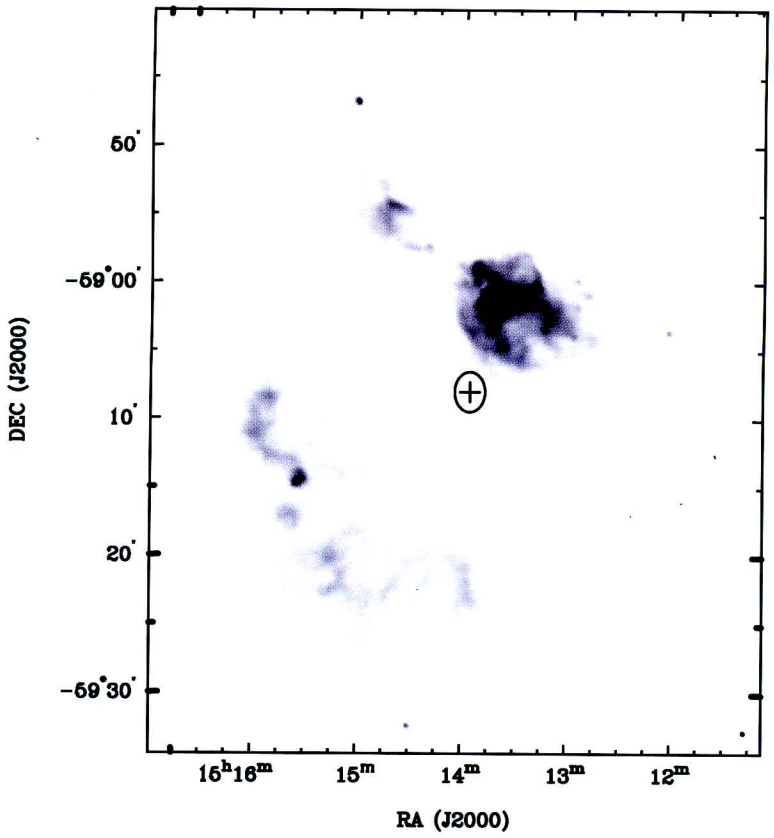


Figure 2.10: 20 cm radio image of SNR G320.4−01.2 by Australian Telescope Compact Array (ATCA) (Gaensler et al., 1999). The cross mark on the center of the panel indicates the pulsar position, while the ellipse shows the 1 $\sigma$ error ellipse for the birthplace of the pulsar.

### 2.5.5 Associating HII-region RCW 89

One of the curious character of the pulsar-SNR system is the existence of a HII region RCW 89 lying on the end point of the northern jet from PSR B1509−58 (Rodgers et al., 1960). The optical nebula RCW 89 coincides with the brightest portion of the northern radio shell of G320.4−0.12. The morphology of the nebula varies with the energy band; in optical RCW 89 shows filamentary structure (Figure 2.11), while in the radio and X-ray bands, it exhibits clumpy structures distributed in a "horseshoe" shape. Figure 2.8 also indicate that clumpy nebula seems to be confining non-thermal pulsar wind within the SNR. The VHE $\gamma$-ray emission asymmetry along the jet axis relative to the pulsar, as shown in Figure 2.9, may be explained by a scenario in which the two jets (south and north) are confined differently by the surrounding medium, as suggested by the appearance of RCW 89. More details are described in §5.1.

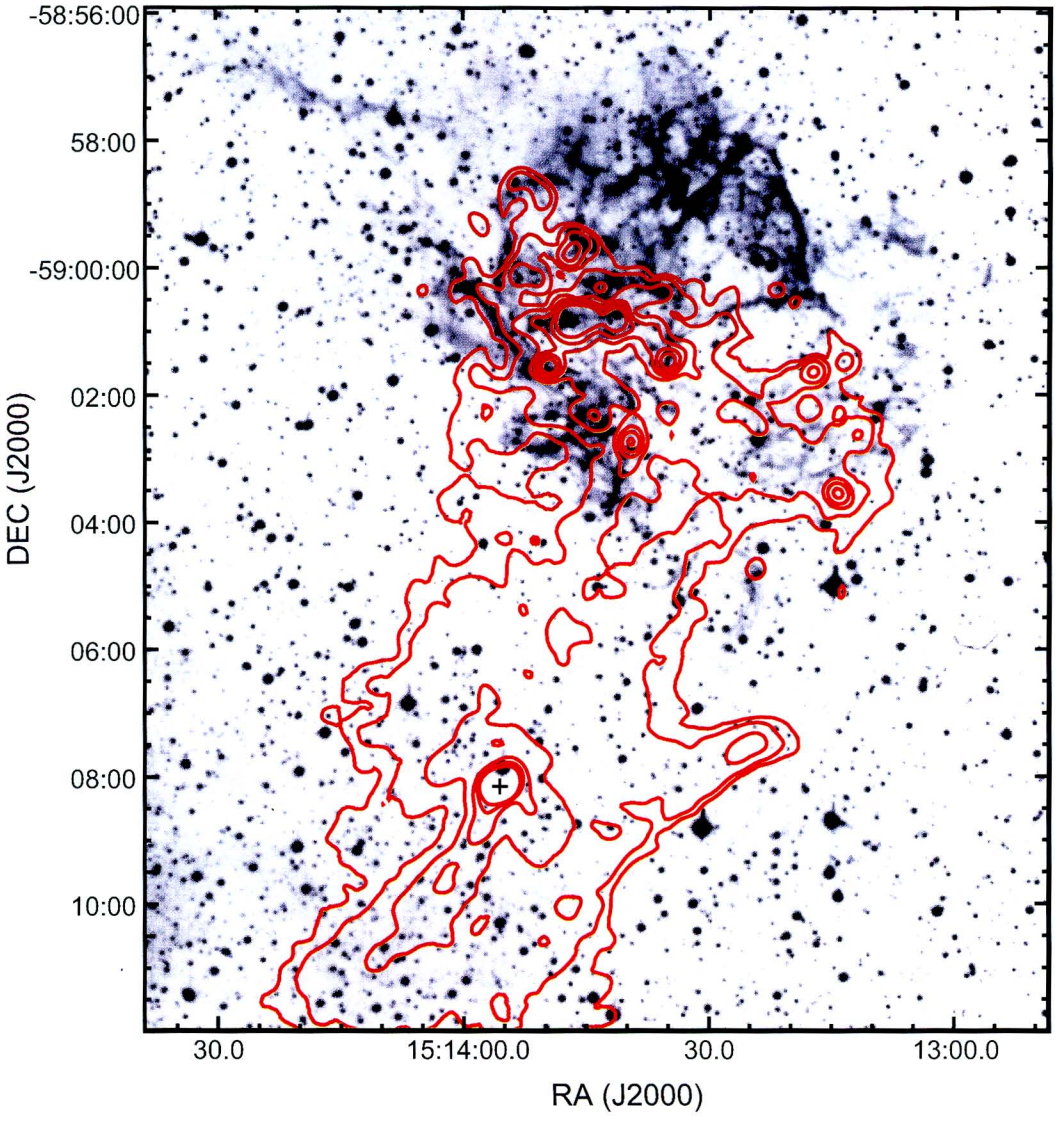


Figure 2.11: HII image of RCW 89 by UK Schmidt Telescope. The contour lines represent X-ray surface brightness measured by *Chandra*

# Chapter 3

# Instrumentation

The *Chandra* X-ray observatory was mainly utilized in this study. Its unprecedented spatial resolution up to sub-arcseconds enables us to investigate some PWNe which have diameters of only a few arcminutes. Here we briefly describe the satellite and on-board instruments, the High Resolution Mirror Assembly (HRMA) and the Advanced CCD Imaging Spectrometer (ACIS).

## 3.1 The *Chandra* X-ray Observatory

### 3.1.1 Mission Overview

The *Chandra* X-ray observatory (Weisskopf et al., 2000b) is the X-Ray component of NASA's four Great Observatories. The other components are the Hubble Space Telescope, the late Compton Gamma-Ray Observatory and the Spitzer Space Telescope. *Chandra* combines a high resolution ( $\sim$ 0.5 arcsecond) X-ray telescope with a suite of advanced imaging and spectroscopic instruments. Figure shows an outline drawing of the *Chandra*.

### 3.1.2 Launch and Orbit

The Observatory was successfully launched by NASA's Space Shuttle Columbia on July 23, 1999. Subsequently an Inertial Upper Stage and Chandra's Internal Propulsion System placed the Observatory in the final orbit after a few passages through the radiation belts. The *Chandra* orbit is highly elliptical and varies with time. As of December 2006 the apogee was $\sim$ 122,500 km and the perigee was $\sim$ 26,300 km. The orbit allows for reasonably high observing efficiency as the satellite spends most of the time well above the radiation belts ( $\sim$ 75%) and long continuous observations, up to $\sim$ 160 ksec, are made possible by the orbital period of 63.5 hours. However there is also a risk of radiation

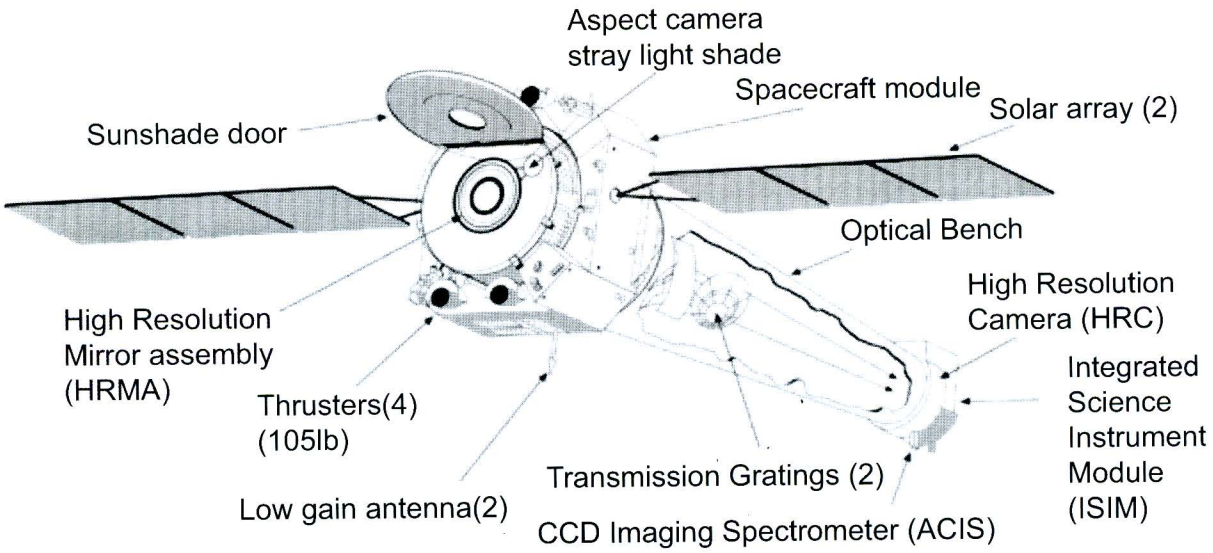


Figure 3.1: The *Chandra* Observatory with certain subsystems labeled (Chandra X-ray Center / NGST).

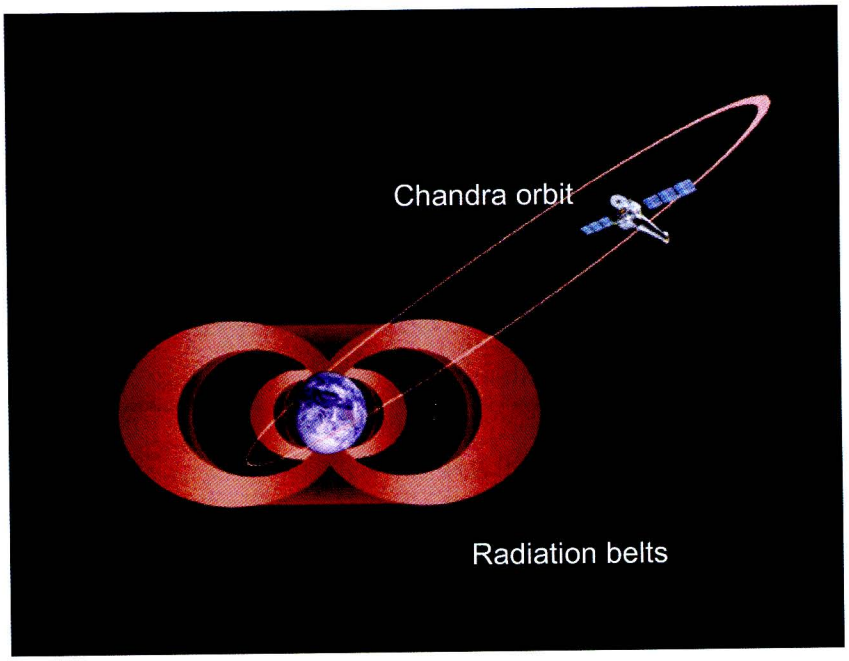


Figure 3.2: A schematic side view of Chandra's orbit, showing the inner and outer radiation belts. The apogee of *Chandra* orbit is $\sim$ 122,500 km as of Dec. 2006 (Chandra X-ray Center / M., Weiss).

damages on the scientific detectors on-board.

### 3.1.3 Unique Capabilities

*Chandra* was designed to provide order-of-magnitude advances over previous X-ray astronomy missions with regards to spatial and spectral resolution. The High Resolution Mirror Assembly (HRMA) produces images with a half-power diameter (HPD) of the point spread function (PSF) of $< 0.5$ arcsec (see §3.4). Both grating systems - the Low Energy Transmission Grating (LETG) and the High Energy Transmission Grating (HETG) - offer resolving powers well in excess of 500 over much of their bandwidth which, together, cover the range from $\sim 0.1$ to 10 keV. These grating systems were not used in our study.

## 3.2 The High Resolution Mirror Assembly

### 3.2.1 Description and Physical Configuration

The *Chandra* telescope consists of a nested set of four paraboloid-hyperboloid (Wolter Type-1) grazing incidence X-ray mirror pairs, namely the High Resolution Mirror Assembly (HRMA). The HRMA provides unprecedented spatial resolution with a half power diameter (HPD) of the point spread function (PSF) of $< 0''.5$. This remarkable feature makes *Chandra* seem to be the supreme observatory in X-rays.

Figure 3.3 shows a schematic view of the HRMA. Incident X-ray photon are condensed by the Parabolic-mirrors and the Hyperbolic-mirrors, sequentially. Finally these X-rays are concentrated on the focal plane 10 meters behind the HRMA. These precisely polished mirrors were fabricated from *Zerodur* glass. Surface of the mirror is coated with iridium. The diameters of mirror pairs ranges from 0.65 m (Inner mirror) to 1.23 m (Outer mirror), which provide a geometrical clear aperture of 1145 $cm^2$. The mass of HRMA is about 1500 kg. Other characteristics are given in Table 3.1.

### 3.2.2 HRMA Effective Area

Since reflectivity depends on energy as well as grazing angle, the HRMA throughput varies with X-ray energy.

Figure 3.4 shows the effective area of the HRMA, based on the mirror model discussed above and scaled by the on-orbit calibrations. The left panel shows the HRMA effective area as a function of X-ray energy (solid line) as well as the net effective area coupled

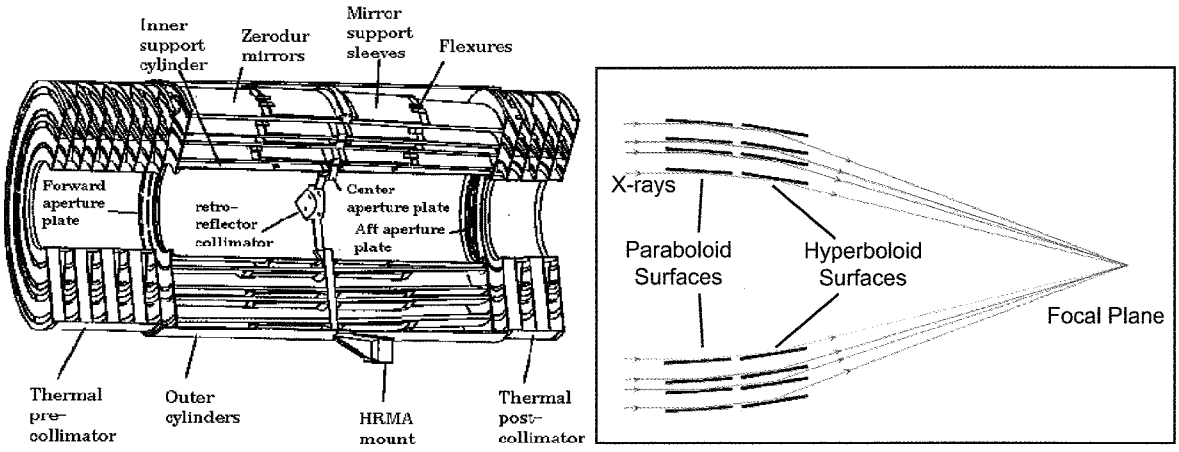


Figure 3.3: **Left** —The 4 nested HRMA mirror pairs and associated structures. **Right** —A schematic of grazing X-ray optics (Chandra X-ray Center, The *Chandra* Proposers' Observatory Guid).

Table 3.1: *Chandra* HRMA Characteristics

| | |
|---|---|
| Optics | Wolter Type-I |
| Mirror coating | Iridium (330 Å, nominal) |
| Mirror outer diameters (1, 3, 4, 6) | 1.23, 0.99, 0.87, 0.65 m |
| Mirror lengths (Pn or Hn) | 84 cm |
| Total length (pre- to post-collimator) | 276 cm |
| Unobscured clear aperture | 1145 $cm^2$ |
| HRMA mass | 1484 kg |
| Focal length | 10.070 $\pm$0.003 m |
| Plate scale | 48.82$\pm$0.02 $\mu$ m $arcsec^{-1}$ |
| PSF FWHM (with detector) | 0.5″ |
| Effective area | 800 $cm^2$ @ 0.25 keV |
| | 400 $cm^2$ @ 5.0 keV |
| | 100 $cm^2$ @ 8.0 keV |
| Ghost-free field of view | 30' diameter |

with ACIS. The right panel shows the effect of off-axis vignetting on the effective area for various energies. The plotted results are averages over the azimuthal angle.

Note that the predicted effective area based the raytracing simulation shows good agreement with the actual measurements both on-ground and on-orbit. Therefore the HRMA seems to retain the same performance as that shown by the ground calibration.

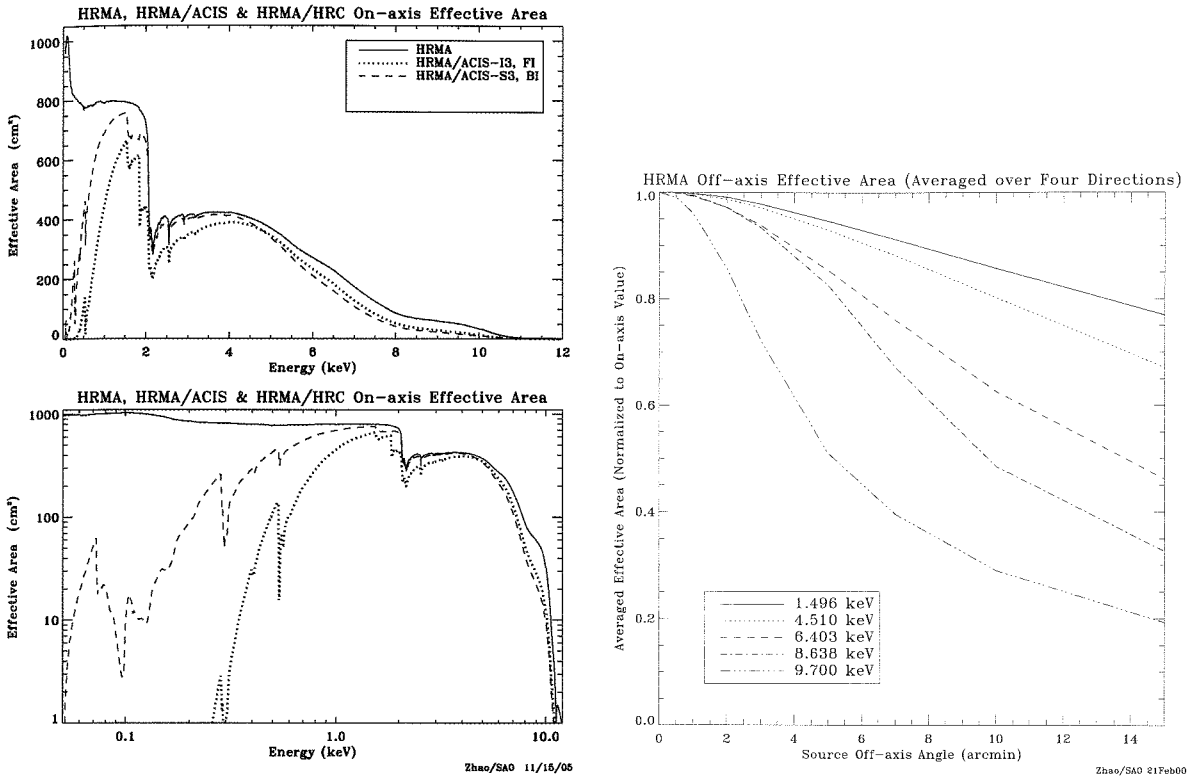


Figure 3.4: **Left** —Energy dependence of the HRMA (ACIS) on-axis effective areas by the raytracing simulation of the HRMA model. The predicted effective area was scaled by the on-orbit calibration. Upper panel and bottom panel show the effective area in linear scale and in logarithmic scale, respectively. The structure near 2 keV is due to the iridium M-edge. Dashed and dotted lines show the net effective areas of the HRMA coupled with the detectors (ACIS-I/S). **Right** —The HRMA effective area versus off-axis angle, averaged over azimuth, for various energies. The Y-axis is normalized by the on-axis effective area. (Chandra X-ray Center, The *Chandra* Proposers' Observatory Guid)

### 3.2.3 Point-Spread Function

The most important character of the HRMA is the spatial resolution. In general, the spatial resolution is defined by the encircled energy fraction that is the two-dimensional integral of the point-spread function (PSF). The spatial resolution depends both on grazing angle and energy. Here we present the optical profile of the HRMA predicted with numerical raytracing calculation based on the HRMA model.

Left panel of figure 3.5 shows the energy dependence of the encircled energy fraction for on-axis condition. Apparently the image size tends to increase as energy rises. For higher energies (8.638 keV and 9.700 keV), the curves are broadened at the bottom. This is because the focus of higher energies does not coincide with the HRMA common focus,

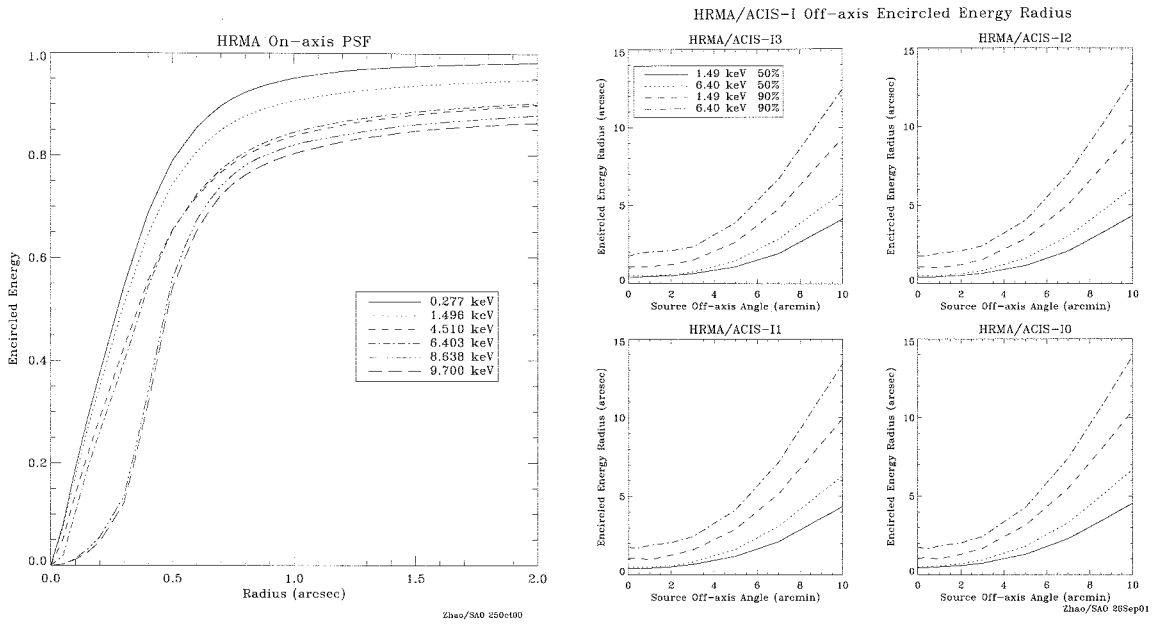


Figure 3.5: **Left** —The Fractional encircled energy as a function of angular radius, calculated for an on-axis point source, at various X-ray energies. The curves are the combined response and centered at the common focus of the full HRMA, i.e. four nested mirror pairs. **Right** —The HRMA/ACIS-I encircled energy radii for circles enclosing 50% and 90% of the power at 1.49 and 6.40 keV as a function of off-axis angle. (Chandra X-ray Center, The *Chandra* Proposers' Observatory Guid)

but is offset by about 0.2", due to a slight tilt of the HRMA mirror pair 6.

Right panel shows the encircled energy radius (50% and 90%) as a function of off-axis angle for the ACIS-I chip-set. The ACIS-I surface is composed by four tilted flat chips which approximate the curved *Chandra* focal plane. The HRMA optical axis passes near the aim point which is located near the inner corner of chip I3. Thus the off-axis encircled energy radii are not azimuthally symmetric. The four panels show these radii's radial dependence in four azimuthal directions - from the aim-point to the outer corners of the four ACIS-I chips. These curves include the blurs due to the ACIS-I spatial resolution and the *Chandra* aspect error.

The morphology of the HRMA PSF is distorted dramatically due to the aberration effects. The PSF distortion effect depends both on off-axis angle and azimuthal angle, like the comatic aberration of an optical telescope. Figure 3.6 illustrate the effect of aberrations on images of off-axis point sources at 1.49 keV and 6.4 keV. When we perform an accurate positional measurement we must consider the effect of aberrations.

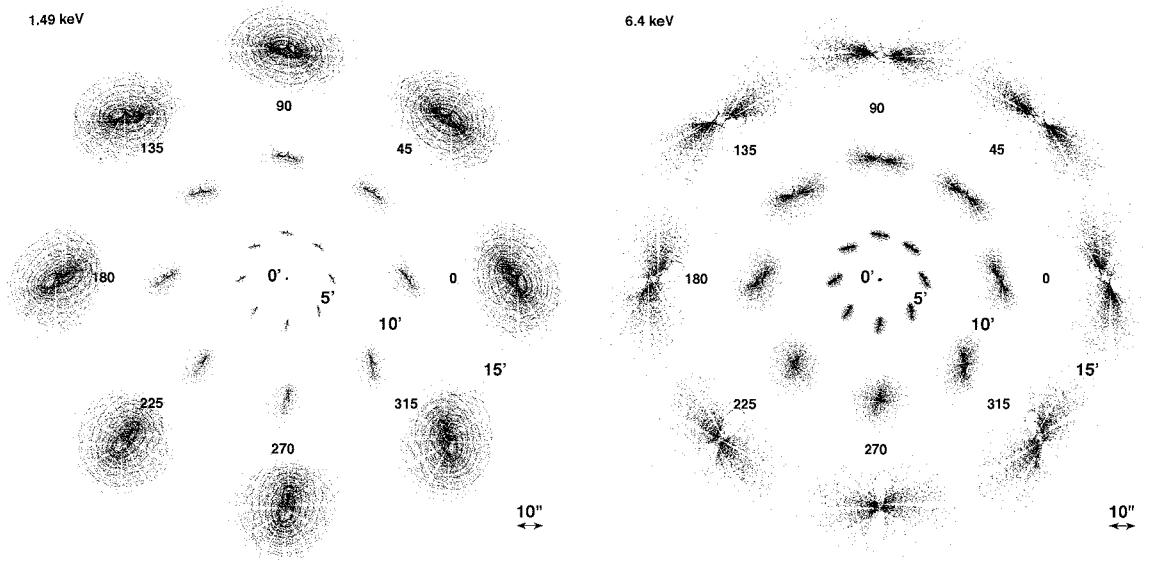


Figure 3.6: Simulated 1.49 keV (Left) and 6.4 keV (Right) images, for the HRMA only. Images are shown with a linear stretch, as they would appear on the sky, at off-axis angles of 5', 10', and 15' from the aim point and various azimuths. The images are all to the same scale, illustrated by the scale bar. The spacing between images is arbitrary. The surface brightness of the images at 10′ and 15′ has been enhanced to show their structures. Spokes in the images are due to shadowing by the mirror support struts. Cusps are due to a slight misalignment of the parabolic and hyperbolic mirrors. (Chandra X-ray Center, The *Chandra* Proposers' Observatory Guid)

## 3.3 Advanced CCD Imaging Spectrometer (ACIS)

### 3.3.1 Overview

*Chandra* has two imaging detectors, the Advanced CCD Imaging Spectrometer (ACIS) and the High Resolution Camera (HRC). In this study we used the ACIS which offers the capability to simultaneously acquire high-resolution images and energy spectra, namely spatially resolved spectroscopy. The instrument can also be used in conjunction with the High Energy Transmission Grating (HETG) or Low Energy Transmission Grating (LETG) to obtain higher resolution spectra.

ACIS contains 10 planar, 1024 x 1024 pixel CCDs; four arranged in a 2x2 array (ACIS-I) and six arranged in a 1x6 array (ACIS-S) which is either for imaging and grating. Two CCDs (ACIS-S1, S3) are back-illuminated (BI) and eight are front-illuminated (FI). The response of the BI devices extends to energies below that accessible to the FI chips reflecting their internal structures (see §3.2.2 ). The configuration of the ACIS chips are

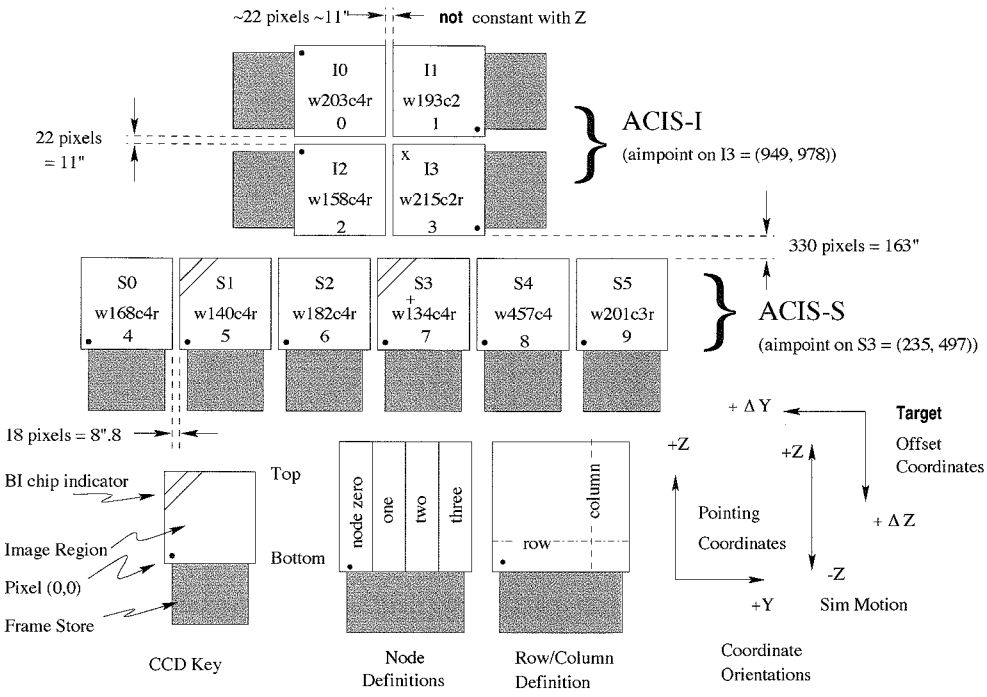


Figure 3.7: A schematic drawing of the ACIS focal plane; insight to the terminology is given in the lower left. The "+" mark and the "x" mark indicate the nominal aim-points on S3 and I3, respectively. The view is along the optical axis, from the source toward the detectors, (-X). The numerous ways to refer to a particular CCD are indicated: chip letter+number, chip serial number, and ACIS chip number. The node numbering scheme is illustrated lower center.(Chandra X-ray Center, The *Chandra* Proposers' Observatory Guid)

shown in Figure 3.7.

In the Early phase of the *Chandra* mission, the gate structures on the surface of FI-CCDs of the ACIS have been damaged by cosmic-rays concentrated by the X-ray mirror in the radiation belt. This accident resulted in a serious degradation of the energy resolutions of FI-CCDs, while BI-devices were not impacted because their gate structures were not directly exposed to the radiation. Therefor chip-average energy resolution of the BI devices is better than that of the FI devices. For the above reason, we should choose ACIS-S3 (BI) for SNRs with prominent line structures.

### 3.3.2 Basic Principles

A CCD is a solid-state electronic device composed primarily of silicon. A "gate" structure on one surface defines the pixel boundaries by alternating voltages on three electrodes spanning a pixel. An electric field is applied to the silicon in the depletion region so that charge moves quickly to the gate surface. The gates allow confined charge to be passed down a "bucket brigade" (the buried channel) of pixels in parallel to a serial readout at one edge by appropriately varying ("clocking") the voltages in the gates.

The ACIS front-illuminated (FI) CCDs have the gate structures facing the incident X-ray beam. Two of the chips on the ACIS-S array (S1 and S3) have had treatments applied to the back sides of the chips, removing insensitive, undepleted bulk silicon material and leaving the photo-sensitive depletion region exposed. These are the back-illuminated (BI) chips and are deployed with the back side facing the HRMA.

Photoelectric absorption of an X-ray in silicon results in the liberation of a proportional number of electrons: an average of one electron-hole pair for each 3.7 eV of energy absorbed. Immediately after the photoelectric interaction, the charge is confined by electric fields to a small volume near the interaction site. Charges in a FI device can also be liberated below the depletion region, in an inactive substrate, from where it diffuses into the depletion region. This charge may easily appear in two or more pixels.

Good spectral resolution depends upon an accurate determination of the total charge deposited by a single photon. This in turn depends upon the fraction of charge collected, the fraction of charge lost in transfer from pixel to pixel during read-out, and the ability of the readout amplifiers to measure the charge. Spectral resolution also depends on read noise and the off-chip analog processing electronics. The ACIS CCDs have readout noise less than 2 electrons RMS. Total system noise for the 40 ACIS signal chains (4 nodes/CCD) ranges from 2 to 3 electrons (rms) and is dominated by the off-chip analog processing electronics. As mentioned above low energy protons encountered during radiation belt passages increased charge transfer inefficiency (CTI) of FI-CCDs, which causes the loss of energy resolution. The ACIS instrument team provides a correction algorithm that recovers much of the lost energy resolution the FI CCDs. The correction recovers a significant fraction of the CTI-induced loss of spectral resolution of the FI-chips. In this study we have adopted the CTI-correction technique via *CIAO 3.4*.

The CCDs have an "active" or imaging section (see Figure 3.7) which is exposed to the incident radiation and a shielded "frame store" region. A typical mode of the ACIS CCD operation is:

(1) the active region is exposed for a fixed amount of time (full frame $\sim$ 3.2 s);

(2) at the end of the exposure, the charge in the active region is quickly ( $\sim$ 41 ms) transferred in parallel into the frame store;

(3) the next exposure begins;

(4) simultaneously, the data in the frame store region is transferred serially to a local processor.

After removing bias, the processor identifies the position and amplitude of any "events" according to a number of criteria depending on the precise operating mode. The position and the amount of charge collected, together with similar data for a limited region containing and surrounding the pixel are classified ("graded"[1]) and then passed into the telemetry stream.

### 3.3.3 Basic Properties

#### Quantum efficiency

The quantum efficiencies near the readout for the ACIS CCDs for the standard grade set, including optical blocking filters and molecular contamination, are shown in left panel in Figure 3.8. While right panel shows the combined HRMA/ACIS on-axis effective areas. The effective areas are for an on-axis point source and a 20 arcsec diameter detection cell.

#### Spatial Resolution & Encircled Energy

The spatial resolution for on-axis imaging with HRMA/ACIS is limited by the physical size of the CCD pixels (24.0$\mu$m $\times$ 24.0$\mu$m $\sim$ 0.492arcsec $\times$ 0.492arcsec) and not the HRMA. This limitation applies regardless of whether the aim-point is selected to be the nominal point on I3 or S3 (Figure 3.7). Left panel in Figure 3.9 shows an in-flight calibration.

#### Energy Resolution

Before the launch the ACIS FI CCDs originally approached the theoretical limit for the energy resolution at almost all energies, while the BI CCDs exhibited poorer resolution. Due to the radiation damages after the launch, the energy resolution of the FI CCDs has become a function of the row number; while it is close to the pre-launch values near the frame store region and substantially degraded in the farthest row. An illustration of the dependence on row is shown by right panel in Figure 3.9. The figure also illustrates the

[1]see (Chandra X-ray Center, The *Chandra* Proposers' Observatory Guid).

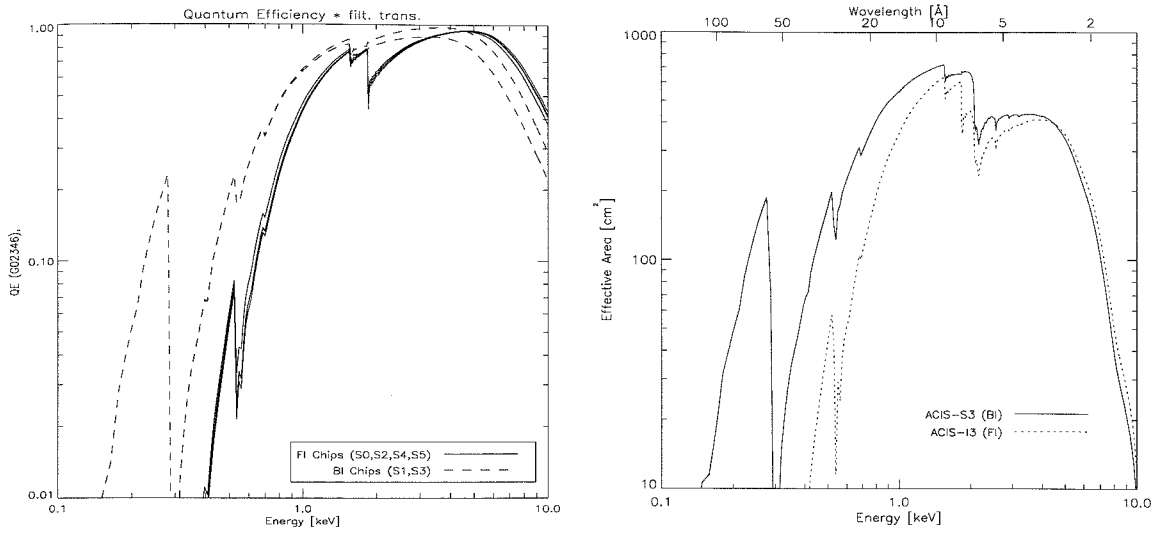


Figure 3.8: **Left**— The quantum efficiency, convolved with the transmission of the appropriate optical blocking filter, of the ACIS CCDs as a function of energy. **Right**— The HRMA/ACIS predicted effective area as a function of energy. (Chandra X-ray Center, The *Chandra* Proposers' Observatory Guid)

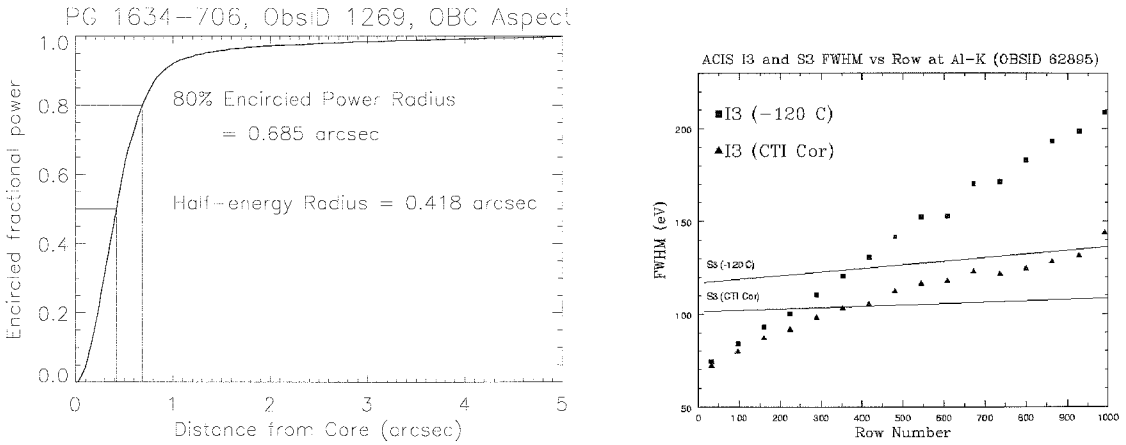


Figure 3.9: **Left**— The on-orbit encircled broad-band energy versus radius for an ACIS observation of point source PG1634-706. The effective energy is 1 keV. **Right**— The energy resolution versus row number for the Al-K line. The square data points are the FWHM of lines averaged over 32-row bins. The triangle data points are the FWHM of CTI-corrected lines. The upper line shows the uncorrected performance of the S3 chip, while the lower line shows the CTI-corrected performance of the S3 chip. These data are from March 2000. (Chandra X-ray Center, The *Chandra* Proposers' Observatory Guid)

improvement by the CTI correction (As of December 2006, data for the two BI chips can also be corrected in the same way, though the effects are more subtle).

### 3.3.4 Operating Modes

The ACIS provide various operating mode. A brief description of the operating mode used in our study is shown here.

#### Timed Exposure (TE) Mode

A timed exposure refers to the mode of operation wherein a CCD collects data (integrates) for a preselected amount of time– the Frame Time. Once the time interval has passed, the charge from the 1024×1024 active region is quickly (41 ms) transferred to the frame-store region and subsequently red out through serial registers. Imaging observations must be operated in the TE-mode. [2]

#### Full Frames / Sub-arrays

It is possible for one to select a sub-array; a restricted region of the CCD in which data will be taken. This operating option provides a shorter readout time than the full frame readout. This is very useful for a bright point source such as a pulsar, since a short frame time suppresses pileup events (described below) to low levels.

The nominal frame time is given by:

$$T \quad (\text{msec}) = 41 \times m + 2.84 \times n + 5.2 + 0.040 \times (m \times q), \tag{3.1}$$

where $q$ is the number of rows separating the sub-array from the frame store region, $n$ is the number of rows in the sub-array, and $m$ is the total number of CCDs that are activated. The frame time is an important parameter for the pile-up correction in spectral model fitting. Examples of sub-arrays are shown in Figure 3.10

### 3.3.5 Telemetry Formats

There are number of telemetry formats available. Specifying a format determines the type of information that is included in the telemetry stream. The number of bits per event depends on which mode and which format is selected. Thus the number of bits per event determines the event rate at which the telemetry will saturate. The data formats which can be selected are described below.

[2]Continuous Clocking (CC) mode provide more quick time response ($\sim$ 3 ms) with one dimension of spatial resolution. In this mode, data is continuously clocked through the CCD.

Table 3.2: ACIS Characteristics

| | |
|---|---|
| Focal plane arrays | I-array (4 CCDs in 2x2) |
| | S-array (6 CCDs in 1x6) |
| CCD format | 1024 × 1024 pixels |
| Pixel size | 23.985 $\mu$m (0.4920 $\pm$ 0.0001 arcsec) |
| Array size | 16.9 × 16.9 arcmin (ACIS-I) |
| | 8.3 × 50.6 arcmin (ACIS-S) |
| On-axis effective Area | 110 cm$^2$ @ 0.5 keV (FI) |
| | 600$^2$ cm @ 1.5 keV (FI) |
| | 40$^2$ cm @ 8.0 keV (FI) |
| FI Quantum efficiency | $>$ 80% @ 3.0$\sim$6.5 keV |
| | $>$ 30% @ 0.7 $\sim$ 11.0 keV |
| BI Quantum efficiency | $>$ 80% @ 0.8 $\sim$5.5 keV |
| | $>$ 30% @ 0.4$\sim$ 10.0 keV |
| System noise | $<$ 2 electrons (rms) per pixel |
| Pulse-height encoding | 12 bits/pixel |
| Event threshold | FI: 38 ADU ( 150-350 eV) |
| | BI: 20 ADU ( 150-220 eV) |
| Minimum row readout time | 2.8 ms (CC-mode) |
| Nominal frame time | 3.2 sec (full frame) |
| Frame transfer time | 40 $\mu$sec (per row) |
| Detector operating temperature | - 90 $\sim$- 120 °C |

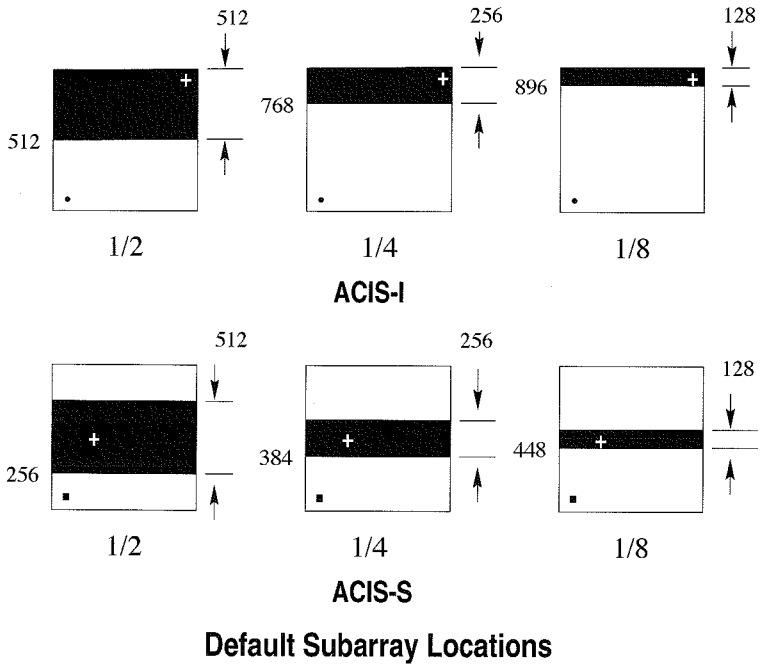


Figure 3.10: Examples of various sub-arrays. The heavy dot in the lower left indicates the terminology. (Chandra X-ray Center, The *Chandra* Proposers' Observatory Guid)

- **Faint**— Faint format provides the event position in detector coordinates, an arrival time, an event amplitude, and the contents of the 3*times*3 pixel island that determines the event grade. The bias map is telemetered separately.

- **Very Faint**— Very Faint format provides the event position in detector coordinates, the event amplitude, an arrival time, and the pixel values in a 5×5 pixel island. This format is only available with the Timed Exposure mode. Events are still graded by the contents of the central 3×3 pixel island. **This format offers the advantage of reduced background after ground processing but only for sources with low counting rates that avoid both telemetry saturation and pulse pileup.**

- **Graded**— Graded format provides event position in detector coordinates, an event amplitude, the arrival time, and the event grade.

### 3.3.6 Inherent phenomenons of CCDs

The charge transfer process and the long frame-time of CCD devices cause the resulting image to have some problems in a certain conditions.

### Pile-up

Pile-up occur es when two or more X-ray photons hit on the same position of the CCD within a frame time interval. Since the HRMA has a good spatial resolution, pile-up can be a serious problem when we observe a bright point source. The fundamental impacts of pileup are:

1 : A distortion of the energy spectrum — the apparent energy is approximately the sum of two (or more) energies.

2 : An underestimate as to the correct counting rate — two or more events are counted as one.

3 : A grade migration — the nominal grade distribution that one expects for X-ray events changes.

A simple illustration of the effects of pileup is given in Figure 3.10.

### Trailing events

It takes 40 $\mu$sec to transfer the charge from one row to another during the process of moving the charge from the active region to the frame-store region. This has the interesting consequence that each CCD pixel is exposed, not only to the region of the sky at which the observatory was pointing during the long (frame time) integration, but also, for 40 $\mu$sec each, to every other region in the sky along the column in which the pixel in question resides. Right panel of figure 3.11 is an example where there are bright features present, so intense, that the tiny contribution of the flux due to trailing is stronger than the direct exposure, hence the trailed image is clearly visible. Trailed images are also referred to as "read out artifact" and "out-of-time images". The user needs to be aware of this phenomenon as it has implications for the data analysis, e.g. estimates of the background. In some cases, the trailed image can be used to measure an unpiled spectrum and can also be used to perform 40 $\mu$sec timing analysis (of extremely bright sources).

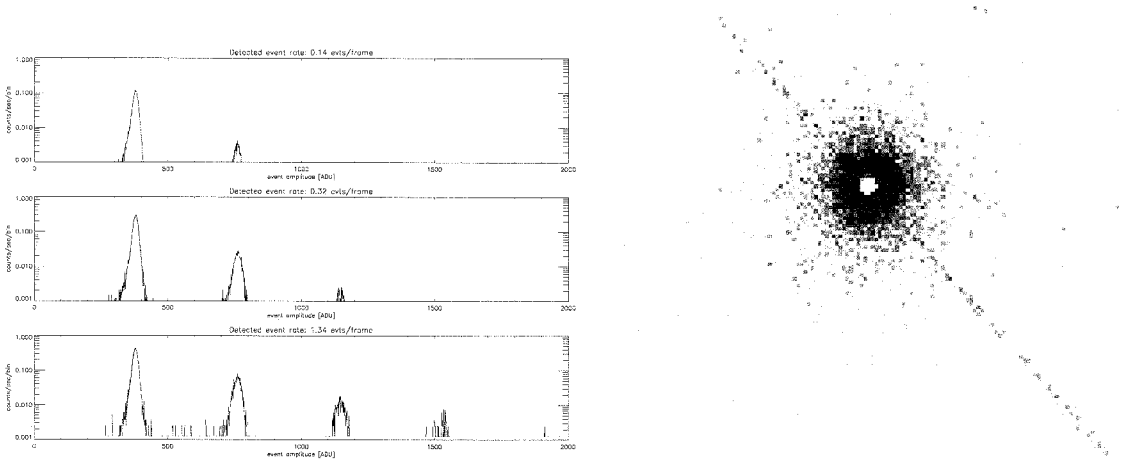


Figure 3.11: **Left**— The effects of pileup as a function of source intensity. Single-photon events are concentrated near $\sim$ 380 ADU, and events with 2 or more photons appear at integral multiples of the line energy. **Right**— Trailed image of a strong X-ray source. The core of the image is faint due to pileup. Most events here are rejected because of bad grades. The readout direction is parallel to the trail. (Chandra X-ray Center, The *Chandra* Proposers' Observatory Guid)

# Chapter 4

# PSR B1509-58 in G320.4−01.2

## 4.1 Observations

The vicinity of PSR B1509−58 has been multiply observed by *Chandra*. For this study, the most recent four observations which are sequentially performed from 2004 to 2005 are utilized. Exposure time of the each observation is about $\sim$ 50 ks. While, for the vicinity of RCW 89, an ACIS-I observation for 19 ks exposure on 2000 and an ACIS-S observation for 30 ks exposure on 2004 are utilized. The observational settings are summarized in Table 4.1.

## 4.2 Data Reductions

Utilizing the observatory's house keeping and configuration information, the raw telemetry data can be refined to maximize *Chandra*'s potential. This process promises to reduce the background events, to improve the energy resolution, and to improve spatial resolution. Applying the same reduction criteria to all the data set to be analyzed assures that those data can be systematically handled in the same way.

The *Chandra X-ray Center* (CXC) distributes the data analysis software package the *Chandra Interactive Analysis of Observations* (CIAO [1] [2]) and the calibration database CALDB, which are standard tool for analysis of *Chandra* data. In this study we utilized CIAO version 4.0 beta and CALDB version 3.4.1.

We have performed the reduction process for the each data set in accordance with the instructions recommended by CXC. The brief outline of the reduction is as follows; (1) applying an ACIS gain map from CALDB, (2) applying the time-dependent ACIS gain cor-

[1] From "s'sciavo", "I am your servant" in Venetian dialect.

[2] An anonymous CIAO user pointed out that the Venetian is a language in its own right, not a dialect.

Table 4.1: Summary of observations of PSR B1509−58 and SNR G320−01.2

| ObsID# | Coordinate[a] (J2000.0) | Date | Detector | Mode[b] | Exposure (s) | PI |
|---|---|---|---|---|---|---|
| 5534 | 15:13:55.60 -59:08:08.9 | 2004/12/28 | ACIS-I | VFaint | 50130 | Slane |
| 5535 | 15:13:55.60 -59:08:08.9 | 2005/02/07 | ACIS-I | VFaint | 43130 | Slane |
| 6116 | 15:13:55.60 -59:08:08.9 | 2005/04/29 | ACIS-I | VFaint | 47650 | Slane |
| 6117 | 15:13:55.60 -59:08:08.9 | 2005/10/18 | ACIS-I | VFaint | 46140 | Slane |
| 0754 | 15:13:55.60 -59:08:08.9 | 2000/08/14 | ACIS-I | Faint | 19280 | Kaspi |
| 5562 | 15:13:34.20 -59:01:58.0 | 2004/12/31 | ACIS-S | VFaint | 29960 | Yatsu |

[a] A coordinate of the aim-point.

[b] Telemetry format described in §3.

rection and the ACIS CTI correction (data sets taken at −120°C only), and (4) applying PHA and pixel randomization. These tasks above are combined in "acis_process_events" in CIAO.

For VFAINT mode data sets, we can also screen out background events using information of 5×5 event island. In this study we applied the "VFAINT Mode background cleaning" only for the observation RCW 89. For bright sources, however, the VFAINT algorithm tends to misjudge a certain amount of source photons to be background events. Therefore we did not apply the VFAINT background cleaning for the other data taken under the VFAINT Mode.

## 4.3 X-ray Imaging

### 4.3.1 Entire structure

Exposure-corrected and smoothed images in the energy range 0.4-2.0 keV (hard-band)and 0.2-8.0 keV (soft-band), encompassing the entire field of view of the ACIS-I array, is shown in Figure 4.1. The gray-scale represents the surface brightness on a logarithmic scale. Because the exposure-correction could not reconstruct the image around the gaps between the CCDs perfectly, the images are still streaky. There are also trailing events because the pulsar is so bright.

Figure 4.2 is the hardness ratio map which indicates the ratio between the count rate in the hard energy band of 2.0-8.0 keV and the total count rate integrated over 0.4-8.0

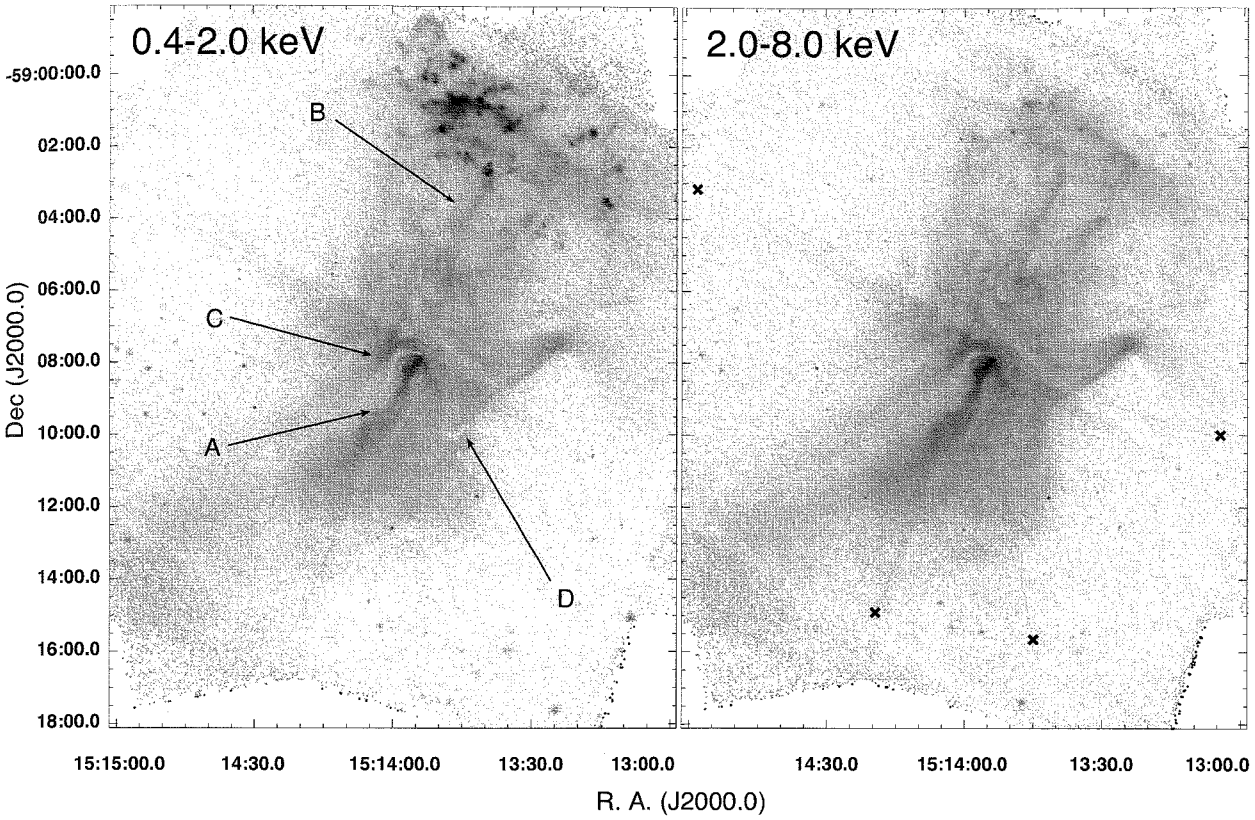


Figure 4.1: *Chandra* image of G320.4−01.2 for 0.4-2.0 keV (Left) and for 2.0-8.0 keV (Right). The images are combining four ACIS-I images (ID = 5534, 5535, 6116, and 6117) and are exposure-corrected. The both images are smoothed with a Gaussian of $\sigma = 2.0''$. The "x" marks in the right panel indicate the trailing events.

keV.

The pulsar wind nebula is very large, almost filling the radio shell of G320.4−01.2. The length the X-ray nebula along the jet-like feature reaches $\sim$16′, which corresponds to $\sim$24 pc for the distance $D = 5.2$ kpc. The south edge of the nebula is more distant ($\sim$ 10′) from the pulsar than the north edge ($\sim$ 6′). While the width of the nebula across the east-west direction is about 8′, which is a half of the length along the axis.

A jet-like feature "A" is blowing from the pulsar directed to southeast. The jet curves around to the east at a distance $\sim$2 arcmin from the pulsar, and is fading abruptly at a separation of $\sim$4 arcmin from the pulsar. Finally, the jet reaches the south radio shell (Fig. 2.10) and stagnates there. The hardness ratio map (Fig. 4.2) indicates that the jet has remarkably hard (or flat) spectrum in comparison with the entire nebula. On the north side of the pulsar, the collimated flow can be clearly identified in the pulsar vicinity within 30 arcsec and then suddenly disappears. At a separation of $\sim$4 arcmin a

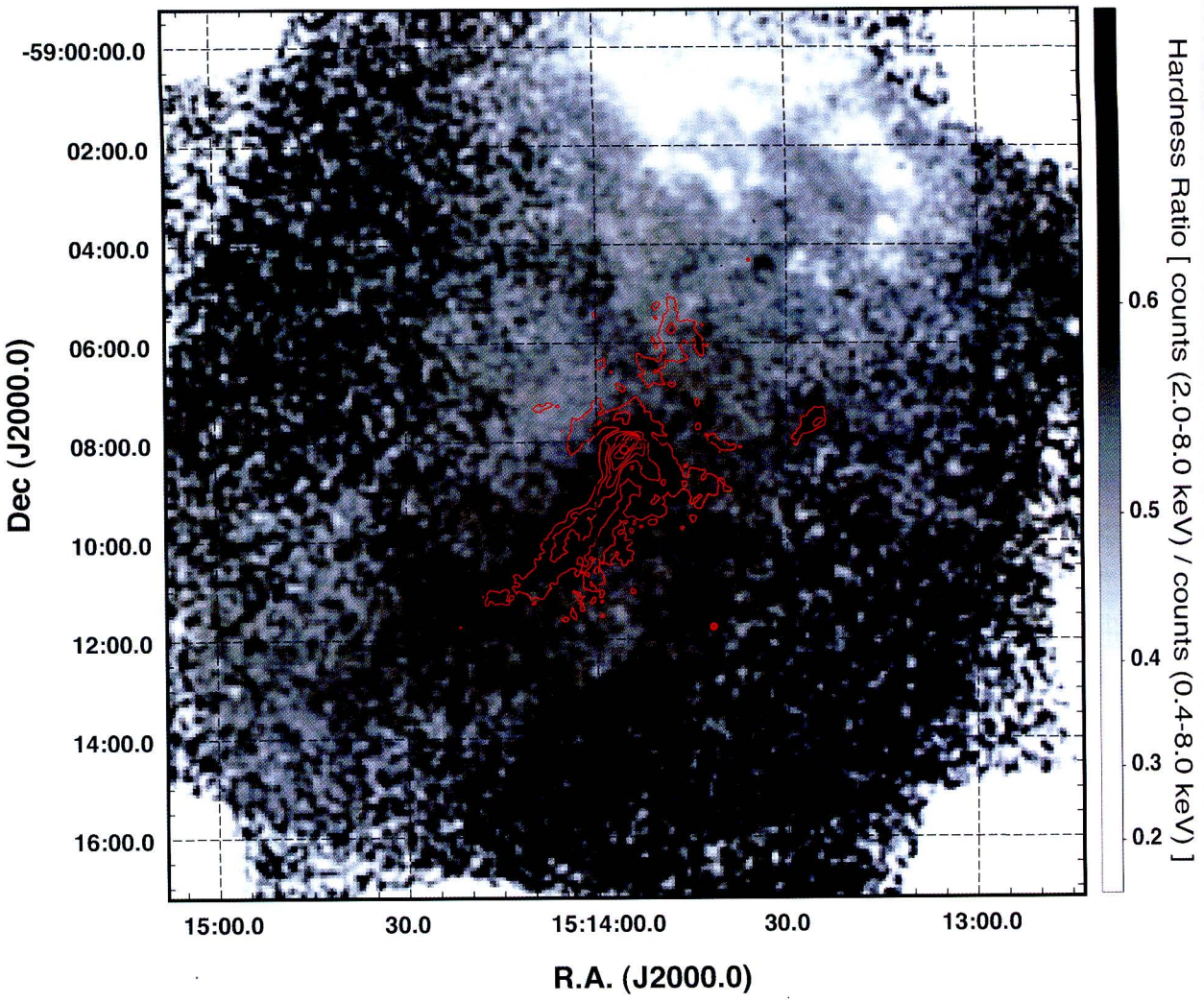


Figure 4.2: Hardness ratio of the PSR B1509−58. The gray scale indicates the ratio of the count rate of high energy band (2.0-8.0 keV) to the total count rate (0.4-8.0 keV). The hardness ratio was calculated with respect to the each $4\times4$ arcsec$^2$ sub-regions. And the resulting map was smoothed with a Gaussian of $\sigma$ =4 arcsec. The red contour indicate the X-ray surface brightness over 0.4-8.0 keV energy band.

jet-like feature "B" appears again. The ratio of the surface brightness between south jet and north implies that the south jet is directed toward us that provides the relativistic boosting of the X-ray flux.

A ring-like structure "C" can be seen at a separation of $\sim$ 60 arcsec from the pulsar, analogous to the outer torus of the Crab nebula. The surface brightness of the north rim of the torus is brighter than that of the other side, implying that the north rim is closer to the observer than is the pulsar, and is produced by a wind whose line-of-sight velocity component is directed toward us.

On the east-side of the pulsar, the surface brightness of the PWN is getting fainter as a function of the distance from the pulsar. In contrast, the west side of the PWN appears to be sharply cut off at 2 arcmin from the pulsar, implying that the pulsar wind is confined by invisible ISM. An evident of filament-like feature, marked as feature "D" in Figure 4.1, was found. These shadow like features are only seen in the soft energy band. Although the optical counterpart are not found in HII image as shown in Figure 2.11, these features can be the filament induced by the Rayleigh-Taylor instability, analogous to the "fingers" in the Crab nebula (Hester et al., 1996). The hardness ratio shown in Figure 4.2 describes the shadow of invisible ISM more clearly. The extremely high hardness ratio seen in the west side of the jet is implying the absorption caused by the invisible ISM which may confine the pulsar wind or may bend the jet to the east.

The spin axis of the pulsar believed to be aligned with the main nebula axis. The ellipticity of the torus implies a inclination angle of $i \sim 30°$ (Gaensler et al., 2002). Figure 4.3 describes the inferred geometry of the PWN of PSR B1509−58.

### 4.3.2 Compact structures around the pulsar vicinity

Figure 4.4 shows a close up view of the PWN just around the pulsar. The FoV covers the feature "C" in Figure 4.1 (Feature "C" is marked as "Outer Torus" in this figure). The spatial resolution of this field is $\sim$0.5 arcsec (HPD). The most intriguing is an indication of "Inner Ring" structure $\sim$ 10 arcsec apart from the pulsar as seen in the Crab nebula. Nevertheless the existence of the ring feature is still ambiguous comparing with the crab, this might be due to the contamination from the bright nebula core.

#### Applying an unsharp mask

In order to visualize the compact structures just around the pulsar, we applied an "unsharp masking" technique, which is a kind of the high-pass filter, to the *Chandra* image.

First of all we generated a low-frequency component image that should be removed. To

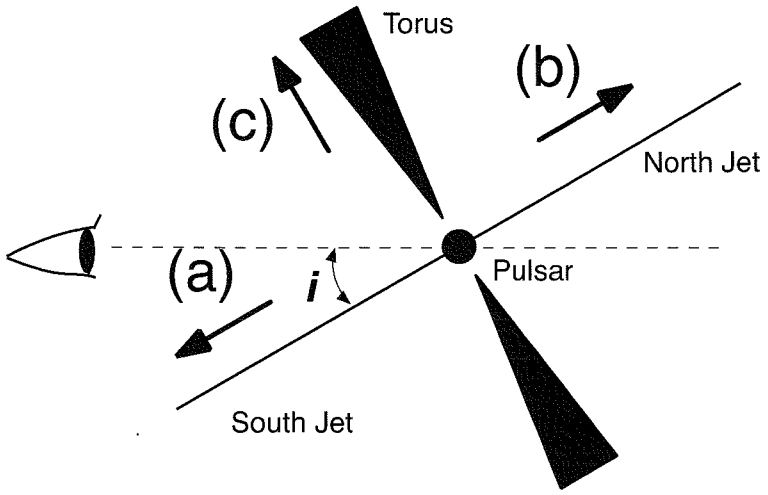


Figure 4.3: Schematic drawing of the geometry of PSR B1509−58. An inclination angle of $\sim 30^{\circ}$ is inferred by the appearance of the torus.

avoid the impact from the bright point sources such as the pulsar, we removed remarkable point sources using *wavdetect* in *CIAO* version 4.0 (Figure B.1-a). The "gap" regions were extrapolated based on the regions just around the point sources using *dmfilth* (Figure B.1-b). Then the "filled-in" image was normalized by exposure map (Figure B.1-c & d). Next the exposure corrected image was smoothed via the tool *aconvolve*. As a convolution kernel, an isotropic Gaussian function was adopted (Figure B.1-e). We also generated a source image in the same method as for the low-frequency image. In this process we only removed two point sources, the pulsar and a background AGN encircled by red lines in Figure B.1-a. The resultant image is shown in Figure B.1-f. Finally the low-pass filtered component was subtracted from the source image.

### Compact structures

The resultant unsharp masked image is shown in Figure 4.5 which was generated from a source image smoothed with a Gaussian of $\sigma = 0.75''$ from which a low-frequency component (a smoothed image with a Gaussian of $\sigma = 3.5''$) was removed. For comparison unsharp masked images with various filtering criteria are shown in Figure B.3.

As shown in the figure, the inner ling is clearly distinguished from the pulsar. The radius of the ring feature appears to be $\sim 10$ arcsec along the major axis, that corresponds to $7.8 \times 10^{17}$ cm for the distance of $d = 5.2$ kpc from the earth. The eccentricity of $\epsilon \sim 0.8$, for the minor axis radius of $\sim 6$ arcsec, implying an inclination angle of $i \sim 53^{\circ}$ which is somewhat smaller than that from the appearance of the outer torus. On the north edge of

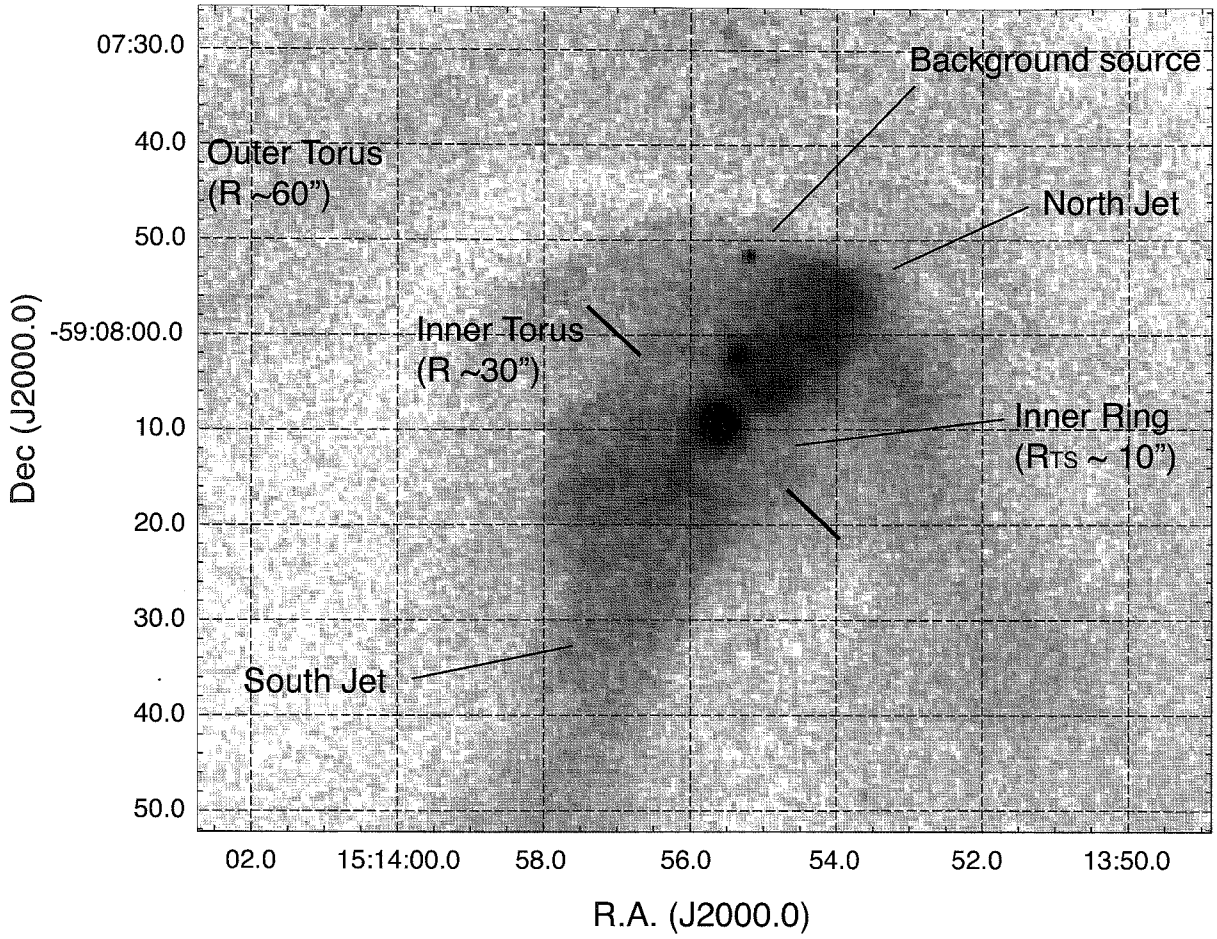


Figure 4.4: A close-up image of PSR B1509−58 over 0.4-8.0 keV energy band. A faint ring-like feature is found at a radius of 9 arcsec centered on the pulsar.

the inner ring, there are emitting blobs, which forms the north jet. These small structures are seen only in the north side of the pulsar. While the south jet appears to be diffuse. The width of the south jet across the flow line is about 20 arcsec at the origin, which just corresponds to the radius of ring feature. The temporal analysis will be shown in below.

## 4.4 Spectroscopy

In this section spatially-resolved spectroscopy are presented. First we show the spectrum of the pulsar. Then we investigate the PWN aim to (1) the azimuthal dependence, (2) the radius dependence, and (3) along the south jet.

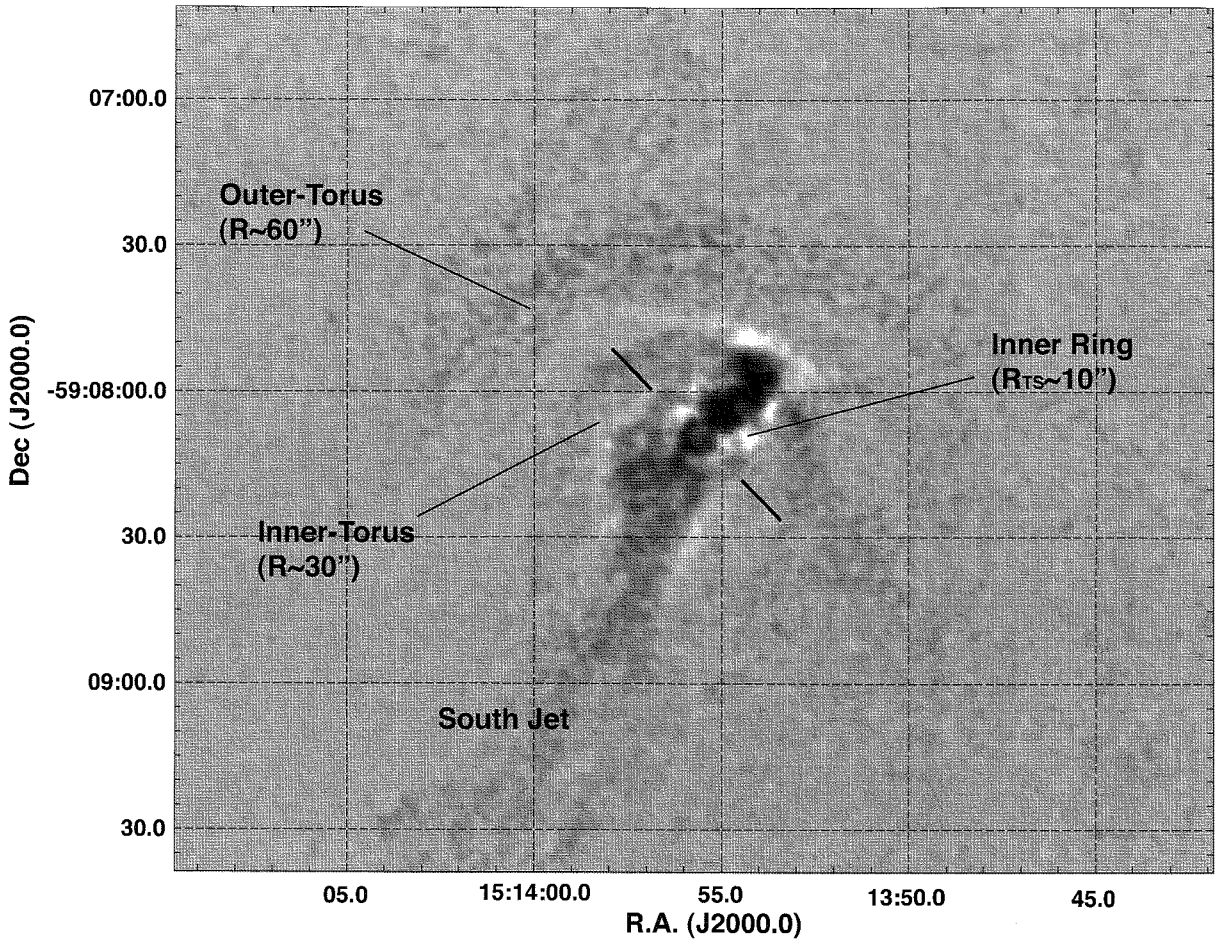


Figure 4.5: Unsharp masked image of the pulsar vicinity. This image was generated from a source image smoothed with a Gaussian of $\sigma = 0.75''$, from which a low-pass image smoothed with a Gaussian $\sigma = 3.5''$ was subtracted.

### 4.4.1 The pulsar

Since the pulsar is so bright so as to make trailing events, it is impossible to avoid the photon pile-up in full frame imaging observation with *Chandra*. Then we utilize a small window mode observation on 2000 by XMM-Newton. Figure 4.6 shows the obtained X-ray spectrum with a power-law function. The model fitting yielded a column density of $N_{\rm H} = 0.88 \pm 0.02 \times 10^{22}$ cm$^{-2}$ and a photon index of $\Gamma = 1.25 \pm 0.02$.

### 4.4.2 The PWN

Then we cut the PWN into sub-regions to investigate the spatial variation of the X-ray spectra. Figure 4.7 describes the sub-regions to be analyzed. The source photons were accumulated from the green lined sub-regions, and the background events were estimated from the box region labeled "BG" in the figure. For the regions within $R \sim 5$ arcmin

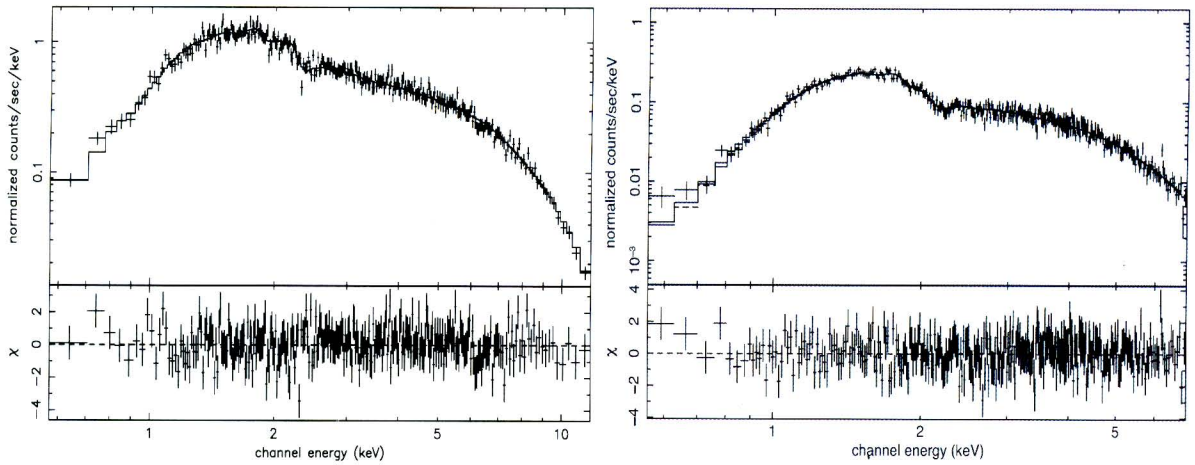


Figure 4.6: **Left**— The X-ray spectrum for the pulsar taken by EPIC-MOS (small-window mode) aboard *XMM-Newton*. Right— The X-ray spectra for the PWN observed by *Chandra*. The source events are accumulated from an annulus region from 1.0 to 1.5 arcmin centered on the pulsar.

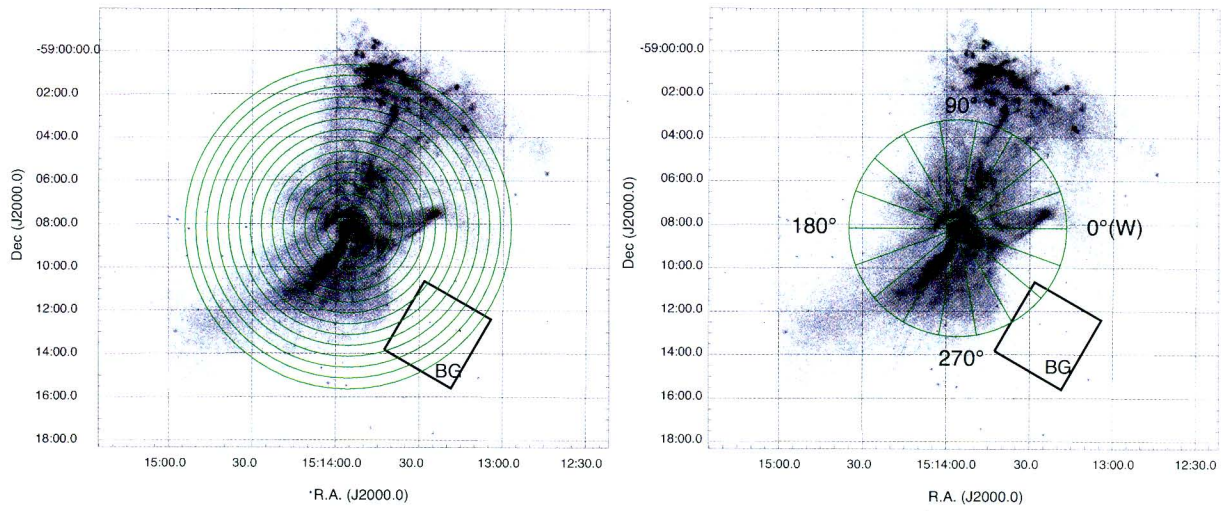


Figure 4.7: Description of the regions which were analyzed. The source regions from which X-ray events were accumulated are presented by green lines. The boxes labeled "BG" show the background regions.

the spectra of the PWN are well explained by absorbed power-low, however, that of the outer regions were contaminated by thermal components from RCW 89. Thus we must consider the complicated hybrid spectral model for this object.

### Radial dependence

In order to study the radial profile, the main nebula within a radius of 7.5 arcmin were divided into 15 annulus regions centered on the pulsar. Each of the region has a width of 0.5 arcmin, except for the innermost region in which the point source within 2.0 arcsec from the centroid was excluded.

In spectral fittings, we applied a two-component model consisting of a non-equilibrium ionization model[3] (NEI) and a power-law function for the synchrotron emission. Based on Yatsu et al. (2006), we used the fixed parameters of a temperature $kT = 0.38$ keV, an ionization parameter $n_e t = 7.1 \times 10^{10}$ s cm$^{-3}$, metal abundances of Ne = 1.00, Mg = 0.92, Si = 0.41, and Fe = 0.32, leaving the normalization variable.

The results of the model fittings are found in Figure 4.8, which describe the spatial variations of (A) hydrogen column density, (B) surface brightness of the thermal component, (C) photon index, and (D) surface brightness of the PWN. Each parameter was plotted as a function of the distance from the pulsar. As seen in the panel (A), the hydrogen column density seems to be a constant value of $\sim 1.0 \times 10^{22}$ cm$^{-2}$ over the entire nebula. The panel (B) indicates that the thermal component from the vicinity of RCW 89 is negligible within $\sim$ 5 arcmin from the pulsar. In the outer region, however, the X-ray spectra cannot be fitted with a single power-law function.

The photon index of the main nebulae increases as the radius increases. The photon index increases rapidly within 3 arcmin from the pulsar, then shows a plateau from 3 to 5 arcmin at which the photon index is $\Gamma$ is $\sim 2.1$. Outside of the radius $R = 5$ arcmin it increases again. In contrast the surface brightness decreases as a function of the radius. Around the core of the nebula within a radius of $\sim$2 arcmin, the surface brightness exhibits a plateau feature. Then it decays exponentially; this slope corresponds to the plateau of the photon index from 3 to 5 arcmin radius. Finally, the surface brightness settles down to a constant value. Because we selected the circular sub-regions, each of the spectrum should contain X-rays from various components of the nebula which may have different spectral features and different line-of-sight-velocities.

## 4.4.3 The azimuthal dependence

For the investigation of the azimuthal variation, we cut the main nebula into 18 sectors centered on the pulsar equiangularly. The outer radius of each sector is $R = 5.0$ arcmin, and the pulsar vicinity within a radius of 0.5 arcmin was excluded. Figure 4.7 (right panel) shows the outline of the azimuthal cut. In this study we defined the azimuthal

[3]"VNEI" model in XSPEC 11.3. We used NEI Version 2.0 based on the APED

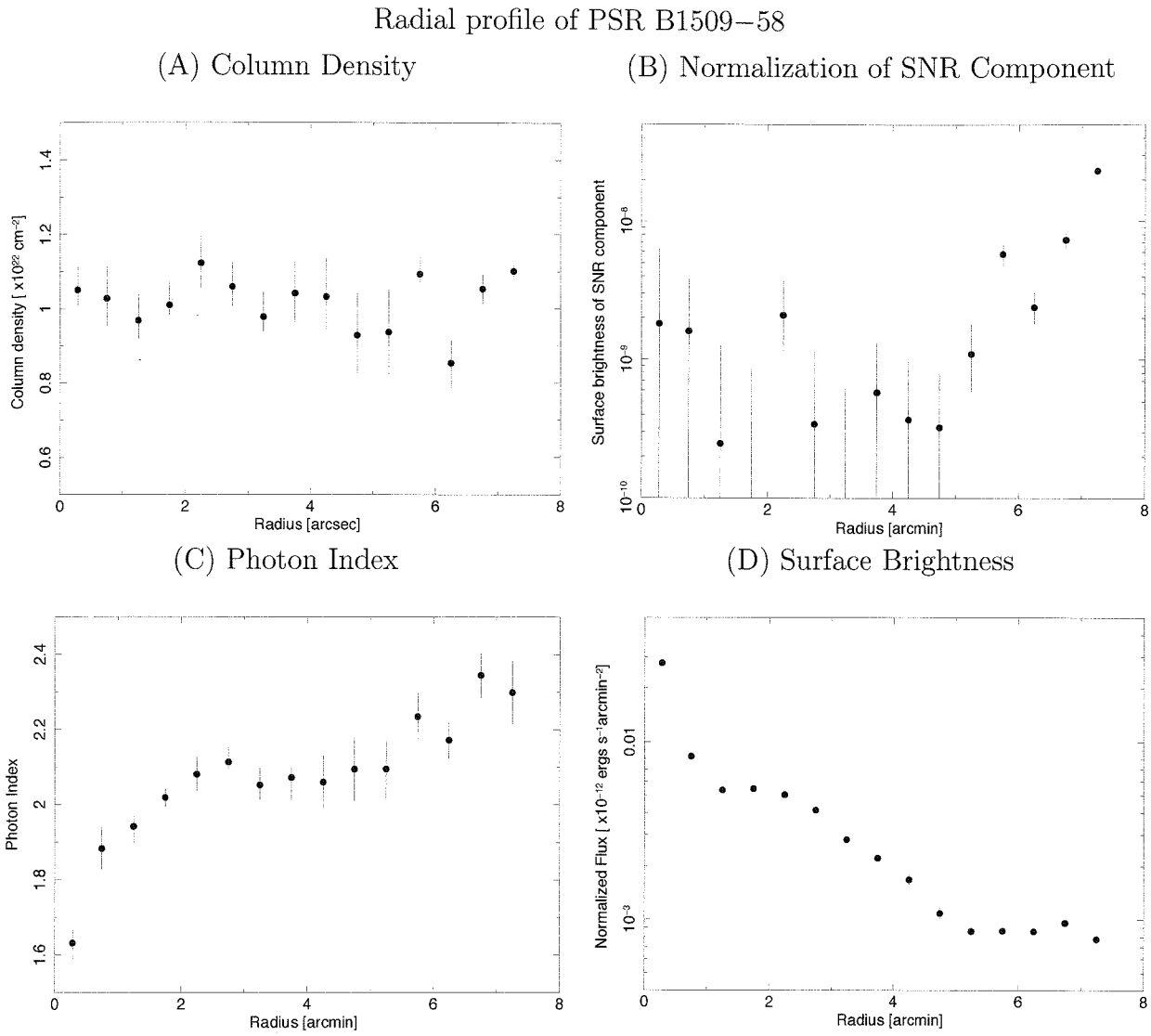


Figure 4.8: Radial profile of the X-ray spectra of PSR B1509−58. The panels describe (A) Hydrogen column density, (B) surface brightness of the thermal component, (C) photon index, and (D) surface brightness of PWN. Each parameters are shown as a function of the distance from the pulsar. The vertical scale of the panel (B) indicates the normalization per unit area, $k$ arcmin$^{-2}$, where $k$ means $k = \frac{10^{-14}}{4\pi R^2} \int n_{\rm e} n_{\rm p} dV$. While the vertical scale of the panel (D) means the energy flux per unit area over an energy band from 0.5 keV to 5.0 keV

angle as anti-clockwise direction from the west. The main purpose of this cut is to find the evidence of the northern jet.

According to the radial profile of the spectra shown above, contamination from RCW 89 is negligible. We therefore employed a single component model consisting of a power-law function for the model fittings.

The resulting spectral parameters are shown in Figure 4.8. The panel (a) $\sim$ (c) present the column density, the photon index, and the energy flux over a energy band of 0.5$\sim$5.0 keV energy range, respectively. Each parameter was plotted as a function of the azimuthal angle.

In contrast to the radial profile above, the column density varies with the azimuthal angle significantly. On $Az = 90°$ (east), the column density has a minimum value of $N_{\rm H} = (7.1 \pm 0.6) \times 10^{21}$ cm$^{-2}$. On the western side of the pulsar, the column density is apparently large. This tendency is consistent with the absorption feature found in Figure 4.1 (labeled as "D").

On a large scale, the photon index of south side of the pulsar is flatter than that of north side. The flattest photon index can be observed in the region along the south jet, $\Gamma = 1.73 \pm 0.07$. By comparing the panel (a) and (b), the column density and the photon index seem to have no correlation. Thus the variation of the column density mentioned above seems to be reliable.

The light curve as a function of the azimuthal angle shows two saw-tooth appearance prominent features because the jets are bending clockwise. One of the peaks at Az $\sim$ 210° (southwest) obviously corresponds to the bright south jet. The other peak stands at the opposite direction of the south jet, Az $\sim$ 70°, which may indicate the existence of the north jet that was ambiguous in the X-ray images shown above. At the direction of Az$\sim$ 10°, a small peak exists, which corresponds to the prominence that extends from the pulsar to northwest.

### 4.4.4 The Torus

Next we focus on the fine profile of the torus within 1 arcmin from the pulsar. We divided the main nebula into several sectors, which were aligned to be fitted with the torus and inner ring of the pulsar. According to the appearance of the nebula, we adopted an eccentricity of $\epsilon \sim 1.2$ for the ellipsoid which encircles the sectors (see §4.3).

For the model fittings, we employed a single component model consisting of an absorbed power-law function. However, it is difficult to determine the column density for each region individually, because the source regions are small. Therefore we fixed the column density at $N_{\rm H} = 1.0 \times 10^{22}$ cm$^{-2}$, in accordance with the radial profile presented

Azimuthal Profile of PSR B1509−58

(a) Column Density

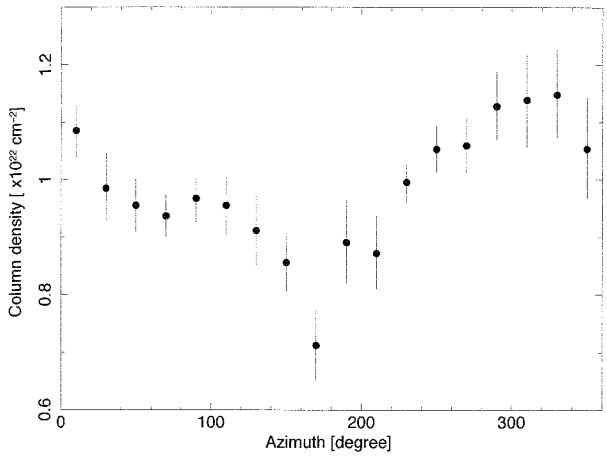


(b) Photon Index

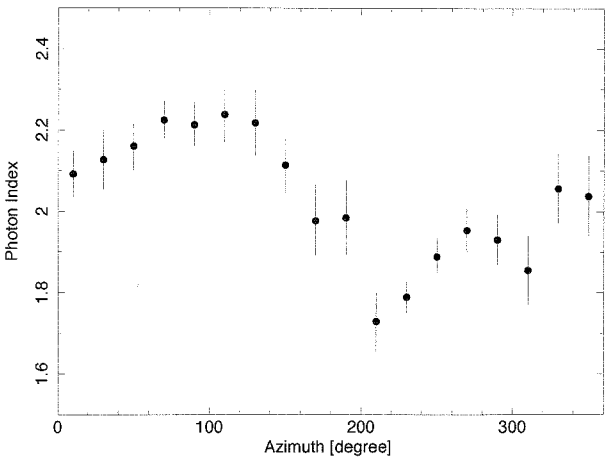


(c) Surface Brightness (Flux)

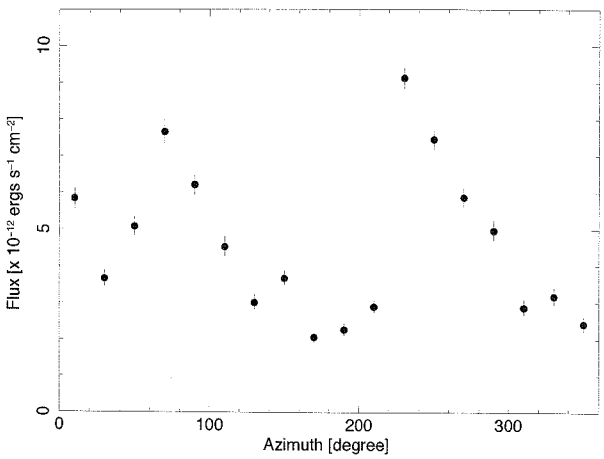


Figure 4.9: Azimuthal profile of the X-ray spectra of PSR B1509−58. Panel (a) ∼ (c) present the column density, the photon index, and the energy flux over 0.5∼5.0 keV energy range, respectively. The origin of azimuthal angle was set to the west.

above and an assumption of that a column density does not change dramatically within a scale of an arcmin. Figure 4.10 shows the regions which were analyzed here. With the above configurations, the four data sets observed in the different epochs could not be explained by the same parameter set, the energy flux varies with the time. This may be caused by the temporal changes of the PWN and from the different settings of instrumentation, such as a roll angle. Thus we allowed the normalizations of the four data sets to vary individually.

The results of model fittings are shown in Figure 4.11 and 4.12, indicating the evolution of the photon index and the surface brightness, respectively. In all panels, colors corresponds to the epochs, 2004-Dec-28 (black; 0 day), 2005-Feb-07 (red; 41 day), 2005-Apr-29 (green; 122 day), and 2005-Oct-18 (blue; 294 day). In the panel of (B: NW-jet) and (C:SE-jet), the horizontal axes are extended by a factor of $1/\cos 53^\circ$ in order to equalize the actual distance from the pulsar.

The photon indices increase along the flow line, as seen in the large scale study. Interestingly the photon indices evolve differently outside of the radius $\sim$ 30 arcsec from the pulsar. The difference between the NE torus and the SE jet is especially prominent; the photon index of NE torus increases, while that of SE jet seems uniform. In NW direction, the photon index increases outside of $R \sim 30$ arcsec. However it is not clear which of the structure, the torus or the jet, dominantly determines the spectral parameters. The outer torus should overlap the north jet in the NW sector as described in Figure 4.3. The SW sector should show the same behavior as the NE torus shows for the axial symmetry, however, the evolution of the photon index in the direction is analogous to that of the SE jet rather than the NE torus. In SW direction the the outer torus is diffusive.

In all directions the surface brightness increase at a radius of $5 \sim 10$ arcsec from the pulsar, corresponding the inner ring (Figure 4.4). In NW direction, the surface brightness suddenly decays at a radius of 30 arcsec. Inside of the radius large temporal changes were revealed which corresponds to small blobs shown in Figure 4.4. While, in contrast, the SE jet decays a exponentially and continuously. The surface brightness in the directions of NE and SW in which the torus structure is dominant evolve similarly. The evolution is characterized by a small increase at the inner ring, a rapid decay outside of the ring, and an increase corresponds to the outer torus. However, there are some differences. The peak brightness of the NE torus is larger than that of SW torus. The radii of the torus in NE and SW direction are also different. These may be caused by the different conditions of surrounding ISM which confines the pulsar wind.

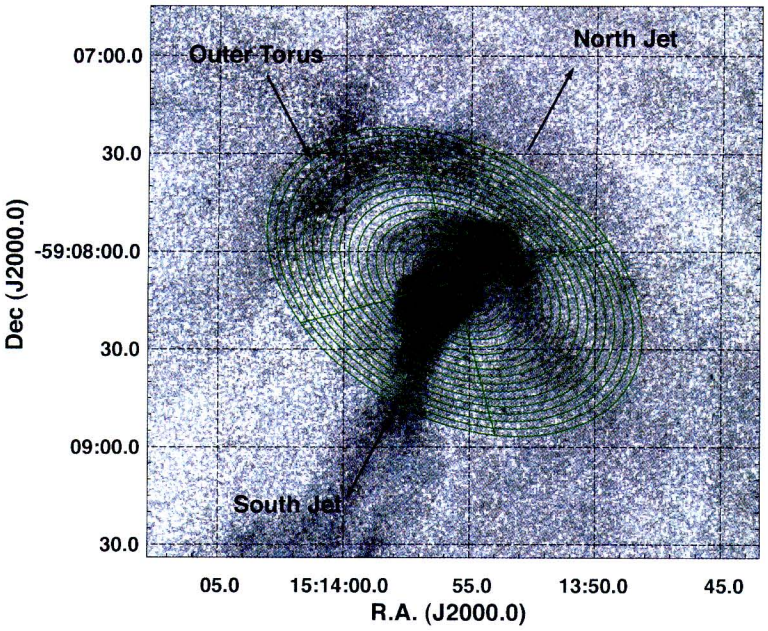


Figure 4.10: The regions to be analysed in the spectroscopy of the torus vicinity. The curvature of the sub-regions were aligned to be fitted with the torus and the inner ring.

### 4.4.5 Along the south jet

Next we aim on the south jet which extends to $\sim$ 8 arcmin from the pulsar. Here the spectral change along the stream line is presented. Figure 4.13 shows the selected regions to be analyzed. The length of the each region is 10 arcsec along the jet, except for two regions at the terminus, whose lengths are 20 arcsec and 30 arcsec, respectively. The width of the each region follows contour lines drew on Figure 4.13.

#### Vertical profile of the Jet

First we investigate the evolution of the vertical profile. Figure 4.15 shows the cross sections of the jet projected on the celestial sphere at various positions. The each panel corresponds to the regions shown in Figure 4.13, respectively.

At the root of the jet, a single peak profile was found. The cross section of the jet is narrowing along the steam. The minimum cross section was observed $\sim$ 40 arcsec apart from the pulsar. In the downstream of the narrowest point, the jet is then broadened and showing double peaked profile. Figure 4.14 shows the width (FWHM) of the jet as a function of distance from the pulsar, describing that the jet pinched at $\sim$ 40 arcsec from the pulsar.

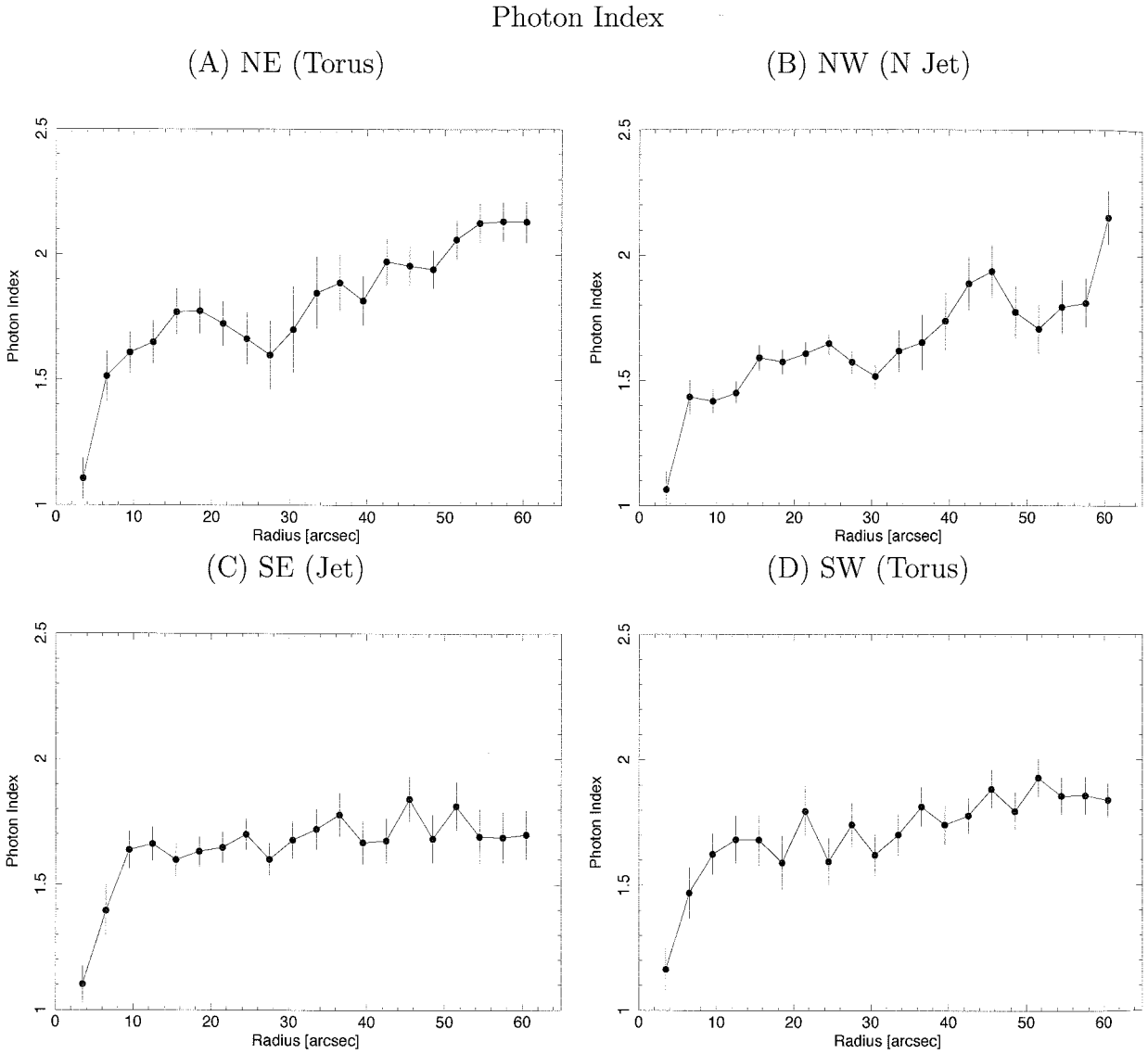


Figure 4.11: The photon index evolution around the torus. Colors corresponds to the epochs, 2004-Dec-28 (black), 2005-Feb-07 (red), 2005-Apr-29 (green), and 2005-Oct-18 (blue). The horizontal axes of panel (B) and (C) are extended by a factor of $1/\cos 53°$.

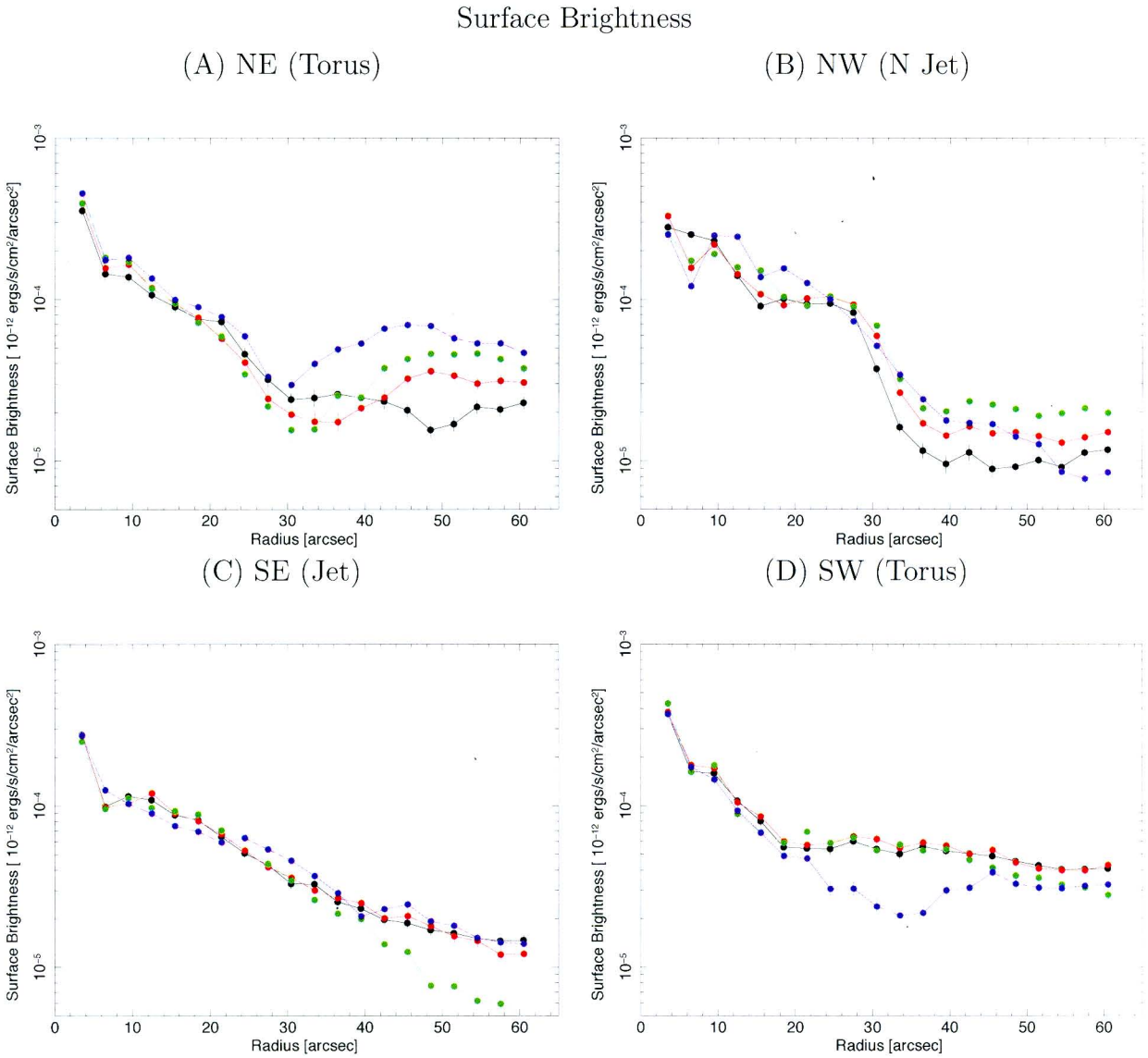


Figure 4.12: The surface brightness evolution around the torus. Colors corresponds to the epochs, 2004-Dec-28 (black), 2005-Feb-07 (red), 2005-Apr-29 (green), and 2005-Oct-18 (blue). The horizontal axes of panel (B) and (C) are extended by a factor of $1/\cos 53°$.

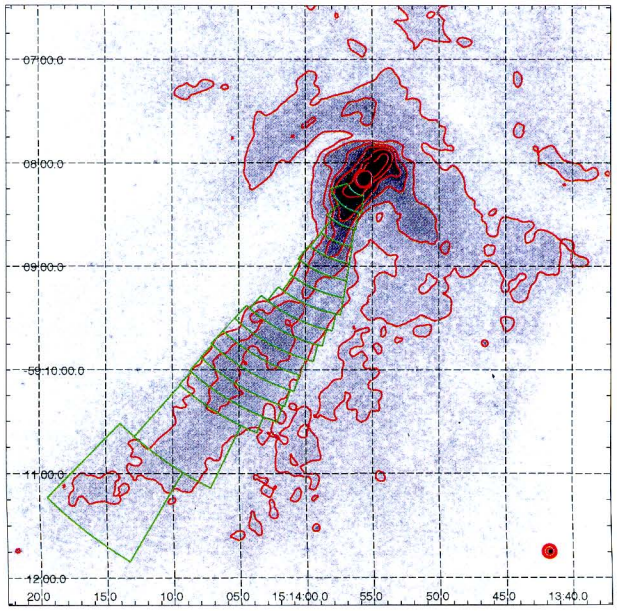


Figure 4.13: Outline drawing of the regions for the spectroscopy along the jet axis. The source events are accumulated from the green fan-shaped regions. The red contour lines indicate the surface brightness of the pulsar wind nebula over an energy band of 0.4-8.0 keV.

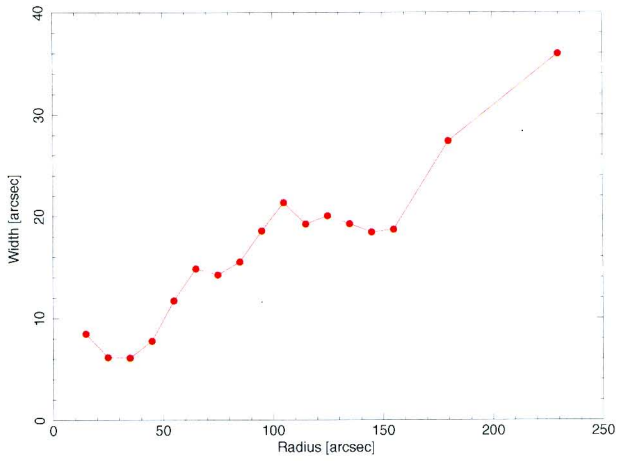


Figure 4.14: Width of the south jet as a function of the distance from the pulsar. The width was defined as the FWHM of the vertical profile of the surface brightness.

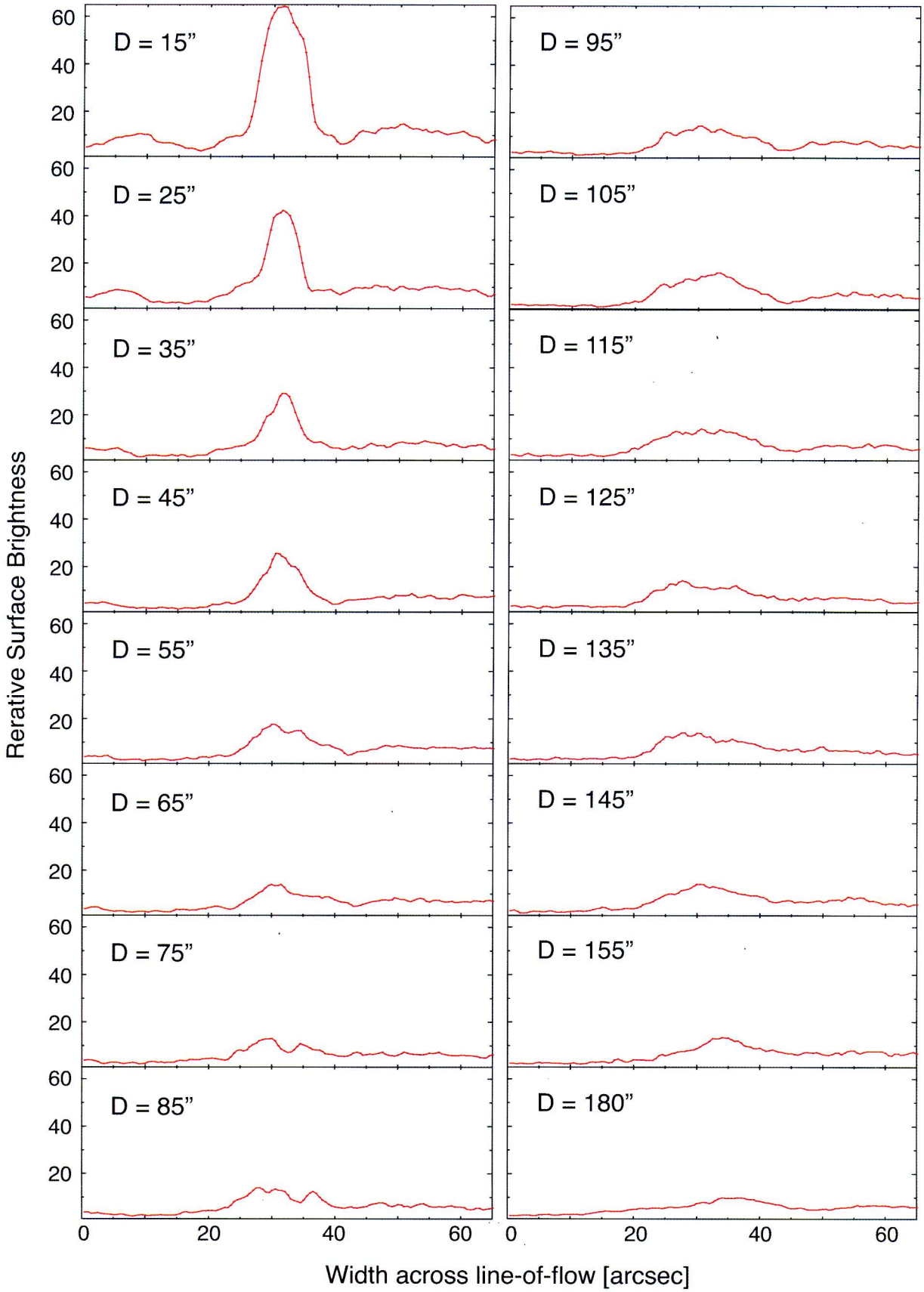


Figure 4.15: The projected vertical profile of the south jet at various positions.

### Spectral evolution along the jet flow

For the spectroscopy we adopted a single component model consisting of an absorbed power-law function. The four data sets observed in different epochs are analyzed simultaneously with a single model because of the poor photon statistics. But in order to explain the temporal changes we allowed the four data sets to have independent normalizations which can change individually.

The obtained spectral parameters were shown in Figure 4.16. Panels of (a)$\sim$ (c) describes variations of the photon index, the surface brightness, and the column density, respectively. As the column density was set to be variable, the photon index contains large uncertainties. For comparison the photon indexes from Figure 4.11 (SE jet) are superimposed (red colored data-series). Then we can see that the photon index increases linearly as a function of radius. The slope is $d\Gamma/dr \sim 1 \times 10^{-3}$ arcsec$^{-1}$. Finally the photon index reaches to $\Gamma = 2.1$ at $\sim 8$ arcmin from the pulsar (see Table 6.1). While, the surface brightness rapidly decreases first, then increases around $r = 100 \sim 150$ arcsec. Interestingly, the evolution of the surface brightness is analogous to the light curve of the NE torus in Figure 4.12, showing a rapid decay and a subsequent moderate increase.

## 4.5 Temporal changes

From the spectroscopy utilizing the data sets in different epochs, the sub-structures in the PWN seem to be temporally changing, as seen in the Crab nebula. In the following section we present temporal changes along the jet.

Figure 4.17 shows the close-up images of the nebula core observed at four epochs, 2004-December-28, 2005-February-07, 2005-April-29, and 2005-October-18. These images are unsharp masked to enhance the compact structures. On the north side of the pulsar, some clumpy structures can be seen, and are moving irregularly. While on the south side, there are only diffuse structures which are expanding outwards from the pulsar.

Figure 4.18 shows the profiles of the surface brightness of the region "S" (upper panel) and the region "N" (lower panel) marked in Figure 4.17. The four data-lines are placed with vertical displacements proportional to the time spans between the observations, from the top to the bottom of the each panel as time progresses. On the south side of the pulsar, only weak gradients were found, but they seem to be moving outward. In region N, a prominent feature exist at the point $\sim 5$ arcsec from the origin. We found that a small peak accompanied by the major peak were extending outwards.

For quantitative discussions, we should measure the velocities of the proper motions. In this study we consider four moving features denoted by dashed lines in Figure 4.18. In

(a) Photon Index

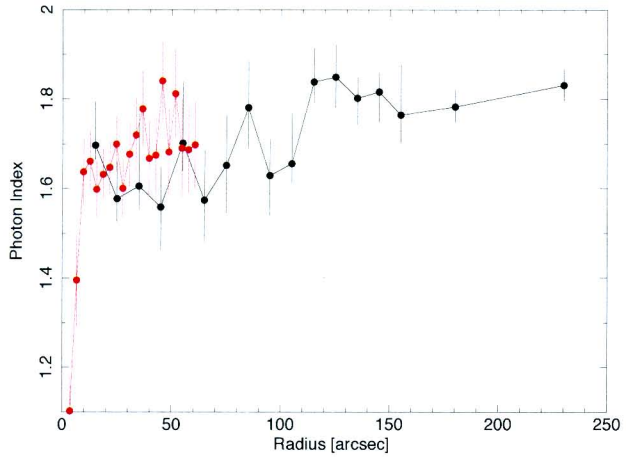


(b) Surface Brightness

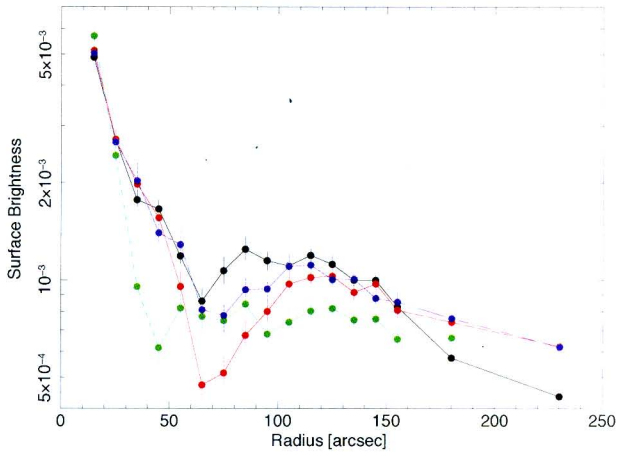


(c) Column Density

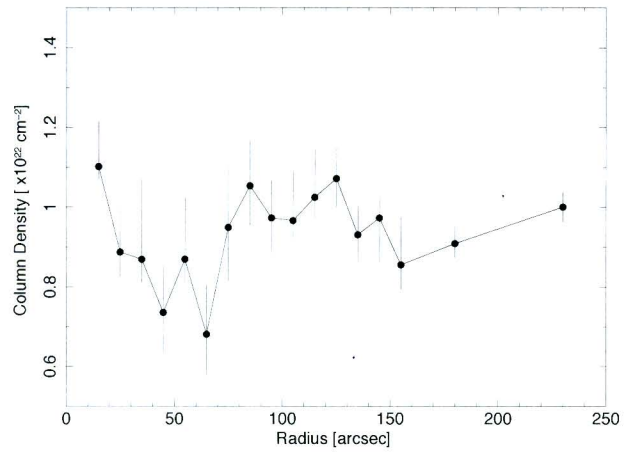


Figure 4.16: Spectral variations along the jet. The Each data points corresponds to the regions drew on Figure 4.13. Red data-series in the panel (a) is from Figure 4.11. Colors in the upper-right panel indicate the epochs of observations, 2004-Dec-28 (black), 2005-Feb-07 (red), 2005-Apr-29 (green), and 2005-Oct-18 (blue).

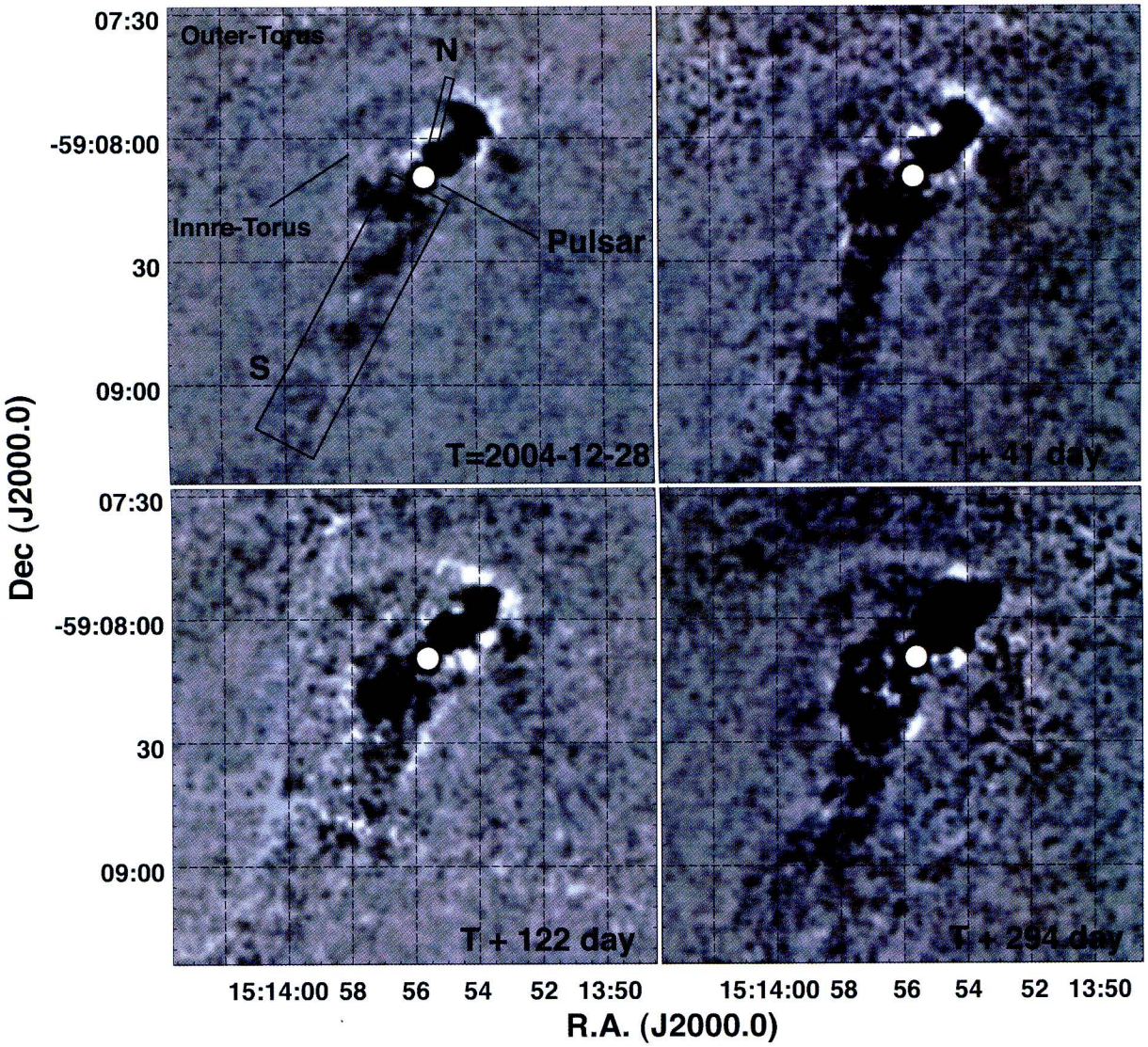


Figure 4.17: The unsharp masked images of the nebula core at four epochs (ObsID: 5534, 5535, 6116, and 6117; see Table 4.1). The rectangles labeled "S" and "N" are the regions from which the surface brightness profiles are generated as shown in Figure 4.18.

order to measure the travel distance we utilized a cross-correlation function, $R$, defined as a function of $k$,

$$R(k) = \frac{1}{\Delta}\int_{x_0-\Delta/2}^{x_0+\Delta/2} f_0(x) f_1(x-k)dx \tag{4.1}$$

$$\sim \frac{1}{\Delta}\sum_{x_0-\Delta/2}^{x_0+\Delta/2} f_{0,i} f_{1,i-k}, \tag{4.2}$$

where $x_0$ and $\Delta$ are constants defining the region to be considered. In this study, $x_0$ was set to be the position of the peak which is focused on, and $\Delta$ was set to be the FWHM of the peak structure. If the profile of surface brightness changes from $f_0$ to $f_1$ in a time

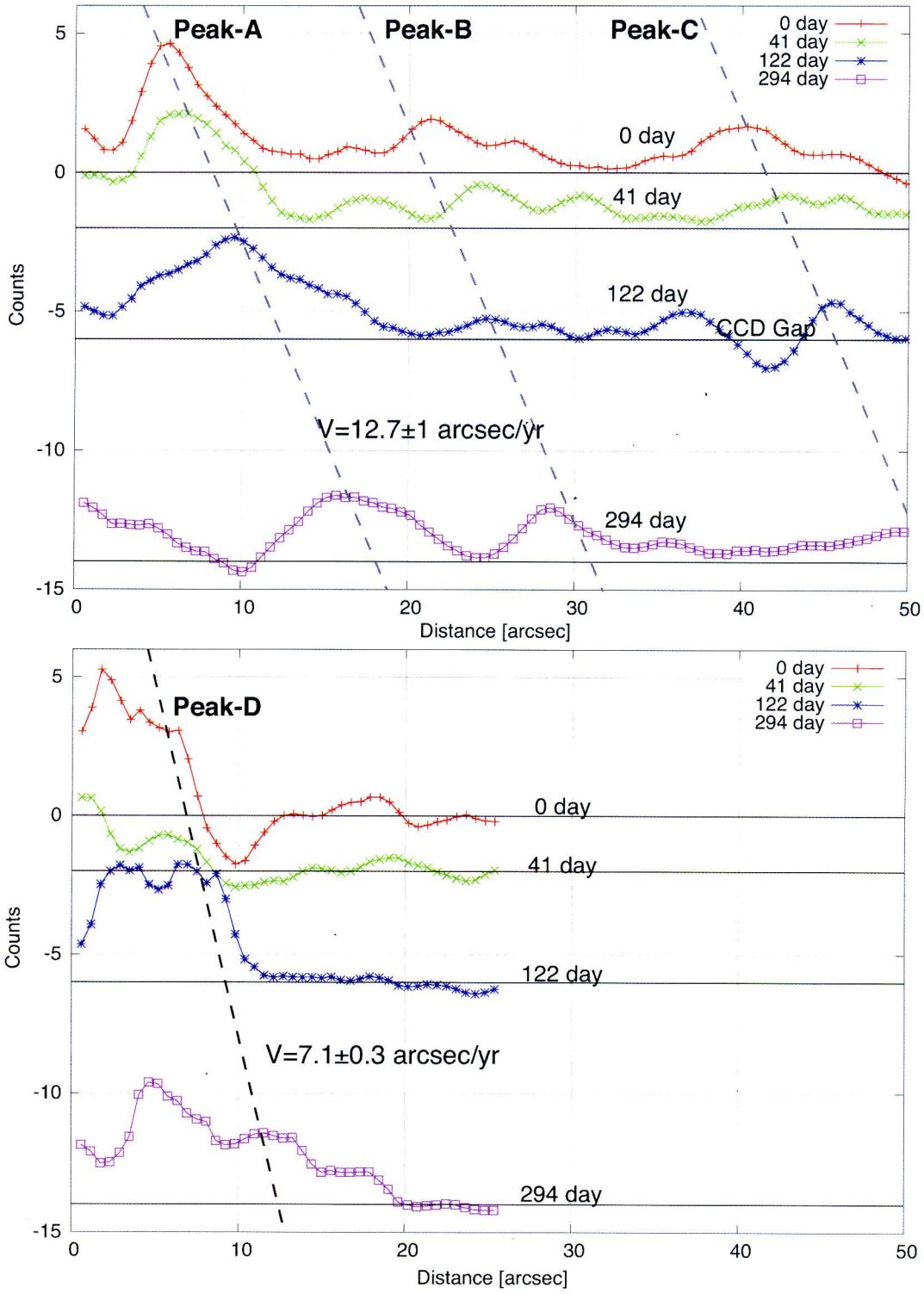


Figure 4.18: Temporal variation of surface brightness profiles along the jet. The upper and lower panels correspond to the region "S" and "N" in Figure 4.17, respectively. Extracted profiles are placed with vertical displacement proportional to the time span between the observations, with the first observation at the top and the 4th observation of the bottom. Horizontal lines indicate the reference point of the four epochs. The inclined dashed lines indicate the motions of the prominent features.

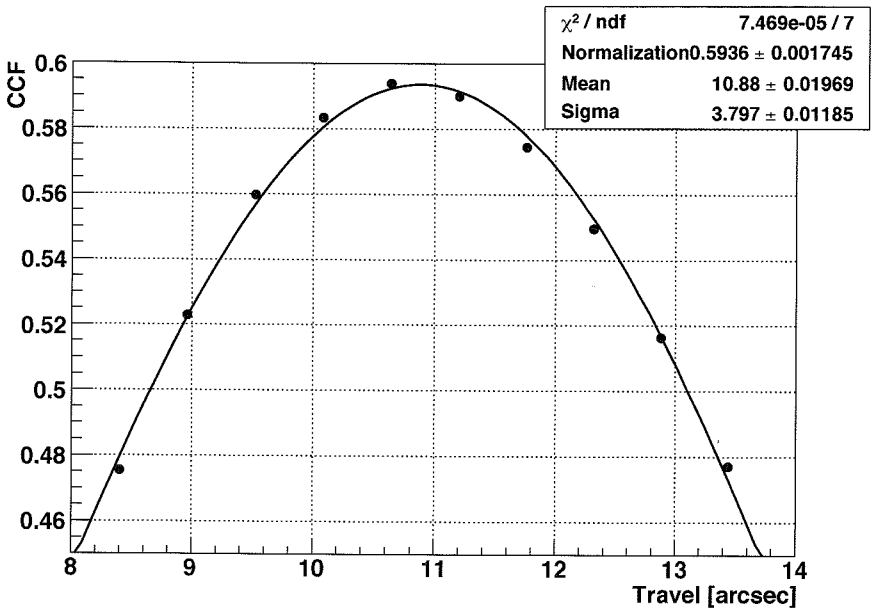


Figure 4.19: The cross correlation function with respect to peak-A (ObsID5534 vs. ObsID6117) shown as a function of travel distance $k$.

interval $t$, a value $k$ that maximizes the cross-correlation-function $R$ corresponds to the travel distance as shown in Figure 4.19.

As we utilized four observations, we can calculate CCFs for 6 different combinations of data pairs for every single peak. The resultant CCFs are shown in Figure B.4, B.5, B.6, and B.7 corresponding to peak-A, peak-B, peak-C, and peak-D in Figure 4.18, respectively.

Figure 4.20 shows the obtained travel distance as a function of time interval. In order to evaluate the velocity we fitted the data with a linear function. From the model fitting we obtained angular velocity of $v_{\rm south} = 12.7 \pm 1.1$ arcsec yr$^{-1}$ for the region-S, which corresponds to $0.74c$ for the inclination angle of $i = 30^\circ$ [4]. While a velocity of $v_{\rm north} = 7.1 \pm 0.3$ arcsec yr $^{-1}$ was obtained for region-N.

[4]Here we have considered the superluminal motion effect; $v_{\rm app} = \frac{v_{\rm real} \sin\theta}{1-\beta\cos\theta}$

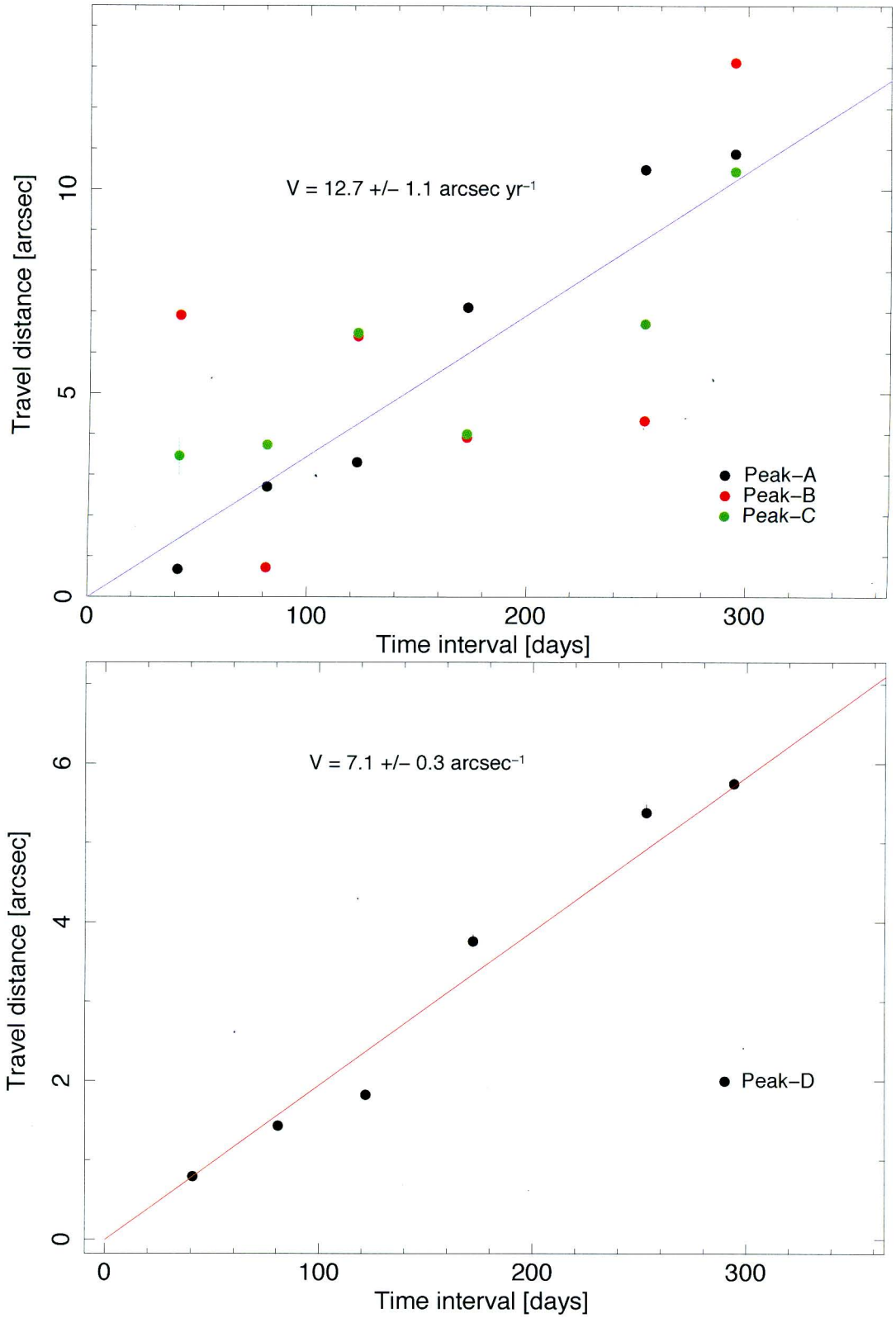


Figure 4.20: Travel distance as a function of time interval of region-S (upper panel) and region-N (lower panel).

# Chapter 5

# HII region RCW 89

In this chapter we present a study of the HII region RCW 89 which is suspected to be interacting with the pulsar jet from PSR B1509−58.

## 5.1 Review

RCW 89 is a mysterious HII region which appears to be located in a pulsar-SNR system of PSR B1509−58 and MSH 15−5*2*. The optical nebula coincides with the brightest portion of MSH 15−5*2* in radio. However the observed morphologies are obviously different in the radio and in the optical: RCW 89 exhibits filamentary structures in the optical (Seward et al., 1983), while the radio emission originates in plasma clumps distributed in a "horseshoe" shape (Gaensler et al., 1999). The non-thermal radio structures are suggesting that there are high energy electrons accelerated up to $\sim$ GeV energies in the vicinity. The X-ray morphology of RCW 89 revealed by *ROSAT* resembles the radio structure rather than that in the optical band (Trussoni et al., 1996; Brazier and Becker, 1997). On the other hand, *ASCA* revealed that thermal emission with prominent line features are dominant in the region of RCW 89 (Tamura et al., 1996). In Yatsu et al. (2005), we show with the *Chandra* data that the thermal X-rays are emitted by the plasma clumps, similar to non-thermal radio emission. The thermal emission with complicated line features are well fitted with the non-equilibrium ionization model. We also discovered the local variations of the plasma temperature $k_{\rm B}T$ and ionization parameter $n_{\rm e}t$ in the vicinity of RCW 89, indicating that the plasma had not been heated simultaneously.

There are some questions to be resolved. The first of these is whether MSH 15−5*2* (or RCW 89) and PSR B1509−58 are physically linked or not. This question arises from the discrepancy between the dynamical age of the SNR and the pulsar's characteristic age. Seward et al. (1983) proposed an interpretation in which the progenitor of PSR B1509−58

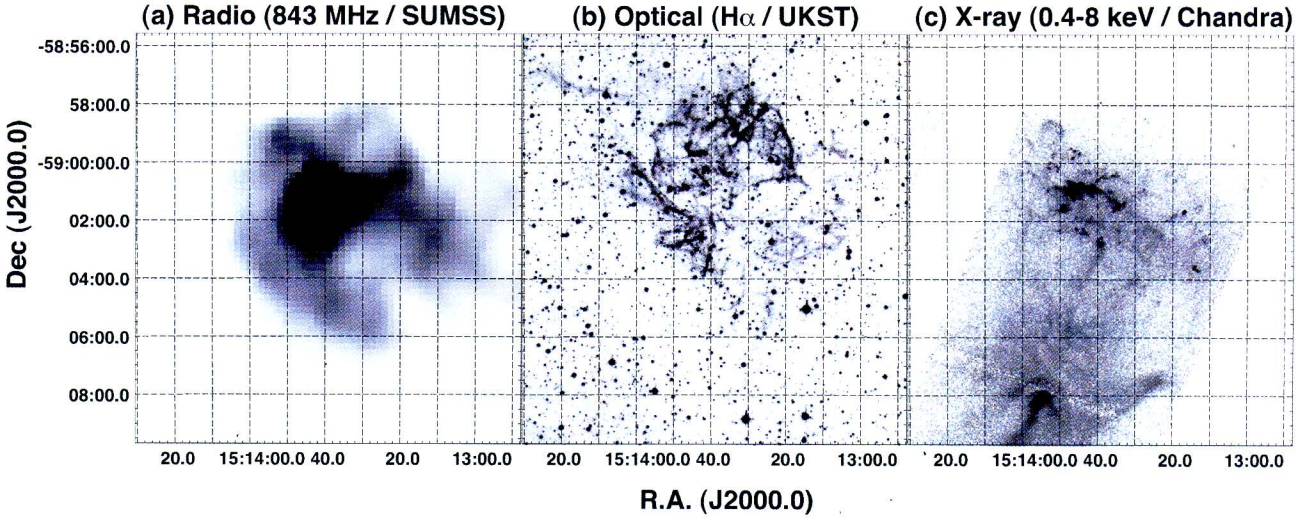


Figure 5.1: Comparison of multi-wavelength observations of RCW 89. (a) shows an 843 MHz radio image taken by *Sydney University Molonglo Sky Survey (SUMSS)*. (b) shows an $H_\alpha$ image taken by *UK Schmidt Telescope (UKST)*. (c) is an X-ray image for 0.4-8.0 keV energy band observed by *Chandra* (ObsID:5562)

exploded in a cavity of a previous supernova. It is supported by the recent HI observation which reveals a small density of ISM around PSR B1509−58 (Dubner et al., 2002). On the other hand, van den Bergh and Kamper (1984) performed optical observations with a 6 yr baseline, however, they could not detect a significant proper motions of RCW 89 which supports the relationship between the SNR and the pulsar.

The energy source of RCW 89 is also puzzling. Manchester (1987) proposed two possible candidates: the pulsar jet and the supernova blast-wave. The pulsar jet hypothesis has been supported by the recently obtained X-ray images in which the counter jet of the pulsar appears to irradiate RCW 89. The existence of the high energy particles was also confirmed by *H.E.S.S.* as mentioned. Despite these preceding studies the blast-weave hypothesis has not been excluded.

In this chapter we present spectral analysis and imaging analysis of RCW 89 utilizing *Chandra* and *XMM-Newton* to clarify the above open questions. First we investigate the condition of plasma. The temperature and emission measure of the plasma may constrain the energy content stored in RCW 89. Moreover the Doppler shifts of the line emissions constrain the radial velocities of the emitting region. Next we measure the proper motion of each knot in RCW 89 by comparing the *Chandra* observations at 2000 (ObsID 754) and 2004 (ObsID 5562).

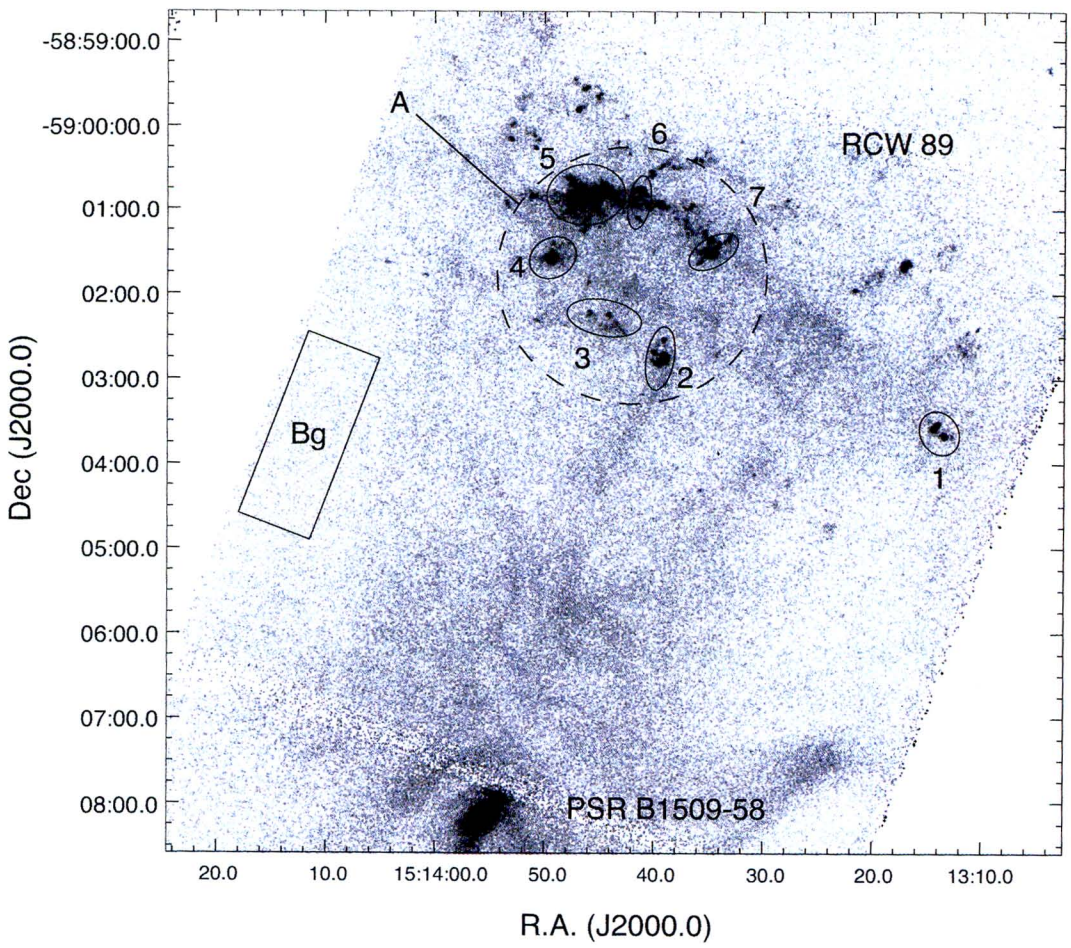


Figure 5.2: X-ray images of RCW 89 taken by *Chandra*. The image was normalized by an exposure map for 1.3 keV (Mg $K_\alpha$) at which RCW 89 exhibits the largest X-ray flux. The ellipse and box regions were selected for succeeding spectral analysis.

## 5.2 Data Analysis

### 5.2.1 *Chandra* observations

We observed RCW 89 with the ACIS-S aboard *Chandra* on 2004 December 31st for a total exposure of 30 ks. The data reduction process were performed in a manner described in §4.2. The usable exposure time was 29575 s after filtering for good time intervals. Figure 5.2 shows an exposure corrected image for 0.4-8.0 keV energy band.

#### Spectral fit to the entire region "A"

The energy spectra of RCW 89 regions are quite complex and show strong emission lines, as well as hard-energy component. We first evaluated the integrated energy spectrum

for the entire region A for the analysis of individual knots in RCW 89 in which the photon statistics was not sufficient to determine the column density $N_{\rm H}$ and the photon index $\Gamma$ for each knot independently. We applied a two-component model consisting of a non-equilibrium ionization model (VNEI version 2.0) for the thermal component and a power-law function for high energy component. In the NEI model, the abundances of Ne, Mg, Si, and Fe, which all have remarkable line emission, were set to be variable. The obtained spectrum (ObsID: 754) was shown in Figure 5.3. The best-fit parameters are shown in Table 5.1. The column density and the photon index were obtained as $N_{\rm H} = (1.18 \pm 0.01) \times 10^{22}$ cm$^{-2}$ and $\Gamma = 2.48 \pm 0.05$ with a $\chi^2_{\rm red} = 1.727$ for 227 d.o.f. The fit is rather poor, which is mainly due to large residuals in the energy range of 1.0-1.3 keV.

### Spectral fit to the individual knots

To determine the spectral parameters for each knot, we adopted results of spectral fits to region A in Figure 5.2 reported in Yatsu et al. (2005).

For the individual spectral analysis we adopted fixed values of $N_{\rm H} = 1.18 \times 10^{22}$ cm$^{-2}$, and $\Gamma = 2.48$ obtained above. As a thermal component, two different plasma models of "NEI" and "MEKAL (equilibrium ionization plasma)" were examined. The obtained best-fit parameters are summarized in Table 5.2. X-ray spectra are found in Figure B.8, B.9

The both models of NEI and MEKAL produced good fits, the resultant reduced-chi-squares, $\chi^2_{\rm red}$, for the two model fittings seems to be similar. The obtained temperatures based on NEI model show a spatial variability in the range from 0.18 to 0.63 keV, as reported by Yatsu et al. (2005). While, on the other hand, the temperatures based on MEKAL model seem to be uniform at $\sim 0.2$ keV. The differences in the temperatures are accounted for by the metal abundances and the normalizations of the continuum components. The MEKAL-fit tends to provide larger metal abundances and normalizations than those from the NEI-fit. By the way, the redshifts of individual knots which can constrain the radial velocity could not determined precisely with the both two models. This is due to the degradation of energy resolution of ACIS (Compare Figure 5.3 with Figure B.8, B.9).[1]

[1]The ACIS-I(FI-chips) in the early phase of the *Chandra* mission provided an excellent energy resolution. Recently ACIS-S3 (BI-chip) has been the best among the all CCDs aboard *Chandra* as explained in §3.3.

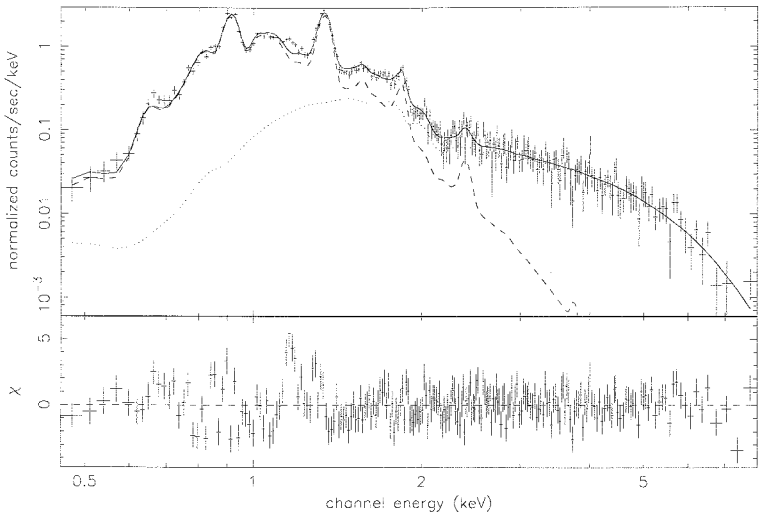


Figure 5.3: An X-ray spectrum of the brightest region in RCW 89 labeled "A" in Figure 5.2 (ObsID: 754, Date: 2000-Aug-14). We used a non-equilibrium ionization model, "VNEI" for the softer thermal component (*dashed line*) and a power-law function for the hard component (*dotted line*).

Table 5.1: Spectral fit to region "A" in Figure 5.2.

| Parameters | Best-fit value |
|---|---|
| Column density ($10^{22}$cm$^{-2}$) | $1.18 \pm 0.01$ |
| *Thermal component* | |
| Temperature (keV) | $0.38 \pm 0.01$ |
| $n_e t$[†1] ($10^{11}$ s cm$^{-3}$) | $0.71 \pm 0.05$ |
| $EM$[†2] ($10^{57}$cm$^{-3}$) | $3.42 \pm 0.03$ |
| Abundance (solar abundance) | |
| Ne | $1.00 \pm 0.03$ |
| Mg | $0.92 \pm 0.02$ |
| Si | $0.41 \pm 0.04$ |
| Fe | $0.32 \pm 0.02$ |
| *Non-thermal component* | |
| Photon index | $2.48 \pm 0.05$ |
| Flux$_{0.5-5.0\mathrm{keV}}$ ($10^{-12}$ ergs s$^{-1}$ cm$^{-2}$) | $8.67 \pm 0.05$ |
| $\chi^2_\nu$ ($\nu$) | 1.727 (227) |

Note: Errors are with 1 $\sigma$ confidence.

†1 Ionization time scale of non-equilibrium ionization plasma.

†2 Emission measure $\int n_e n_H dV \, (d_L/5.2\mathrm{kpc})^2$ ( $d_L$ is the distance to RCW89).

Table 5.2: Spectral fits to the individual knots of RCW 89 with *Chandra* data (ObsID: 5562).

| Region | $kT$ (keV) | $n_e t$ ($10^{11}$cm$^{-3}$s) | Redshift ($10^{-3}z$) | Ne | Mg | Si | Fe | Norm ($10^{-2}$ $k^{\dagger}$) | Flux$_{PL}$ ($10^{-13}$ergs s$^{-1}$cm$^{-2}$) | $\chi^2_{red}$/d.o.f |
|---|---|---|---|---|---|---|---|---|---|---|
| | | | | | (Solar abundance) | | | | | |
| | | | | *NEI + Power-law* ($N_H = 1.18 \times 10^{22}$cm$^{-2}$, $\Gamma = 2.48$) | | | | | | |
| 1..... | $0.42^{+0.20}_{-0.06}$ | $0.6^{+1.5}_{-0.3}$ | $9.0^{+6.8}_{-6.4}$ | $1.98^{+2.50}_{-0.68}$ | $1.54^{+2.10}_{-0.56}$ | $0.00^{+0.36}_{-0.00}$ | $0.55^{+1.20}_{-0.25}$ | $0.26^{+0.10}_{-0.16}$ | $2.8^{+0.6}_{-1.4}$ | 0.668/69 |
| 2..... | $0.18^{+0.07}_{-0.02}$ | $470^{+30}_{-460}$ | $6.5^{+5.2}_{-4.8}$ | $1.22^{+0.64}_{-0.14}$ | $3.14^{+0.76}_{-1.10}$ | $3.21^{+1.80}_{-1.40}$ | $0.50^{+0.36}_{-0.50}$ | $0.55^{+0.42}_{-0.29}$ | $6.9^{+1.0}_{-0.9}$ | 0.766/100 |
| 3..... | $0.39^{+0.12}_{-0.21}$ | $0.11^{+0.83}_{-0.04}$ | $2.7^{+9.1}_{-2.8}$ | $0.85^{+0.44}_{-0.15}$ | $1.47^{+1.00}_{-0.88}$ | $0.40^{+0.44}_{-0.32}$ | $1.10^{+0.90}_{-0.82}$ | $0.58^{+0.55}_{-0.33}$ | $5.1^{+1.2}_{-1.5}$ | 0.700/93 |
| 4..... | $0.37^{+0.02}_{-0.05}$ | $1.3^{+0.4}_{-0.6}$ | $3.4^{+2.4}_{-0.6}$ | $1.31^{+0.35}_{-0.26}$ | $1.24^{+0.44}_{-0.26}$ | $0.40^{+0.19}_{-0.20}$ | $0.44^{+0.20}_{-0.13}$ | $0.84^{+0.25}_{-0.08}$ | $3.0^{+1.0}_{-1.2}$ | 0.707/100 |
| 5..... | $0.38^{+0.03}_{-0.02}$ | $0.71^{+0.07}_{-0.11}$ | $2.8^{+1.6}_{-0.0}$ | $1.57^{+0.09}_{-0.08}$ | $1.07^{+0.10}_{-0.05}$ | $0.55^{+0.13}_{-0.08}$ | $0.56^{+0.05}_{-0.07}$ | $3.68^{+0.22}_{-0.42}$ | $4.9^{+1.3}_{-1.3}$ | 1.229/135 |
| 6..... | $0.49^{+0.03}_{-0.07}$ | $0.42^{+0.08}_{-0.14}$ | $8.9^{+1.2}_{-3.5}$ | $2.03^{+0.52}_{-0.26}$ | $1.39^{+0.25}_{-0.21}$ | $0.35^{+0.15}_{-0.14}$ | $0.34^{+0.25}_{-0.11}$ | $0.59^{+0.17}_{-0.21}$ | $2.1^{+0.9}_{-0.9}$ | 0.978/96 |
| 7..... | $0.63^{+0.09}_{-0.17}$ | $0.24^{+0.18}_{-0.07}$ | $2.8^{+2.7}_{-1.0}$ | $2.83^{+1.30}_{-0.75}$ | $2.03^{+0.61}_{-0.58}$ | $0.76^{+0.26}_{-0.33}$ | $0.57^{+0.14}_{-0.12}$ | $0.21^{+0.14}_{-0.06}$ | $3.6^{+1.5}_{-1.7}$ | 0.724/95 |
| | | | | *MEKAL + Power-law* | | | | | | |
| 1..... | $0.21^{+0.03}_{-0.03}$ | — | $9.5^{+7.1}_{-7.2}$ | $2.43^{+2.10}_{-0.83}$ | $3.50^{+2.80}_{-1.30}$ | $0.29^{+1.50}_{-0.30}$ | $0.64^{+0.74}_{-0.38}$ | $1.08^{+1.20}_{-0.58}$ | $3.4^{+1.0}_{-1.0}$ | 0.698/70 |
| 2..... | $0.21^{+0.02}_{-0.02}$ | — | $2.6^{+4.2}_{-0.8}$ | $1.57^{+0.49}_{-0.38}$ | $2.36^{+0.86}_{-0.67}$ | $1.15^{+1.20}_{-1.00}$ | $0.44^{+0.29}_{-0.20}$ | $2.15^{+1.10}_{-0.57}$ | $6.5^{+1.0}_{-1.1}$ | 0.665/101 |
| 3..... | $0.15^{+0.02}_{-0.03}$ | — | $3.5^{+11.0}_{-3.2}$ | $1.19^{+0.27}_{-0.52}$ | $3.25^{+1.50}_{-1.10}$ | $9.50^{+38.0}_{-6.20}$ | $3.33^{+20.8}_{-3.30}$ | $6.5^{+15.0}_{-3.8}$ | $6.7^{+0.9}_{-0.9}$ | 0.704/94 |
| 4..... | $0.22^{+0.01}_{-0.01}$ | — | $4.8^{+1.6}_{-2.3}$ | $1.60^{+0.26}_{-0.26}$ | $2.93^{+0.44}_{-0.37}$ | $2.07^{+0.84}_{-0.85}$ | $0.68^{+0.14}_{-0.15}$ | $2.10^{+0.29}_{-0.12}$ | $4.7^{+0.8}_{-1.0}$ | 0.766/101 |
| 5..... | $0.21^{+0.01}_{-0.01}$ | — | $2.4^{+0.5}_{-0.1}$ | $2.21^{+0.13}_{-0.16}$ | $2.85^{+0.32}_{-0.17}$ | $3.23^{+0.47}_{-0.36}$ | $0.97^{+0.08}_{-0.09}$ | $11.83^{+0.20}_{-0.18}$ | $10.4^{+1.2}_{-1.2}$ | 1.367/136 |
| 6..... | $0.23^{+0.01}_{-0.01}$ | — | $10.8^{+1.7}_{-5.2}$ | $2.73^{+0.67}_{-0.55}$ | $3.33^{+0.86}_{-0.51}$ | $1.54^{+0.75}_{-0.40}$ | $0.41^{+0.17}_{-0.12}$ | $2.26^{+0.31}_{-0.67}$ | $4.2^{+1.0}_{-0.5}$ | 0.941/98 |
| 7..... | $0.23^{+0.01}_{-0.01}$ | — | $2.5^{+3.2}_{-0.8}$ | $3.14^{+1.67}_{-0.77}$ | $4.54^{+2.80}_{-1.20}$ | $2.91^{+1.10}_{-1.30}$ | $0.53^{+0.47}_{-0.24}$ | $1.29^{+0.54}_{-0.51}$ | $5.1^{+1.2}_{-0.9}$ | 0.834/96 |

Note — Errors are with 90% confidence level.

$^{\dagger}$ $k$ is defined as $(10^{-14}/4\pi d^2) \int n_e n_p dV$

### 5.2.2 *XMM-Newton* observation

As the *Chandra* data shown above had only a limited photon statistics, then we tried to improve the quality of our spectral determinations by the *XMM-Newton* data. MSH 15−5*2* has been observed by *XMM-Newton* repeatedly. We used 25 ks long data-set of an observation from 2004 Sep. 14 (ObsID:027050201). The background activity during that observation was considerably lower and we obtained $\sim$ 22.8 ks useful data after a GTI selection. In the observations of MOS cameras were operated in Full Window mode with medium thick filters. The EPIC data were reprocessed with the *XMMSAS* version 7.0. In the spectral analysis described below, we used the MOS1 and MOS2 data which have better energy resolution. For spectroscopy source events were accumulated from circular regions of 600 pixels radius, centered on the five different emission blobs, marked "1", "2", "4", and "7" on Figure 5.4. We fitted these data with two component model of "thermal (VNEI or VMEKAL) + Power-Law").

In order to obtain stable results we fixed the column density $N_{\rm H}1.18 \times 10^{22}$ cm$^{-2}$ and the photon index $\Gamma = 2.48$, those were from *Chandra* observation. The configurations of the plasma model were the same as those for the *Chandra* data. For comparison we also examined MEKAL model with variable $N_{\rm H}$ and $\Gamma$[2]. The results of model fittings are summarized in Table 5.3. The temperatures of individual knots based on NEI model are different from each other, while the temperature based on MEKAL model appears to be uniform ($kT$ $\sim$0.2 keV), as seen in *Chandra* data. The obtained normalizations for continuum components are one order magnitude larger than those from *Chandra* data, caused by the different region selection.

Thanks to the good energy resolution[3] of *EPIC-MOS1/2* redshift of the each knots are determined precisely. The obtained redshift from three models show the same tendency:

- knot-1$\sim$ 2: Large redshift (the knots are running away from the Earth.)
- knot-3$\sim$ 7: Small redshift (the knots should have small radial velocities.)

Note that the obtained redshift distribution is similar to that from the past *Chandra* observation (Yatsu et al., 2005).

[2]We could not obtained stable results with NEI model with variable $N_{\rm H}$ and $\Gamma$.

[3]Compare the *Chandra* data (Figure B.8, B.9) with the *XMM* data (Figure B.11, B.12)

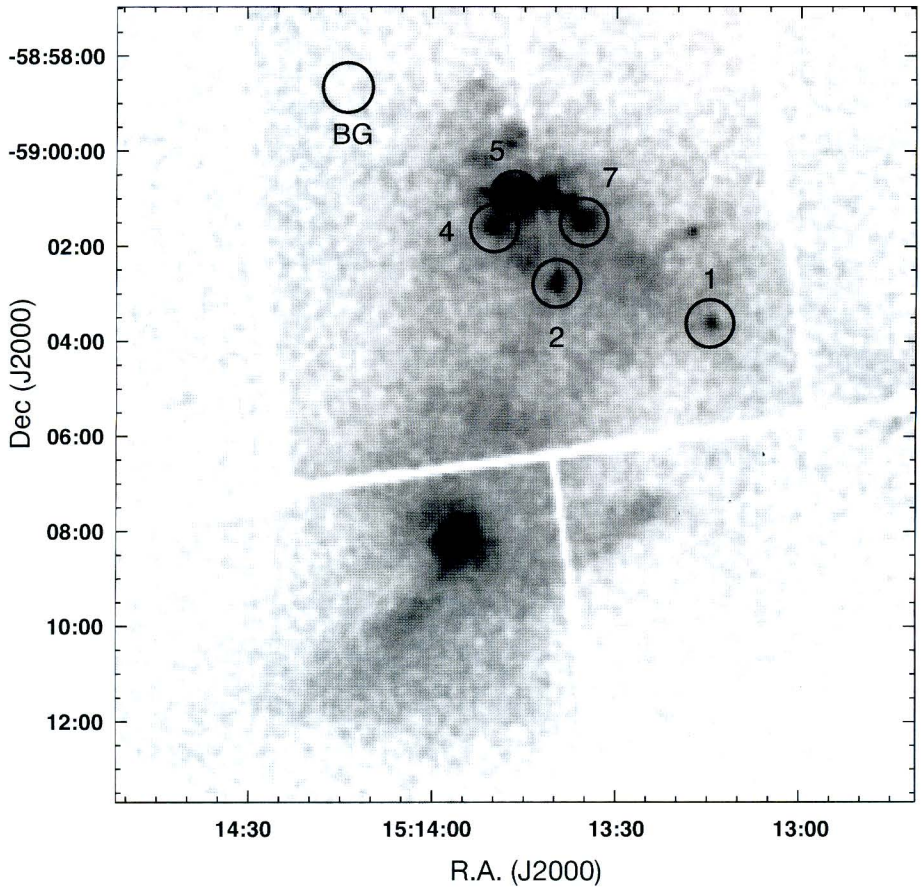


Figure 5.4: X-ray image taken by *XMM-Newton*. From the circular regions labeled 1∼7, source events were accumulated. Background events were evaluated from the region labeled "BG".

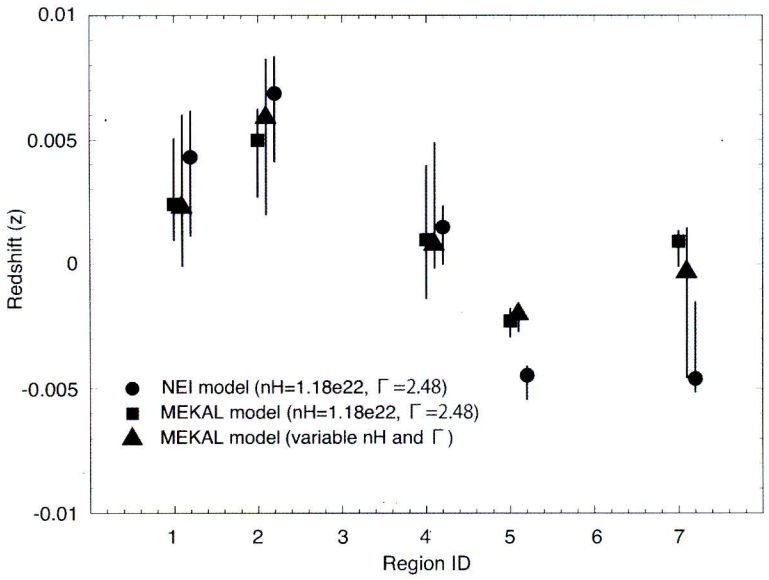


Figure 5.5: Variation of redshift in RCW 89.

Table 5.3: Spectral fit to RCW 89 with *XMM*-Data

| Region | $N_{\rm H}$ ($10^{22}{\rm cm}^{-2}$) | $kT$ (keV) | $n_{\rm e}t$ ($10^{11}{\rm cm}^{-3}{\rm s}$) | Redshift ($\times10^{-3}$) | Ne | Mg | Si | Fe | Norm ($10^{-2}k^{\dagger}$) | PhotIndx | Flux$_{\rm PL}$ ($10^{-12}$ergs s$^{-1}$ cm$^{-2}$) | $\chi^2_{\rm red}$/d.o.f. |
|---|---|---|---|---|---|---|---|---|---|---|---|---|
| | | | | | | (solar abundance) | | | | | | |
| *NEI + Power-law* ($N_{\rm H} = 1.18 \times 10^{22}{\rm cm}^{-2}$, $\Gamma = 2.48$) | | | | | | | | | | | | |
| 1..... | — | $0.37^{+0.07}_{-0.08}$ | $0.76^{+1.4}_{-0.38}$ | $4.3^{+1.9}_{-3.2}$ | $1.38^{+0.62}_{-0.36}$ | $1.08^{+0.68}_{-0.33}$ | $0.21^{+0.45}_{-0.21}$ | $0.10^{+0.16}_{-0.10}$ | $0.67^{+0.55}_{-0.22}$ | — | $1.26^{+0.11}_{-0.11}$ | 1.154/141 |
| 2..... | — | $0.22^{+0.03}_{-0.01}$ | $7.1^{+2.5}_{-1.5}$ | $6.87^{+1.5}_{-2.7}$ | $1.26^{+0.15}_{-0.12}$ | $2.28^{+0.54}_{-0.28}$ | $0.62^{+0.83}_{-0.62}$ | $0.52^{+0.12}_{-0.12}$ | $4.5^{+0.9}_{-1.0}$ | — | $1.94^{+0.09}_{-0.09}$ | 1.115/208 |
| 4..... | — | $0.31^{+0.05}_{-0.04}$ | $1.12^{+0.96}_{-0.24}$ | $1.5^{+8.4}_{-1.5}$ | $0.90^{+0.21}_{-0.21}$ | $0.96^{+0.29}_{-0.24}$ | $0.36^{+0.18}_{-0.18}$ | $0.26^{+0.05}_{-0.07}$ | $2.59^{+0.97}_{-0.67}$ | — | $1.47^{+0.08}_{-0.09}$ | 1.238/208 |
| 5..... | — | $0.35^{+0.01}_{-0.01}$ | $0.88^{+0.09}_{-0.08}$ | $-4.47^{+0.36}_{-0.96}$ | $1.21^{+0.06}_{-0.05}$ | $1.04^{+0.05}_{-0.05}$ | $0.67^{+0.09}_{-0.09}$ | $0.50^{+0.03}_{-0.03}$ | $5.18^{+0.09}_{-0.11}$ | — | $1.07^{+0.09}_{-0.09}$ | 1.615/246 |
| 7..... | — | $0.50^{+0.05}_{-0.04}$ | $0.48^{+0.12}_{-0.07}$ | $-4.61^{+3.1}_{-0.54}$ | $2.16^{+0.33}_{-0.13}$ | $1.61^{+0.39}_{-0.27}$ | $0.52^{+0.20}_{-0.19}$ | $0.61^{+0.12}_{-0.15}$ | $0.46^{+0.06}_{-0.06}$ | — | $1.46^{+0.09}_{-0.10}$ | 1.337/204 |
| *MEKAL + Power-law* ($N_{\rm H} = 1.18 \times 10^{22}{\rm cm}^{-2}$, $\Gamma = 2.48$) | | | | | | | | | | | | |
| 1..... | — | $0.18^{+0.03}_{-0.03}$ | — | $2.4^{+2.6}_{-1.4}$ | $1.69^{+0.96}_{-0.45}$ | $3.4^{+1.5}_{-0.9}$ | $2.4^{+3.1}_{-1.8}$ | $0.30^{+0.54}_{-0.30}$ | $3.6^{+5.6}_{-1.9}$ | — | $1.39^{+0.09}_{-0.08}$ | 1.191/142 |
| 2..... | — | $0.19^{+0.01}_{-0.01}$ | — | $5.0^{+1.3}_{-2.3}$ | $1.30^{+0.31}_{-0.23}$ | $2.68^{+0.28}_{-0.53}$ | $0.71^{+1.2}_{-0.69}$ | $0.51^{+0.13}_{-0.19}$ | $5.4^{+1.8}_{-1.4}$ | — | $1.99^{+0.09}_{-0.11}$ | 1.157/209 |
| 4..... | — | $0.18^{+0.01}_{-0.01}$ | — | $1.0^{+3.0}_{-2.3}$ | $1.20^{+0.22}_{-0.08}$ | $2.72^{+0.69}_{-0.27}$ | $3.00^{+1.3}_{-0.95}$ | $0.61^{+0.35}_{-0.12}$ | $8.6^{+2.8}_{-0.3}$ | — | $1.67^{+0.08}_{-0.08}$ | 1.372/209 |
| 5..... | — | $0.19^{+0.00}_{-0.00}$ | — | $-2.29^{+0.50}_{-0.63}$ | $1.39^{+0.09}_{-0.05}$ | $2.41^{+0.10}_{-0.14}$ | $3.11^{+0.27}_{-0.38}$ | $0.72^{+0.07}_{-0.04}$ | $21.0^{+0.3}_{-3.4}$ | — | $1.57^{+0.07}_{-0.11}$ | 1.868/247 |
| 7..... | — | $0.24^{+0.01}_{-0.01}$ | — | $0.91^{+0.42}_{-0.99}$ | $1.86^{+0.20}_{-0.17}$ | $3.06^{+0.33}_{-0.31}$ | $2.02^{+0.69}_{-0.68}$ | $0.28^{+0.07}_{-0.06}$ | $1.9^{+0.1}_{-0.1}$ | — | $1.56^{+0.08}_{-0.09}$ | 1.278/205 |
| *MEKAL + Power-law* ($N_{\rm H}$ & $\Gamma$ variable ) | | | | | | | | | | | | |
| 1..... | $0.66^{+0.13}_{-0.22}$ | $0.27^{+0.02}_{-0.02}$ | — | $2.3^{+3.7}_{-2.4}$ | $3.0^{+2.5}_{-1.2}$ | $8.5^{+14}_{-4.6}$ | $3.0^{+3.5}_{-3.0}$ | $0.07^{+0.20}_{-0.07}$ | $0.12^{+0.52}_{-0.10}$ | $2.38^{+0.15}_{-0.16}$ | $1.14^{+0.12}_{-0.13}$ | 1.080/140 |
| 2..... | $1.09^{+0.04}_{-0.08}$ | $0.20^{+0.02}_{-0.02}$ | — | $5.9^{+2.3}_{-3.9}$ | $1.39^{+0.35}_{-0.26}$ | $2.95^{+0.81}_{-0.65}$ | $0.77^{+0.88}_{-0.77}$ | $0.40^{+0.11}_{-0.19}$ | $3.0^{+1.8}_{-1.1}$ | $2.47^{+0.15}_{-0.15}$ | $1.93^{+0.31}_{-0.23}$ | 1.152/207 |
| 4..... | $0.91^{+0.08}_{-0.11}$ | $0.23^{+0.02}_{-0.02}$ | — | $0.80^{+4.1}_{-0.95}$ | $1.57^{+0.48}_{-0.34}$ | $3.79^{+1.4}_{-0.91}$ | $2.3^{+1.4}_{-1.0}$ | $0.37^{+0.13}_{-0.09}$ | $1.26^{+0.66}_{-0.52}$ | $2.67^{+0.17}_{-0.17}$ | $1.82^{+0.25}_{-0.18}$ | 1.221/207 |
| 5..... | $1.07^{+0.01}_{-0.02}$ | $0.21^{+0.01}_{-0.01}$ | — | $-2.00^{+0.44}_{-0.70}$ | $1.74^{+0.09}_{-0.09}$ | $3.24^{+0.14}_{-0.21}$ | $3.32^{+0.37}_{-0.45}$ | $0.76^{+0.06}_{-0.04}$ | $0.10^{+0.01}_{-0.01}$ | $3.40^{+0.06}_{-0.28}$ | $3.89^{+0.38}_{-0.80}$ | 1.562/245 |
| 7..... | $1.17^{+0.06}_{-0.07}$ | $0.22^{+0.02}_{-0.01}$ | — | $-0.31^{+1.7}_{-4.2}$ | $1.71^{+0.22}_{-0.22}$ | $2.73^{+0.27}_{-0.32}$ | $2.12^{+0.81}_{-0.53}$ | $0.33^{+0.13}_{-0.08}$ | $3.4^{+1.9}_{-1.1}$ | $2.33^{+0.17}_{-0.12}$ | $1.43^{+0.19}_{-0.17}$ | 1.281/203 |

Note — Errors are with 90% confidence level.

$^{\dagger}$ $k$ is defined as $\left(10^{-14}/4\pi d^2\right) \int n_{\rm e} n_{\rm p} dV$.

## 5.3 Imaging Analysis

In order to investigate the proper motion of each plasma clump in RCW 89, we compare the data taken on 2004 December (ObsID 5562) to archival *Chandra* data taken on 2000 August 14 (ObsID: 754). For the sub-arc-seconds scale astrometry, these observational data sets were re-calibrated using *CIAO* version 3.2.2 and *CALDB* version 3.1.0 to use of the latest gain maps and to correct geometry of the data set. In the process of acis_event_process, the Pixel Randomization [4] was removed to improve the spatial resolution of on-axis source.

Next we corrected the aspect offset to improve absolute astrometry. We modified the coordinate information in the data-set of former observation (ObsID: 754) based on the aspect offset which has been reported by the *Chandra aspect team* [5]. While the aspect offset for the data of latter observation (ObsID: 5562) has not been available. Thus the proper motion measurement comparing two 2-D images requires two original anchor points in the FoV. Unfortunately, there are no appropriate point sources such as background AGN, therefore we adopted the pulsar PSR B1509−58 as one of the anchor points. Note that the pulsar apparently had not moved in the last decade (Kaspi et al., 1994; Gaensler et al., 2002). To determine the differential of the roll angle between the two images, we used three point sources on the ACIS-S2 chip, corresponding to stars in the USNO catalog: U0300_2316145 (15:13:30.321, -58:55:07.54), U0300_23165096 (15:13:36.686, -58:56:12.26), and U0300_23166719 (15:13:39.403, -58:57:00.22). The *Digital Sky Survey (DSS)* observations show that these objects had not moved from 1980 to 1997.

As shown in Figure 5.6, these two data-sets were observed with the different aimpoint configurations, therefore we could not compare directly these two images due to the optical distortion. In order to exclude the distortion in the off-axis field, the positions of the source objects were calculated by *Sherpa* (Freeman et al., 2001), which provides a sub-arcsec accuracy astrometry based on the 2-D imaging analysis utilizing a point-spread-function as the convolution kernel. The kernel PSFs were made from the PSF libraries in *CALDB* version 3.1.0. As a model function for 2-D fitting we used a 2-D Gaussian function "gauss2d". In this analysis we used images with 1×1 pixel resolution (1 pixel = 0.492").

Figure 5.7 shows the *Chandra* images of PSR B1509−58 at different off-axis angles (panel 1-a and 2-a). While the center panels (1-b and 2-b) are the simulated images by *Sherpa* based on the PSF of the *HRMA*. For comparison panel 1-c shows the result of

[4] In default configuration the *CXC* standard data processing randomizes the positions of events to avoid any possible aliasing affects associated with the instrumental grid structures.

[5] For information on the aspect correction, see http://cxc.harvard.edu/ciao/threads/arcsec_correction/

model fitting (residual plot). The two images, ID754 and ID5562, provided position errors of the pulsar $(\sigma_\alpha, \sigma_\delta)_{754} = (0''.048, 0''.048)$ and $(\sigma_\alpha, \sigma_\delta)_{5562} = (0''.14, 0.''059)$, respectively. With reference to the pulsar position, we can compare the two images with an aspect uncertainty of $\sigma_\alpha = 0''.15, \sigma_\delta = 0''.074$ [6]. On the other hand we also obtained a twist angle between the two images with respect to the pulsar $\Delta\theta_{\rm roll} = 0°.14 \pm 0°.07$ based on the positions of three reference stars. In the position measurements of the individual knots, we could not determine the parameters, position, PSF-FWHM, ellipticity and elongation direction at the same time for the data-set of ID754 (off-axis, 15 ks) caused by its low photon statistics and a large distortion of the PSF. Therefore we first analyzed the data-set of ID5562 (on-axis, 30 ks) and determined the geometries of the individual knots. Next we analyzed the data of ID754 with these obtained geometrical parameters to be fixed.

We measured proper motions of 10 Major plasma clumps in RCW 89 with 4.3 yr baseline. In Figure 5.8, the proper motions are represented as vectors. The length of a vector represents 50 times the traveled angular distance on the sky plane. The crosses indicate the position uncertainty of 1 $\sigma$ confidence level. The radial motion of the each plasma clump from the pulsar is summarized in Table 5.4. The region names are described in Figure 5.8. From these measurements, most of the plasma clumps appear to be moving away from the pulsar. On average the transverse velocity in the radial direction from the pulsar is about $4200 \pm 500(d/5.2{\rm kpc})$ km s$^{-1}$. This result is inconsistent with previous optical observation of van den Bergh and Kamper (1984).

[6]Errors are with 90% confidence level.

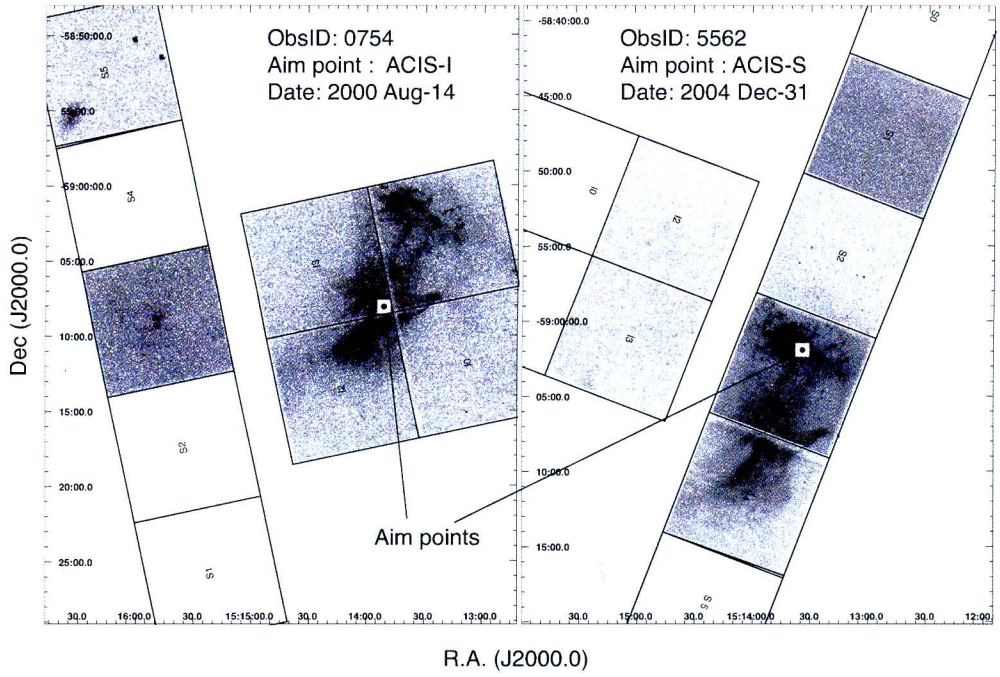


Figure 5.6: FoV of the two *Chandra* observations, ObsID-754 (Left) and ObsID-5562 (Right). The box regions labeled I0∼S5 indicate the arrangement of individual CCD chips. The aim points are indicated by the white-colored open boxes.

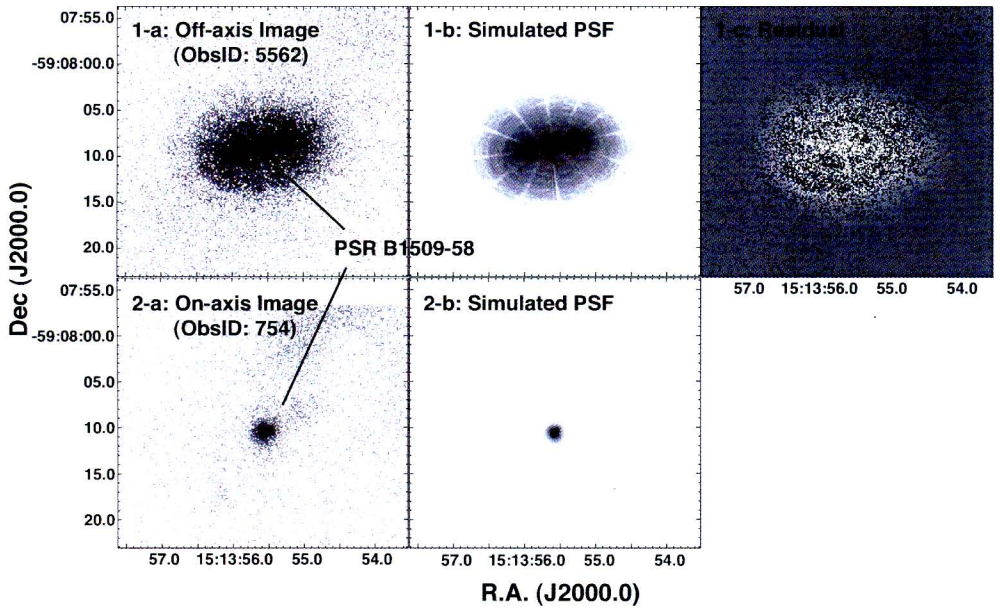


Figure 5.7: PSF variations of the two *Chandra* observations. Upper and lower panels indicate the off-axis (ObsID: 5562) and on-axis (ObsID: 754) images of PSR B1509−58, respectively. The left panels show the observed images of the pulsar, while the center panels show the simulated images.

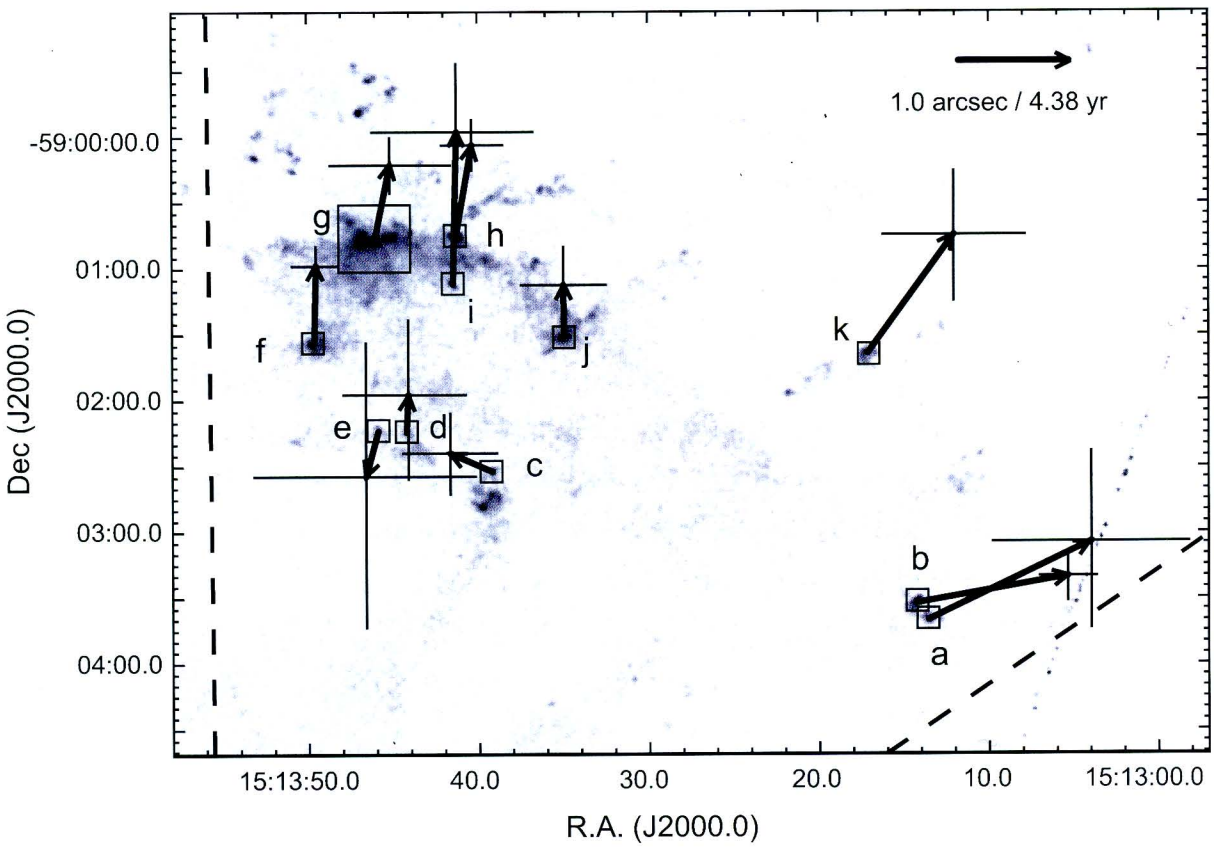


Figure 5.8: Vector map of the proper motion of each plasma clump in RCW 89. For better visibility the length of all vectors is scale by 50 times the actual distance the object has moved in the plane of the sky. The crosses indicate the positional uncertainty of a 1 $\sigma$ confidence level, which is not containing the uncertainty caused by the roll angle. Dashed lines indicate the direction of the pulsar PSR B1509−58.

Table 5.4: Results of position measurements

| Region-#[a] | Coordinate (J2000.0) | | Radial distance[b] | Radial proper motion | Travel time[c] |
|---|---|---|---|---|---|
| | R.A. | Dec | (arcmin) | (arcsec $yr^{-1}$) | (yr) |
| A..... | $15^h13^m13^s.901$ | $-59°03'40''.93$ | $7'.00$ | $0''.36 \pm 0''.20$ | $1160 \pm 640$ |
| B..... | $15^h13^m14^s.537$ | $-59°03'32''.82$ | $7'.02$ | $0''.27 \pm 0''.06$ | $1550 \pm 330$ |
| C..... | $15^h13^m39^s.295$ | $-59°02'32''.66$ | $5'.99$ | $0''.01 \pm 0''.09$ | $60000 \pm 1000000$ |
| D..... | $15^h13^m44^s.375$ | $-59°02'14''.93$ | $6'.08$ | $0''.08 \pm 0''.18$ | $5000 \pm 11000$ |
| E..... | $15^h13^m46^s.024$ | $-59°02'13''.72$ | $6'.04$ | $-0''.10 \pm 0''.31$ | $-4000 \pm 12000$ |
| F..... | $15^h13^m49^s.776$ | $-59°01'34''.92$ | $6'.62$ | $0''.16 \pm 0''.05$ | $2460 \pm 720$ |
| G..... | $15^h13^m46^s.312$ | $-59°00'47''.62$ | $7'.45$ | $0''.16 \pm 0''.06$ | $2800 \pm 1100$ |
| H..... | $15^h13^m41^s.458$ | $-59°00'46''.27$ | $7'.61$ | $0''.19 \pm 0''.06$ | $2370 \pm 690$ |
| I..... | $15^h13^m41^s.630$ | $-59°01'08''.52$ | $7'.26$ | $0''.31 \pm 0''.15$ | $1410 \pm 700$ |
| J..... | $15^h13^m35^s.122$ | $-59°01'31''.50$ | $7'.14$ | $0''.10 \pm 0''.08$ | $4300 \pm 3600$ |
| K..... | $15^h13^m17^s.381$ | $-59°01'39''.86$ | $8'.16$ | $0''.30 \pm 0''.14$ | $1610 \pm 760$ |
| Average... | | | | $0''.17 \pm 0''.02$ | $1730 \pm 220$ |

Note— Errors are with 1 $\sigma$ confidence.

[a] Regions as marked in Fig. 5.8.

[b] Radial distance from the pulsar in Fig.

[c] Travel time of each clump from the pulsar obtained by dividing the radial distance by the radial proper motion.

# Chapter 6

# Discussion

In this chapter we discuss the obtained results of spatially resolved spectroscopy as shown above. First we consider the pulsar wind nebula comparing with the recent results of numerical studies. Then we discuss the HII region RCW 89 which provides the information of the relation between the large radio SNR G320.4−01.2 and the young pulsar PSR B1509−58.

## 6.1 Spatial variation of the column density

In §4.4 we discovered spatial variations of the column density in the vicinity of SNR G320.4−01.2. The distribution of the absorbers were clearly shown as shadow-like features in the hardness ratio map (Figure 4.2); the west edge of the PWN and a part of south jet ∼5 arcmin apart from the pulsar. These features are not found in the usual X-ray images. In this section we discuss the shadow-like features.

### 6.1.1 Measurement of the column density

In order to evaluate the amount of the absorbers the column densities at the shaded regions were measured. Figure 6.1 shows the six selected regions for the column density measurements, labeled A∼ F. For the spectral fitting we used an absorbed power-law function. The results are listed in Table 6.1. The column density toward region A is $2.47 \times 10^{22}$ cm$^{-2}$, which is more than twice the average. The filament like feature F also has a significantly large column density of $1.27 \times 10^{22}$ cm$^{-2}$. Region C and E which

are aligned along the jet axis show different column densities of $1.15 \times 10^{22}$ cm$^{-2}$ and $0.79 \times 10^{22}$ cm$^{-2}$, respectively.

### 6.1.2 What's absorbing the X-rays?

It is the problem whether the ISM which absorbs the soft X-rays from the PWN is correlated or not with the surrounding SNR. The absorbing local dense ISM can be wherever on the line of sight between the SNR and the earth. However we suggest that the local dense clouds are associated with the SNR from the following reasons.

First of all, the sharp cut-off seen in western edge of the PWN should be considered. The torus structure in PWNe are believed to be generated by rotating magnetic field, then PWNe should have axisymmetric structure. Therefore the observed east-west asymmetry in the equatorial direction strongly implies the physical relation between the pulsar wind and the dense ISM clouds at the western side of the pulsar.

### 6.1.3 Constraints on the proton number density

#### Based on the pressure balance between the PWN and the ISM

From the X-ray spectroscopy, we can constrain the inner pressure of the PWN at the western edge. Assuming the equipartition condition, the pressure of the synchrotron gas can be constrained as $3 \times 10^{-12} f^{-4/7}$ dyn cm$^{-2}$, where $f$ is the filling factor (or the uncertainty factor) of the volume, which should be $\sim 0.5$ for a torus geometry with an opening angle of $\sim 15°$ (see §2.3). Assuming a pressure balance between the pulsar wind and the confining ISM at the western edge of the PWN, the number density of the ISM can be estimated.

Supporting our hypothesis, Dubner et al. (2002) discovered HI nebula around the vicinity of G320.4−01.2. Adopting a typical temperature of HI nebula of $T \sim 100$ K, the number density of the invisible ISM can be constrained as

$$n_{\rm p} = 140 f^{-4/7} \left( \frac{T_{\rm HI}}{100 \text{ K}} \right)^{-1} \quad \text{cm}^{-3}. \tag{6.1}$$

For a filling factor of $f = 0.5$ this equation provides a number density of $\sim 200$ cm$^{-3}$, which is one order of magnitude larger than the atomic density of $n_{\rm p} \sim 10$ cm$^{-3}$ from the HI observations. The HI regions distributed in the PWN axis are shown in Figure 6.2.

#### Based on the column density

The number density of the absorbing ISM can be also estimated by using the local variation of column density. The difference between region A and the average column density

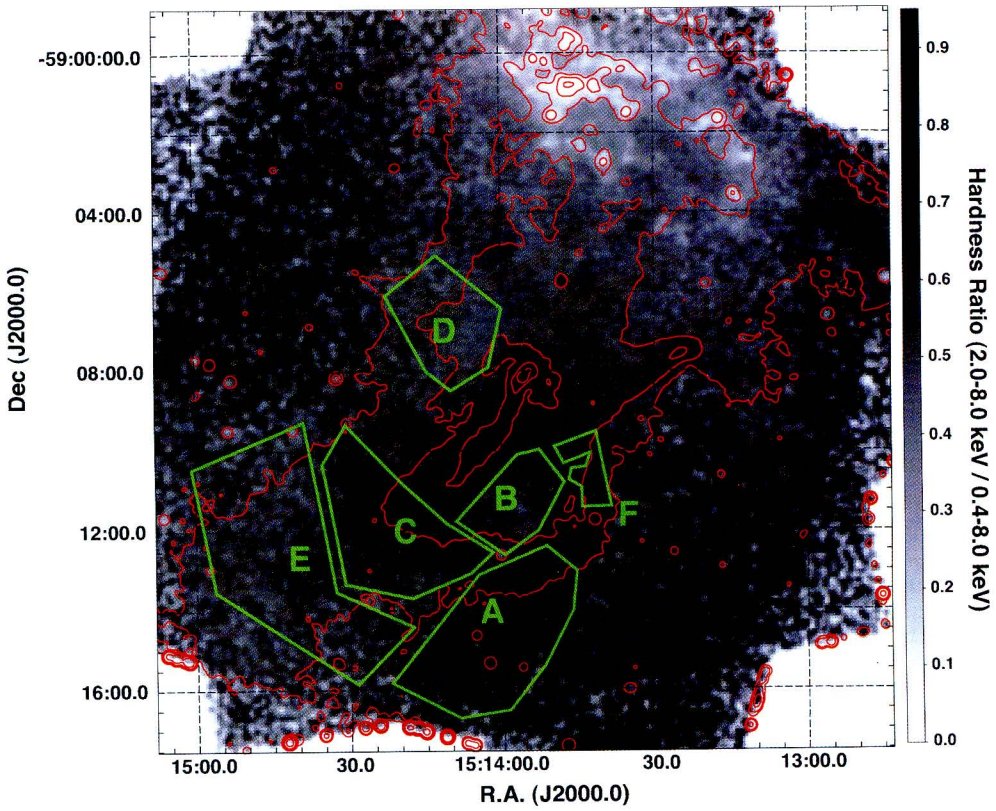


Figure 6.1: Selected regions for absorption measurements. Green marks indicate the selected regions labeled "A∼F". The gray scale and the red contours indicate the X-ray hardness ratio and the surface brightness over 0.4−8.0 keV, respectively.

Table 6.1: Results of the absorption measurements. The regions are corresponds to Figure 6.1.

| Region | $N_{\rm H}$ ($10^{22}$ cm$^{-2}$) | Photon Index | Flux(0.5-5.0 keV) ($10^{-12}$ ergs s$^{-1}$cm$^{-2}$) |
|---|---|---|---|
| A..... | $2.47^{+0.11}_{-0.10}$ | $2.40^{+0.28}_{-0.11}$ | $2.15^{+0.12}_{-0.12}$ |
| B..... | $0.96^{+0.02}_{-0.01}$ | $1.96^{+0.04}_{-0.01}$ | $6.96^{+0.12}_{-0.07}$ |
| C..... | $1.15^{+0.02}_{-0.01}$ | $1.95^{+0.05}_{-0.02}$ | $6.22^{+0.14}_{-0.08}$ |
| D..... | $0.92^{+0.02}_{-0.01}$ | $2.26^{+0.05}_{-0.01}$ | $6.11^{+0.16}_{-0.07}$ |
| E..... | $0.79^{+0.02}_{-0.01}$ | $2.11^{+0.03}_{-0.06}$ | $3.93^{+0.12}_{-0.08}$ |
| F..... | $1.27^{+0.06}_{-0.06}$ | $1.85^{+0.06}_{-0.06}$ | $1.21^{+0.04}_{-0.04}$ |
| RCW 89..... | 1.18 | 2.48 | |

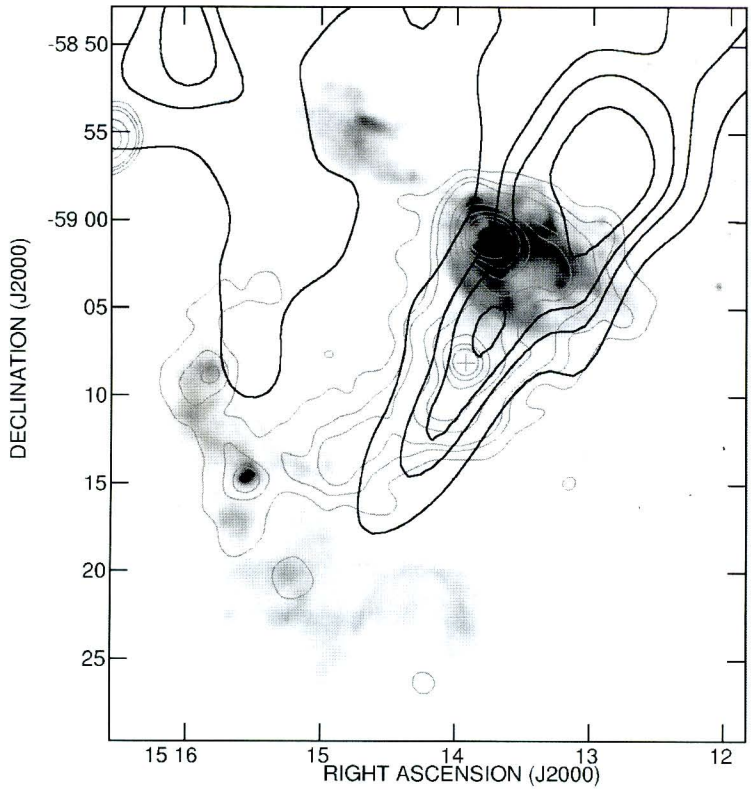


Figure 6.2: Comparison between radio continuum (gray scale), X-rays (gray contour lines), and HI (black contours) in the velocity range +10 to +20 km $s^{-1}$ (Dubner et al., 2002). The HI contours are 3, 3.6, 4.2, and 4.5 mJy $beam^{-1}$ km $s^{-1}$. The cross mark indicates the position of the pulsar PSR B1509−58.

is about $1.5 \times 10^{22}$ $cm^{-2}$. Adopting a depth of the local ISM ∼15 pc which corresponds to the radius of SNR G320.4−01.2, we obtained an ion density of $n_p \sim 300$ $cm^{-3}$. While in the case of region C and E along the south jet, the difference of the column density is $(3.6 \pm 0.3) \times 10^{21}$ $cm^{-2}$. For a depth of ∼15 pc, we found an ion density of $\sim 80$ $cm^{-3}$.

The region F that covers the small filament structures shows a significantly large column density that equals to $1.27 \times 10^{22}$ $cm^{-2}$. Comparing it with the nearby region "B", we found a column density difference of $\Delta N_H = (0.31 \pm 0.06) \times 10^{22}$ $cm^{-2}$. Assuming that the filament-like features have a depth of ∼1 pc[1], which is equal to the length of the filaments, we found a number density of $n_p \sim 1000$ $cm^{-3}$. The resulting atomic density is much larger than the value of $n_p \sim 20$ $cm^{-3}$ predicted by the pressure balance assumption.

The atomic densities of region A and C from the X-ray absorption show a good agreement with that obtained from the pressure balance assumption. These results may suggest that the western edge of the PWN is confined by dense ISMs. The discrepancy in the

[1] 1 pc corresponds to an angular size of ∼ 40 arcsec at 5.2 kpc from the earth.

atomic densities between our calculation and the HI observations may be explained by the non-uniform distribution of the surrounding matter. In fact, the beam size of the HI observation was $4.0\times2.7$ arcmin$^2$, which seems to be insufficient to resolve the fine structures.

On the other hand the origin of the cold ISMs are still unclear. The estimated total mass of the HI region was 2700 $M_\odot$ (Dubner et al., 2002), which cannot be explained by an SN ejecta ($\sim 20M_\odot$) or swept-up ISMs ($\sim$ a few $100M_\odot$). Thus we suggest that the dense matter confining the PWN are originated in the existing cold ISMs which are distributed nonuniformly around the SNR.

On the other hand, the filament-like features (region F) have extremely high density compared to a typical HI region ($\sim$ 10 cm$^{-3}$). However the estimated number density seems to be reliable because of the apparent compact structures. The optical nebula RCW 89 also has similar filamentary structures. Previous infrared-optical spectroscopic observations revealed its number density of $n_{\rm p} \sim 10^3 - 10^4$ cm$^{-3}$ (Seward and Harnden, 1982), which is consistent with that of feature F. It is therefore inferred that RCW 89 and feature F may have some relations or have the common origin.

## 6.2 Nature of the double Tori

PSR B1509−58 possesses nested ring structures lying on the equatorial plane relative to the spin axis. In this section we discuss the phenomena on the equatorial plane by comparing it with the case of Crab nebula.

### 6.2.1 Spectral evolution on the equatorial plane

As shown in §4.4 PSR B1509−58 has a central concentrated surface brightness profile, which may caused by its comparatively small angular size or the contamination from the bright jet structure coming towards us. For this reason, it is difficult to compare the surface brightness evolution of PSR B1509−58 with those of the Crab nebula, in a simple way. However, as shown in Figure 4.4, PSR B1509−58 possesses apparently different morphology; the nested double tori structures which are lying at $\sim$ 30 arcsec and $\sim$ 60 arcsec from the pulsar, respectively.

At a view point of spectroscopy, these two tori, calling the inner-torus and the outer-torus, seems to be completely different. The inner-torus has a constant photon index of $\Gamma \sim 1.6$ that is the same as those just behind the termination shock which stands at $\sim$10 arcsec from the pulsar. In contrast, the photon index in the outer-torus obviously gets steeper as the radius increases from $\Gamma = 1.6$ to 2.1. The measured interval of the photon

index variation is $\Delta\Gamma \sim 0.5$, which implies that the observed spectral evolution is caused by the synchrotron cooling (Kardashev, 1962).

In case of the Crab nebula, the post shock photon index is $\Gamma = 2.1$ and it does not change within the torus. According to Kennel and Coroniti (1984a), the evolution of the surface brightness in the torus can be explained by the compression of the toroidal magnetic field, which enhances the synchrotron energy loss. Thus the bright torus seen in the Crab nebula simply corresponds to the region in which most of the X-ray emitting particles radiate their energies. As a result, the photon index outside of the torus is steeper than $\Gamma = 2.1$, and the surface brightness decays rapidly.

This is immediately confirmed by the comparison between $t_{\rm flow}$ and $t_{\rm sync}$, which are the time for particles to take to flow from the pulsar to the inner-torus, and the synchrotron lifetime of the particles, respectively. For a less magnetized pulsar wind with $\sigma \ll 1$, the bulk velocity in the post-shock flow at a distance $r$ from the pulsar is (Kennel and Coroniti, 1984a)

$$v(r) = \frac{c}{3}\left(\frac{r_{\rm TS}}{r}\right)^2, \tag{6.2}$$

where $r_{\rm TS}$ is the distance from the pulsar to the termination shock. Integrating this yields:

$$t_{\rm flow} = \int_0^r \frac{dr}{v(r)} = \frac{r_{\rm TS}}{c}\left(\frac{r}{r_{\rm TS}}\right)^3. \tag{6.3}$$

On the other hand, the synchrotron cooling time scale for the electrons emitting at energy $\epsilon$ keV in a magnetic field $B\mu$G is (§A.3)

$$t_{\rm sync} = 55\left(\frac{B}{1\ \mu{\rm G}}\right)^{-3/2}\left(\frac{\epsilon}{1\ {\rm keV}}\right)^{-1/2} \quad {\rm kyr}. \tag{6.4}$$

For the Crab nebula, we adopted $r_{\rm TS} \sim 0.15$ pc and $B \sim 100\mu$G, and the radius of $r_{\rm torus} \sim 0.4$ pc from the X-ray observations. For the X-ray energy of $\epsilon = 5$ keV, we find $t_{\rm flow} \sim 30$ yr and $t_{\rm sync} \sim 25$ yr, which are comparable as expected.

Now we apply the similar calculation to the inner-torus of PSR B1509−58. In order to estimate the synchrotron cooling time scale $t_{\rm sync}$, the magnetic field strength in the PWN must be known. Applying the equipartition condition (§A.5), we can roughly estimate the magnetic field of the emitting volumes from the results of spectroscopy (4.10). Note that the theoretical model proposed by Kennel and Coroniti (1984b) predicted that the post shock magnetic field in the PWN is generally weaker than that obtained from the equipartition argument. Therefore the obtained magnetic field here is an upper limit. For simplification we assumed a geometry of a partial spherical shell with an opening angle of 45°. For a radius of $R$ and a thickness of $dR$, the volume of the spherical shell is

$$V = 2\pi\left(1 - \cos 45^\circ\right) R^2 dR \tag{6.5}$$

$$= 8.6 \times 10^{50} r^2 dr f \left(\frac{d_{5.2}}{5.2 \text{ kpc}}\right)^3 \quad \text{cm}^3 \tag{6.6}$$

where $r$ and $dr$ are the radius and the thickness in unit of arcsec, respectively. $f$ is a filling factor (or an uncertainty). Although this volume may be slightly larger than that expected from a thin torus , it is still a good approximation. In fact, we should set the filling factor to be $f \sim 0.5$ for a torus with an opening angle of $\sim 15°$, the resulting magnetic field increases by only a factor of $f^{-2/7} \sim 1.2$ (§A.5). Figure 6.3 and 6.4 show the variations of the magnetic field (panel-c), the total energy presents in the region (panel-d), and the pressure of the synchrotron gas (panel-e), for the north-east sector and the south-west sector, respectively. For comparison the variations of the surface brightness and the photon index are shown in panel (a) and (b), respectively. From the figure we find a magnetic field of $B \sim 20 f^{-2/7} \mu$G at the inner torus. While, in the outer-torus, the magnetic field is $B \leq 10 \mu$G, which is consistent with the magnetic field of whole nebula based on the spectral cooling break (Frail et al., 1996; Gaensler et al., 2002)

$$B_{\rm n} = 8.0 \left(\frac{t_{\rm sys}}{1700 \text{ yr}}\right)^{-2/3} \left(\frac{\epsilon_{\rm s}}{1 \text{ keV}}\right)^{-1/3} \quad \mu\text{G}, \tag{6.7}$$

where $t_{\rm sys}$ is the age of the system and $\epsilon_{\rm s}$ is the cooling break energy, which should be lower than 1 keV (based on the lower limit of the observed energy band).

For a magnetic field of $B \sim 25 \mu$G, the synchrotron lifetime of the electrons radiating at 5 keV is $t_{\rm sync} \sim 200$ yr. On the other hand, for $r_{\rm TS} = 0.25$ pc and $r_{\rm Torus} = 0.75$ pc, we obtained $t_{\rm flow} \sim 22$ yr. Remarkably these two time scales are different. In order to burn off the synchrotron electrons within 22 yr, a magnetic field of $B \sim 100 \mu$G is required, and it sounds unlikely. As mentioned above, the actual magnetic field in the nebula core may be smaller than that from the equipartition assumption, further widening the discrepancy between the two timescale. The timescale of $t_{\rm flow}$ is expected to be longer, in other word, the velocity of the particle flow in the torus should be much slower. If that is the case, the $\sigma$ parameter must be small. In next section we estimate the flow velocity in the torus.

### 6.2.2 Bulk velocity of the torus

It is essential to know the flow velocity to understood what happens in the inner torus. In the following section we estimate the flow velocity in the torus.

#### Based on the Energy budget

First we estimate the flow velocity based on the energy budget. As the torus is driven by the pulsars spin energy, the injected energy should be $\phi \dot{E}$, where $\phi$ is the fraction of the

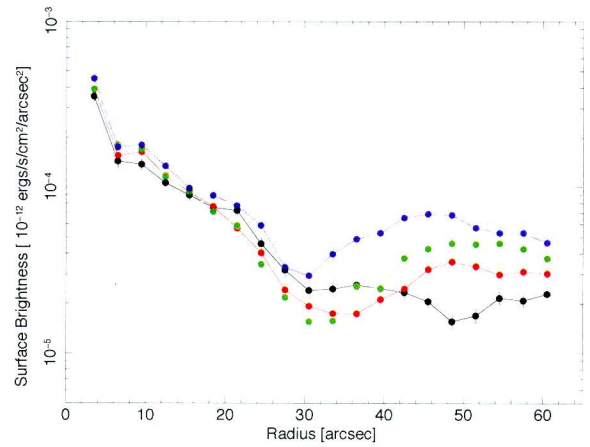


(a)Surface Brightness

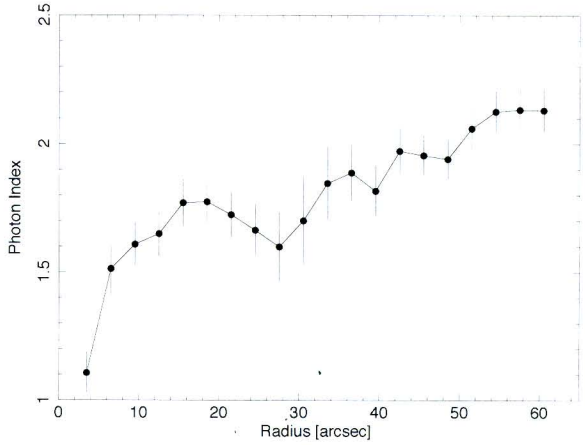


(b)Photon Index

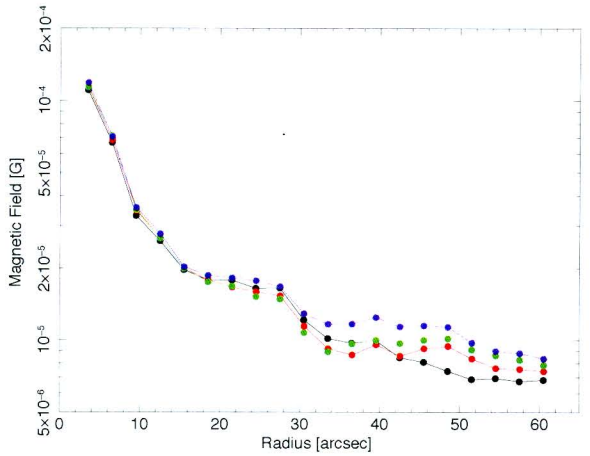


(c)Magnetic Field

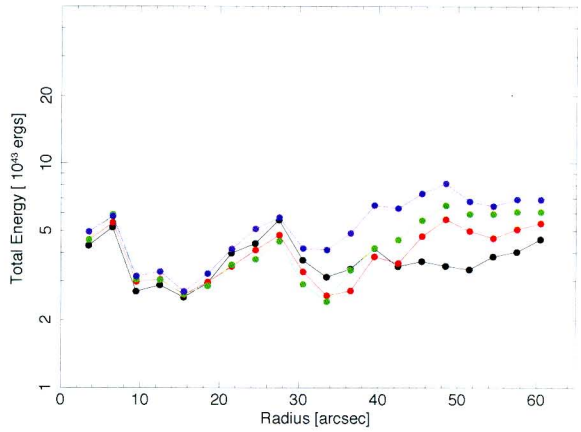


(d)Total Energy in the region

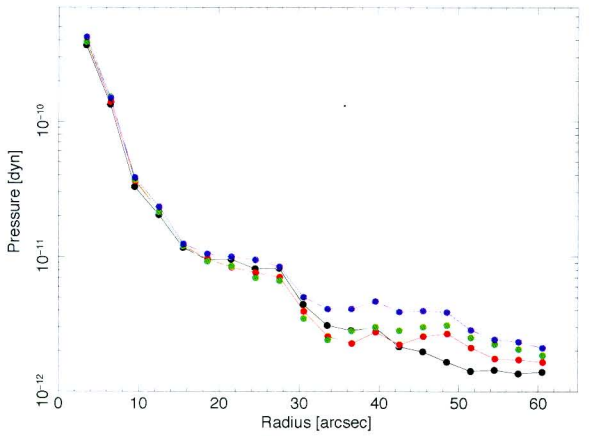


(e)Pressure

Figure 6.3: Magnetic field (c), total energy present in the region (d), and pressure (e) from the equipartition argument are shown as a function of radius. For comparison surface brightness (a) and Photon Index (b) are shown. Colors corresponds to the epochs, 2004-Dec-28 (black), 2005-Feb-07 (red), 2005-Apr-29 (green), and 2005-Oct-18 (blue).

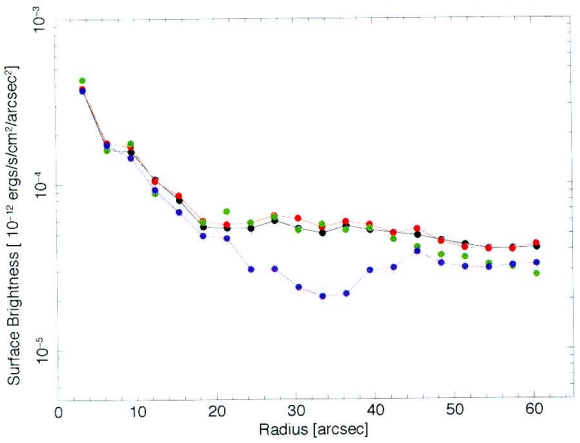


(a)Surface Brightness

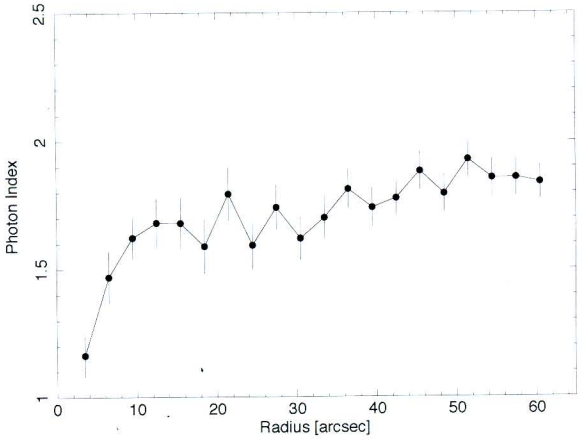


(b)Photon Index

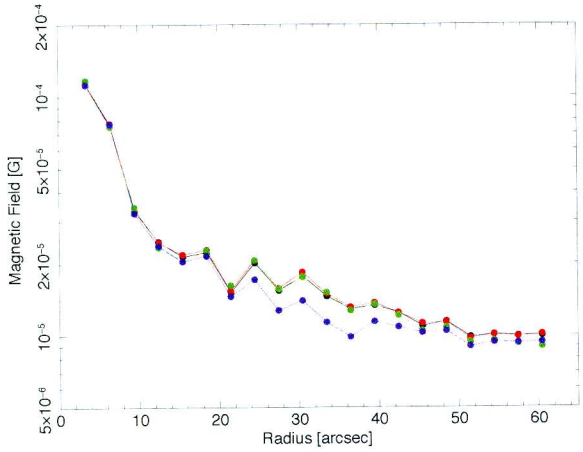


(c)Magnetic Field

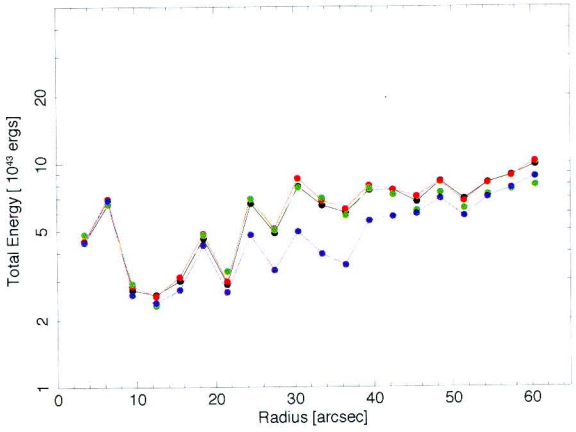


(d)Total Energy in the region

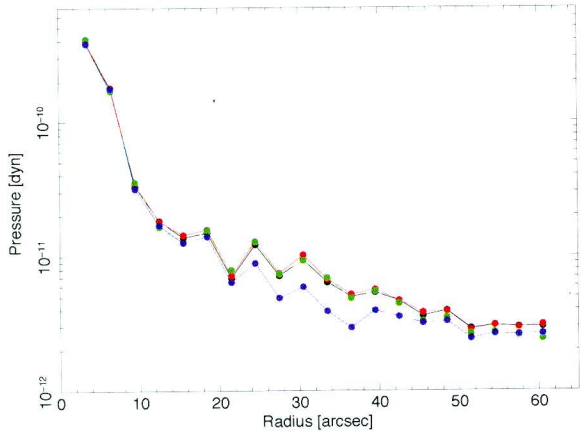


(e)Pressure

Figure 6.4: Magnetic field (c), total energy present in the region (d), and pressure (e) from the equipartition argument are shown as a function of radius. For comparison surface brightness (a) and Photon Index (b) are shown. Colors corresponds to the epochs, 2004-Dec-28 (black), 2005-Feb-07 (red), 2005-Apr-29 (green), and 2005-Oct-18 (blue).

spin-down energy which injected into the torus. Then the energy presents in the annulus region with a width of $\Delta R$ can be described as a function of a flow velocity $v_{\rm flow}$,

$$\Delta W = \frac{\Delta R}{v_{\rm flow}} \dot{E}\phi \tag{6.8}$$

The panel (d) in Figure 6.3 shows the amount of energy present in the torus based on the equipartition assumption. We obtained that a 1/4 part of annulus with $\sim 2.4 \times 10^{17}$ cm (= 3 arcsec) has $\Delta W/4 \sim 5 \times 10^{43}$ ergs. And then we find

$$v_{\rm flow} = \frac{\Delta R}{\Delta W} \dot{E}\phi = 0.7\phi c. \tag{6.9}$$

If $\phi$ is 0.5, the above equation yields to a $v_{\rm flow} \sim 0.35c$, which is consistent with the predicted value by Kennel and Coroniti (1984a).

### Based on the Lorentz boost

The half circle (or arc-like) morphology bisected by the symmetry axis of the nebula implies the *Lorentz* boost by the bulk motion as seen in the inner-torus. By using the brightness ratio of the torus, we can also constrain the bulk velocity of the flow. This technique have been applied to the Crab nebula by Pelling et al. (1987).

The apparent boost that power-law photons received is modified by the factors

$$\left[\frac{\sqrt{(1-\beta^2)}}{1-\beta\cos\theta}\right]^{\Gamma-1} \left[\frac{\sqrt{(1-\beta^2)}}{1-\beta\cos\theta}\right]^{-2}, \tag{6.10}$$

where $\theta$ is the angle measured in the observer's frame between the direction of the flow and the line of sight and $\Gamma$ is the photon index. And then the intensity ratio of the north side and the south side of the torus is

$$R = \left(\frac{1+\beta\cos\theta}{1-\beta\cos\theta}\right)^{\Gamma+1} \tag{6.11}$$

The parameters of $\Gamma = 1.6$ and $R \sim 3$ for the inner-torus have been already known from the *Chandra* observations. Assuming the inclination angle of $i \sim 50°$ which corresponds to $\theta \sim 40$ yields the flow velocity of $\beta \sim 0.28$ ($\beta \sim 0.43$ for $i \sim 30°$).

The velocity estimations in the two different ways both provided to a $v_{\rm flow} \sim 0.3c$, which is consistent with the value expected by the relativistic strong shock (KC-model). At the same time, these velocity estimations make the discrepancy between $t_{\rm flow}$ and $t_{\rm sync}$ a serious problem.

The observed rapid evolution of the spectral index requires a large magnetic field which can rapidly cool down the relativistic pair plasma. At the same time, the result implies

that the emitting particles lose their energies through the synchrotron radiation and burn off there. Therefore it is valid to argue that the inner-torus is the analog of the X-ray torus seen in the Crab nebula, although the rapid cooling requires a unlikely larger magnetic field than that expected by the traditional KC-model with less magnetized ($\sigma \sim 0.003$) pulsar wind.

### 6.2.3 What's the Outer-Torus?

In the outer-torus, the photon index gets steeper, implying that the synchrotron cooling break passes through the observing energy band (8 keV to 0.4 keV). Therefore it is impossible to explain the brightening at the outer torus with an uniform electron density and magnetic field.

#### Magnetic field evolution in the outer-torus

Although DeLaney et al. (2006) reported that the outer-torus moves inward with a velocity of $\sim 0.03c$, the half circle (or arc-like) morphology bisected by the symmetry axis of the nebula implies a *Lorentz* boost with bulk motion. Using Eq. (6.11) the flow velocity becomes $v_{\rm flow} \sim 0.22c$ for the same intensity ratio of $R \sim 3$ and an inclination angle of $i \sim 50^\circ$ ($v_{\rm flow} \sim 0.35c$ for $i \sim 30^\circ$). The obtained flow velocity is slightly slower than that of the inner-torus. Note that Kennel and Coroniti (1984a) expected a flow velocity of $v_{\rm flow} \propto (r/r_{\rm TS})^{-2}$, assuming a constant electron density. If the KC model is true the velocity in the outer-torus should be smaller than $0.08c$.

Here we consider the conservation law of the magnetic flux, $rvB = {\rm const}$ to evaluate the magnetic field in the outer-torus. Based on the above relation between $v$ and $B$, we find a relation

$$B_{\rm out} = \frac{r_{\rm in}}{r_{\rm out}} \frac{v_{\rm in}}{v_{\rm out}} B_{\rm in}, \tag{6.12}$$

where $v_{\rm in/out}$ and $r_{\rm in/out}$ are the flow velocities and the radii of the inner-torus and the outer-torus, respectively. For the observed parameters of $r_{\rm in}/r_{\rm out} = 1/2$, $v_{\rm in} = 0.28c$, and $v_{\rm out} = 0.22c$, we find a magnetic field of $B_{\rm out} \sim 10$ $\mu$G, showing a good agreement with the magnetic field based on the equipartition argument as shown in Figure 6.3.

The above calculations strongly support the equipartition in the region $r = 30 \sim 60$ arcsec from the pulsar. It is also implied that the brightening at the outer-torus caused by a local increase of magnetic field cannot be expected because the magnetic field already reaches equipartition at the inner-torus, in which the magnetic pressure prevents further compression. Therefore it is difficult to understand the outer-torus without an increase of electron density or an external energy injection.

In conclude, the above rough estimations of the flow velocities in the inner-torus and the outer-torus provided a velocity larger than that expected from a less magnetized pulsar wind with $\sigma \sim 0.003$. According to the KC-model the obtained flow velocity $v_{\rm flow} \sim 0.29c$ at the inner-ling (for $i = 50°$) requires a comparatively large magnetization parameter of $\sigma \sim 0.1$ (see Figure 2.4).

## 6.3 Inner Ring

It is essential to know the radius of pulsar wind termination shock for understanding the mechanism which forms the structures of a PWN. So far, the termination shocks by the pulsar winds have been observed only in the Crab nebula (Weisskopf et al., 2000a). In this section we discuss the ring feature discovered near around PSR B1509−58 comparing with the inner ring of the Crab nebula.

### 6.3.1 Appearance

According to the KC model (Kennel and Coroniti, 1984b), the pulsar wind is cold inside the termination shock. Thus the free flowing region should not be radiative, as seen in the Crab nebula. In case of PSR B1509−58 the region within the ring feature is also dark. Comparing with the tori which is strongly affected by the Lorentz boost, the surface brightness of the ring feature appears to be uniform, so that we can distinguish the south edge of the ring. For the Crab, Weisskopf et al. (2000a) pointed out that the surface brightness of the inner ring is more uniform in azimuth, indicating that relativistic beaming is less significant for it than for the torus. The observed properties can distinguish the ring from the tori and the hypothesis that the ring structure represents the termination shock can be suggested.

By the way the ring shows an obvious elliptic shape, implying that the shock front has an ellipsoid or a ring structure rather than a sphere. Regarding the issue, recent numerical simulations predicts a shock front with an oblate shape for an un-isotropic pulsar wind (Komissarov and Lyubarsky, 2003; Del Zanna et al., 2004). As shown above we obtained an inclination angle of the spin axis, $i \sim 53°$ from the ellipticity of the ring feature, which is much larger than $i \sim 30°$ from the appearance of the torus (Gaensler et al., 2002). The inclination angle of the system has long been discussed, however it has been still unsettled. The suggested inclination angles are in the range from 30° to 70° (Brazier and Becker, 1997). We also reported an inclination angle of $i \sim 50°$ based on the observation of RCW 89 (Yatsu et al., 2005). The newly obtained inclination $\sim 50°$ seems

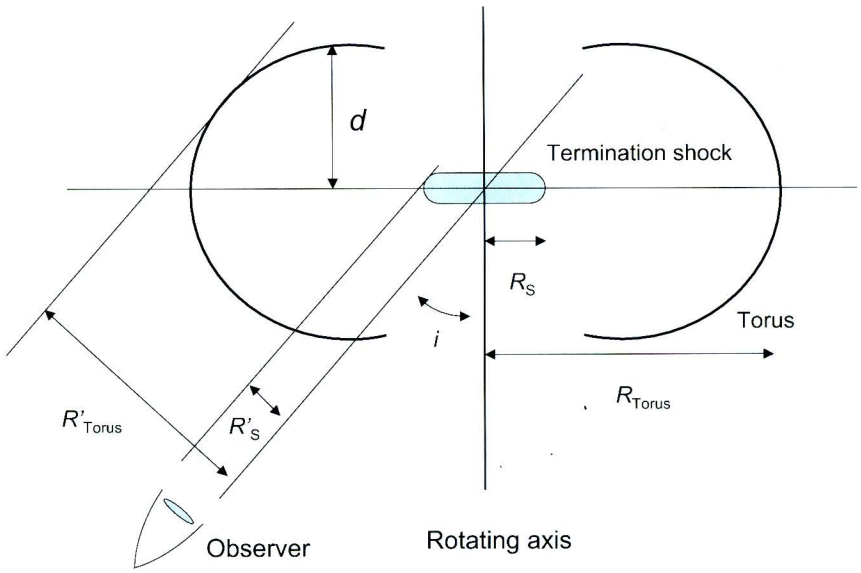


Figure 6.5: A schematic drawing of the torus and the shock fronts.

to be reliable, which gives the smaller flow velocities of the tori than that with $i \sim 30°$[2].

If this is the case the discrepancy of the ellipticity between the tori and the inner ring may be solved. For this problem the recent MHD simulation by Del Zanna et al. (2004) can provide a hint that the tori can be thicker, likely to be a doughnut-like structure. Figure 6.5 shows a schematic drawing of a thick torus (or doughnut) with a thickness of $\sim 2d$. Adopting radii of $R_{\rm TS} = 10$ arcsec and $R_{\rm Torus} = 30$ arcsec and inclination of $i = 50°$, we can estimate the thickness of $d$, which can explain the previously reported inclination angle of $i' \sim 30°$ According to the geometry the apparent radius of the torus should be $R'_{\rm Torus} = d + (R_{\rm Torus} - d)\cos i$. Combining with $\cos i' = R'_{\rm Torus}/R_{\rm Torus}$, we find

$$d = \frac{\cos i' - \cos i}{1 - \cos i} R_{\rm Torus} \sim 13 \quad \text{arcsec.} \tag{6.13}$$

This result corresponds to a thickness of $2d = 2.0 \times 10^{18}$ cm for the distance of 5.2 kpc, and seems to agree with the simulations.

[2]The inclination angle $i = 30°$ requires large flow velocity $\sim 0.43c$ at the inner torus, which results in unlikely larger magnetization parameter $\sigma > 0.1$.

### 6.3.2 Pressure balance at the ring feature

At the termination shock, a pressure balance between the cold pulsar wind and the "thermalized[3]" post-shock plasma is expected, as seen in the Crab nebula. Based on the X-ray image (Fig.4.5), we obtained a radius of the ring structure $r \sim 10$ arcsec, which corresponds to $7.8 \times 10^{17} d_{5.2}$ cm for the distance of 5.2 kpc to the pulsar. Assuming that the most of the pulsar's rotating energy $\dot{E} = 1.8 \times 10^{37}$ ergs s$^{-1}$ is transferred into the relativistic pulsar wind at the light cylinder, we find the ram pressure of the pulsar wind at the ring structure

$$p_* = \frac{\dot{E}}{4\pi r_{\rm TS}^2 \phi c} \tag{6.14}$$

$$= 7.84 \times 10^{-11} \phi^{-1} \left( \frac{d}{5.2 \text{ kpc}} \right)^{-2} \quad \text{dyn cm}^{-2}, \tag{6.15}$$

where $\phi$ is the fraction of a sphere covered by the wind.

On the other hand, the inner pressure of the nebula is roughly estimated by assuming the equipartition condition as shown in §6.2. Panel (e) in Figure 6.3 and 6.4 show the pressure variations of the synchrotron gas as a function of radius from the pulsar. At $r = 10$ arcsec where the ring feature exists, we find a synchrotron pressure of $p_{\rm n} = 3 \times 10^{-11} f^{-4/7}$ dyn ($f \sim 0.5$ for a thin torus). Note that the obtained inner pressure is a lower limit since the post shock flow with a small $\sigma$ is believed to be in the particle dominant condition, rather than the equipartition. Taking into account the fact mentioned above, $p_*$ and $p_{\rm n}$ are comparable, implying the pressure balance between the cold wind and the post-shock flow at the ring feature. We can therefore consider the ring structure to be the termination shock of the pulsar wind.

### 6.3.3 Estimation of the $\sigma$ parameter

Now we know the most important parameter $R_{\rm TS}$ to calculate the magnetization parameter $\sigma$, let us estimate it. As the shock transforms the kinetic energy into the thermal energy, $\sigma$ can be rewritten as

$$\sigma = \frac{B_1^2/4\pi}{[\text{kinetic energy density}]} \sim \frac{B_1^2/4\pi}{[\text{post shock thermal energy density}]} \sim \frac{B_1^2/4\pi}{B_{\rm Eq}^2/4\pi} \tag{6.16}$$

for $\sigma \ll 1$, where $B_1$ is the toroidal magnetic field just upstream of the shock. Combining this equation with the equation of continuity $r_{\rm TS}^2 c/3 = r_{\rm n}^2 v_{\rm n}$ and the flux conservation law of $r_{\rm TS} c B_1 = r_{\rm n} B_{\rm Eq}$ yields

$$\frac{r_{\rm n}}{r_{\rm TS}} \sim \frac{1}{3\sqrt{\sigma}}. \tag{6.17}$$

[3]In a metaphorical sense. see §2.2

Substituting $r_{\rm TS} = 10$ arcsec and $r_{\rm n} = 30$ arcsec, we obtained $\sigma \sim 0.01$, which is somewhat larger than that of the Crab nebula by Kennel and Coroniti (1984a) ($\sigma = 0.003$). Moreover, in the above calculation an assumption of the constant mass density was included. The observed flow velocity in the inner-torus also requires a rather large magnetization parameter ($\sigma \sim 0.1$, see Figure 2.4). Mori et al. (2004) also reported a larger magnetization parameter of $\sigma \sim 0.03$, encouraging above estimations.

## 6.4 Nature of the pulsar Jet

### 6.4.1 Velocity of the Jet

From the observed temporal changes of the jets, we can constrain the bulk velocity of the collimated outflow along the spin axis. The observed angular velocities of the outflow toward south and north directions were $\sim 12.7 \pm 1.1$ arcsec yr$^{-1}$ and $\sim 7.1 \pm 0.3$ arcsec yr$^{-1}$, respectively.

Considering the distance to the object, the obtained angular velocities correspond to apparent velocities $v_{\rm south} \sim 1.04c$ and $v_{\rm north} \sim 0.58c$ for a distance of $D = 5.2$ kpc. Note that the measured velocity of south jet appears to exceed the light speed, probably due to aberration of light. In order to investigate the actual velocity of the jet, we must take into account the inclination angle of the pulsar's spin axis. At this moment we know two plausible values of $i \sim 30°$ reported by Gaensler et al. (2002) and $i \sim 50°$ based on the appearance of the newly discovered inner-ring. As shown in §6.8 we also discussed the problem on the basis of the observations of RCW 89, although we could not judge between the two candidate values.

Assuming that the both side of the jets have the same velocities, the flow velocity and the inclination angle of the spin axis can be calculated simultaneously. Using the "superluminal motion" the flow velocity $v_{\rm jet}$ for an inclination angle of $i$ is described as

$$v_{\rm south} = \frac{v_{\rm jet} \sin i}{1 - \beta_{\rm jet} \cos i} \tag{6.18}$$

$$v_{\rm north} = \frac{v_{\rm jet} \sin i}{1 + \beta_{\rm jet} \cos i} \tag{6.19}$$

where $\beta_{\rm jet} = v_{\rm jet}/c$. In Figure 6.6 these two equations are plotted as functions of inclination angle $i$ (line-(a) and line-(b)). The lower limit of the south jet is also found as $v_{\rm south} \geq 0.72c$ at a inclination angle of $i \sim 43°$. Dividing Eq. (6.18) by Eq. (6.19) yields the relation of $i$ and $\beta_{\rm jet}$ as

$$\cos i = \frac{v_{\rm south} - v_{north}}{v_{\rm south} + v_{\rm north}} \beta_{\rm jet}^{-1}. \tag{6.20}$$

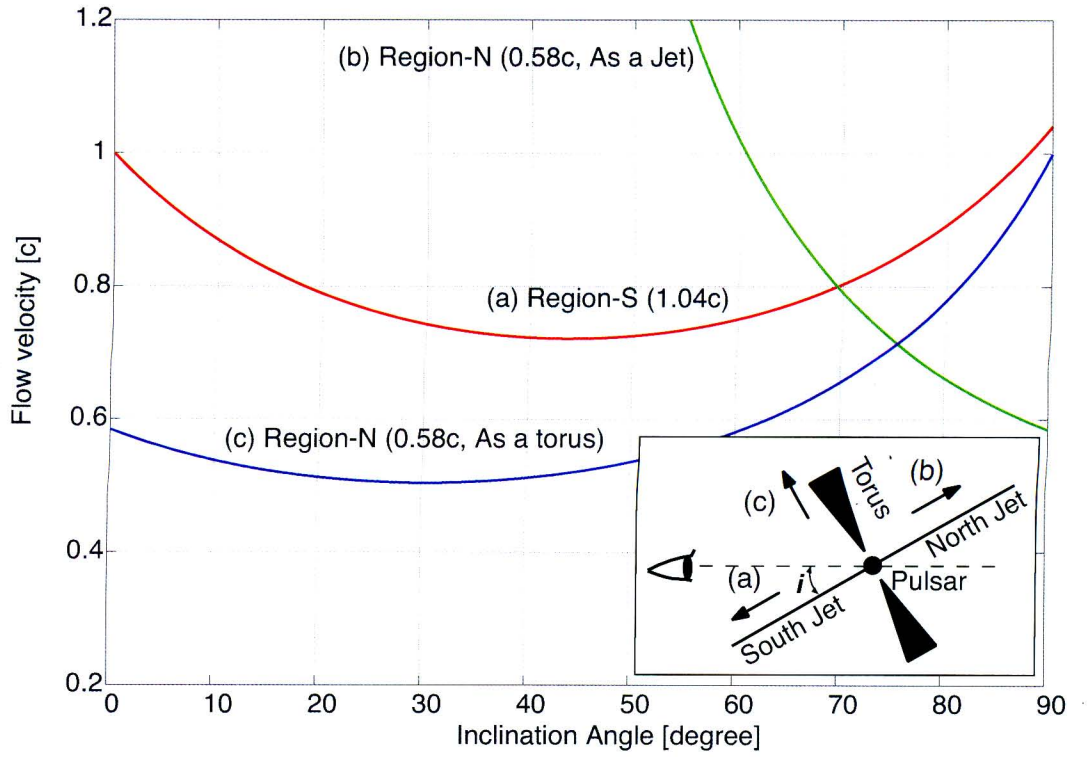


Figure 6.6: Expected flow velocity as a function of inclination angle of the pulsar's spin axis. Three lines correspond to (a) the velocity of the outflow in Region-A assumed to be the south jet (Eq. (6.18) with $v_{\rm south} = 1.04c$), (b) the velocity of the outflow in Region-B assumed to be the north jet (Eq. (6.19) with $v_{\rm north} = 0.58c$), and (c) the velocity of the outflow assumed to be the torus.

Substituting Eq. (6.20) into Eq. (6.18) and (6.19) gives a flow velocity of $v_{\rm jet} \sim 0.8c$ and an inclination angle of 70°. The resultant inclination angle, however, seem to be unacceptable because this cannot explain the observed ring and tori features around the pulsar [4].

### What we have seen in the region-N

The above large inclination angle was caused by the large angular velocity observed in the region "N" in Figure 4.17. In other words, it is doubtful that the observed proper motion in region-N is identified as the counter jet. If we adopt an allowance range of the inclination angle, $30° \leq i \leq 50°$, the velocity of the south jet should be in the range from $0.74c$ to $0.73c$. If this is the case, the north jet, which is running away from the earth, must be faded by the *Lorentz* boost. According to Eq. (6.11), the brightness ratio

[4] If this is the case the inner ring should have a semiminor axis of $r_{\rm min} = 3.4$ arcsec, which may not be distinguished from the pulsar.

between the south side and north side with respect to the pulsar is expected to be larger than $R > 10$ (for $i = 53°$, $v_{\rm jet} = 0.73c$, $\Gamma = 1.5$). This result means that we cannot detect faint features in the north jet through the bright X-ray torus.

The alternative answer for the question what is running away from the pulsar can be a moving wisp in the inner-torus. Assuming a geometry shown in Figure 6.6 (inner panel) in which the wisp is moving along the vector (c), we can evaluate the velocity of moving wisp as shown as a blue line labeled "(c)" in Figure 6.6. The lower limit of the velocity is $v_{\rm wisp} \sim 0.5c$, which seems consistent with the crab nebula in which wisps are moving at a velocity $\sim 0.45c$ (Mori, 2002).

The obtained velocity of the moving wisp is about twice the velocity calculated in §6.2. This discrepancy may be explained by the numerical study of the wind termination shock reported by Del Zanna et al. (2004); Bucciantini (2006). As shown in Figure 2.7, an anisotropic pulsar wind generate a oblate wind termination shock. Due to the oblate shape of the shock, the flow is slowed down to speed $\sim c/3$ close to the equator (region "C" in Fig. 2.7), which is consistent with the KC-model. However at higher latitudes, where the shock is oblique, the post shock flow is still super-fastmagnetosonic (region "B" in Fig. 2.7). As a result, the torus can have a double-layered structure: the inner part moves with speed $\sim c/3$, while the outer channels have velocity $\sim 0.5c$. So the wisp may be running along the outer channels.

A wave propagation in the torus also possesses a potential to provide an explanation for the moving wisp. Since the wisp is propagating radially from the central pulsar the wave should be exactly perpendicular to the toroidal magnetic field. In this case the fast-mode magnetosonic wave should be considered. In a relativistic plasma, the phase velocity of the fast magnetosonic wave $v_{\rm F}$ is expressed as

$$v_{\rm F} = \frac{\sqrt{c_{\rm s}^2 + v_{\rm A}^2}}{\sqrt{1 + v_{\rm A}^2/c^2}}, \tag{6.21}$$

where $c_{\rm s}$ is the sound speed ($0.58c$ for a relativistic gas). $v_{\rm A}$ is the Alfvén velocity defined as

$$v_{\rm A} = \frac{c}{\sqrt{1 + \left[4\pi(\rho c^2 + 4p)\right]/B^2}} \approx \frac{c}{\sqrt{1 + 16\pi U/3B^2}}, \tag{6.22}$$

where $p$ is the relativistic pressure, $U$ is the energy density of the relativistic plasma. For the equipartition condition the Alfvéen velocity amounts to $v_{\rm A} \sim 0.63c$. Then we obtained a velocity of fast mode magnetosonic wave $v_{\rm F} \sim 0.72c$, which is however unlikely faster than the observed wisp.

Finally we summarize the evaluated flow velocities for the inclination angles of $i = 30°$ and $50°$ in Table 6.2. This flow velocity within $\sim 30$ arcsec from the pulsar is consistent

with the velocity of $v_{\rm jet} = 0.6c$ reported by DeLaney et al. (2006), they measured the velocity at 1~2 arcmin from the pulsar with 3 yr baseline.

**What is moving ?**

There remains a question what is moving at a velocity of $\sim 0.7c$ in the jet region. This problem is essential to think about the energy budget of the jet. The possible answers for the question are: (1) a propagating wave, or (2) a physical motion of the pair plasma. As shown above, the fast magnetosonic velocity $v_{\rm F} \sim 0.72c$ is reasonable to explain the observed jet velocity.

The observed temporal changes can be also caused by the physical motion of the plasma, because several 2D relativistic MHD simulations predicted the existence of collimated out flow at a velocity of $0.4 \sim 0.7c$ (Komissarov and Lyubarsky, 2003; Del Zanna et al., 2004). In fact, Gaensler et al. (2002) reported the velocity estimation based on the Lorentz boost which yields to a $v_{\rm jet} \sim 0.5c$. Their results strongly support the hypothesis of the physical motion. In the next section we will consider this question in the spectroscopic point of view.

### 6.4.2 Spectral evolution along the jet

As shown above the photon index in the south jet moderately increases from 1.6 to 2.1 (see Table 6.1) along the flow line. Assuming a constant velocity of the jet $v_{\rm jet} = 0.7c$ corresponding to $\sim$ 12.7 arcsec yr$^{-1}$, it takes, however, only ~40 yr to travel from the pulsar to the cooled region (R $\sim$ 8 arcmin), because the observed flow speed was so fast. And such rapid cooling requires an unrealistic strong magnetic field of $B \sim 100\mu$G. In order to compare the cooling time and the dynamical time scale, we first calculate the magnetic field strength in the jet assuming the equipartition condition. For the calculation we adopted a cylindrical geometry with a length of 10 arcsec as an emitting volume. The diameter of the each cylinder corresponds to the width of the regions shown in Figure 4.13.

Table 6.2: Summary of the evaluations of the flow velocities

| Region | $i = 30°$ | $i = 50°$ | Note |
|---|---|---|---|
| South Jet | $0.74c$ | $0.73c$ | $\geq 0.72c$ |
| Wisp | $0.50c$ | $0.55c$ | $\geq 0.50c$ |
| Inner Torus | $0.43c$ | $0.29c$ | from *Lorentz* boost (See §6.2) |
| Outer Torus | $0.35c$ | $0.22c$ | from *Lorentz* boost (See §6.2) |

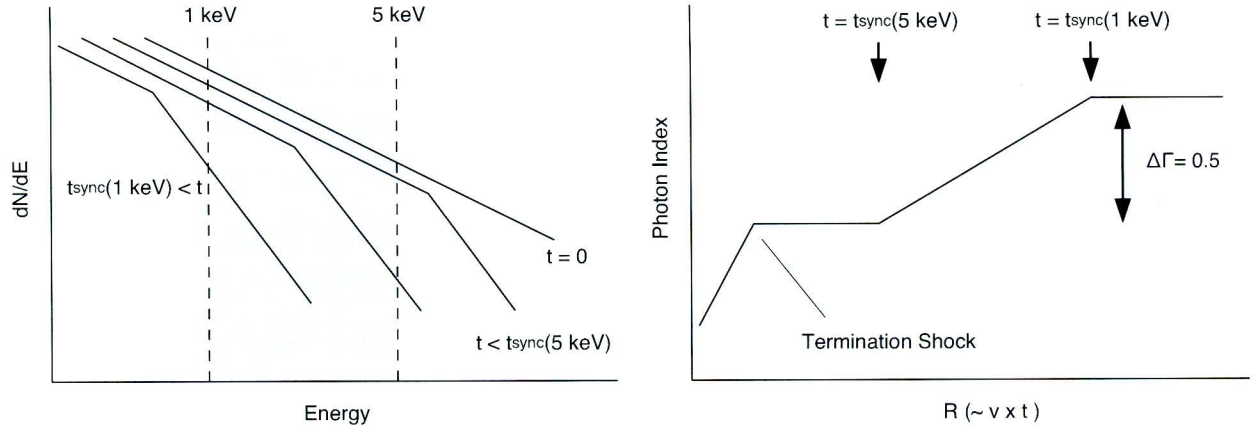


Figure 6.7: Schematic drawing describing a typical evolution of a power law spectrum (Left) and a corresponding photon index (Right).

The results are shown in Figure 6.8. The magnetic field variations are shown in the panel (a) and are decreasing as a function of radius. The highest field strength of $B \sim 70\mu$G are seen at $R = 30$ arcsec. At ~50 arcsec from the pulsar, the magnetic field drops down to $\sim 30\mu$G. The large fluctuation of the magnetic field at $R = 50 \sim 100$ is caused by the large uncertainty of the photon index. Finally the magnetic field settles down at $20\mu$G.

The life time of the electrons emitting at 1 keV in a magnetic field of $B = 50\mu$ G is

$$t_{\rm sync} \sim 160 \left(\frac{B}{50\ \mu{\rm G}}\right)^{-3/2} \left(\frac{\epsilon}{1\ {\rm keV}}\right)^{-1/2} \quad {\rm yr} \tag{6.23}$$

which is three times larger than the time scale of the flow $t_{\rm flow} \sim 50$ yr. Another curious profile was found, it seems that the photon index evolved "linearly" as a function of radius (or distance) from the pulsar. If recently accelerated electrons are supplied into the jet, the photon index plot should show a plateau feature with a constant photon index of $\sim 1.5$ at the beginning, and then it should increase after $t_{\rm sync}$ as shown in Figure 6.7. However the obtained spectra do not show the expected evolution with plateau feature as seen in the NE-torus (Fig. 4.11). This result may imply that the synchrotron electrons are already partially cooled at the root of the jet, although the initial photon index coincides with that in the torus because the break energy is slightly higher than the observed energy band.

If this is the case, we can constrain the slope of the photon index. Adopting the change in the spectral index of $\Delta\Gamma = 0.5$ that is expected by the synchrotron cooling (Kardashev, 1962), the slope of the spectral index can be written as

$$\frac{d\Gamma}{dr} = \frac{\Delta\Gamma}{\Delta t\ v_{\rm jet}} = \frac{0.5}{(t_{\rm sync,1keV} - t_{\rm sync,5keV})\ v_{\rm jet}} \tag{6.24}$$

$$= 4.7 \times 10^{-4} \left( \frac{B}{50\ \mu\mathrm{G}} \right)^{3/2} \left( \frac{v_{\mathrm{jet}}}{12.7\ \mathrm{arcsec\ yr^{-1}}} \right)^{-1} \quad \mathrm{arcsec^{-1}}. \tag{6.25}$$

Although there still remains a large uncertainty in the magnetic field (here we have roughly assumed a constant value of $B \sim 50\mu$G), which, however, seems to agree well with the observed value of $\Delta\Gamma/\Delta r \sim 1 \times 10^{-3}$ arcsec$^{-1}$. At the same time, the hypothesis of the partially cooled flow permits the jet to have a velocity of $v_{\mathrm{jet}} \sim 0.7c$.

### 6.4.3 Energy budget

Next, we consider the energy presents in the jet. Panel (b) in Figure 6.8 indicate the internal energy present in cylindrical region with a length of 10 arcsec. At the origin, the jet has a energy of $4 \times 10^{43}$ ergs within a 10 arcsec long region. Adopting a flow velocity of 11 arcsec yr$^{-1}$, we find an energy injection of $L_{\mathrm{jet}} = 1.4 \times 10^{36}$ ergs s$^{-1}$ into the jet, which corresponds to 7.8% of the total spin down luminosity of $\dot{E} = 1.8 \times 10^{37}$ ergs s$^{-1}$. The obtained injection rate is rather large, because the above estimation accounts only for the emitting matter. Moreover there is the counter jet, which should have the same amount of energy as the south one. Thus the pair of jets require at least ~15 % of the total spin down energy. Although this injection rate is much larger than that from past observation ~0.5 % for the south jet was reported by Gaensler et al. (2002) (they assumed a smaller flow veocity).

The internal energy seems to be increasing along the jet. If there are no extra energy injection mechanism or particle acceleration, this tendency indicates the deceleration of the jet. For the changes of internal energy from $4 \times 10^{43}$ to $6 \times 10^{43}$ (at $R \sim 150$ arcsec), a decelerated velocity of $v_{\mathrm{jet}} \sim 0.5c$ is expected. The obtained velocity at the downstream agrees with the preceding observations made by DeLaney et al. (2006). The obtained weak deceleration is obviously different from that of torus. Note that the above calculation did not consider the energy loss via synchrotron radiation, thus the obtained deceleration is only a lower limit.

## 6.5 Comparing with theoretical models

First of all we must point out that the structure of the south jet at the pulsar vicinity is remarkably different from that seen in the crab. Figure 6.9 compares the structures of the jet just around the pulsars, PSR B1509−58 (left) and the crab (right). In case of the crab nebula, the jet seems to sprout out from the pulsar directly. Even *Chandra* cannot resolve the origin of the jet. While the jet of PSR B1509−58 has a broad base

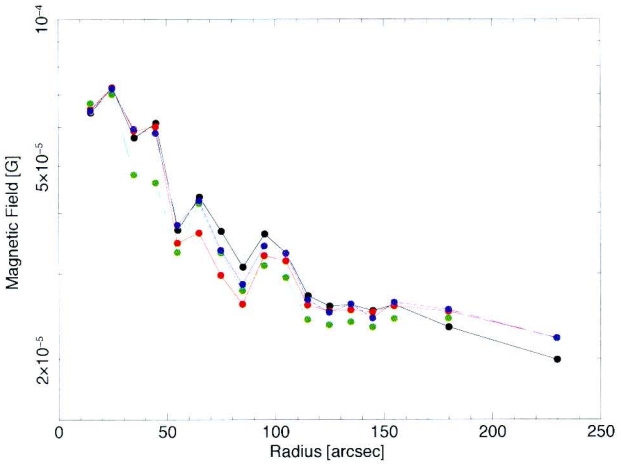


(a) Magnetic Field

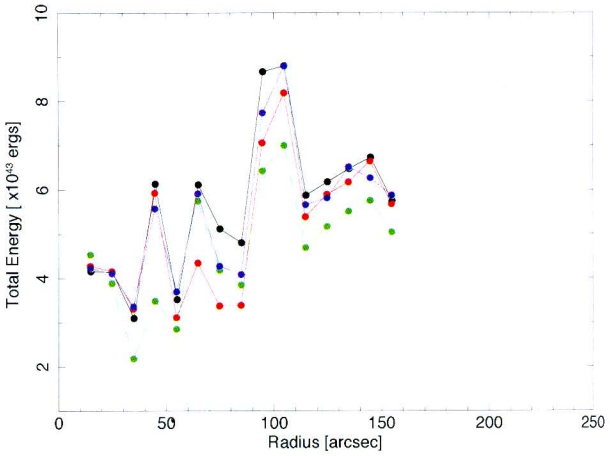


(b) Total energy in the region

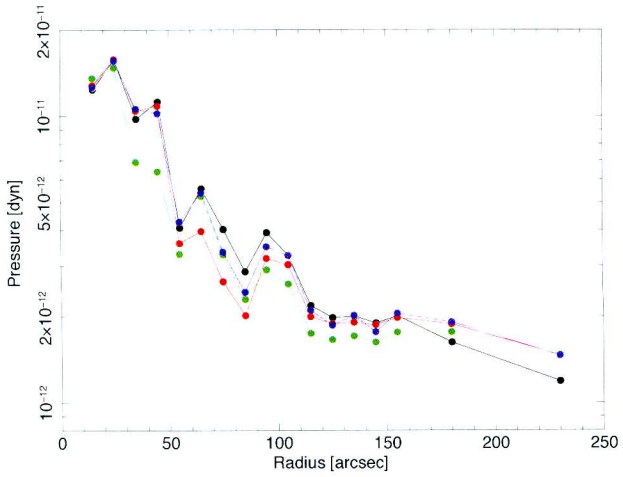


(c) Pressure

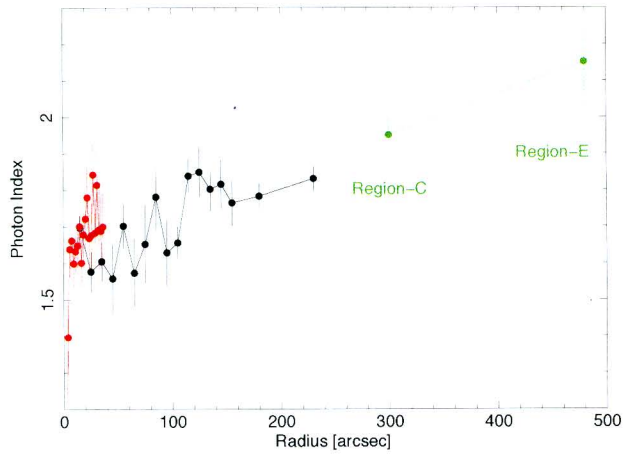


(d) Photon Index

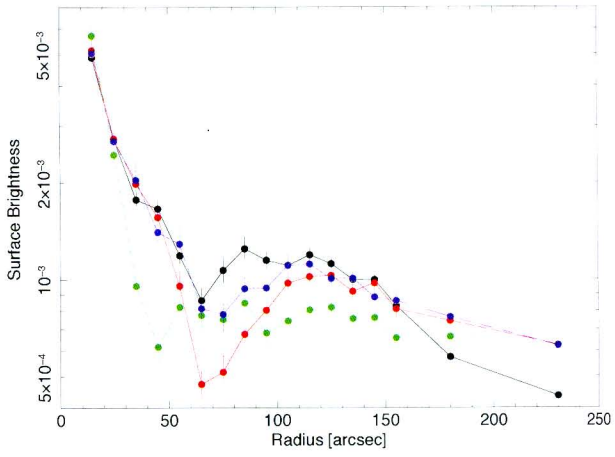


(e) Surface brightness

Figure 6.8: The magnetic field (a), the internal energy (b) and the pressure (c) in the south jet obtained from the equipartition argument. For comparison, the photon index and the surface brightness are also shown at the bottom. The internal energies are calculated only for the regions within 150 arcsec from the pulsar.

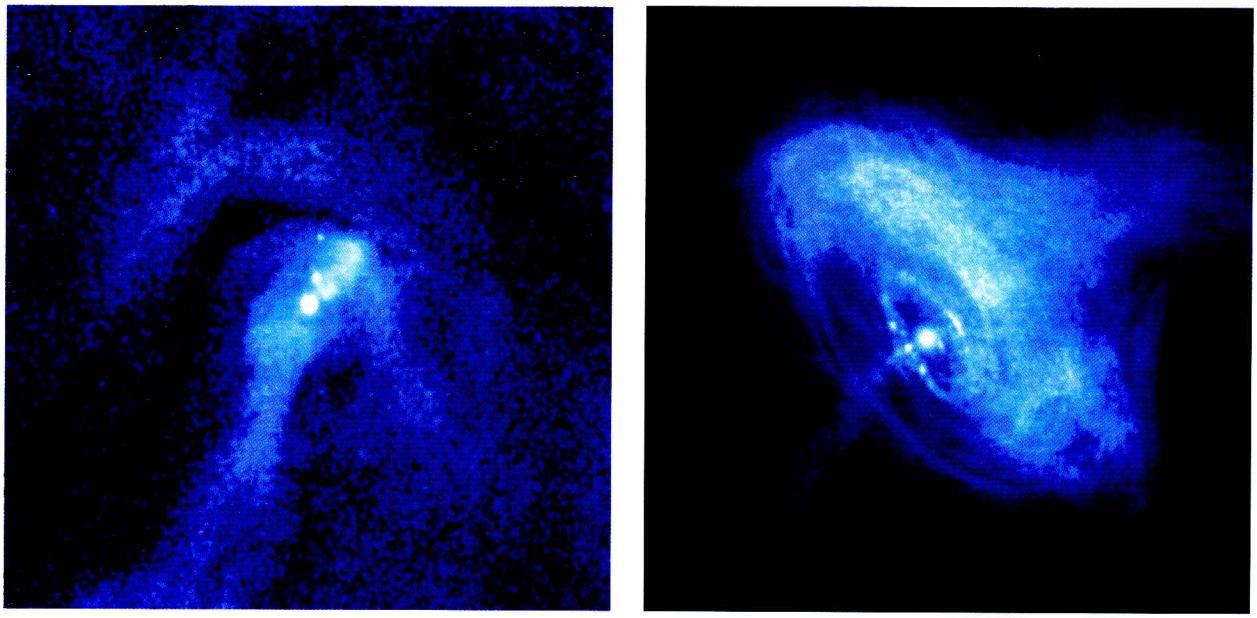

Figure 6.9: Comparison of the structure of the jets of PSR B1509−58 (left) and that of crab (right).

with a radius of $\sim$ 10 arcsec. Also the jet is itself broad and brighter than its torus. As argued in §6.3, the ring feature should be the wind termination shock, the south jet of PSR B1509−58 may flow out from the vicinity of the shock front or from the inner-torus, namely the post shock region.

The observed appearance of the base of the jet from PSR B1509−58 seems to match the theoretical model suggesting that the hoop stresses in the pulsar wind collimates the poloidal flow (§2.3). This model is of course introduced for the crab nebula. However it is difficult to explain the jet in the Crab nebula because the self-collimation process in ultra-relativistic flow neaby the pulsar is extremely ineffective.

In contrast, in the down stream of the shock, the hoop stress is believed to be able to squeeze the "mildly relativistic" flow towards the rotating axis. The observed features are indicating that this model can be applied to PSR B1509−58.

Now we can compare the observed morphology with the recent relativistic MHD simulations which take into account the hoop stress. Especially Del Zanna et al. (2004) provided the detailed images of pulsar jet for various configurations. They argued that a comparatively large magnetization parameter of $\sigma > 0.01$ is required to generate jets.

On the other hand, we have detected and identified the inner ring and the torus in the PWN of PSR B1509−58. Consequently a constraint on the magnetization parameter of $\sigma > 0.01$ was yielded based on the apparent features, showing a good agreement with the simulations by Del Zanna et al. (2004).

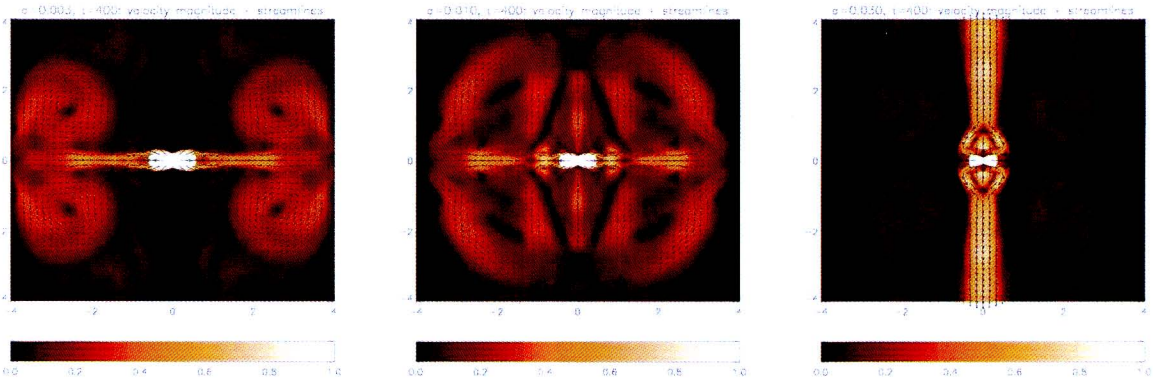

Figure 6.10: 2D relativistic MHD simulations for the wind magnetization parameters of $\sigma = 0.003$ (left), 0.01 (center), and 0.03 (right) by Del Zanna et al. (2004). The pulsar's magnetic dipole is assumed to be aligned with the rotation axis. Gray scale and vectors indicate velocity magnitudes and streamlines, respectively.

Figure 6.10 shows the results of 2-D RMHD simulations for various magnetization parameters by Del Zanna et al. (2004). PSR B1509−58 seems to have intermediate properties between the magnetization of $\sigma = 0.01$ and 0.03. Here we enumerate the points of agreement:

1. broad based jet from the post shock region ($\sigma = 0.03$).
2. thick torus with a small radius ($\sigma = 0.01$).
3. jet velocity of $v_{\rm jet} = 0.7c$.

These simulations describe complicated streamlines around the root of jet, indicating that the jet originated in the equatorial flow diverted by the hoop stress. If the simulations is true the rapid cooling along the jet can be explained by the equatorial flow which must be cooled in the inner-torus. Figure 6.11 schematically describes the scenario. Blue dashed lines on the left panel indicate the region where we have analysed. The corresponding photon index evolutions are shown in (a) and (b). Most of energies of the rotating power is thought to be ejected into the equatorial plane and then a part of them are squeezed by the hoop stress toward the rotating axis. Thus the root of the jet should be already partialy cooled. We therefore argue that the jet of PSR B1509−58 may be originated in diverted equatorial flow.

By the way, the crab also possesses jets. According to the numerical simulations, a jet requires a magnetization of $\sigma > 0.01$, larger than the classical predictions. Actually Mori et al. (2004) reported a magnetization of $\sigma \sim 0.03$, which actually satisfies the condition.

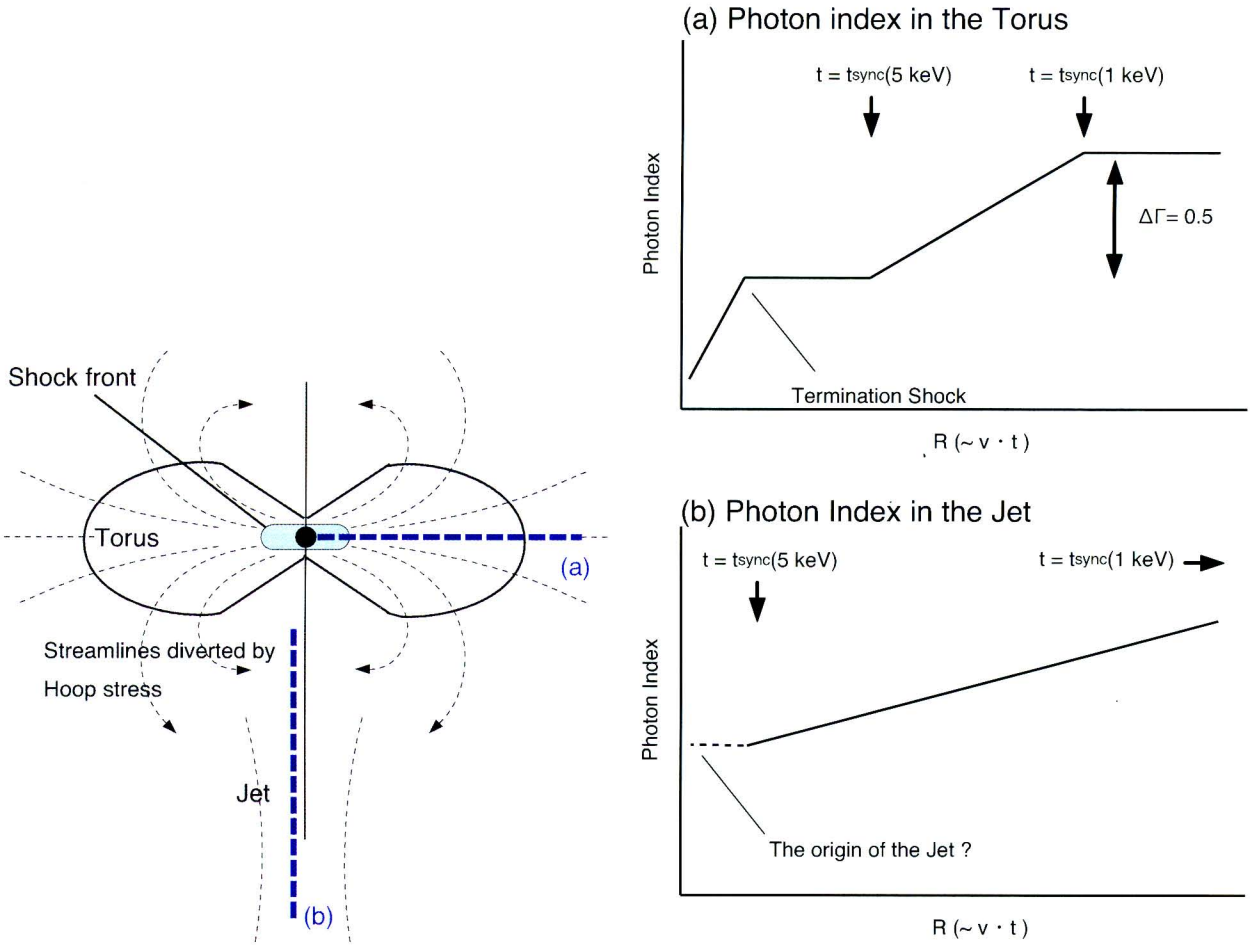


Figure 6.11: Schematic view of the stream lines near around the pulsar (left) and corresponding spectral indexes along the line (a) and (b).

Now a question arises why those two PWNe are obviously different. At this moment it is difficult to find the answer, however, the above 2D simulation provided a hint. The simulations in Figure 6.10 assumed of a magnetic dipole aligned with the rotating axis (a perfectly aligned magnetic rotator). In order to suit the results to the crab, namely to put the jet closer to the pulsar, the equatorial magnetic field were suppressed. For this purpose, a dipole field were inclined and the jets successfully got closer to the pulsar (see Del Zanna et al. (2004)). In fact the magnetic dipole can be misaligned with the rotating axis. Although the mechanism that vanishes the equatorial magnetic fields is still unclear, the vanishment can be correlated with the twist angle between the magnetic dipole and the rotating axis. One suggested that the twist angle may be constrained by the breaking index(Thompson et al., 2002). So there may be some relations between the braking indexes and the morphology of the jet.

# RCW 89

van den Bergh and Kamper (1984) have shown that the optical filaments in MSH 15−52 are not moving significantly. In contrast, our X-ray observation revealed that the X-ray emitting regions are moving at $\sim$ 4200 km s$^{-1}$. In this chapter we consider the detected proper motions of RCW 89.

## 6.6 Proper motion of RCW 89

As shown in Figure 5.8, each emitting region seems to be running away in the opposite direction of the pulsar, though there remains an uncertainties from the roll angle correction. To confirm the relationship between the pulsar and the proper motion of RCW 89, we calculated the travel time of the each emitting region from the pulsar to the current location assuming a constant velocity, so that the obtained value can be only an upper-limits of the travel time. The calculated travel times of 11 individual plasma clumps are shown in Table 5.4. The obtained travel times are concentrated in a range from 1000 to 3000 yr except for three knots labeled "c", "d", and "e" lying on the south edge of RCW 89. The mean value of the travel times is $1730 \pm 220$ yr, which is almost the same as the characteristic age of the pulsar 1700 yr. This remarkable coincidence in the time scales strongly implies a relationship between the pulsar and RCW 89. This observational result requires an extreme low number density of surrounding ISM, smaller than 0.1 cm$^{-3}$ as claimed by Seward et al. (1983).

Here we want to resolve an open question: what is moving at a velocity of $\sim$4200 km s$^{-1}$ ? There are two possible interpretation. One is that the X-ray emission of RCW 89 is from the fast expanding SN ejecta, and the other is the proper motion represent only the propagation of the shock front which heat the existing ISM. In past, van den Bergh and Kamper (1984) reported that the optical filaments were not moving in their 6 yr base-line optical observation. This result can be reconciled with our X-ray observation if the latter interpretation of the propagation model is adopted.

## 6.7 Redshift variation in RCW 89

### 6.7.1 Radial velocity from the redshift

To resolve that question the Doppler shift may provide decisive information. In Yatsu et al. (2005), we claimed that the Doppler shift of the plasma clump in RCW 89 is significantly different each other based on the ACIS-I spectroscopy. However we could not determine the Doppler shift precisely using *Chandra* observation (ID5562) caused by the energy resolution degradation. Then we checked another X-ray observation with *XMM-Newton* on 2005 September, and detected a non-uniformity of the redshift in the vicinity of RCW 89 as shown in Figure 5.5. The radial velocity of an object can be expressed as a function of its redshift,

$$z_{\rm i} + 1 = \sqrt{\frac{1+\beta_{\rm i}}{1-\beta_{\rm i}}}, \tag{6.26}$$

where $z_{\rm i}$ is a redshift of a plasma cloud labeled "i" and $\beta_{\rm i}$ is a radial velocity in units of the light speed $c$. For the case of small redshifts $|z| < 10^{-2}$, the radial velocity yields to an approximal relation

$$v_{\rm rad,i} \approx 300 \times \left(\frac{z}{10^{-3}}\right) \quad {\rm km\ s^{-1}}. \tag{6.27}$$

Therefore we obtained a peak-to-peak velocity differential of $\sim 3400$ km s$^{-1}$ based on the spectral fitting with NEI-model (corresponding to square data series in Figure 5.5).

### 6.7.2 Model dependence of the redshift

The centroid energy of a line emission from a plasma nebula varies with its temperature; as the temperature rises, the centroid energy of an emission line shifts higher. If the measured plasma temperature is overestimated, the resultant redshift will be smaller than the true value. Actually the temperature of knot-5 and 7 based on NEI-model were apparently higher than that based on MEKAL-model, and then the resultant redshifts of them based on NEI-model are smaller than that based on MEKAL-model.

It is difficult to determine which model is more applicable, NEI or MEKAL, however, the ranges of the radial velocity dispersions from the NEI-model and that from the MEKAL-model give an upper limit and a lower limit, respectively. It is therefore inferred that the radial velocity dispersion is at least 2200 km s$^{-1}$, which is based on MEKAL-model with fixed $N_{\rm H}$ and $\Gamma$.

According to these results, the proper motion of $\sim 4200$ km s$^{-1}$ observed in RCW 89 can be explained by the physical motions of plasma clouds rather than the propagating shock front.

## 6.8 Geometry of RCW 89

### 6.8.1 Reconstruction of 3D geometry

The 3-dimensional geometry of RCW 89 can be estimated assuming that the plasma clouds are lying on a shell with a radius of $R$ expanding at $v_{\rm shell}$. A schematic image of the model is shown in Figure 6.12. For $v_{\rm shell} = 5000$ km s$^{-1}$ and $R \sim 7$ arcmin, which corresponds to $3.2 \times 10^{19}$ cm, we can estimate the position along the line of sight, $Z_{\rm i}$ as

$$Z_{\rm i} = R\frac{v_{\rm rad,i}}{v_{\rm shell}} \tag{6.28}$$

$$= 1.7 \times 10^{18} \left(\frac{R}{7\ \text{arcmin}}\right)\left(\frac{z_{\rm i}}{10^{-3}}\right)\left(\frac{v_{\rm shell}}{5000\ \text{km s}^{-1}}\right)\left(\frac{d}{5.2\ \text{kpc}}\right) \quad \text{cm}. \tag{6.29}$$

Figure 6.13 shows the 3-dimensional position of the each plasma knot plotted on $X$(R.A.)-$Z$(Depth) and $Y$(Dec)-$Z$(Depth) planes. Note that the SNR system is approaching us at $\sim$ 70 km s$^{-1}$ due to the rotation of the Galaxy, however, the systematic velocity is negligibly small comparing with the radial velocity caused by the local proper motions.

### 6.8.2 Constraint on the inclination angle

As shown in Figure 6.13 RCW 89 seems to be lying in the direction perpendicular to the line-of-sight from the pulsar. If RCW 89 is lying on the terminus of the jet, the inclination angle of the spin axis should be $i \sim 90°$. However this result is inconsistent with the visibility of the torus which should be on the equatorial plane, from which Gaensler et al. (2002) obtained an inclination angle of $i \sim 30°$. While, on the other hand, we also obtained $i \sim 50°$ from the appearance of the inner ring. The obtained 3-D geometry still contains large uncertainties, such as a gain offset or a galactic rotation. It is therefore difficult to obtain strong constraint on the inclination angle from the above results. However, the velocity differential along line of sight ($\Delta v_{\rm rad} \geq 2200$ km s$^{-1}$) seems to be reliable.

Using the inclination angle $i$ between the pulsar spin axis and the line of sight and the opening angle $a$ of of the jet, the apparent radial velocity $v_{\rm rad}$ is described as

$$v_{\rm rad,max} = v_{\rm shell} \cos(i - a) - v_{\rm gal}, \tag{6.30}$$

$$v_{\rm rad,mix} = v_{\rm shell} \cos(i + a) - v_{\rm gal}, \tag{6.31}$$

where $v_{\rm gal}$ is the systematic radial velocity due to the galactic rotation. Using equation 6.30 and 6.31 gives a relation

$$v_{\rm shell} = \frac{\Delta v_{\rm rad}}{2 \sin i \sin a}, \tag{6.32}$$

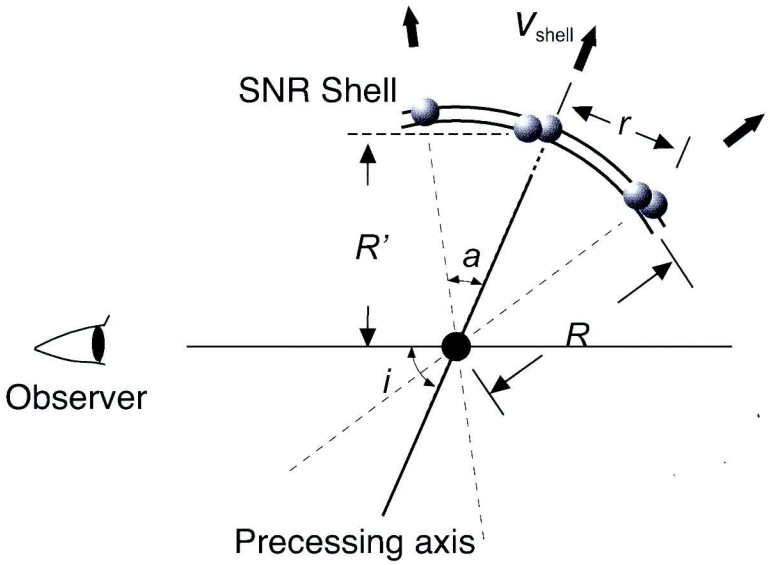


Figure 6.12: Schematic drawing of the geometry of the pulsar and RCW 89.

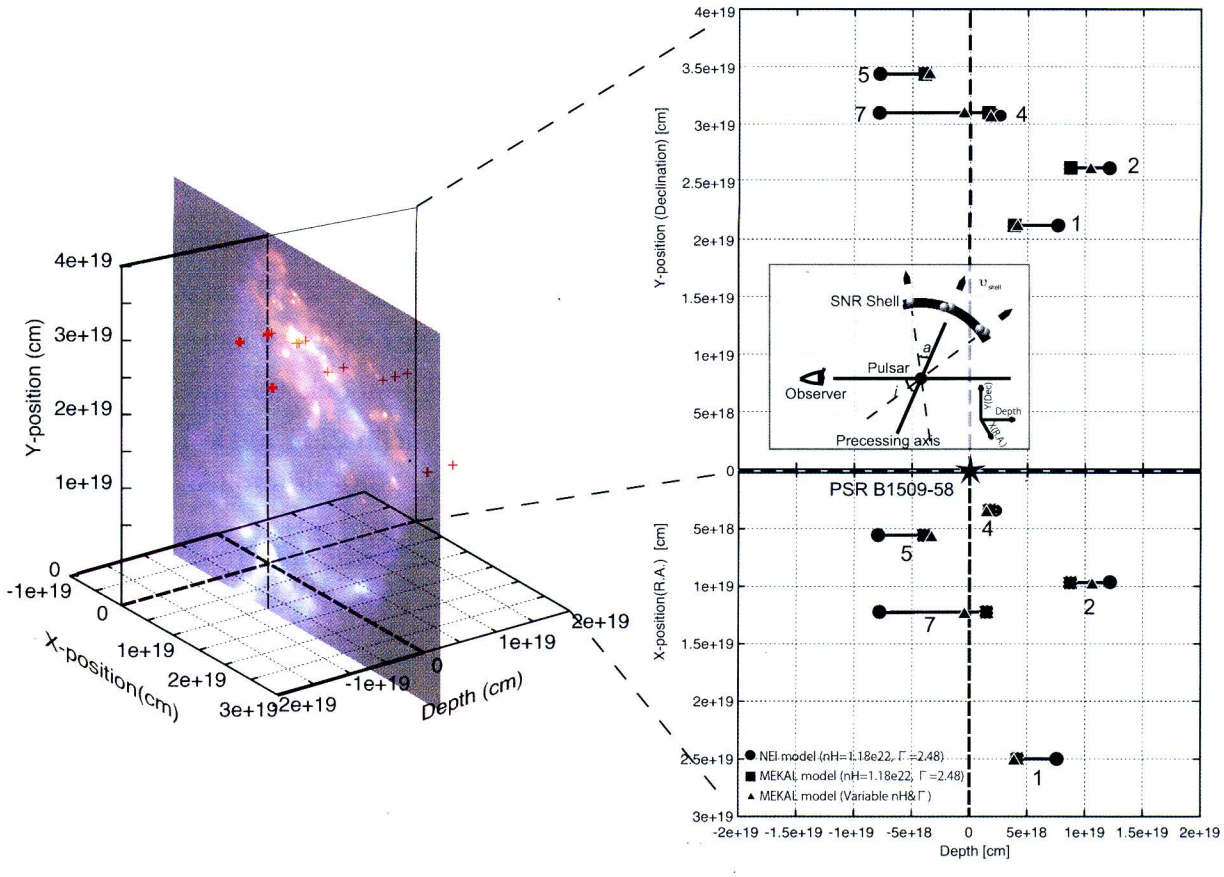


Figure 6.13: 3-dimensional position of plasma blobs in RCW 89, plotted on Dec-Depth plane (Upper panel) and on R.A.-Depth plane (Lower panel).

where $\Delta v_{\rm rad} = v_{\rm rad,max} - v_{\rm rad,min}$. Now we know $\Delta v_{\rm rad}$ is in a range from 2200 to 3400 km s$^{-1}$ from the redshift measurements of RCW 89, while the radial component of the proper motion from the pulsar, $v_{\rm trans} \sim 0.17$ arcsec yr$^{-1}$, constrains the expanding velocity of the shell $v_{\rm shell}$ as

$$\begin{aligned} v_{\rm shell} &= \frac{v_{\rm trans}}{\sin i} \\ &= \frac{4.2 \times 10^3}{\sin i} \left( \frac{d}{5.2 \text{ kpc}} \right) \left( \frac{v_{\rm trans}}{0.17 \text{ arcsec yr}^{-1}} \right) \quad \text{km s}^{-1}. \end{aligned} \tag{6.33}$$

The opening angle $a$ is obtained from the observable parameters of the radius of RCW 89 $r$ and the apparent distance from the pulsar to RCW 89 $R'$ as

$$\sin a = \frac{R'}{r} \sin i. \tag{6.34}$$

Combining equation (6.32), (6.33) and (6.34) yields the relation of the distance $d$ and the inclination angle $i$ as

$$\left( \frac{d}{5.2 \text{ kpc}} \right) = \frac{1}{2 \sin i} \left( \frac{\Delta v_{\rm rad}}{4200 \text{ km s}^{-1}} \right) \left( \frac{R'}{r} \right) \left( \frac{v_{\rm trans}}{0.17 \text{ arcsec yr}^{-1}} \right)^{-1}. \tag{6.35}$$

Figure 6.14 describes the accepted range of the inclination angle according to the above equation with an assumption of $R'/r \sim 2$. Blue line and red line describe the allowable ranges of the inclination angle for $\Delta v_{\rm rad} = 3400$ km s$^{=1}$ based on NEI-model and $\Delta v_{\rm rad} = 2200$ km s$^{=1}$ based on MEKAL-model, respectively. The figure indicates that the inclination angle is in a range from 25° to 45° in case of $\Delta v_{\rm rad} = 2200$ km s$^{-1}$ (MEKAL-model). This result agrees well with the inclination angle of $i \sim 30°$ reported by Gaensler et al. (2002). While on the other hand, if we adopt NEI-model, the inclination angle becomes larger, $i \geq 40°$, which seems to be fit with the inclination angle $i \sim 53°$ based on the appearance of the inner ring of the pulsar.

Note that the above constraints on the inclination angle are only rough estimations because this contour map describing allowable range does not consider the uncertainties from $R'/r$ and $v_{\rm trans}$. Nevertheless the observed proper motions and the redshift variation in RCW 89 are well explained by the isotropic expansion from the pulsar. The large expanding velocity $v_{\rm shell} \geq 4200$ km s$^{-1}$ can account for the discrepancy between the age of the pulsar and the SNR, namely the actual age of the SNR should be young as well as the pulsar is. Therefore the discovery of the proper motions can be an observational proof of the physical association between the pulsar and the SNR. At this moment it is still unclear why the optical filaments in RCW 89 are not moving. For this problem further radio, optical and X-ray observations are expected.

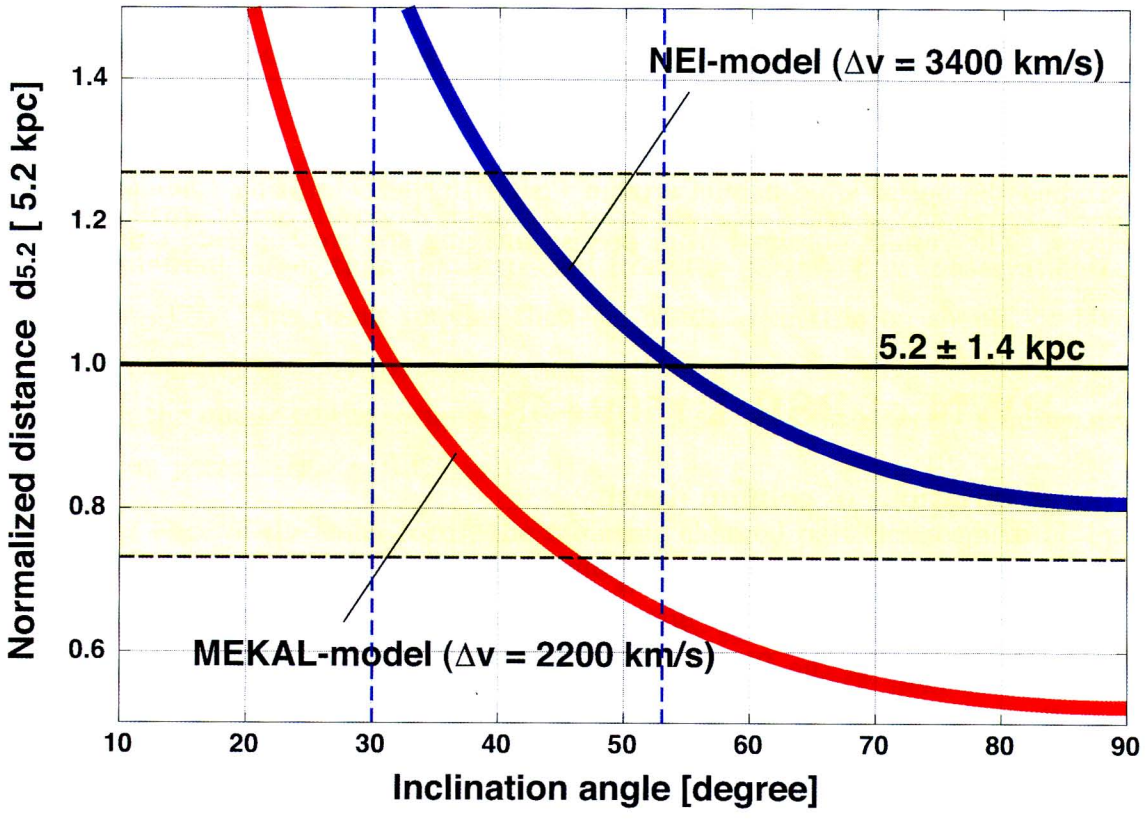


Figure 6.14: Allowable range of the inclination angle. Blue and red lines describe the allowable ranges of the inclination angle for $\Delta v_{\rm rad}$ = 3400 km s$^{=1}$ based on NEI-model and $\Delta v_{\rm rad}$ = 2200 km s$^{=1}$ based on MEKAL-model, respectively. This figure does not consider the uncertainties of $R'/r$ and $v_{\rm trans}$.

# Chapter 7

# Conclusion

We studied the pulsar wind nebula around PSR B1509−58 utilizing *Chandra* X-ray observatory. The results obtained from precise imaging spectroscopy are summarized as follows:

## 7.1 PWN of PSR B1509−58

### (1) Local variations of column density

We discovered variations of hydrogen column density around SNR G320.4−01.2, therefore X-rays from the PWN are partly absorbed. These absorption features are remarkably seen in western edge of the PWN, at which the nebula pressure is balancing with the surrounding medium. The pressure balance condition and the column density variation imply a number density of $n_{\rm ISM} = 10 \sim 100$ cm$^3$, which corresponds to a typical number density of HI region. Considering past radio observations, discovered dense ISMs may be correlate with the HI regions on the direction of G320.4−01.2.

### (2) Discovery of the wind termination shock

A ring feature which seems to coincide with a wind termination shock was discovered. The radius of the ring is about $R_{\rm TS} \sim 10$ arcsec, corresponding to $7.8 \times 10^{17}$ cm for a distance of 5.2 kpc. The X-ray synchrotron luminosity around the ring feature implies that the ram-pressure of the pulsar wind and the inner pressure of the nebula are balancing at the ring. We therefore conclude that the ring feature can be analogous to the inner ring seen in the Crab nebula. We also obtained an inclination angle of spin axis $i \sim 53°$ based on the ellipticity of the ring.

The shock radius provided a constraint on a wind magnetization of $\sigma \geq 0.01$, which is

much larger than that predicted by KC-model. However this large magnetization can explain the observed large flow velocity in the X-ray inner-torus and the rapid spectral evolution as mentioned below.

### (3) The double tori

The PWN around PSR B1509−58 possesses nested double tori structure, the inner-torus ($R < 30$ arcsec) and the outer-torus ($R > 30$ arcsec). From the viewpoint of spectroscopy, the inner-torus, in which the spectral photon index is constant at $\Gamma = 1.6$, seems to be a counterpart of the X-ray torus seen in the Crab nebula.

**Inner torus:** Adopting the inclination angle of $i \sim 53°$, the X-ray intensity ratio between the south side and the north side of the torus provides a flow velocity of $v_{\rm flow} \sim 0.29c$, which is somewhat larger than that expected from the particle flux conservation law of $v_{\rm flow} \propto (r/r_{\rm TS})^{-2}$. This result implies that the wind magnetization should be large as obtained. Adopting the flow velocity of $v_{\rm flow} \sim 0.29c$ yields the time taken for particles to flow from the pulsar to the torus, $t_{\rm flow} \sim 8.5$ yr. The fast flow velocity requires a large magnetization parameter $\sigma \sim 0.1$.

At the outer edge of the inner-torus, the radiating charged particles seem to be burned out and then the photon index gets steeper. If the energy dissipation of the particles are only due to synchrotron radiation, an abnormally strong magnetic field of $\sim 200\mu$G is required, while the equipartition argument provides a magnetic field of $B \sim 30\mu$G at $r \sim 30''$.

From a temporal analysis we discovered a moving wisp from the termination shock to the outer edge of the inner-torus. For the inclination angle of $i \sim 53°$ we obtained a velocity of $\sim 0.5c$, which is somewhat larger than the bulk velocity obtained from the *Lorentz* boost. This moving wisp can be interpreted as a propagation of magnotosonic wave or an actual fast magnetosonic stream originated in the oblique shock at the higher latitude region.

**Outer torus:** In the outer-torus ($30'' \leq r \leq 60''$) the photon index increases as a function of radius. The X-ray luminosity of the outer-torus provides equipartition magnetic field of $B \sim 10\mu$G, which corresponds to the magnetic field of the entire nebula $\sim 8\mu$G. The obtained weak magnetic field could not explain the brightening at the outer torus under the constant number density condition.

The X-ray intensity ratio between the south edge and the north edge of the outer-torus can be explained by the Lorentz boost with assumptions of a flow velocity of $v_{\rm flow} \sim 0.22c$ and an inclination angle of $i = 53°$.

### (4) the Jets

By comparing a series of four *Chandra* observations from 2004 to 2005, we obtained a flow velocity in the south jet $v_{\rm jet} \sim 0.7c$, which is consistent with past observations. Because of the large Lorentz boost, the apparent temporal changes seem to be physical motions of the plasma. Based on the equipartition argument, the energy injection rate into the south jet amounts to 7.8 % of the total spin-down luminosity for a flow velocity of $v_{\rm jet} \sim 0.7c$. On the other hand, the spectral evolution along the streamline is faster than that expected from an equipartition condition. Therefore it is difficult to explain the rapid cooling by a simple scenario in which recently accelerated particles are injected into the south jet directly.

The root of the south jet extends beyond the termination shock, obviously different from the jet in the Crab nebula. This appearance of the broad based jet resembles a scenario of collimation of jets beyond the termination shock (Lyubarsky, 2002). In fact, recent 2-D relativistic MHD simulations succeeded in forming a poloidal flow by the magnetic hoop stress which diverts the equatorial flow towards the poloidal direction. The self collimation process requires somewhat highly magnetized wind, which is consistent with the obtained magnetization of $\sigma \geq 0.01$. If the axisymmetric jets were made from the back flow diverted from the torus, the observed rapid spectral evolution could be explained by the synchrotron cooling in the torus.

## 7.2 RCW 89

### (1) Detection of proper motion

Proper motions of the individual knot in RCW 89 were discovered by the *Chandra* observations with 4.3 yr base line. The obtained vector map indicated that RCW 89 is expanding radially from the central pulsar. The averaged velocity of radial components amounts to $4200 \pm 500$ km s$^{-1}$. The mean value of the travel time from the pulsar to the current position of RCW 89 is $1730 \pm 220$ yr, which is almost the same as the characteristic age of the pulsar 1700 yr. The coincidence in the time scale implies a relationship between the pulsar and RCW 89.

### (2) Redshift variation

From the spectral analysis of *XMM-Newton* observation, we detected a significant redshift variation in RCW 89 vicinity. This results indicate that a velocity differential of $\geq 2200$ km s$^{-1}$ exists in RCW89. According to this result, the proper motion of $\sim 4200$ km s$^{-1}$ can be explained by the physical motions of plasma clouds rather than the propagating shock front.

### (3) 3-dimensional geometry

Based on the 2-dimensional velocity information, we reconstructed the 3-dimensional geometry of RCW 89 assuming that the plasma clouds are lying on the uniformly expanding SNR shell. And we confirmed that RCW 89 is extended over $\sim$ 10 pc along the line-of-sight. Moreover we constrained the inclination angle of the jet axis of the pulsar. Assuming the same geometrical condition as the above yielded allowable ranges of the inclination angle $25^\circ \leq i \leq 45^\circ$ based on MEKAL model and $i \geq 40^\circ$ for NEI model. The observed proper motions and the redshift variations in RCW 89 are well explained by the isotropic expansion of plasma, which is probably an SN ejecta, from the pulsar. The large proper motion of 4200 km s$^{-1}$ can account for the discrepancy between the age of the pulsar and the SNR. Therefore the discovery of the proper motion can be the first observational proof of the physical association between the pulsar and the SNR.

# Appendix A

# Synchrotron Emission

## A.1 Synchrotron Energy loss

Synchrotron radiations are originated in relativistically gyrating electrons in a magnetic field. When a particle with charge $q$ is accelerated by $\dot{u}$, the charged particle radiates electromagnetic waves and loses their kinetic energy. The emissivity is described by *Larmor's formula*;

$$P = \frac{2q^2\dot{u}^2}{3c^3} \tag{A.1}$$

For the synchrotron radiation, we apply the *Larmor's formula* to a gyrating charged particle at a frequency of $\omega_B = \frac{qB}{\gamma mc}$. Using the Liènard-Wiechert potentials yields synchrotron energy loss rate,

$$-\left(\frac{dE}{dt}\right) = 2\sigma_T c U_B \gamma^2 \beta^2 \sin^2\theta, \tag{A.2}$$

where $\sigma_T$ is the Thomson cross section $6.65 \times 10^{-25}$ cm$^{-2}$, $c$ is the light speed, $U_B$ is a magnetic energy density, $B^2/4\pi$, $\beta$ is a velocity of the gyration motion, and $\theta$ is a pitch angle between the magnetic field and the direction of acceleration.

Assuming an isotropic distribution of pitch angles, we can averaged over the synchrotron emissivity, yielding

$$-\left(\frac{dE}{dt}\right) = \frac{4}{3}\sigma_T c U_B \gamma^2 \beta^2 \sin^2 \tag{A.3}$$

$$= 1.058 \times 10^{-15} B^2 \gamma^2 \beta^2 \quad \text{ergs s}^{-1}. \tag{A.4}$$

This is the averaged energy loss rate by synchrotron radiation for single charge.

## A.2 Power spectrum of synchrotron

The power spectrum of synchrotron radiation from a single charge strongly depends on its *Lorentz* factor $\gamma$. It is because the radiation at a specific frequency which depends on the gyro-frequency is selectively intensified by the *Lorentz* beaming.

The emission spectrum of a single electron can be described as a function of gyration frequency of $\omega$,

$$P(\omega) = \frac{\sqrt{3}q^3 B \sin\theta}{2\pi m_e c^2} F\left(\frac{\omega}{\omega_c}\right), \tag{A.5}$$

where $\omega_c$ is the critical frequency given by $\frac{3\gamma^2 qB\sin\theta}{2m_e c}$. The function $F(x)$ describing the power spectrum of synchrotron emission is calculated by Abramowitz and Stegun (1965). Asymptotic forms of $F(x)$ for small and large values of $x$ are:

$$F(x) \sim \frac{4\pi}{\sqrt{3}\Gamma(1/3)}\left(\frac{x}{2}\right)^{1/3}, \quad (x \ll 1), \tag{A.6}$$

$$F(x) \sim \left(\frac{\pi}{2}\right)^{1/2} e^{-x} x^{1/2}, \quad (x \gg 1). \tag{A.7}$$

As the function $F(x)$ gives the maximum value at $x = 0.29$, the spectrum of synchrotron from a single charge has a peak flux at a frequency of $\omega = 0.29\omega_c$. Thus we obtain an unique relationship between the typical synchrotron frequency $\nu_{sync}$ between the parameters of the source,

$$\nu_{sync} = 0.29 \times 2\pi/\omega_c \tag{A.8}$$

$$= 1.22 \times 10^6 \gamma^2 B \quad \text{Hz}. \tag{A.9}$$

## A.3 Cooling time scale

As shown above, an electron in a magnetic field will lose its energy by the synchrotron radiation. Dividing the kinetic energy of the electron by the energy loss rate Eq. A.3 yields the typical time-scale of synchrotron burn-off as

$$t_{cool} = \frac{3m_e c}{4U_B \sigma_T \gamma}. \tag{A.10}$$

By using Eq. A.9 and A.10 we derived the cooling time for the electrons radiating X-rays of $\epsilon$ keV in magnetic field $B$ as,

$$t_{cool} = 39\left(\frac{B}{1\mu\text{G}}\right)^{-3/2}\left(\frac{\epsilon}{1\text{keV}}\right)^{-1/2} \quad \text{kyr} \tag{A.11}$$

## A.4 Synchrotron spectrum of a power-law electron energy distribution

In the universe, relativistic electrons radiating the synchrotron emission usually have power-law energy spectra, caused by some kind of statistical particle acceleration process.

Thus radiation spectrum per unit volume of an energy distribution of $N(E)dE = \kappa E^{-p}dE$ in case of a random magnetic field can be obtained by integrating Eq. A.5 coupled with the distribution function:

$$J(\nu) = \frac{\sqrt{e3}q^3 B\kappa}{4\pi\epsilon_0 c m_e}\left(\frac{3qB}{2\pi\nu m_e^3 c^4}\right)^{(p-1)/2} a(p), \tag{A.12}$$

where

$$a(p) = \frac{\sqrt{\pi}}{2}\frac{\Gamma\left(\frac{p}{4}+\frac{19}{12}\right)+\Gamma\left(\frac{p}{4}-\frac{1}{12}\right)+\Gamma\left(\frac{p}{4}+\frac{5}{4}\right)}{(p+1)\,\Gamma\left(\frac{p}{4}+\frac{7}{4}\right)}. \tag{A.13}$$

## A.5 Equipartition Condition

By assuming the minimum energy requirements, we can briefly estimate how much relativistic particle energy there is.

Suppose a source has luminosity density $L_\nu$ at frequency $\nu$ and its volume is $V$. The spectrum of the radiation is of power-law form, $L_\nu \propto \nu^{-\alpha}$, and the emission mechanism is assumed to be synchrotron radiation. The luminosity can be related to the energy spectrum of the energy spectra of the ultra-relativisitc electrons and the magnetic filed $B$ present in the source through,

$$L_\nu = J(\nu)VN(\nu) \tag{A.14}$$

$$= A(\alpha)V\kappa B^{1+\alpha}\nu^{-\alpha}, \tag{A.15}$$

where $p = 2\alpha + 1$, and $A(\alpha)$ is a function of $\alpha$,

$$A(\alpha) = 2.344\times10^{-25}(1.253\times10^{37})^{\alpha}a(2\alpha+1). \tag{A.16}$$

The total energy present in the source responsible for the synchrotron emission is

$$W_{total} = \eta V\int_{E_{min}}^{E_{max}} E\kappa E^{-p}dE + V\frac{B^2}{2\mu_0}, \tag{A.17}$$

in which the first term and second term in the right side represent the particle energy and the magnetic energy in the source region, respectively. The constant $\eta$ accounts for the contribution from the protons. For the proton contribution we assumed a ratio of the

energies of protons to that of electrons $\mu = \epsilon_p/\epsilon_e$. The total energy including the protons can be presented by

$$\epsilon_{tot} = (1+\mu)\epsilon = \eta\epsilon_e. \tag{A.18}$$

Substituting Eq. A.15 into Eq. A.17 to cancel $\kappa$ in terms of $L_\nu$ and $B$, we obtained $W_{total}$ as a function of $B$ and $L_\nu$,

$$W_{total} = G(\alpha)\eta L_\nu B^{-3/2} + V\frac{B^2}{2\mu_0}, \tag{A.19}$$

where $G(\alpha)$ is a constant which depends weakly on $\alpha$, $\nu_{max}$, and $\nu_{min}$. From above analysis,

$$G(\alpha) = \frac{1}{a(p)(p-2)}\left[\nu_{min}^{-(p-2)/2} - \nu_{max}^{-(p-2)/2}\right]\nu^{(p-1)/2} \times \frac{(7.41\times10^{-19})^{-(p-2)}}{2.34\times10^{-25}}(1.25\times10^{37})^{-(p-1)/2} \tag{A.20}$$

The frequencies of $\nu_{min}$ and $\nu_{max}$ correspond to $E_{min}$ and $E_{max}$, respectively, and are obtained from the relation Eq. A.8.

By minimising Eq. A.19 with respect to $B$, the minimum total energy can be found;

$$W_{total}(\min) = \frac{7}{6\mu_0}V^{3/7}\left[\frac{3\mu_0}{2}G(\alpha)\eta L_\nu\right]^{4/7}, \tag{A.21}$$

at a magnetic field of

$$B_{min} = \left[\frac{3\mu_0}{2}\frac{G(\alpha)\eta L_\nu}{V}\right]^{2/7}. \tag{A.22}$$

**Assumptions in this study**

In order to calculate the magnetic field strength for the equipartition condition, we must calculate the constant $G(\alpha)$ which depends on $\nu_{max}$ and $\nu_{min}$, which are unknown in usual. Thus we adopt approximations of $\nu \sim \nu_{min}$ and $\nu_{max}^{-(p-2)/2} \sim 0$. In this study we adopt a observing frequency of $\nu = 2.4\times10^{17}$ Hz, corresponding to 1 keV X-ray photon.

The utilized data matrices of $a(p)$ and $G(\alpha)$ are shown in Figure A.1. For flatter spectra $\Gamma < 1.5$ $(p < 2.0)$, we could not neglect the contribution from $\nu_{max}^{-(p-2)/2}$, and then we could not obtain an unique value of $G(\alpha)$. We therefore used fixed values of $G(\alpha)$ for $\Gamma < 1.5$ as shown in Figure A.1.

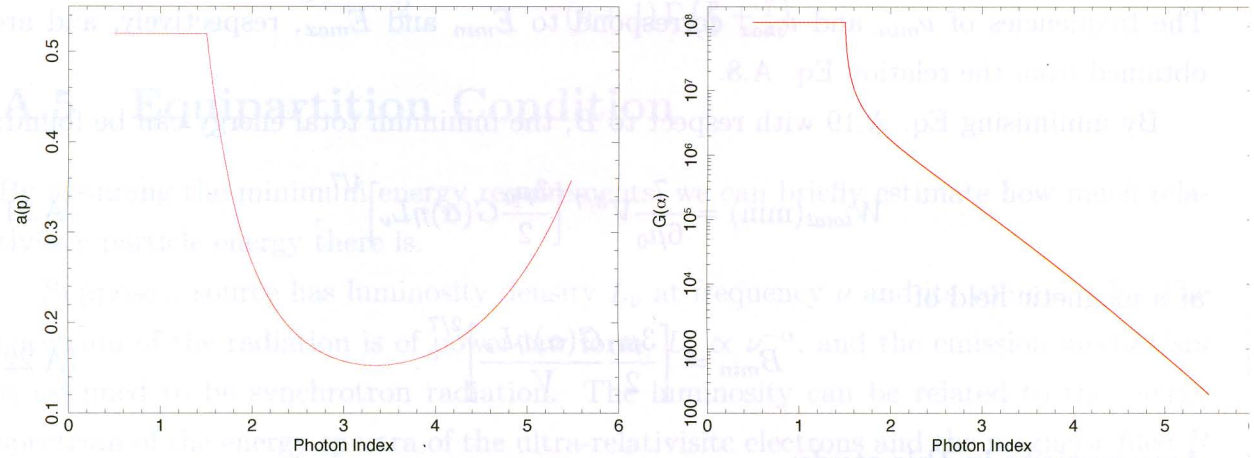


Figure A.1: Utilized data tables for $a(p)$ (Left), and $G(\alpha)$ (Right). We used fixed parameter for photon indeces of $\Gamma < 1.5 \quad (p < 2)$

# Appendix B

# Analysis

## B.1 Point source reduction and exposure correction

## B.2 Unsharp Masking technique

## B.3 Temporal analysis

### B.3.1 South jet

### B.3.2 North jet

## B.4 X-ray Spectra of RCW 89

### B.4.1 Chandra Data (ObsID: 5562)

### B.4.2 XMM-Newton Data (ObsID: 027050201)

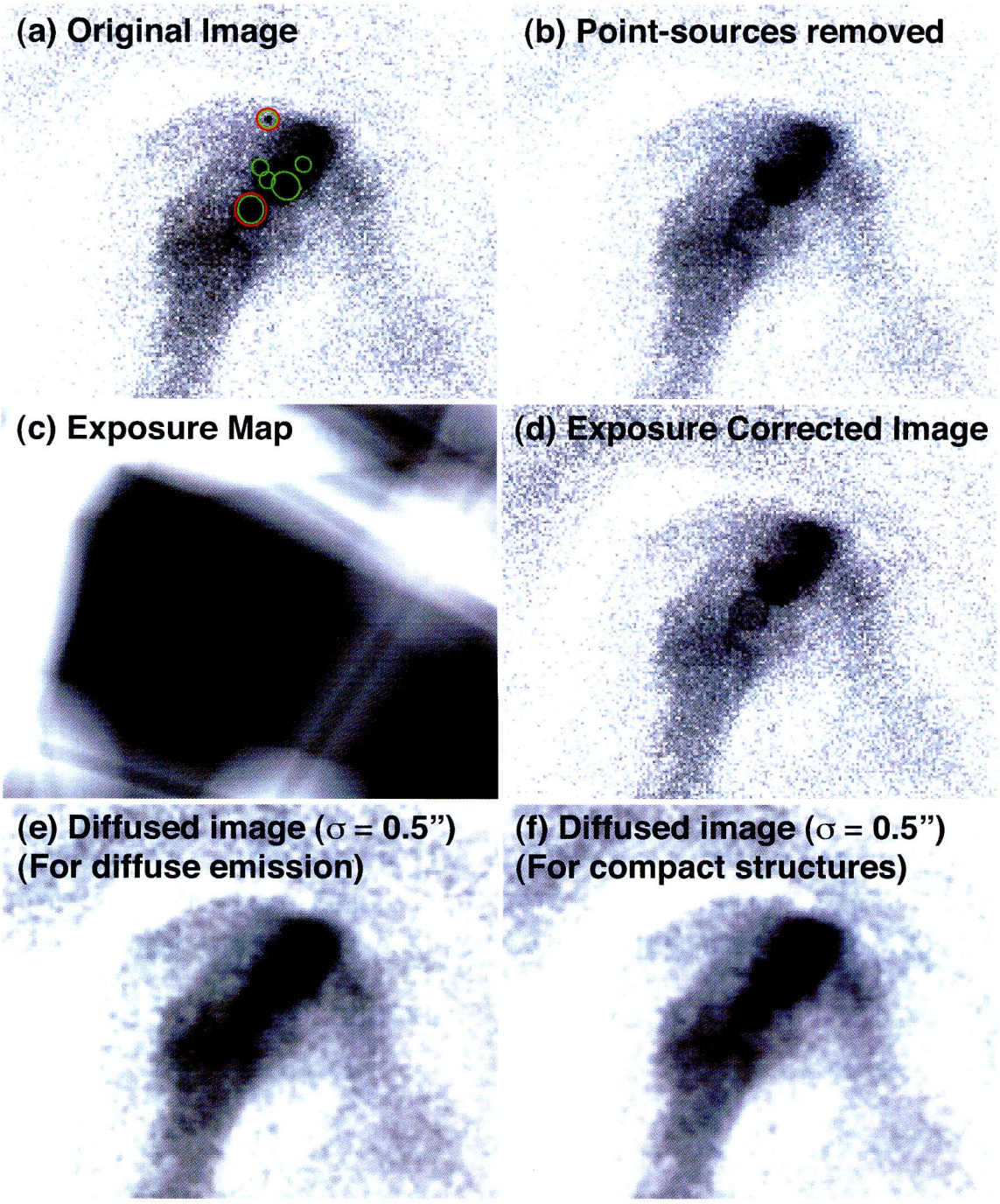


Figure B.1: Inter mediate products generated in the point source elimination process. Encircled regions in panel-(a) are removed. For low-frequency component image(panel-e), we removed all compact sources in the image (green circles), while we excluded only the pulsar and background AGN (red circles) from the image for the source image.

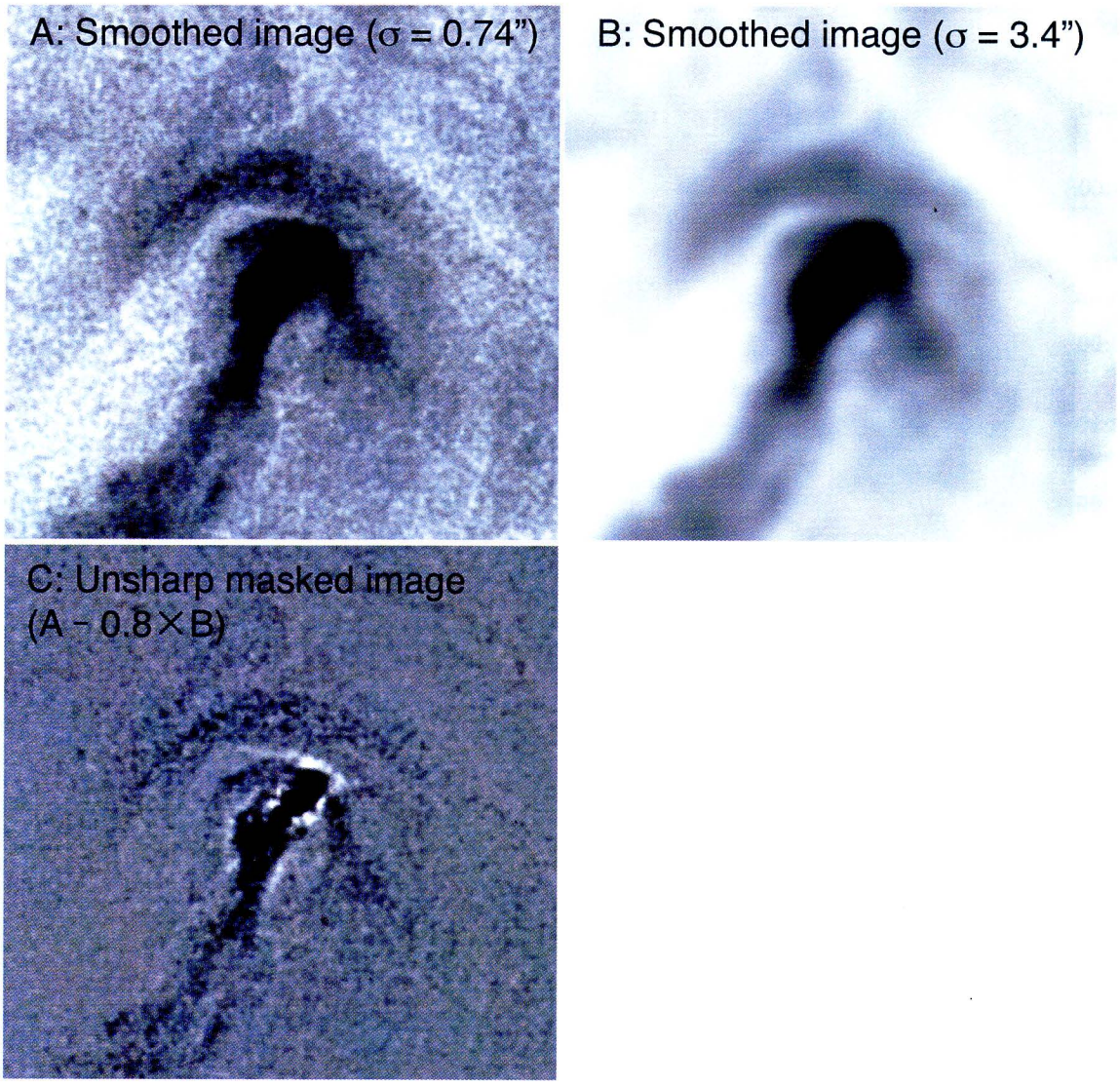


Figure B.2: Subtraction of the low frequency component (un-sharp masking). Panel-A is a source image smoothed with a Gaussian of $\sigma = 0''.74$. While panel-B is a low frequency image smoothed with a Gaussian of $\sigma = 3''.4$. Panel-C is the resultant un-sharp masked image.

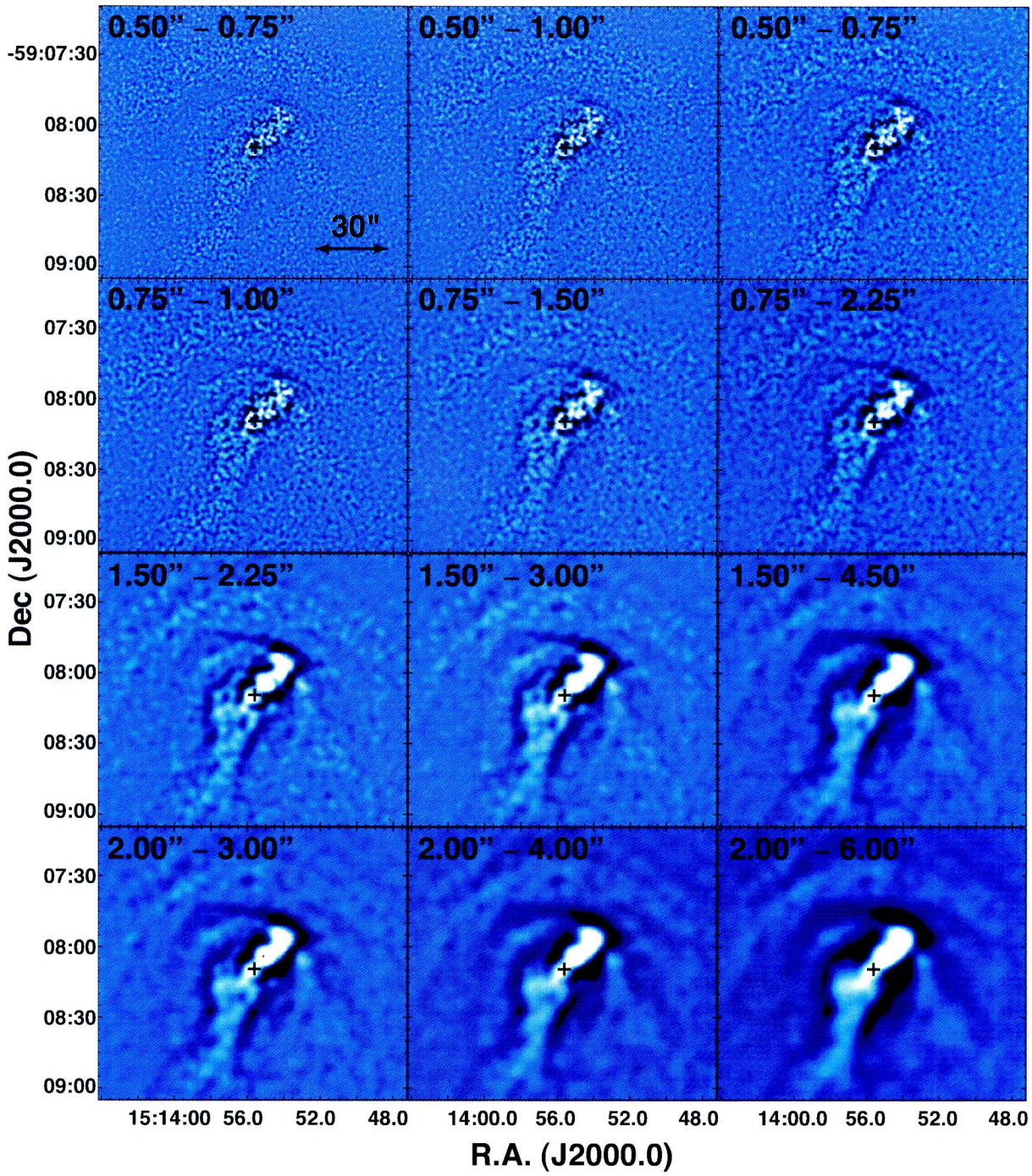


Figure B.3: Un-sharp masked images with various filtering criteria. The label in each panel indicates the radius of convolution kernels for the source image and the low-pass image, respectively. The cross marks indicate the position of the pulsar.

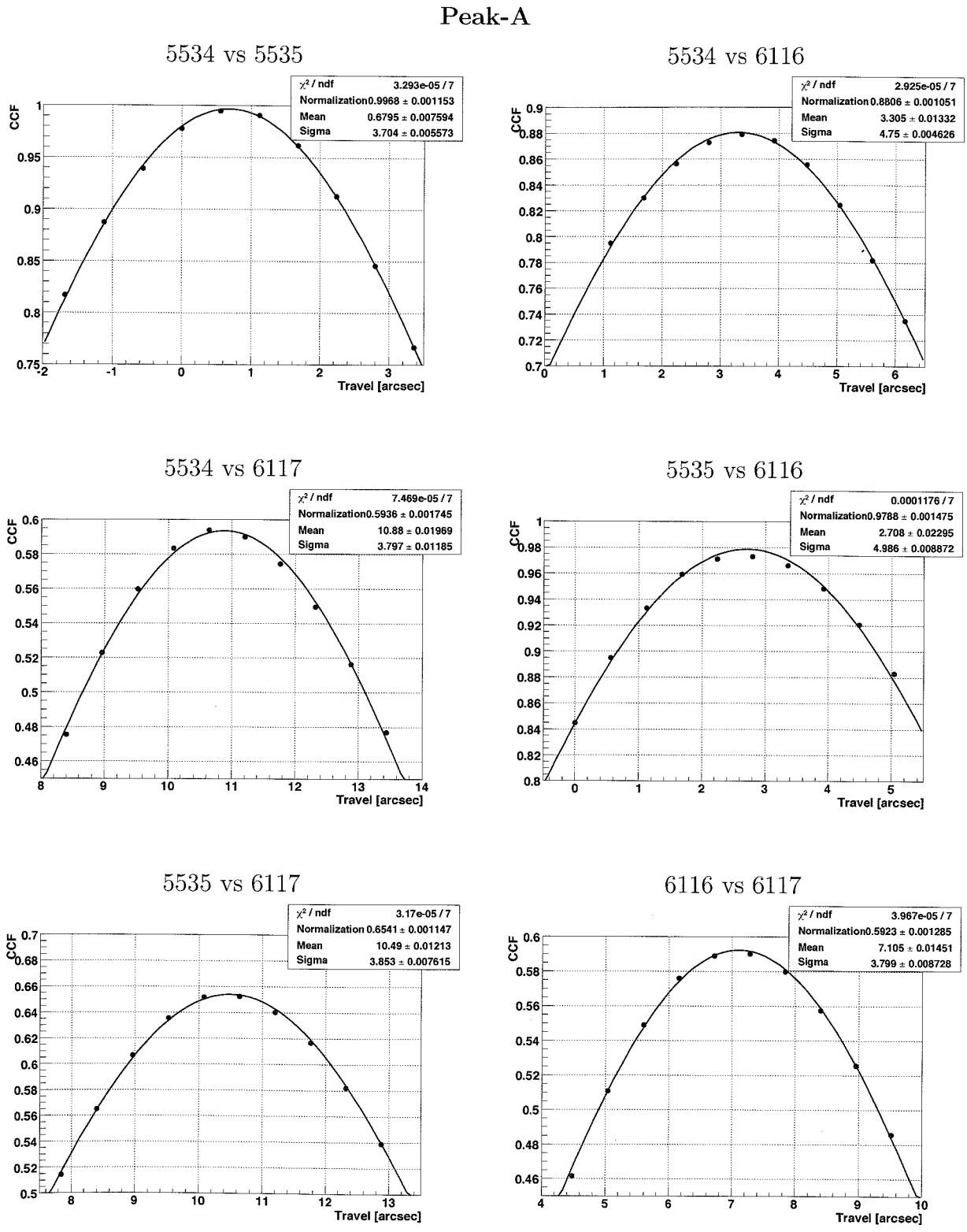


Figure B.4: Cross correlation functions of peak-A (Figure 4.18) as a function of travel distance. CCFs were integrated over $\Delta = 15$ bins. For model fittings, we adopted a Gaussian function.

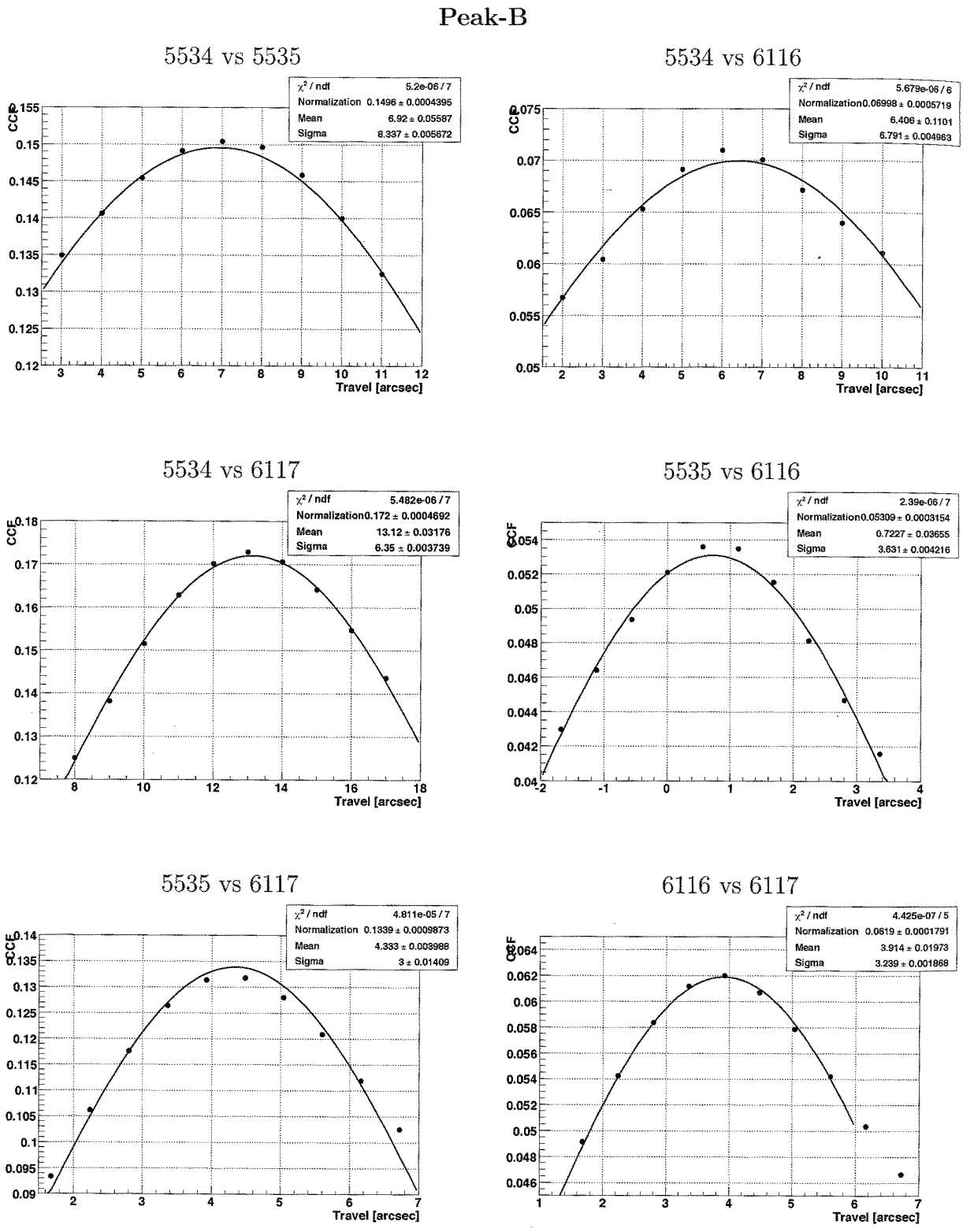


Figure B.5: Cross correlation functions of peak-B (Figure 4.18) as a function of travel distance. CCFs were integrated over $\Delta = 15$ bins. For model fittings, we adopted a Gaussian function.

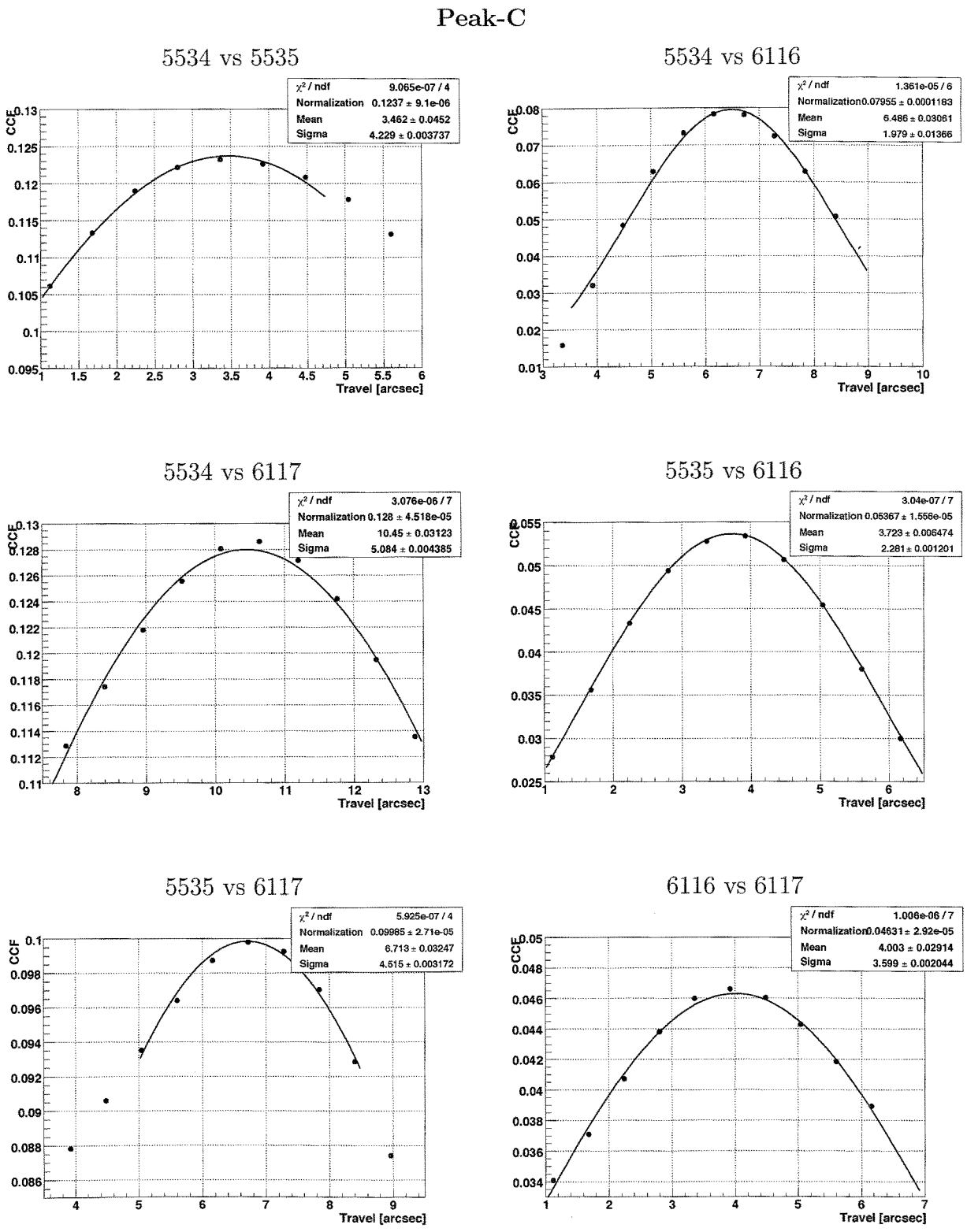


Figure B.6: Cross correlation functions of peak-C (Figure 4.18) as a function of travel distance. CCFs were integrated over $\Delta = 15$ bins. For model fittings, we adopted a Gaussian function.

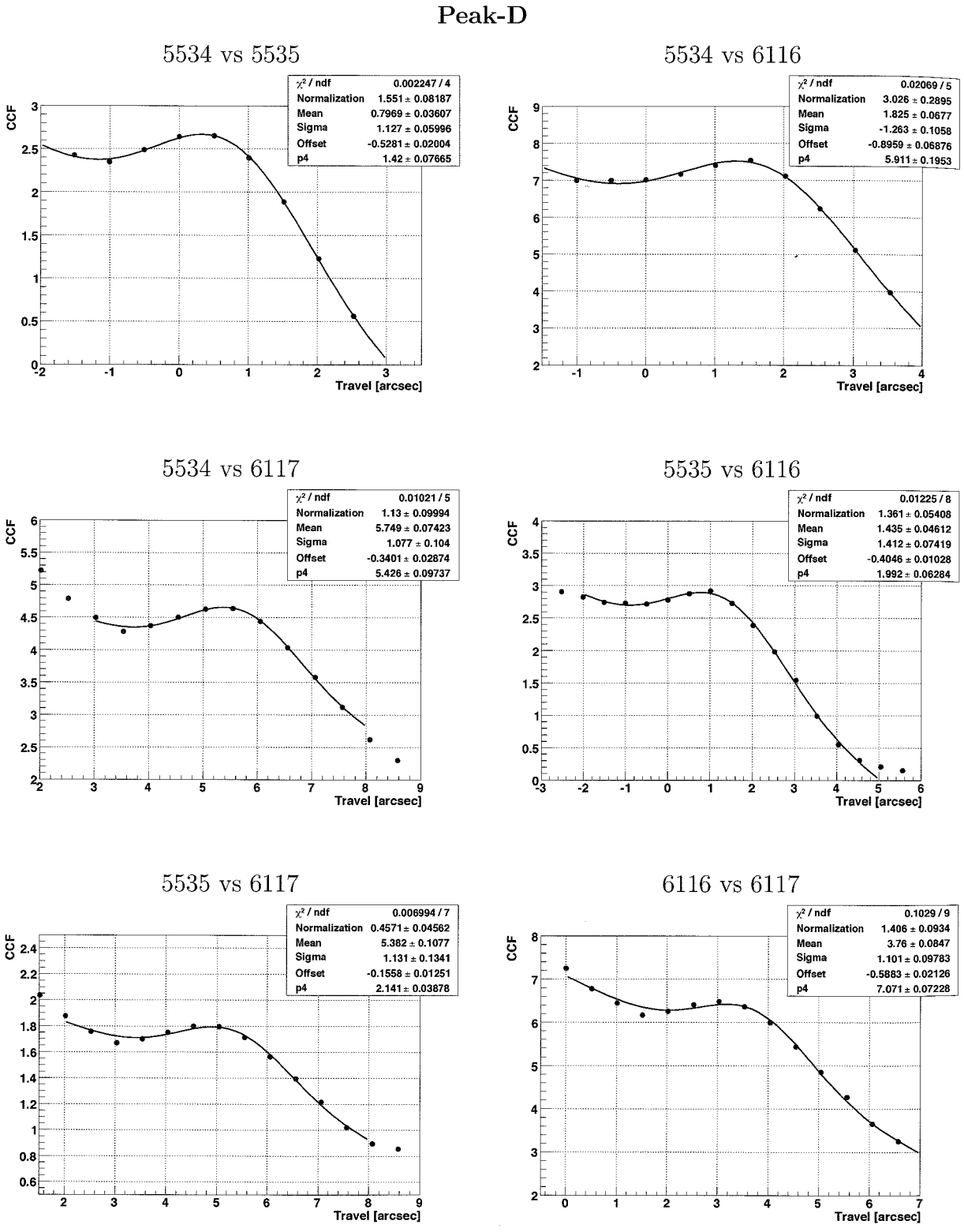


Figure B.7: Cross correlation functions of peak-D (Figure 4.18) as a function of travel distance. CCFs were integrate over $\Delta = 7$ bins. For model fittings, we adopted a two component model consisting of a Gaussian function and a linear function.

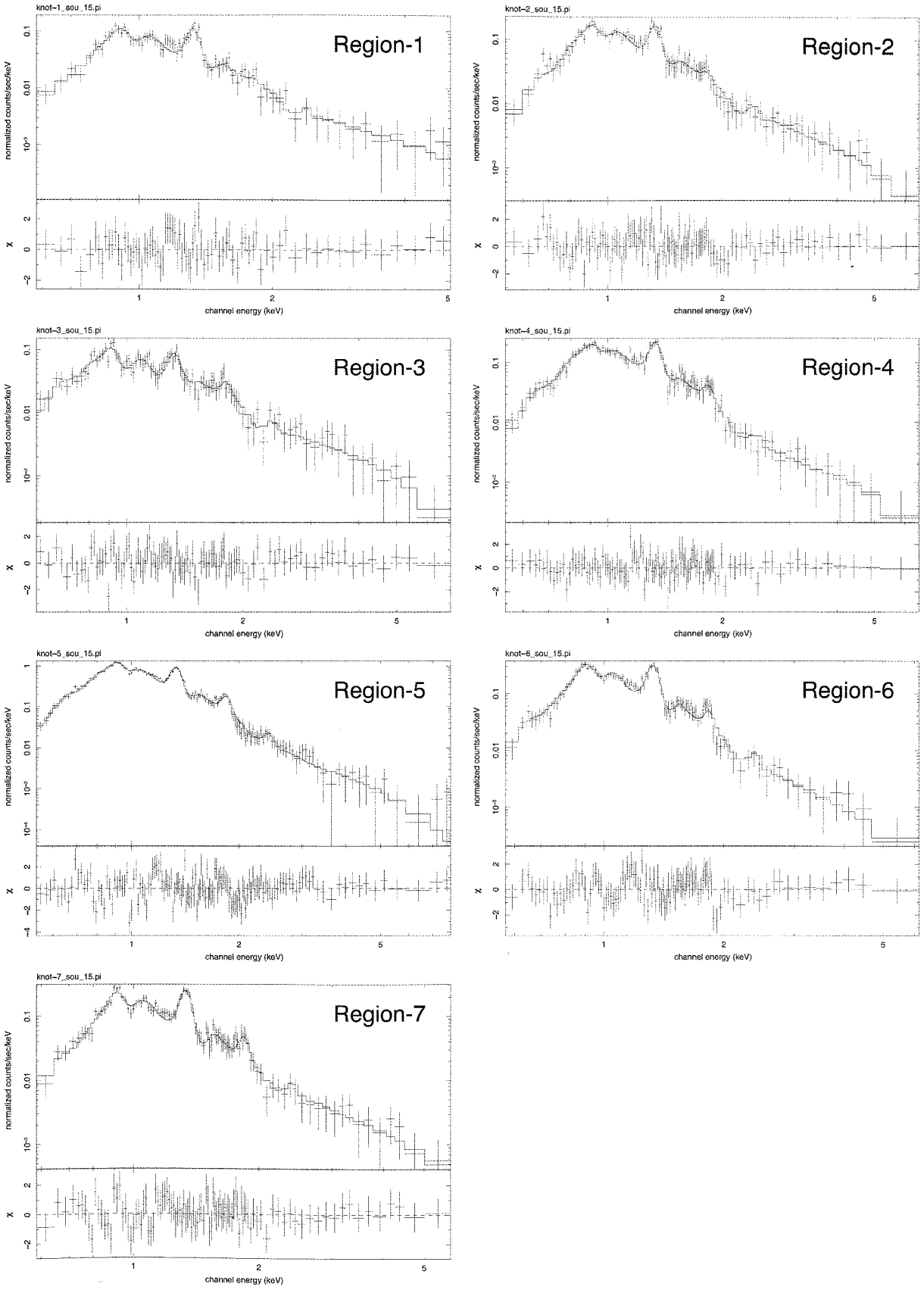


Figure B.8: Spectral fit to *Chandra* data of RCW 89 with NEI model

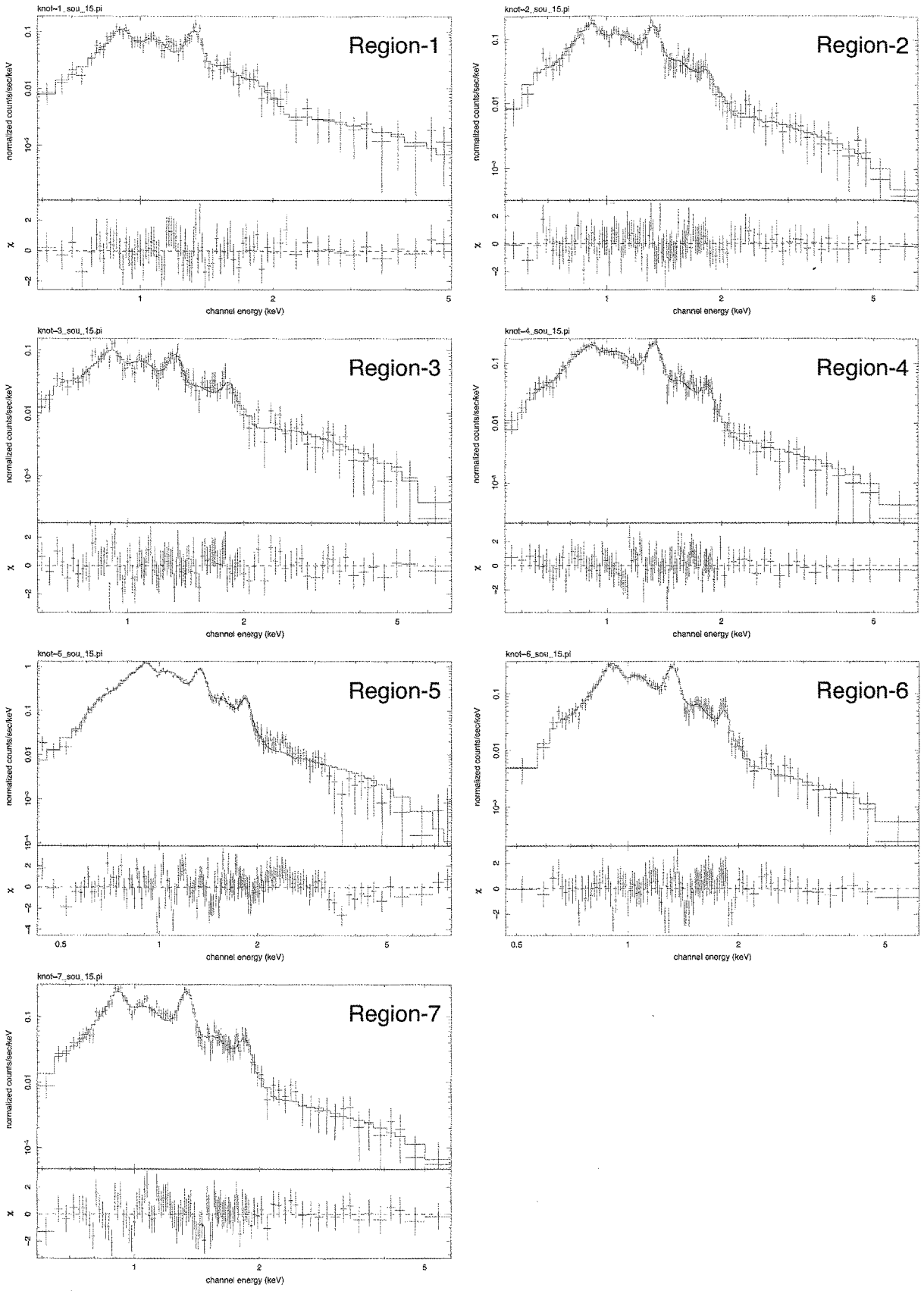


Figure B.9: Spectral fit to *Chandra* data of RCW 89 with MEKAL model

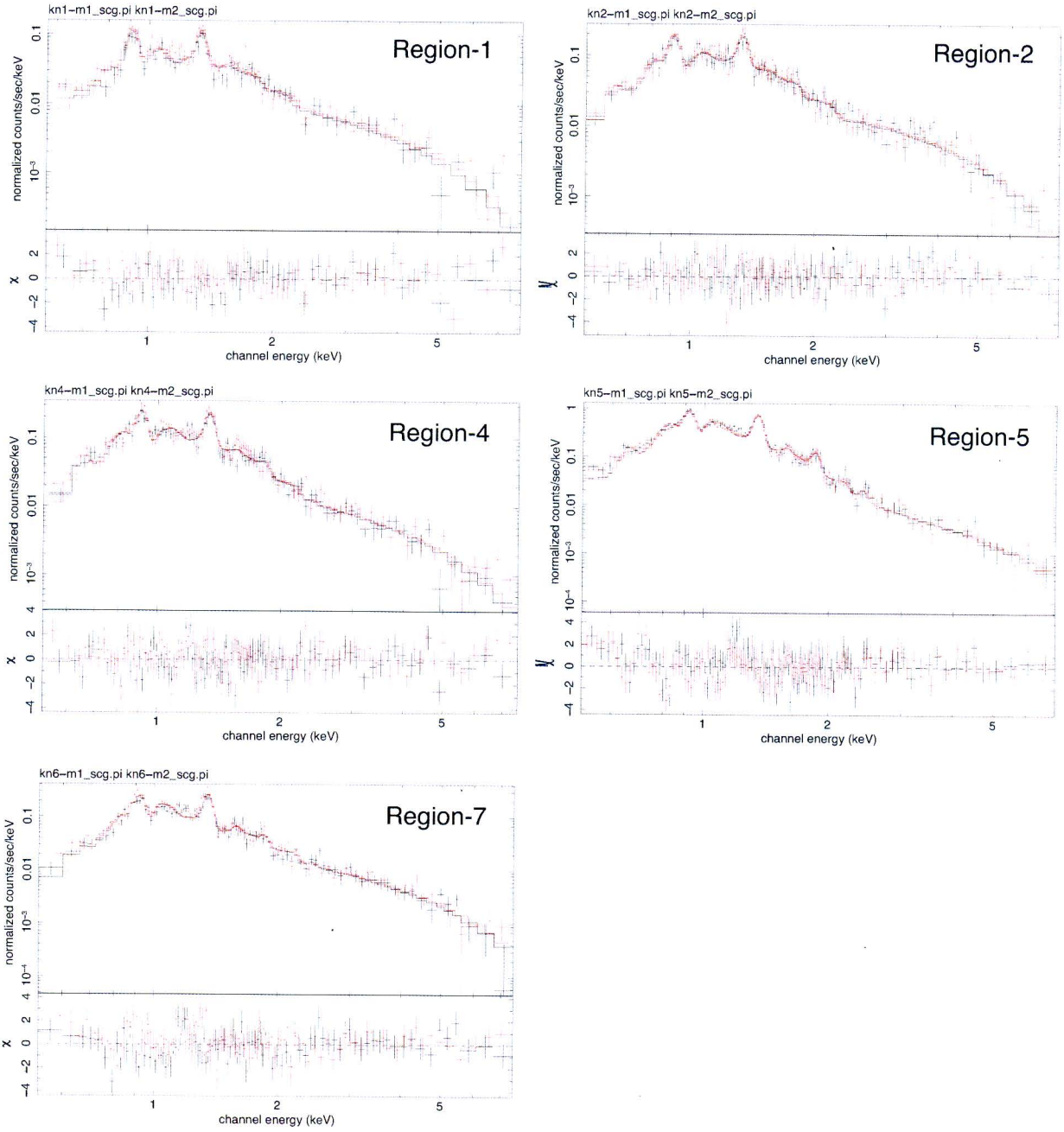


Figure B.10: Spectral fit to *XMM* data of RCW 89 with NEI model (with $N_{\rm H} = 1.18 \times 10^{22}{\rm cm}^{-2}$ and $\Gamma = 2.48$). Black and red data series are from MOS1 and MOS2, respectively.

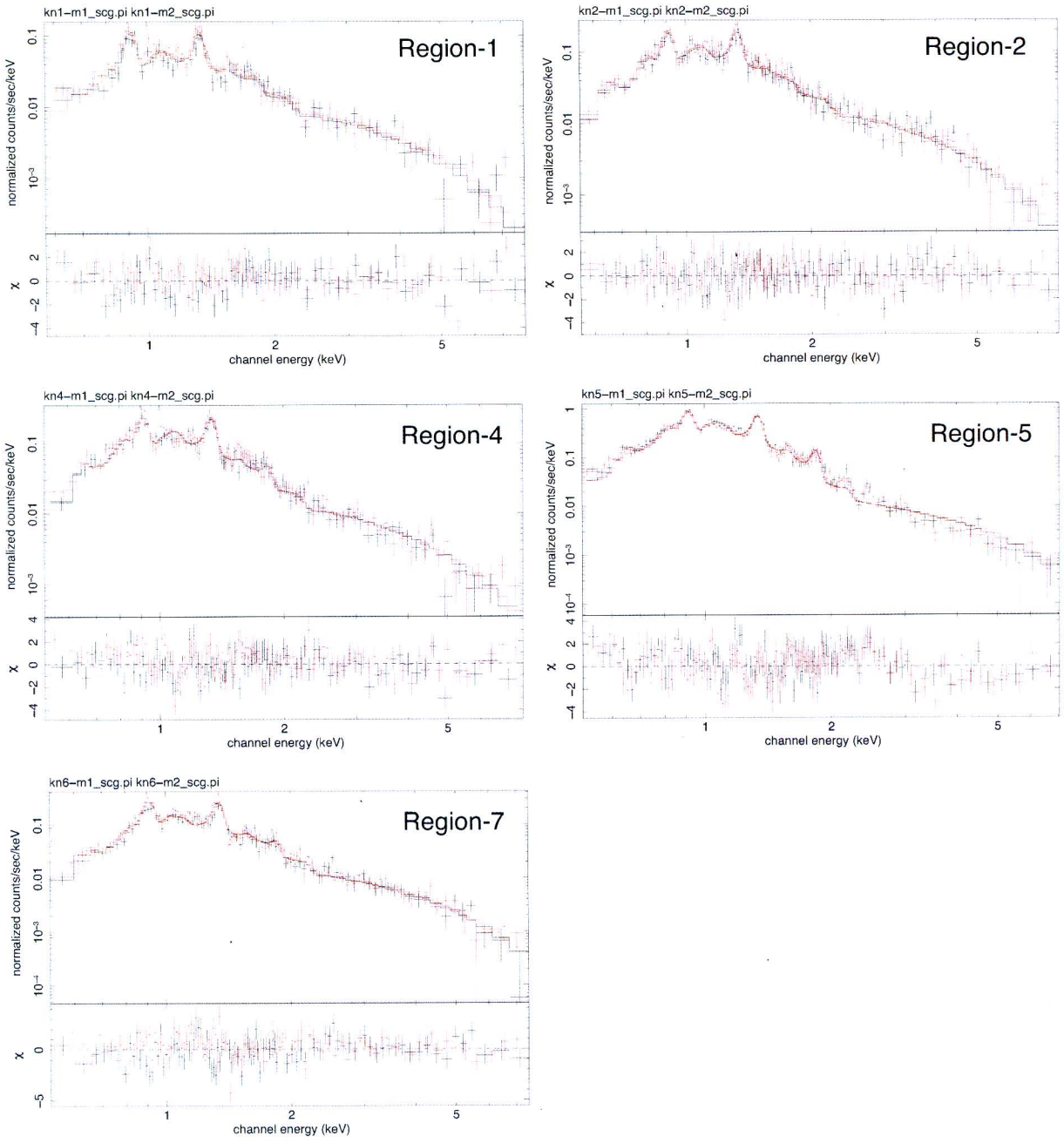


Figure B.11: Spectral fit to *XMM* data of RCW 89 with MEKAL model (with $N_{\rm H} = 1.18 \times 10^{22}{\rm cm}^{-2}$ and $\Gamma = 2.48$). Black and red data series are from MOS1 and MOS2, respectively.

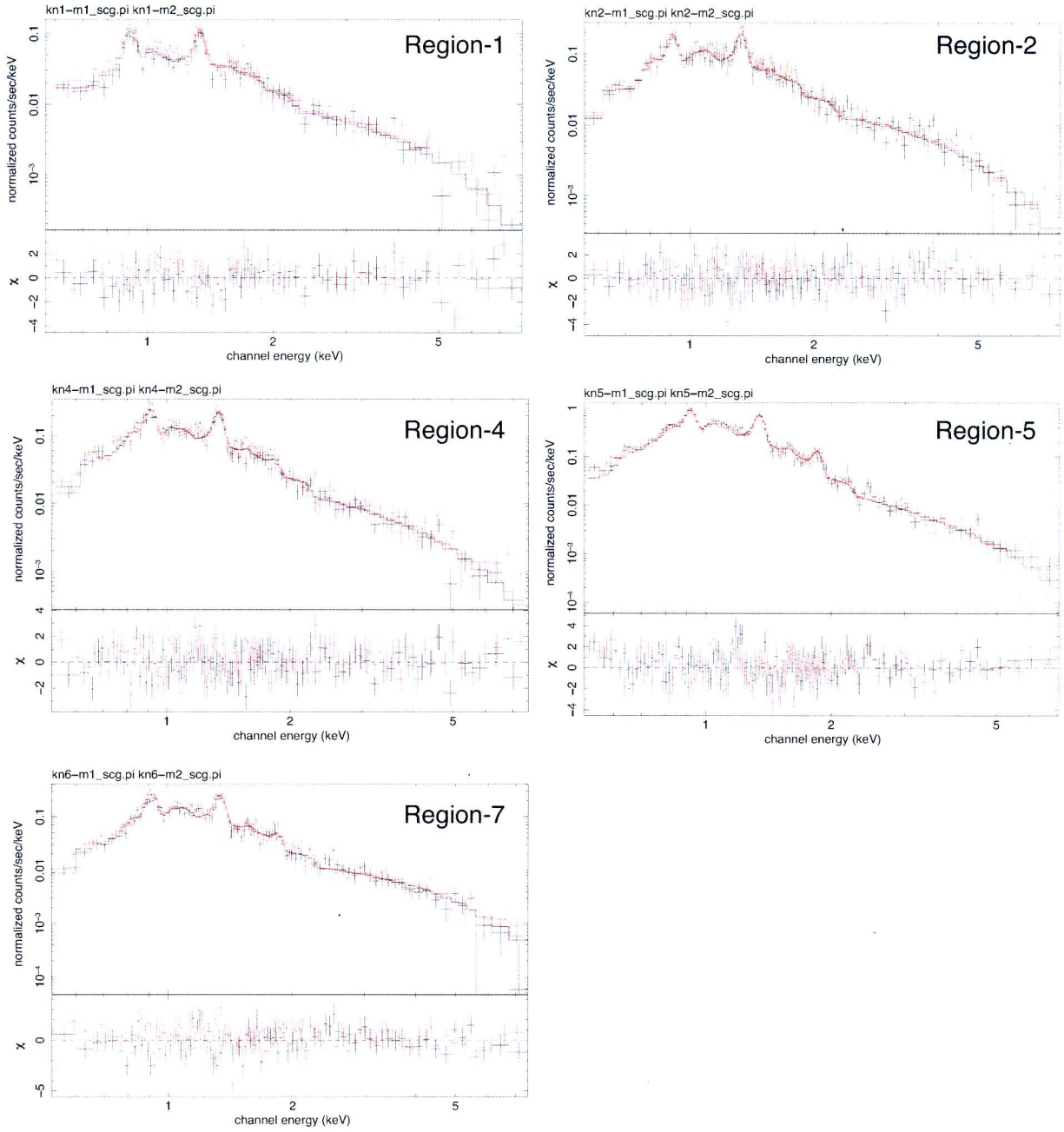


Figure B.12: Spectral fit to *XMM* data of RCW 89 with MEKAL model (with variable $N_{\mathrm{H}}$ and $\Gamma$). Black and red data series are from MOS1 and MOS2, respectively.

# Bibliography

Aharonian, F., Akhperjanian, A. G., Aye, K.-M., Bazer-Bachi, A. R., Beilicke, M., Benbow, W., Berge, D., Berghaus, P., Bernlöhr, K., Boisson, C., Bolz, O., Braun, I., Breitling, F., Brown, A. M., Bussons Gordo, J., Chadwick, P. M., Chounet, L.-M., Cornils, R., Costamante, L., Degrange, B., Djannati-Ataï, A., O'C. Drury, L., Dubus, G., Emmanoulopoulos, D., Espigat, P., Feinstein, F., Fleury, P., Fontaine, G., Fuchs, Y., Funk, S., Gallant, Y. A., Giebels, B., Gillessen, S., Glicenstein, J. F., Goret, P., Hadjichristidis, C., Hauser, M., Heinzelmann, G., Henri, G., Hermann, G., Hinton, J. A., Hofmann, W., Holleran, M., Horns, D., de Jager, O. C., Khélifi, B., Komin, N., Konopelko, A., Latham, I. J., Le Gallou, R., Lemière, A., Lemoine-Goumard, M., Leroy, N., Lohse, T., Martineau-Huynh, O., Marcowith, A., Masterson, C., McComb, T. J. L., de Naurois, M., Nolan, S. J., Noutsos, A., Orford, K. J., Osborne, J. L., Ouchrif, M., Panter, M., Pelletier, G., Pita, S., Pühlhofer, G., Punch, M., Raubenheimer, B. C., Raue, M., Raux, J., Rayner, S. M., Redondo, I., Reimer, A., Reimer, O., Ripken, J., Rob, L., Rolland, L., Rowell, G., Sahakian, V., Saugé, L., Schlenker, S., Schlickeiser, R., Schuster, C., Schwanke, U., Siewert, M., Sol, H., Steenkamp, R., Stegmann, C., Tavernet, J.-P., Terrier, R., Théoret, C. G., Tluczykont, M., Vasileiadis, G., Venter, C., Vincent, P., Völk, H. J., and Wagner, S. J.: 2005, *A&A* **435**, L17

Bogovalov, S. V.: 2001, *A&A* **371**, 1155

Brazier, K. T. S. and Becker, W.: 1997, *MNRAS* **284**, 335

Bucciantini, N.: 2006, in *36th COSPAR Scientific Assembly*, Vol. 36 of *COSPAR, Plenary Meeting*, pp 191–+

Chandra X-ray Center, *The Chandra Proposers' Observatory Guide*, http://cxc.harvard.edu/proposer/POG/html/

Chandra X-ray Center / M., Weiss, *Illustration of Chandra's Orbit*, http://chandra.harvard.edu/resources/illustrations/orbit/

Chandra X-ray Center / NGST, *View labeled sketches of the CXO*, http://chandra.harvard.edu/resources/illustrations/craftIllustrations.html

Del Zanna, L., Amato, E., and Bucciantini, N.: 2004, *A&A* **421**, 1063

DeLaney, T., Gaensler, B. M., Arons, J., and Pivovaroff, M. J.: 2006, *ApJ* **640**, 929

Dubner, G. M., Gaensler, B. M., Giacani, E. B., Goss, W. M., and Green, A. J.: 2002, *AJ* **123**, 337

Frail, D. A., Giacani, E. B., Goss, W. M., and Dubner, G.: 1996, *ApJ* **464**, L165+

Freeman, P., Doe, S., and Siemiginowska, A.: 2001, in J.-L. Starck and F. D. Murtagh (eds.), *Proc. SPIE Vol. 4477, p. 76-87, Astronomical Data Analysis, Jean-Luc Starck; Fionn D. Murtagh; Eds.*, pp 76–87

Gaensler, B. M., Arons, J., Kaspi, V. M., Pivovaroff, M. J., Kawai, N., and Tamura, K.: 2002, *ApJ* **569**, 878

Gaensler, B. M., Brazier, K. T. S., Manchester, R. N., Johnston, S., and Green, A. J.: 1999, *MNRAS* **305**, 724

Goldreich, P. and Julian, W. H.: 1969, *ApJ* **157**, 869

Helfand, D. J., Gotthelf, E. V., and Halpern, J. P.: 2001, *ApJ* **556**, 380

Hester, J. J., Mori, K., Burrows, D., Gallagher, J. S., Graham, J. R., Halverson, M., Kader, A., Michel, F. C., and Scowen, P.: 2002, *ApJ* **577**, L49

Hester, J. J., Stone, J. M., Scowen, P. A., Jun, B.-I., Gallagher, III, J. S., Norman, M. L., Ballester, G. E., Burrows, C. J., Casertano, S., Clarke, J. T., Crisp, D., Griffiths, R. E., Hoessel, J. G., Holtzman, J. A., Krist, J., Mould, J. R., Sankrit, R., Stapelfeldt, K. R., Trauger, J. T., Watson, A., and Westphal, J. A.: 1996, *ApJ* **456**, 225

Kardashev, N. S.: 1962, *Soviet Astronomy* **6**, 317

Kaspi, V. M., Manchester, R. N., Siegman, B., Johnston, S., and Lyne, A. G.: 1994, *ApJ* **422**, L83

Kennel, C. F. and Coroniti, F. V.: 1984a, *ApJ* **283**, 694

Kennel, C. F. and Coroniti, F. V.: 1984b, *ApJ* **283**, 710

Komissarov, S. S. and Lyubarsky, Y. E.: 2003, *MNRAS* **344**, L93

Lyubarsky, Y. E.: 2002, *MNRAS* **329**, L34

Manchester, R. N.: 1987, *A&A* **171**, 205

Manchester, R. N., Tuohy, I. R., and Damico, N.: 1982, *ApJ* **262**, L31

Mori, K.: 2002, *Ph.D. thesis*, Osaka Univ.

Mori, K., Burrows, D. N., Hester, J. J., Pavlov, G. G., Shibata, S., and Tsunemi, H.: 2004, *ApJ* **609**, 186

Pavlov, G. G., Teter, M. A., Kargaltsev, O., and Sanwal, D.: 2003, *ApJ* **591**, 1157

Pelling, R. M., Paciesas, W. S., Peterson, L. E., Makishima, K., Oda, M., Ogawara, Y., and Miyamoto, S.: 1987, *ApJ* **319**, 416

Rodgers, A. W., Campbell, C. T., and Whiteoak, J. B.: 1960, *MNRAS* **121**, 103

Seward, F. D. and Harnden, Jr., F. R.: 1982, *ApJ* **256**, L45

Seward, F. D., Harnden, Jr., F. R., Murdin, P., and Clark, D. H.: 1983, *ApJ* **267**, 698

Shibata, S., Kawai, N., and Tamura, K.: 1998, in N. Shibazaki (ed.), *Neutron Stars and Pulsars: Thirty Years after the Discovery*, pp 457–+

Shibata, S., Tomatsuri, H., Shimanuki, M., Saito, K., and Mori, K.: 2003, *MNRAS* **346**, 841

Tamura, K., Kawai, N., Yoshida, A., and Brinkmann, W.: 1996, *PASJ* **48**, L33

Thompson, C., Lyutikov, M., and Kulkarni, S. R.: 2002, *ApJ* **574**, 332

Trussoni, E., Massaglia, S., Caucino, S., Brinkmann, W., and Aschenbach, B.: 1996, *A&A* **306**, 581

Ulmer, M. P., Matz, S. M., Wilson, R. B., Finger, M. J., Hagedon, K. S., Grabelsky, D. A., Grove, J. E., Johnson, W. N., Kinzer, R. L., Kurfess, J. D., Purcell, W. R., Strickman, M. S., Kaspi, V. M., Johnston, S., Manchester, R. N., Lyne, A. G., and D'Amico, N.: 1993, *ApJ* **417**, 738

van den Bergh, S. and Kamper, K. W.: 1984, *ApJ* **280**, L51

van der Swaluw, E., Achterberg, A., Gallant, Y. A., and Tóth, G.: 2001, *A&A* **380**, 309

Weisskopf, M. C., Hester, J. J., Tennant, A. F., Elsner, R. F., Schulz, N. S., Marshall, H. L., Karovska, M., Nichols, J. S., Swartz, D. A., Kolodziejczak, J. J., and O'Dell, S. L.: 2000a, *ApJ* **536**, L81

Weisskopf, M. C., Tananbaum, H. D., Van Speybroeck, L. P., and O'Dell, S. L.: 2000b, in J. E. Truemper and B. Aschenbach (eds.), *Proc. SPIE Vol. 4012, p. 2-16, X-Ray Optics, Instruments, and Missions III, Joachim E. Truemper; Bernd Aschenbach; Eds.*, Vol. 4012 of *Presented at the Society of Photo-Optical Instrumentation Engineers (SPIE) Conference*, pp 2–16

Yatsu, Y., Kawai, N., Kataoka, J., Kotani, T., Tamura, K., and Brinkmann, W.: 2005, *ApJ* **631**, 312

Yatsu, Y., Kawai, N., Kataoka, J., Tamura, K., and Brinkmann, W.: 2006, *The X-ray Universe* pp 379–380

# Acknowledgement

I would like to express my deep and sincere gratitude to Prof. Nobuyuki Kawai for the persistent guidance for 6 years in Tokyo Institute of Technology from my undergraduate years. His intriguing lecture on astrophysics (particularly on pulsars) motivated me to go into astrophysics. I wish to thank Dr. Jun Kataoka for valuable advices on astrophysics and experimental technique throughout my graduate course.

I am deeply grateful to Prof. Wolfgang Brinkmann for his careful instructions in editing papers and proposals. Moreover he kindly provided me *XMM-Newton* data for this work. I would like to thank Prof. Shinpei Shibata who described for me the current theoretical understandings of pulsar wind nebulae. Prof. Koji Mori kindly provided me a copy of his PhD thesis, which is now my bible of the PWN physics. Prof. Toshio Terasawa gave me useful advices for this work. I would like to take this opportunity to thank them.

My special thanks go to Mr. Makoto Arimoto and Mr. Yoshikazu Kanai for giving their precious time on the data analysis for this work. My thanks are also due to Mr. Nicolas Vasquez for revision of the manuscript. I am thankful for all the encouragement and support from Dr. Masaru Ueno, Dr. Mikio Morii, Dr. Rie Sato, and all members of Watanabe-Kawai Laboratory.

I gratefully acknowledge the *Chandra* science team and NASA for making available the data used herein. I am very proud to use this unprecedented excellent observatory in human history.

Finally I would like to express thanks to my parents, Kunio Yatsu and Hiroko Yatsu, for giving me an opportunity to experience the frontier of space science that had been exactly my childhood dream.